

A novel microfabrication platform for hybrid multilayer MEMS

Thèse N° 9657

Présentée le 6 août 2019

à la Faculté des sciences et techniques de l'ingénieur
Laboratoire de bio- et nano-instrumentation
Programme doctoral en microsystemes et microélectronique

pour l'obtention du grade de Docteur ès Sciences

par

Nahid HOSSEINI

Acceptée sur proposition du jury

Prof. J. Brugger, président du jury
Prof. G. Fantner, directeur de thèse
Prof. H.-J. Hug, rapporteur
Dr C. Su, rapporteur
Prof. Ph. Renaud, rapporteur

2019

Acknowledgments

My PhD has been the most remarkable time of my life. The laboratory for Bio and Nano Instrumentation (LBNI) welcomed me and there, I evolved and learned how to become a researcher. Along with my scientific growth, I started my family, and now I am honored that I have a son, Michael, and I am waiting for our second child. This all happened because my supervisor, Prof. Georg E. Fantner, trusted me to start my PhD in his research group. I sincerely thank Georg, who consistently provided me with whatever resources I needed to grow in my work, be it scientific advice, financial supports, collaborations or freedom to explore new ideas. He is a man with boundless creativity and enthusiasm for research works.

I am thankful to the members of LBNI, Santiago Andany, Matthias Neuenschwander, Charlène Brillard, Melanie Hannebelle, Mustafa Kangül, Barney Drake, Bahareh Ghadiani, Samuel Leitao, Navid Asmari, Alex Eskandarian, Joelle Ven and Chen Yang as well as our administrative assistants, Mmes. Ingrid Margot, Ruth Fiaux and Tamina Sissoko for being part of my PhD journey. I would like to especially thank our former colleague, Dr. Jonathan D. Adams, who made me familiar with the microfabrication world. Former colleagues, Oliver Peric, Maja Dukic-Pjanic, Adrian Nievergelt and Pascal Odermatt, made my start in the lab exciting and smooth. My special thanks are extended to the staff of the centre of micronanotechnology (CMI), and particularly to Giancarlo Corradini for his creative ideas for wire bonding my devices. I am grateful to the members of GETec Microscopy in Vienna, Dr. Ernest Fantner, Dr. Marcel Winhold, and Dr. Chris Schwalb, whom I have had the pleasure to work during my PhD. I am thankful to Vladimir Stavrov for providing me with the necessary instrumentation and advice. I would like to express my appreciation to Prof. Andras Kis and Yen-Cheng Kung for their collaboration and helpful discussions. I would like to acknowledge the collaboration and help from Prof. Dirk Grundler, Maria Carmen Giordano, and Dr. Vinayak Shantaram Bhat.

The advice given by the thesis committee members, Prof. Hans J. Hug, Prof Chanmin Su, Prof. Jürgen Brugger, and Prof. Philippe Renaud helped me to improve my dissertation.

I would like to offer my special thanks to all of my dear friends and Sabrina Fantner for staying with us as we fumbled our way through the early days of parenthood.

I am thankful to my parents for giving me life to enjoy the sweet taste of growth. With all of my heart, I appreciate my mother's support. She has been my hero in my life not only due

to her positive attitude to life but also due to her endless support and care. Maman Zinat, Thank you!

Now it comes to my loves, my husband Hossein and my son Michael. The loving care of Hossein and his encouragement helped me to experience a joyful PhD along with my personal life within the past years. He has given up so much to make my career a priority in our lives. My sweetheart, Michael, gave me vigor and motivation with his smiles. Michael, honey, thank you for your presence and your smiles! And finally, this little one that I am carrying inside for the moment was with me during my PhD private defense. Yes, we did it together!

Lausanne, July 2019

This dissertation is dedicated to my mother, Mrs. Zinat Kamandloo!

Abstract

En microscopie à force atomique (AFM), la force d'interaction pointe-échantillon peut être mesurée à l'aide de deux techniques de détection principales : la détection par faisceau optique (OBD) et la détection électrique. Cependant, la commodité de la méthode de détection électrique pour les mesures AFM se fait au détriment d'un bruit de force supérieur à celui de la méthode optique. Dans le procédé de détection électrique, il y a un compromis à faire entre la réduction du bruit de la force et le maintien des caractéristiques du cantilever (par exemple, la fréquence de résonance, la constante de rappel et la dimension plane) dans les limites pratiques. Le cœur de mes recherches a été de développer des cantilevers hybrides multicouches à détection électrique avec une sensibilité de force supérieure d'un ordre de grandeur aux cantilevers en silicium de l'état de l'art. En utilisant une approche d'ingénierie des matériaux et des techniques de fabrication standard, les cantilevers introduits sont conçus de manière à ce qu'un noyau de polymère soit pris en sandwich entre deux films minces durs. Les cantilevers multicouches à détection électrique sont conçus pour être épais et mous. Ils combinent en conséquence une sensibilité de déflexion accrue avec une faible constante de rappel et augmentent ainsi de la sensibilité de force. Les cantilevers multicouches développés sont conçus de manière à respecter les limites pratiques d'un cantilever fonctionnel pour les mesures AFM dynamiques.

La sensibilité de force élevée des cantilevers multicouches hybrides est accompagnée d'une bande passante de détection élevée. Ceci est dû au fait que le matériau viscoélastique est la couche structurelle principale, ce qui entraîne un facteur de qualité faible et donc une bande passante élevée. En termes de vitesse d'imagerie, les cantilevers multicouches surpassent leurs homologues en silicium. En plus, ils sont hermétiquement scellés et peuvent être déployés pour une variété d'applications de microscopie à sonde à balayage (SPM) dans des liquides, ainsi que dans l'air et sous vide avec des revêtements métalliques multifonctionnels.

Le processus de fabrication adaptable des cantilevers multicouches peut incorporer des capteurs de contrainte à facteur de jauge élevé récemment développés pour une augmentation supplémentaire de la sensibilité à la déflexion. Comme preuve de concept, je montre que des piézo-résistances MoS_2 de type atomique peuvent être incorporées aux cantilevers du SU8. Cependant, les piézo-résistances MoS_2 ont une très importante résistance, ce qui a un effet

négligable sur le bruit de force des cantilevers. Une stratégie courante pour atténuer cette résistance élevée consiste à doper les piézo-résistances MoS_2 . Dans ce travail, je montre que le SU8 peut servir de couche de cantilever structurelle, de source de dopage de type n et d'une solution d'encapsulation pour les piézo-résistances MoS_2 .

Outre la résolution de la force et la capacité de suivi, la qualité et la répétabilité de toute image AFM sont également corrélées à la forme de la pointe du cantilever (netteté) et à sa durabilité. Les cantilevers en SU8 ont montré une très bonne capacité de suivi, mais les polymères sont soumis à un taux d'usure élevé en tant que matériau de pointe. Dans le cadre de mes recherches, j'ai également mis au point des méthodes de fabrication permettant d'intégrer des pointes en nitrure de silicium à faible taux d'usure dans des cantilevers SU8 purs, ainsi que dans les cantilevers multicouches à noyau de polymère.

En outre, pour prolonger la facilité d'utilisation et la polyvalence de l'AFM, un scanner en boucle fermée basé sur un capteur de déplacement piézo-résistif à paroi latérale est présenté. Un tel schéma en boucle fermée compense les non-linéarités du scanner piézo-tube, à savoir l'hystérésis, le fluage et la dérive. Ce système en boucle fermée remodèle le signal du piézo-tube via notre contrôleur Proportionnel-Intégral (PI) développé à base de FPGA.

Mots clés.

AFM, sensibilité de force, scellé hermétiquement, cantilever hybride multicouche, piézo-résistance MoS_2 , noyau en polymère, à détection électrique, SU8, durabilité de la pointe

Abstract

In Atomic force microscopy (AFM), the tip-sample interaction force can be measured through two primary detection techniques: optical beam detection (OBD) and electrical (self-sensing) readout. Compared to the optical method, the convenience of the self-sensing readout AFM measurements comes at the cost of higher force noise. In the self-sensing method, there is a trade-off between reducing the force noise and maintaining the cantilever characteristics (e.g. resonance frequency, spring constant, quality factor, and planar dimension) within the practical limits. The core of my research was the development of hybrid multilayer self-sensing cantilevers with up to one order-of-magnitude better force sensitivity than state-of-the-art silicon self-sensing cantilevers. Thanks to a material engineering approach combined with non-standard fabrication methods, the developed cantilevers are designed such that a polymer core is sandwiched between two hard thin films. The multilayer self-sensing cantilevers are designed to be thick and soft, thus combining increased deflection sensitivity with low spring constants, and hence increasing the force sensitivity.

The high force sensitivity of the hybrid multilayer cantilevers is accompanied by a high detection bandwidth in AC modes. This originates from having a viscoelastic material as the main structural layer, which causes low quality factor and hence high tracking bandwidth. In terms of the imaging speed, the multilayer cantilevers show four times faster response compared to their silicon counterparts. In addition, the hermetically sealed self-sensing multilayer cantilevers can be deployed for various scanning probe microscopy (SPM) applications in liquid as well as in air and vacuum with additional coatings.

For even further increase of the deflection sensitivity, newly developed high-gauge factor strain sensors can be incorporated to the multilayer cantilevers governed by their adaptable process flow. As a proof of concept, I show that atomically thin MoS₂ piezoresistors can be incorporated into SU8 cantilevers. However, the MoS₂ piezoresistors have very high

resistance, which has an adverse effect on the force noise of the cantilevers. One common strategy to alleviate this high resistance is doping the MoS₂ piezoresistors. In this work, I show that SU8 can act as a structural cantilever layer as well as an n-type doping source and an encapsulation solution for the MoS₂ piezoresistors.

In addition to the force resolution and the tracking ability, the quality and the repeatability of any AFM image is also correlated with the cantilever tip shape (sharpness) and durability. SU8 cantilevers have shown very good tracking ability but polymers are subjected to high wear-rate as a tip material. In the scope of my research, I have also developed fabrication recipes to integrate sharp, low wear-rate, silicon nitride tips into the pure SU8 cantilevers as well as the polymer-core multilayer cantilevers.

Furthermore, to extend the ease of use and versatility of AFM, a closed-loop scanner based on a sidewall piezoresistive displacement sensor is presented. Such a closed loop scheme compensates the piezotube scanner nonlinearities, namely hysteresis and creep. This closed-loop system reshapes the piezotube drive signal through our developed FPGA-based Proportional-Integral (PI) controller.

Keywords.

AFM, force sensitivity, hermetically sealed, hybrid multilayer cantilever, MoS₂ piezoresistor, polymer-core, self-sensing, SU8, tip durability

Table of Contents

List of abbreviations	3
1. Introduction.....	5
1.1 Atomic force microscopy	5
1.2 My thesis contribution.....	15
2. Integration of sharp silicon nitride tips into high-speed SU8 cantilevers in a batch fabrication process.....	20
2.1 Abstract.....	21
2.2 Introduction	21
2.3 Cantilever fabrication	22
2.4 Results	24
2.5 Discussion.....	27
2.6 Conclusion.....	28
2.7 Acknowledgment.....	28
3. Batch fabrication of multilayer polymer cantilevers with integrated hard tips for high-speed atomic force microscopy.....	29
3.1 Abstract.....	30
3.2 Introduction	30
3.3 Fabrication.....	31
3.4 Results	33
3.5 Discussion.....	35
3.6 Conclusion.....	36
3.7 Acknowledgments	36
4. A novel microfabrication platform for hermetically sealed, hybrid multilayer AFM cantilevers	37
4.1 Abstract.....	37
4.2 Introduction	38
4.3 Multilayer, polymer-core self sensing cantilevers.....	40
4.4 Results and discussion	42
4.5 Acknowledgment.....	46
4.6 Methods	46
4.7 Supplementary information.....	50
4.8 Microfabrication challenges.....	51
5. Self-sensing SU8 cantilevers based on MoS₂ piezoresistors.....	56
5.1 Device design and fabrication process.....	57
5.2 Characterization of MoS ₂ -SU8 cantilevers.....	58
5.3 Toward successful fabrication	59
5.4 Conclusion.....	61

6. Air and water-stable n-type doping and encapsulation of MoS2 flexible devices with SU8.....	63
6.1 Abstract	63
6.2 Introduction	64
6.3 Results.....	65
6.4 Conclusion	70
6.5 Methods.....	71
6.6 Acknowledgements.....	73
6.7 Supplementary Information.....	73
7. A monolithic MEMS position sensor for closed-loop high-speed atomic force microscopy.....	77
7.1 Abstract	78
7.2 Introduction	78
7.3 Experimental setup and controller implementation	80
7.4 Discussion	87
7.5 Conclusion	88
7.6 Methods.....	88
7.7 Acknowledgment	89
7.8 Toward further extension of the closed-loop scanner.....	90
8. Conclusion and outlook	92
8.1 Tip-integrated SU8 cantilevers	92
8.2 Tip-integrated, hybrid multilayer cantilevers.....	93
8.3 Self-sensing, hybrid multilayer cantilevers.....	93
8.4 Self-sensing SU8 cantilevers based on MOS2 piezoresistors	95
8.5 SU8, a simple and stable doping and encapsulation approach for MoS2 devices	96
8.6 Nonlinearity compensation of the AFM piezo scanners using a monolithic MEMS position sensor in a closed loop scheme	97
8.7 Overall outlook.....	97
9. Bibliography	98
10. Appendix A	109
11. Appendix B.....	114
12. CV.....	179

List of abbreviations

2D: Two-Dimensional

AFM: Atomic Force Microscopy

Al: Aluminum

AM: Amplitude Modulation

Au: Gold

BCB: Benzocyclobutene

BHF: Buffered Hydrogen Fluoride

BSG: Borosilicate Glass

CNT: Carbon Nanotube

Cr: Chromium

CVD: Chemical Vapor Deposition

DRIE: Deep Reactive Ion Etching

EBID: Electron Beam Induced Deposition

FET: Field Effect Transistor

FIB: Focused Ion Beam

FPGA: Field Programmable Gate Array

GaN: Gallium Nitride

GBL: Gamma-Butyrolactone

GF: Gauge Factor

h-BN: Hexagonal Boron Nitride

HF: Hydrogen Fluoride

HOPG: Highly Oriented Pyrolytic Graphite

HS-AFM: High Speed Atomic Force Microscopy

Inst. Amp: Instrumentation Amplifier

KOH: Potassium Hydroxide

KPFM: Kelvin Probe Force Microscopy

LEFID: Local Electric Field Induced Deposition

LOR: Lift-Off Resists

LPCVD: Low Pressure Chemical Vapor Deposition

LSNT: Low Stress Nitride

MEMS: Microelectromechanical Systems

MF: Magnetic Force Microscopy

MoS₂: Molybdenum disulfide

NEMS: Nanoelectromechanical Systems

OBD: Optical Beam Detection

PAG: Photo Acid Generator

PCB: Printed Circuit Board

PGMEA: Propylene Glycol Monomethyl Ether Acetate

PI: Proportional-Integral

PR: Photo Resist

PSD: Position Sensitive Detector

PSG: Phosphorus Silicate Glass

PS-LDPE: Polystyrene-Low Density Polyethylene

Pt: Platinum

Q-factor: Quality factor

RMS: Root Mean Squared

SEM: Scanning Electron Microscopy

Si: Silicon

SiN: Silicon Nitride

SMM: Scanning Microwave Microscopy

SOI: Silicon On Insulator

SPM: Scanning Probe Microscopy

Ti: Titanium

TIA: Transimpedance Amplifier

TMDC: Transition Metal Dichalcogenide

Chapter 1

1. Introduction

1.1 Atomic force microscopy

1.1.1 Basic operation modes

In the early 1980s, scanning probe microscopes (SPMs) amazed the world with the first real-space atomic-scale images of silicon (111) surface, with monoatomic step lines of 3-angstrom height [1]. G. Binnig, C. F. Quate and Ch. Gerber then invented atomic force microscopy (AFM) in 1986, which was one of the SPM techniques that offered a broader range of applications [2]. Principally, AFM is a force sensor that scans the sample surface and reveals the surface morphology such that the applied force on the sensor is constantly controlled. The force probe, called cantilever, is composed of three parts: a cantilever chip body, a beam and a sharp tip (Figure 1-1(a)).

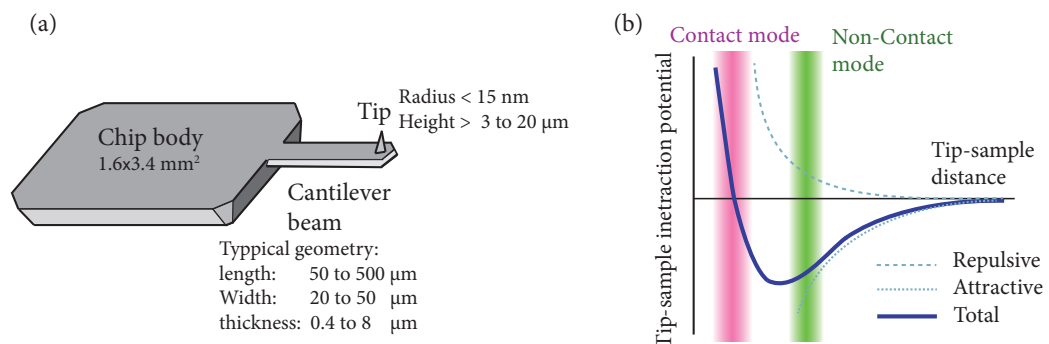


Figure 1-1 AFM cantilever detects tip-sample forces. (a) An AFM cantilever is composed of a chip body for device handling, a beam, and a fine tip. (b) The total tip-sample interaction potential at the close tip-sample distances is composed of Van der Waals attractive forces and electrostatic repulsive forces.

The Lennard-Jones interaction potential explains a qualitative sketch of the tip-sample interaction in AFM. At large tip-sample distances attractive Van der Waals forces appear,

while at short distances repulsive forces arise due to the overlap of electron orbitals of tip and sample (Pauli repulsion). Figure 1-1(b) displays how tip-sample interaction potential act at different tip-sample distances. Long-range forces (capillary, magnetic and electrostatic) are important in multiple SPM methods such as conductive force microscopy or magnetic force microscopy.

In order to keep the cantilever force at a constant value, a scanner moves the sample (sample-scan), or the cantilever (tip-scan) up and down in a feedback loop. The topography image is generated in a raster scan according to the error signal generated from the feedback controller.

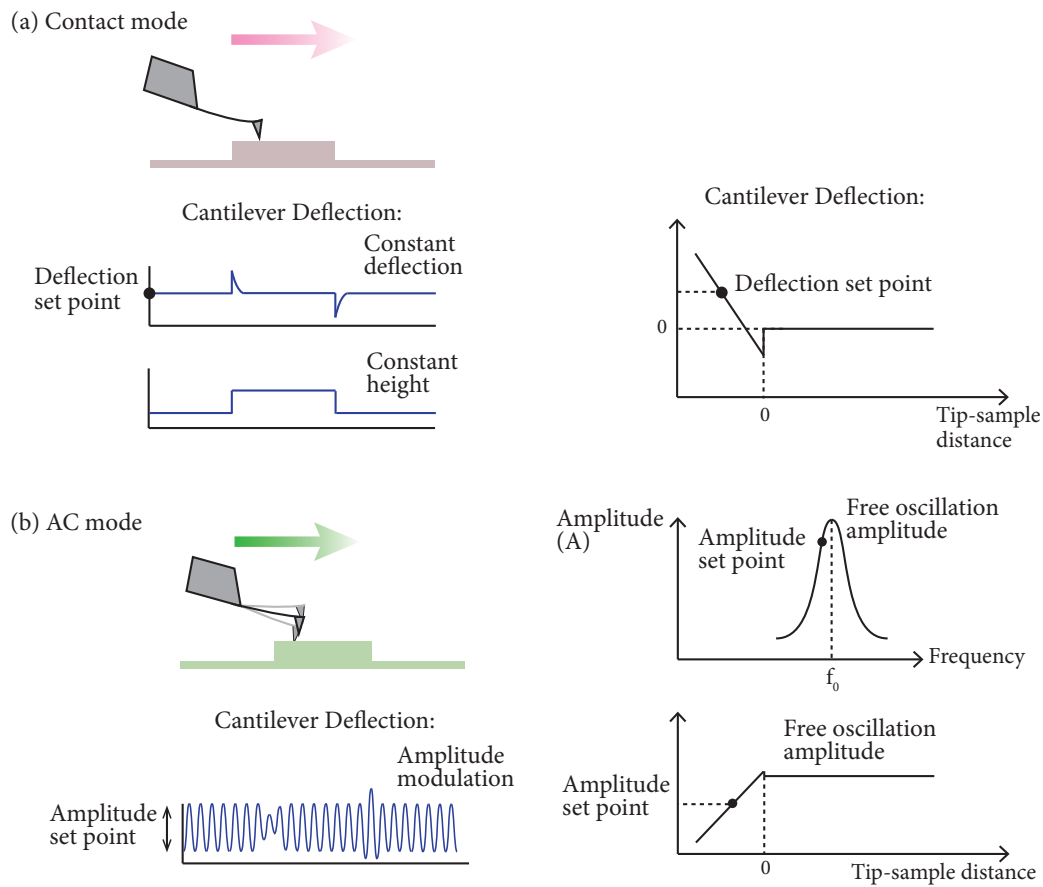


Figure 1-2 Two commonly used AFM operation modes. (a) Contact mode AFM operates based on static measurement of the cantilever deflection in a feedback loop (constant deflection) or without a feedback loop (constant height), (b) Intermittent mode operates based on exciting the cantilever at its resonance frequency and uses resonance amplitude in a feedback loop (Amplitude modulation) to control the tip-sample distance.

Contact-mode AFM:

Constant force: Once the cantilever is in the repulsive region, one can set a deflection setpoint and use the measured deflection of the cantilever as input to a feedback controller to

adjust the cantilever z-position. This technique applies large lateral forces on the sample and the cantilever tip.

Constant height: When imaging atomically flat surfaces, one straightforward approach is measuring the deflection of the cantilever when the scanner is at a fixed height with respect to the base of the tip. It means the Z-scanner is not controlled in any fashion and there is no control on the tip-sample interaction force. Figure 1-2(a) presents the principal of contact mode AFM.

Dynamic force microscopy (AC-AFM):

In 1987, Martin et al. introduced an AFM setup, which uses a vibrating cantilever that enables a precise force control near the sample surface [3]. This operation technique works based on oscillating the cantilever close to its resonance frequency at proximity to the surface. The gradient of the tip-sample interaction force modifies the effective spring constant of the cantilever and induces a change in the vibration amplitude (ΔA) due to a shift in the resonance frequency. Comparing the cantilever amplitude/frequency with the amplitude/frequency set point and modifying the Z-scanner position in a feedback loop allows for holding the tip-sample interaction force constant. Figure 1-2(b) displays the basics of AC-AFM in amplitude modulation (AM-AFM).

1.1.2 History of AFM cantilever fabrication

First AFM probes were made of a foil strip, which was etched and bent toward the sample. Fabricating these probes was very time consuming and required a lot of manual skill [4]. In 1990, Albrecht et al. introduced fabrication methods for AFM cantilevers including: 1- SiO_2 and Si_3N_4 cantilevers without tips, 2- Si_3N_4 cantilevers with integrated pyramidal tips formed by using an etched mold on the (100) plane of silicon, 3- SiO_2 cantilevers with conical tips made through a two-stage isotropic and anisotropic etching of a small silicon post, and 4- SiO_2 cantilevers with tetrahedral tips formed through anisotropic etching of a corner of a small silicon post to a sharp point [5]. In 1991, Buser et al. described meander-shape, tip-integrated monocrystalline silicon levers with a square cross section for force/friction microscopy [6]. Enormous efforts have been carried out to produce sharp AFM tips, for instance by oxide sharpening [7], nanowire attachment (e.g. silver [8], [9], GaN [10]), Chemical Vapor Deposition (CVD) growth of carbon nanotubes [11], 3D printing [12], half pyramid tip etching [13], Focused Ion Beam (FIB) tip patterning [14], [15], Electron Beam Induced Deposition (EBID) [16], [17], and Local Electric Field Induced Deposition (LEFID) [18], [19]. Most of these techniques are based on special treatments on individual cantilevers and are not part of a batch fabrication process.

1.1.3 Cantilever deflection measurement

In AFM the information about the surface topography is measured by transducing the tip-sample interaction force to an electrically measurable quantity, e.g. voltage (V). The first cantilever deflection sensor was based on electron tunneling [2], which enabled atomic-scale images, but the tunneling tip had to be a few nanometers away from the cantilever. This made operation very difficult. Very soon, other techniques were introduced where, in contrast to tunneling technique, the deflection sensors were far from the cantilever at distances from micrometers to centimeters. In 1988, Meyer et al. developed an optical approach to measure the cantilever deflection [20]. In the optical beam detection (OBD) technique, a laser beam is reflected off the backside of the cantilever and the position of the reflected spot is monitored by a position sensitive detector (PSD). In early uses of the OBD method, a small mirror was glued on the backside of the cantilever. One year later, Rugar et al. introduced a fiber-optic displacement sensor for atomic force microscopy [21]. In 2000, Brugger et al. developed a micromachining process for capacitive probes, consisting of two adjacent silicon beams with a $1.5\mu\text{m}$ air gap [22]. The tip-sample interaction force deflects the AFM beam, which changes the air gap and consequently, the capacitance between the two beams. The capacitance change was then measured through an electronic circuit [23]–[26].

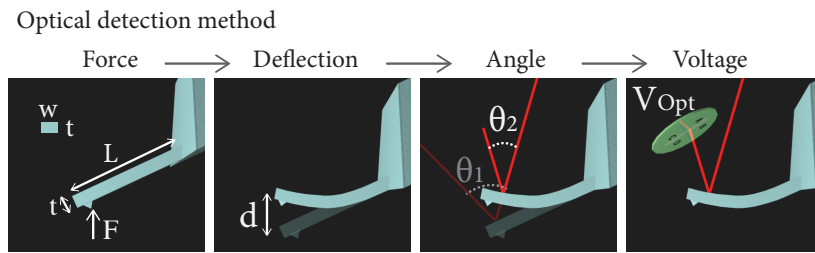


Figure 1-3 The basics of the OBD method: the tip-sample interaction force (F) is transduced to a measurable voltage (V_{Opt}).

Among abovementioned deflection measurement techniques, the OBD method has become the most popular to measure the tip-sample interaction forces. Figure 1-3 displays the basics of the OBD technique: force (F) causes deflection (d), at the free end of the cantilever, which consequently changes the bending angle (θ) of the incident laser beam and hence the position of the reflected laser beam on a quadrant photodiode.

The optical deflection sensitivity is defined as the output voltage (V_{Opt}) divided by the induced deflection (d) and is determined as follow:

$$DS_{Optical} = \frac{3 \left(1 - \left(\frac{l_b}{2L} \right)^2 \right) a}{L} \quad (1)$$

where L is the length of the cantilever and l_b is the diameter of the laser beam; and a is a constant dependent on usual sensitivity of the OBD method and is independent of how the cantilever is loaded.

The OBD method has shown excellent performance for general AFM purposes. However, it is less suitable for applications where there is no optical access to the cantilever [27], [28], in-vivo measurements [29], applications requiring multiple parallel sensors [30], or applications in automation that require levels of robustness that is difficult to achieve with the complexity of the OBD method. In addition to the development of the OBD technique, multiple techniques with on-chip deflection measurement were developed. In 1993, Tortonese et al. disclosed the first batch-fabricated silicon cantilevers with integrated piezoresistive strain sensors [31]. The cantilever deflection was measured from the resistance change of a doped silicon piezoresistor in a Wheatstone bridge configuration. Such a self-sensing scheme was then further developed including doped silicon and polysilicon piezoresistive [32]–[39], piezoelectric [40]–[43], magnetic [44], [45], and thin metal films [46], [47] techniques. In these cases, an applied force (deflection) results in a cantilever bending that introduces a strain (ϵ) at the cantilever base and is determined by the cantilever length (L) and thickness (t). This strain is then transduced to a measurable voltage (V_{Elc}) via the gauge factor ($G.F.$) of the sensing material. Figure 1-4 displays the basics of the self-sensing method, where l_s and t_s are the length and the thickness of the sensing element, respectively, and V_B is the bias voltage of the Wheatstone bridge. The deflection sensitivity for the self-sensing read-out follows the formula:

$$DS_{Self-Sen.} = \frac{3}{8} \frac{V_B G.F. \left(1 - \frac{l_s}{2L} \right) (t - t_s)}{L^2} \quad (2)$$

The deflection sensitivity in the self-sensing method scales linearly with the cantilever thickness (t). It is important to note that the optical deflection sensitivity (V_{Opt}/d) stays constant when changing the cantilever thickness.

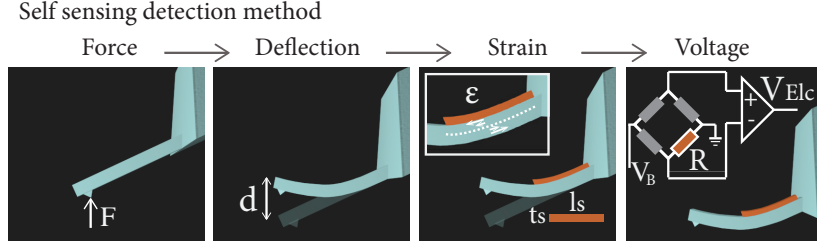


Figure 1-4 The basics of the self-sensing method: the tip-sample interaction force (F) is transduced to a measureable voltage (V_{Elc}).

1.1.4 Minimum detectable force gradient

As discussed earlier, for imaging applications in AM- AFM, the vibration amplitude (A) of the resonating cantilever (close to its resonance frequency, ω_0), provides a feedback signal that allows the tip-sample spacing to be held at a constant level. The gradient of the tip-sample interaction force (F') modifies the effective stiffness of the cantilever and hence the resonance frequency of the cantilever:

$$\tilde{k} = k - F', \quad F' = \frac{\partial F}{\partial z} \quad (3)$$

$$\tilde{\omega}_0 = \frac{1}{2\pi} \sqrt{\frac{\tilde{k}}{m_{eff}}} \quad (4)$$

where \tilde{k} and $\tilde{\omega}_0$ are the modified spring constant and the modified resonance frequency under the force gradient F' , and m_{eff} is the effective mass of the cantilever. At frequency $\omega_m \approx \omega_0(1 \pm 1/\sqrt{8Q})$, the amplitude of the cantilever vibration has the most significant change for a given $\Delta\omega$ where Q is the quality factor of the cantilever vibration.

$$\frac{\partial A}{\partial \omega} = \frac{4A_0Q}{3\sqrt{3}\omega_0} \quad (5)$$

The cantilever resonance response is steeper for a high Q -factor cantilever and, it translates to the larger change in the cantilever oscillation amplitude in response to a change in force gradient.

For $F' \ll k$, the resonance shift can be expressed as $\Delta\omega = \omega_0 F' / 2k$ which corresponds to:

$$\Delta A = \frac{2A_0Q}{3\sqrt{3}k} F' \quad (6)$$

Therefore, one can measure the change in the vibration amplitude (ΔA) in order to determine the force gradient and thus determine the force itself through numerical integration.

Measuring the minimum detectable force gradient is limited by the integrated deflection noise in the cantilever vibration amplitude. In a well designed OBD system, the thermomechanical fluctuation of the cantilever at ω_m dominates the noise and with the measurement bandwidth B , causes the relevant deflection noise:

$$N = \sqrt{\frac{4K_B T Q B}{k \omega_m}} \quad (7)$$

where K_B is the Boltzmann constant. This thermomechanical fluctuation comes from the fact that the cantilever is in thermal equilibrium with its environment. The smallest force gradient then can be obtained by setting $N = \Delta A$:

$$F'_{\min, Cl} = \frac{1}{A_0} \sqrt{\frac{27kK_B T B}{Q \omega_0}} \quad (8)$$

This means that in order to reduce the minimum detectable force gradient, the designer has to make cantilevers with low spring constant and high Q-factor.

For the self-sensing cantilevers, the deflection noises coming from the resistors have to be added to the thermomechanical noise of the cantilever. Two fundamental resistor noises include Johnson noise and flicker noise. The Johnson noise comes from the thermal motion of carriers within the resistor and is dependent on the resistance R and temperature T of the resistor. It is independent of frequency. In a balanced Wheatstone bridge, the Johnson noise is measured for a single resistor, so the overall Johnson noise voltage of the Wheatstone bridge in the frequency bandwidth B is:

$$\bar{V}_J = \sqrt{4K_B T R B} \quad (9)$$

The flicker noise is caused by the defects in the bulk of the material and causes fluctuation in the resistor conductance. The flicker noise depends on the bias voltage and is inversely proportional to the number of carriers in the resistor.

$$\bar{V}_f = \sqrt{\frac{\alpha V_{bridge}^2}{2N} \ln\left(\frac{f_{\max}}{f_{\min}}\right)} \quad (10)$$

The parameter α depends on the crystal lattice quality and is measured experimentally. In this formula, f_{\max} is the upper measurement frequency, and f_{\min} is the lower frequency ($B=f_{\max}-f_{\min}$).

The overall root mean square voltage noise of the resistor R is the sum of the uncorrelated noise sources:

$$\bar{V}_R = \sqrt{V_J^2 + V_f^2} \quad (11)$$

The deflection noise associated with the resistor R in the self-sensing method is inversely proportional to the cantilever deflection sensitivity ($DS_{Self-Sen.}$) through the following equation:

$$F'_{\min, Elc} = \frac{1}{A_0} \times \frac{\bar{V}_R}{DS_{Self-Sen.}} \left(\frac{3\sqrt{3}k}{2Q} \right) \quad (12)$$

This means in addition to the cantilever thermomechanical noise, the minimum detectable force gradient in the self-sensing method is limited by the integrated voltage noise resulting from the resistance R . This extra voltage noise, \bar{V}_R , makes the self-sensing method ill-suited for measuring small force gradients. However, in the repulsive regime, the force gradient is high compared to the small force gradients in the attractive regime.

1.1.5 Force sensitivity

Force sensitivity, defined as V/F , is a measure of how precisely the cantilever responds to the external forces and is obtained by dividing the deflection sensitivity (V/d) over the spring constant (F/d). The analytical formula for the optical force sensitivity (V_{Opt}/F) is:

$$FS_{Optical} = \frac{12L^2 \left(1 - \left(\frac{l_b}{2L} \right)^2 \right) a}{EWt^3} \quad (13)$$

where L , W , t and E are length, width, thickness and Young's modulus of the cantilever respectively.

For the self-sensing cantilevers, the force sensitivity is obtained as:

$$FS_{Self-Sen.} = \frac{3LV_B GF \cdot \left(1 - \frac{l_s}{2L} \right) \left(1 - \frac{t_s}{t} \right)}{2EWt^2} \quad (14)$$

To increase the electrical force sensitivity (V_{Elc}/F), much effort had gone in improving the transduction of strain into voltage [35], [48]–[50]. Another way is to increase the transduction from force to strain, which can be achieved through geometric optimization.

As mentioned earlier, the strain varies linearly with the thickness of the cantilever, with the strain in the neutral axis of the cantilever being zero, and maximum at the top and bottom sides. This offers the possibility to obtain very high deflection sensitivities (V_{Elc}/d) by making the cantilever thicker [51]. Unfortunately, this also increases the cantilever spring constant and is therefore detrimental to the force sensitivity. The spring constant $k = EWt^3/4L^3$ is proportional to the cube of the cantilever thickness and also Young's modulus of the cantilever material. One approach to increase the electrical force sensitivity is to decrease the

cantilever spring constant by reducing the thickness while accepting that the electrical deflection sensitivity is decreased too. As long as the spring constant goes down faster than the deflection sensitivity, this results in a net gain in force sensitivity. Reducing the cantilever spring constant by reducing the thickness has yielded good force sensitivity for static applications [46], [52]. For dynamic measurements, the resonance frequency of the cantilever, and the minimum required thickness of the sensing material creates a limit of how thin the cantilever can be.

1.1.6 Cantilever mechanical bandwidth

The resolution of cantilever deflection measurements is strongly dependent on the measurement techniques and detection bandwidth of the cantilever [53]. The detection bandwidth is a measure of how fast a cantilever response to external inputs and is of great concern for AFM measurements.

By growing the applications of AFM, increasing of nanocharacterization speed has also been one of the main driving forces in development in the AFM field [54]–[57]. Every major supplier has brought a high-speed AFM (HS-AFM) on the market during the last five years. However, the speed limit in large part is still due to AFM cantilever detection bandwidth. The mechanical bandwidth of a cantilever operated in AC mode is proportional to the ratio ω_0/Q , where ω_0 is the fundamental resonance frequency and Q is the quality factor (Q-factor) of the cantilever. The Q-factor of an oscillating cantilever can be measured through the mean stored energy divided by the dissipated energy per cycle.

A cantilever working in tapping mode has the equation of motion:

$$m\ddot{z}(t) + \frac{m\omega_0}{Q}\dot{z}(t) + kz(t) = A\sin(\omega_d t) + F(z) \quad (15)$$

where m is the effective mass of the cantilever, z is vertical tip displacement, k is the cantilever spring constant, A and ω_d are the cantilever drive signal and the excitation frequency respectively. In this formula, $F(z)$ is the tip-sample interaction force.

When an oscillating cantilever experiences a change in the boundary condition (topography change), it requires several cycles to reach its new steady state amplitude. A cantilever with higher resonance frequency goes through this number of cycles faster. The transient response due to topography changes follows an exponential path with a time constant inversely proportional to Q-factor. Therefore, a cantilever with lower Q-factor requires less number of cycles to pass the transient response.

In 1993, Mertz et al. [58], and in 2000, Sulchek et al. [59] showed that one could modify the Q-factor externally using active Q control, which is based on velocity ($\dot{z}(t)$) feedback, to

suit the imaging speed (see Figure 1-5). The probe velocity is accessible by differentiating the displacement signal, or by shifting the displacement phase by $\pi/2$, through a control circuit. The drawback of the differentiation method is that it amplifies the high-frequency noise signals. Using the approach of $\pi/2$ phase shift in a feedback loop, $Q(s)$ has the transfer function of:

$$Q(s) = G e^{-T_d s} \quad (16)$$

when applied to the cantilever sinusoidal displacement, $Q(s)$ applies gain G and delays the cantilever displacement signal by $T_d = \pi/2$. The modified Q-factor then takes the form of:

$$Q_{Controlled} = \frac{1}{\left(\frac{1}{Q} + \frac{G}{m\omega_0} \right)} \quad (17)$$

This method increases the risk of instability when reducing the Q-factor due to pushing the poles of the second resonance mode closer to the $j\omega$ axis (resulted from the phase delay for a high value of G). In an attempt to find a solution for the instability problems associated with the Q-factor control, in 2013, Fairbarin and Moheimani introduced a resonant controller to modify the Q-factor. Their technique relies on approximating a differentiator over narrow range frequencies and applying a gain at those frequencies [60].

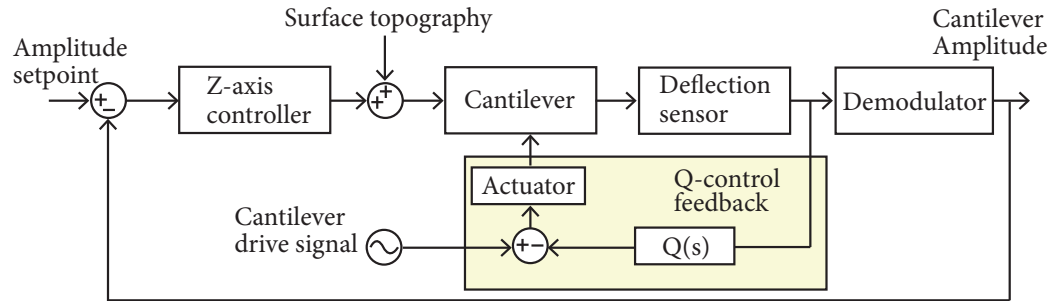


Figure 1-5 The schematic of the Q-control feedback loop inside the z-axis feedback loop.

To avoid the need for an additional controller circuit for high-speed applications, one appropriate technique would be decreasing the Q-factor and increasing the resonance frequency of the cantilever through cantilever material engineering. The fundamental resonance frequency of a rectangular cantilever beam is defined as $f_0 = \frac{0.56}{L^2} \sqrt{\frac{I}{A}} \sqrt{\frac{E}{\rho}}$, where I is the second moment of area and A is the cross-sectional area of the cantilever beam. In this formula, E and ρ are Young's modulus and the density of the cantilever material, respectively. A main area of research has been in the speed increase through miniaturization of the cantilevers [55]. However, cantilevers cannot be made infinitely small for imaging due to

practical limits. As the size of the cantilever becomes smaller than the size of the laser spot ($2\mu\text{m}$ - $10\mu\text{m}$), it becomes necessary to develop customized detection hardware [61].

Adams et al. [62] have shown that by making cantilevers out of polymers, the Q-factor reduces due to intrinsic damping properties of viscoelastic materials. It was demonstrated that the imaging bandwidth of SU8 cantilevers is more than one order of magnitude higher compared to commercial silicon cantilevers for identical planar geometries, spring constants and resonance frequencies. However, polymer tips are subjected to high wear-rate [63], which causes serious image artifacts. Given the fact that any AFM image is a convolution of the surface features and the tip shape, damaged tips can potentially produce deceptive patterns and mislead AFM users.

1.2 My thesis contribution

1.2.1 Integration of silicon nitride tips into high-speed polymer cantilevers in a batch fabrication process

The early goal of my PhD research was integrating “hard tips” into the SU8 cantilevers to improve the image quality and repeatability. In this scope, I developed a microfabrication process for integrating moulded silicon nitride tips into the SU8 cantilevers in a batch fabrication process. The main concept of my work was to partially embed the moulded silicon nitride tip into the cantilever beam such that the tip protrudes out from the surrounding polymer. The probes then have the benefit of fast mechanical responses governed by the polymer beam along with tips made of materials with acceptable durability. Chapter 2 of my thesis is dedicated to this work and the achieved results.

1.2.2 Hermetically sealed, multilayer self-sensing cantilevers

The low Q-factor of polymer cantilevers comes at a price of low mechanical excitation efficiency when shaking the cantilever at resonance with a dither piezo. The low excitation efficiency burdens practical difficulties to locate the fundamental resonance frequency accurately among parasitic peaks. The second stage of my research was developing a wafer-scale microfabrication process to address the problem mentioned above. The principal of our technology is the use of non-traditional MEMS materials in combination with traditional MEMS materials and fabrication methods to make hybrid multilayer AFM cantilevers. The fabrication process is based on polymer bonding of two pre-processed wafers, with subsequent release of the multilayer cantilever via KOH wafer through etching. The fabricated cantilever is then composed of a polymer core, encapsulated between two hard thin films (e.g. silicon nitride) where the cantilever tip is made of silicon nitride, and the cantilever chip body

is made of silicon. The Q-factor of hybrid multilayer cantilevers is higher than pure SU8 cantilevers but still lower than traditional cantilevers. This work is presented in chapter 3 of my thesis.

By introducing the multilayer technology, we propose an alternative way to increase the electrical force sensitivity of the self-sensing cantilevers by increasing the cantilever thickness, while maintaining the spring constant at a low level. We have developed AFM cantilevers consisting of a polymer core and embedded electronic strain sensors, sandwiched between ultra-thin silicon nitride layers (with high in-plane stiffness and low out-of-plane stiffness). By making the bulk of the cantilevers out of polymer (which is much softer than conventional AFM cantilever material), we can design our cantilevers to be thick, yet still soft. The increased thickness directly translates to an increased strain at the outer layer of the cantilever, where the strain sensors are located (see Figure 1-6).

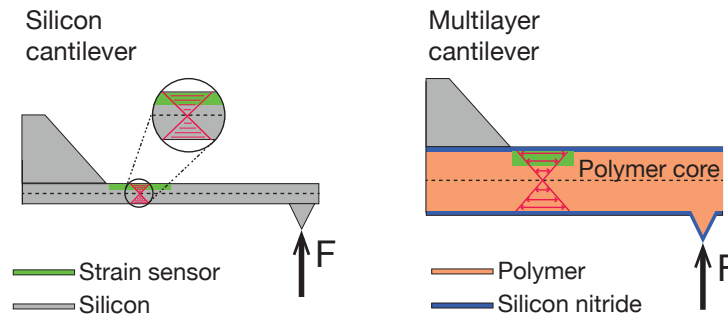


Figure 1-6 The schematic of a self-sensing silicon cantilever compared to a self-sensing multilayer cantilever. Red lines shows how strain is distributed along the cantilever thickness. Strain varies linearly with the cantilever thickness. A multilayer cantilever is composed of a polymer core sandwiched between two hard thin films (silicon nitride). Compared to the silicon cantilever, a multilayer cantilever can be made thick but still soft. Hence, the deflection sensitivity is larger for a multilayer cantilever compared to a silicon cantilever with the same planar dimension and similar cantilever stiffness.

The developed self-sensing hybrid multilayer cantilevers have shown up to one order of magnitude better force sensitivity, compared to state-of-the-art silicon self-sensing AFM cantilevers. This is achieved while they still meet the practical limits (resonance frequency =10kHz-1MHz, $k=0.1-60\text{N/m}$) of a functional cantilever for dynamic AFM measurements. The multilayer geometry has an advantage over pure polymer cantilevers that a thin layer of hard material distributes the strain in the plane of the cantilever to avoid local stiffening and stress concentration [64].

Self-sensing AFM cantilevers are of particular interest for applications where bulky OBD measurements are difficult to implement, such as in a vacuum chamber of an SEM. In this work, we show that the self-sensing multilayer cantilevers allow for higher scan rates compared to their silicon counterpart, governed by the low Q-factor of the multilayer cantilevers.

The fabrication procedure of the self-sensing multilayer cantilevers allows for embedding the strain sensing elements safely inside, hence we can expand the use of self-sensing multilayer cantilevers to applications where the cantilever and the tip need to be coated with electric or magnetic materials, for instance, magnetic force microscopy (MFM) and Kelvin Probe Force Microscopy (KPFM). Furthermore, hermetically sealed self-sensing multilayer cantilevers can be immersed in opaque, salty and corrosive liquids due to the high chemical resistance of the cantilever shell material (e.g. silicon nitride). In this work, I have presented the applications of the self-sensing multilayer cantilevers in liquid, as well as in MFM and KPFM measurements. Chapter 4 of my thesis is dedicated to this work and the achieved results.

The flexible microfabrication recipe of our multilayer MEMS devices is developed such that it welcomes newly developed strain sensing elements. By incorporating high G.F. sensing elements, for example, MoS₂ piezoresistors, we can still gain in terms of the deflection sensitivity.

1.2.3 MoS₂ based self-sensing cantilevers, fabrication and doping/encapsulation strategies

Molybdenum disulfide (MoS₂) is classified as a transition metal dichalcogenides (TMDCs). Under applied strain, atomically thin MoS₂ shows piezoresistive effect determined by the rate of band-gap change and hence, the electrical conductivity change [65]. The gauge factor of bilayer MoS₂ piezoresistors is around 200, which is about one order of magnitude higher than polysilicon. From the mechanical point of view, MoS₂ has a high Young's modulus of ~ 270 GPa, and it can withstand in-plane strain levels as high as 11% (it is 0.7% for silicon)[66], [67]. This high gauge factor plus the high mechanical flexibility of atomically thin MoS₂ makes it an appealing material as a strain sensor. The high mechanical flexibility of MoS₂ piezoresistor is particularly interesting since the contribution of the sensing element to the total cantilever stiffness would become negligible. In collaboration with LANES group at EPFL, we developed a microfabrication procedure to incorporate MoS₂ piezoresistors into SU8 cantilevers. Chapter 5 explains the associated process flow and accomplished results.

However, the high gauge factor of MoS₂ piezoresistors comes at the price of a very high electrical resistance (order of gigaohm) and therefore, a high Johnson noise downgrades the force noise of MoS₂ based MEMS devices. The most common approach to minimize the resistance of MoS₂ piezoresistors is to reducing the contact resistance (width of the Schottky barriers at the metal contacts) through doping the MoS₂ layer. However, the traditional

doping methods, dopant diffusion and ion-implantation, are not suitable for atomically thin MoS₂ layers since there is no precise control on the doping depth in the nm-range.

Among different techniques to dope MoS₂ [68]–[71], Surface doping is an efficient approach due to the large surface to volume ratio of TMDCs. This method relies on surface charge transfer between the surface of MoS₂ and the adjacent material. For instance, Kiriya et al. have shown that Benzyl Viologen can be used for the surface n-type doping of MoS₂ based on surface charge transfer method [72]. Still, these doping techniques lack in air and water stability. Besides, the doping effect disappears with time.

During the microfabrication of the MoS₂ based SU8 cantilevers, we noticed that the resistance of MoS₂ piezoresistors was reduced after SU8 encapsulation. To further evaluate this observation, we measured the doping effect of SU8 on MoS₂ using bottom-gated field effect transistors (FET) fabricated on SiO₂/p⁺⁺ Si substrates. The results of the four probe measurements and Raman spectroscopy confirmed the n-type doping effect of SU8, which can be finely tuned by going through thermal cycles. It is also shown that SU8 could act as a stable water and gas barrier so it can be employed as a doping source as well as an encapsulation layer.

The low-temperature process and the mechanical flexibility of SU8 make it an ideal material to use it for doping and encapsulation of flexible MoS₂ based FETs. We have realized flexible MoS₂ FETs with SU8 encapsulation on Polyimide with devices showing only minor changes in performance after 100 cycles of bending. Chapter 6 of my thesis is devoted to this research and the results.

1.2.4 Piezoresistive displacement sensors for closed loop AFM scanners

Development of piezoelectric actuators is essential for a large variety of scanning probe microscopy (SPM) applications [73][74]. Traditionally, in AFM applications the piezoelectric scanner raster scans the sample area. However, inherent nonlinearity of piezo actuators, such as hysteresis and creep, significantly distorts positioning accuracy [75], [76].

Several approaches have been attempted to compensate for these nonlinearities [77][78]. For instance, Mokaberi et al. has estimated the drift and compensated it by using a Kalman filter [79]. Zhang et al. have developed model-based feed-forward control for hysteresis compensation through designing an iterative learning control based on the Preisach hysteresis model [80]. This method is based on extensive mathematical calculation since the hysteresis is scan-size and scan-speed dependent. Another approach is using a feedback control technique by integrating a displacement sensor into the piezo actuator. In such a closed loop system, a proportional-integral (PI) controller compares the triangular reference signal with the measured displacement signal (from the displacement sensor) and reshapes the piezo

actuator drive signal to counterbalance the nonlinearities. For example, capacitive sensors [81] are easy to implement but very much sensitive to changes in environmental conditions such as temperature. In addition, capacitive sensors do not provide sufficient bandwidth for high-speed AFM applications. Optical measurements, on the other hand require bulky and expensive equipment [82][83].

An alternative approach is utilizing piezoresistive sensors for direct measurement of the piezo actuator trajectory in a closed loop configuration. Given the fact that the resonance frequency of the scanner is mass dependent, the piezoresistive sensor needs to be light, so it does not add to the total mass of the piezoelectric scanner. This is especially important for high-speed applications, where the fundamental resonance frequency of the piezo actuator limits the nano-positioning bandwidth.

To extend the ease of use of our scanners, I integrated a high bandwidth, high-resolution, and lightweight sidewall piezoresistive displacement sensor into a commercially available AFM piezoelectric scanner as well as our homebuilt high-speed scanner. The closed-loop scanner controller was implemented on a field programmable gate array (FPGA). In chapter 7, it is shown that the scanner nonlinearities are well compensated using our developed closed-loop system for moderate scan rates as well as high scan rates.

Note:

Based on EPFL rules, my PhD thesis is composed of my research papers.

Chapter 2

2. Integration of sharp silicon nitride tips into high-speed SU8 cantilevers in a batch fabrication process

The mechanical bandwidth of the AFM cantilevers is limited by their resonance frequency and mechanical quality factor. Increasing the detection speed of the cantilevers by increasing the resonance frequency through miniaturization has faced the limit of the laser spot size (optical beam deflection method). Introducing polymer cantilevers with low mechanical quality factor and hence high tracking bandwidth has shown great promise for high-speed AFM imaging purposes. Although, polymer tips wear down quickly which restricts further use of polymer cantilevers for high-speed AFM applications. In this work, we have developed a batch fabrication process to integrate silicon nitride tips into SU8 cantilevers while the high tracking bandwidth is still preserved.

I was involved in the development of the microfabrication process, and I fabricated the cantilevers in the clean room. I performed all of the experiments as well as image processing and evaluation. Finally, I have written the paper, including the configuration of all the figures.

This is a copy of an article:

Hosseini N, Neuenschwander M, Peric O, Andany SH, Adams JD, Fantner GE. Integration of sharp silicon nitride tips into high-speed SU8 cantilevers in a batch fabrication process. In revision, *Beilstein journal of nanotechnology*, (2019).

2.1 Abstract

Polymer cantilevers have been shown to outperform their silicon or silicon nitride analogues when it comes to AFM imaging speed in amplitude modulation mode by up to one order of magnitude. However, making the tip of the cantilever out of polymer does not meet the requirements for tip sharpness and durability [63]. Merging the high imaging bandwidth of polymer cantilevers with making sharp and wear resistant tips is essential for future adoption of polymer cantilevers in routine AFM use. In this work we have developed a batch fabrication process to integrate silicon nitride tips with average tip radius of $9\text{nm} \pm 2\text{nm}$ into high-speed SU8 cantilevers. Key aspects of the process are mechanical anchoring of a moulded silicon nitride tip and a two-step release process. The fabrication recipe can be modified for any photo-patternable polymer cantilever.

2.2 Introduction

Atomic Force Microscopy (AFM) cantilevers have been developed for numerous AFM applications since the invention of scanning probe microscopy (SPM) [84]. The quality and accuracy of an AFM image is strongly dependent on the tip geometry since the image topography is the convolution of surface topography and cantilever tip geometry [85]. More precisely, resulting images are subject to an effect of dilation. AFM images with tip artifacts can seriously mislead users and reduce the image quality [86]. New tip fabrication methods have enabled increased sharpness and uniformity, so that commercial AFM cantilevers now have a consistent tip quality. A range of specialized AFM techniques require custom tip designs, including high speed AFM [87], [88] high resolution electrochemical and nano-electrical imaging [89], [90], Raman spectroscopy [91], nano-indentation [92], nano-mechanical machining [93], plasmonic applications [94], [95], and micro-scale grapping tools [96].

In parallel with the developments of AFM cantilevers made out of traditional materials (e.g. silicon, silicon nitride, and silicon oxide), polymer cantilevers have gained attention due to their ease of fabrication, versatility [97]–[101], and their potential for fabricating low spring constant cantilevers [102]. For example, the microfabrication process of SU8 cantilevers has high fabrication yield and easy bottom-up recipe, where the SU8 tip can be directly incorporated into the SU8 cantilever. Despont et al. have shown AFM image of DNA-plasmid molecule using SU8 cantilevers [103]. SU8 based hall sensor cantilevers have also been presented by Sch. Mouaziz et al [104].

In addition, SU8 cantilevers have shown up to one order of magnitude enhanced performance for High Speed Amplitude Modulation AFM (HS-AM-AFM) due to their low mechanical quality factor and hence high mechanical bandwidth [62]. A tip made of SU8 or other structural polymers can be integrated onto a polymer cantilever using a moulding process. These tips have been demonstrated with an acceptable radius for many imaging purposes [102]. However, the wear rate of SU8 is very high [63], which makes this and other polymers non-ideal as a tip material. Some attempts at coating a SU8 tips with a more wear-resistant materials have been made but this results in a blunt tip [105].

Lee et al. have shown that hydrogel AFM cantilevers fabricated by replica moulding and UV curing have great potential for tuning the mechanical properties, tip shape and surface functionalization [106]. However, the fabrication of hydrogel probes requires processes that involve individual cantilever alignment and bonding [107].

The present work aims to overcome the primary limitation of polymer AFM cantilevers, namely the poor wear rate of polymer tips, by integrating a tip element made of a traditional tip material. In this work we have developed a batch fabrication process to integrate silicon nitride tips onto SU8 cantilevers. The whole structure, except the tip, is made of SU8 to benefit from ease of fabrication and high speed imaging capability, while oxide-sharpened silicon nitride tips provide tip sharpness and tip wear resistivity. The tip is anchored securely by being partially embedded in the polymer cantilever.

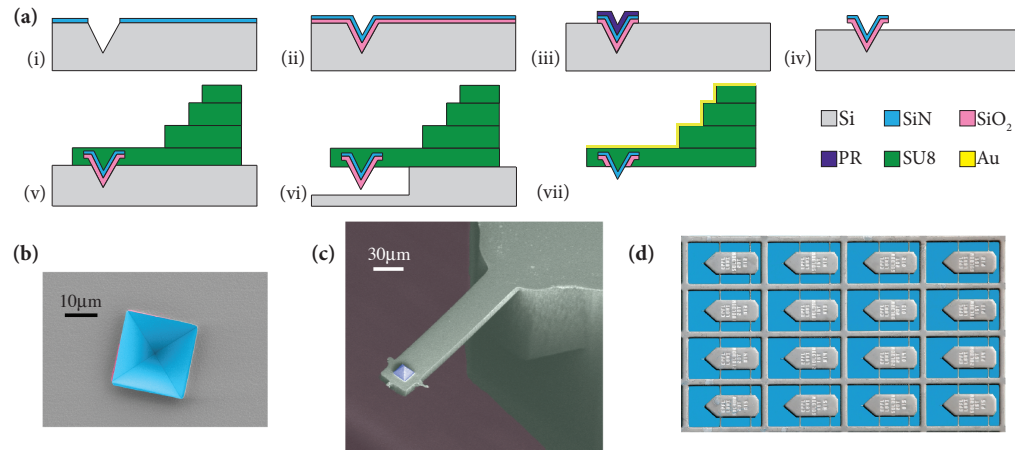


Figure 2-1 Batch fabrication process of LSNT-tips SU8 cantilevers. (a) A summarized process flow. (b) SEM image of the LSNT and the silicon oxide layers where the silicon underneath has been etched (step iv). (c) SEM image of a single cantilever. The pyramidal tip consists of four {111} -planes and has a half-cone angle of 35°. It is aligned with the cantilever. (d) Optical photograph of the released cantilevers.

2.3 Cantilever fabrication

The cantilever is made of SU8 and the tip is entirely covered with low stress silicon nitride (LSNT). Pyramidal tips are made based on the indirect tip fabrication process [108], by

etching a mould into a 380- μm -thick single-sided-polished (100)-plane silicon wafer. Figure 2-1(a) shows a summarized process flow, outlining the important steps:

(i) A 20nm LSNT thin film is deposited by LPCVD onto a silicon wafer. Circular openings (20 μm diameter) are then patterned by E-Beam lithography, yielding very high circularity. The LSNT mask is dry etched before the moulds are structured by anisotropic KOH (40% at 60°C) etching. The formation of {111}-plane facets results in four-sided pyramidal pits. The diameter of the circular openings defines the final height of the tips and can be tuned. (ii) The LSNT mask is then removed in HF 50%. Afterwards, 400nm wet silicon oxide and 100nm LSNT are deposited on the wafer. The 400nm silicon oxide layer improves the tip sharpness through oxidation sharpening [109]. Studies report a 30% decrease of the oxide thickness along the sharp silicon ridges after wet oxidation at 900-950°C [110]. Due to the nonlinear growth of silicon oxide, the oxide thickness becomes smaller at the inside corner of the pyramidal moulds compared to the mould faces. The silicon oxide layer finds a concave curvature on each face of the 4-sided pyramidal moulds, which is then projected to the subsequent LSNT layer. The tip shape and sharpness are significantly affected by the curvature of the LSNT layer at the inside corner of the pyramidal moulds. (iii) The silicon oxide and the LSNT layers are patterned by photolithography to cover only the etched pits. (iv) Deep Reactive Ion Etching (DRIE) is used to etch silicon vertically and laterally (4 μm and 1 μm respectively) in order to provide access for SU8 to fill the base of the tips in the subsequent steps. Figure 2-1(b) shows a SEM image of this step. (v) All the SU8 (GM1050, GM1060 and GM1075, Gersteltec, Pully, Switzerland) structural layers, cantilever beam and three chip body layers are patterned by photolithography. A three-layer chip body with offset between the successive layers is required especially for shorter cantilevers, so that the chip body does not obstruct the path of the laser for optical readout. The chip body layer thicknesses are, from bottom to top, 30 μm , 120 μm and 150 μm respectively. The geometry of the SU8 beam defines the cantilever's resonance frequency (f_0) and spring constant (k). (vi) The process is designed for top-release, so the wafer is treated with DRIE to create a freestanding SU8 beam with the embedded silicon nitride tip encased in a protective oxide. (vii) The release process is finished by placing the wafer in KOH (23% at 90°C) to separate the SU8 cantilevers from the wafer. The silicon oxide layer on the tips is then stripped in BHF. The process is completed by titanium-gold (5nm-20nm) sputtering on the chip-body side of the cantilevers. This layer serves as the reflective metal coating required for optical beam deflection read-out. Figure 2-1(c) and (d) show an SEM and an optical image of the released cantilevers made with this process.

2.4 Results

Primary research goals in fabrication of AFM cantilevers for general imaging purposes are to make sharp tips with well-established tip durability and high detection speed and sensitivity. The detection speed in amplitude-modulation mode is related to the cantilever's tapping bandwidth. This is given by $BW = \pi f_0/Q$, where f_0 is resonance frequency and Q is quality factor [111]. The resonance frequency for a rectangular cantilever with homogenous material properties and no external load is given by $f_0 = \frac{1.758}{\pi l^2} \sqrt{\frac{I}{A}} \sqrt{\frac{E}{\rho}}$, where E is the elastic modulus, I the second moment of area, ρ the density and A the cross-sectional area of the cantilever beam. Thus, the resonance frequency depends on the cantilever material properties, which are presented as $\sqrt{\frac{E}{\rho}}$. On the other hand, Q is strongly influenced by the intrinsic damping η_i of the cantilever material. Therefore, optimizing the ratio $\pi f_0/Q$ is translated to optimizing the ratio $\eta_i \sqrt{\frac{E}{\rho}}$, which has been defined as material bandwidth product. In this regard, SU8 cantilevers have shown high imaging speed due to the high materials bandwidth product, which mainly results from the high intrinsic damping properties of the polymer. Such cantilevers have high resonance frequency and low Q -factor for a given size and stiffness [62]. For any allowable cantilever size and f_0 , we expect a one order of magnitude increase in tracking bandwidth by switching from conventional materials (e.g. silicon and silicon nitride) to SU8. However, SU8 tips wear down quickly and become blunt when they encounter hard surfaces with high aspect ratio features.

To quantify the tip sharpness of LSNT-tip SU8 cantilevers, 20 randomly chosen cantilevers have been tested with a polycrystalline titanium roughness sample. The images were taken using a NanoScope-V controller and Multi-Mode-VAFM with a J scanner (Bruker) in tapping mode. The imaging conditions were as follow: scan size $2\mu\text{m}$, number of pixels 512×512 , and scan rate 1Hz, free amplitude 123nm and setpoint at 95% of the free amplitude. With these parameters, we estimated the tip-sample forces using the Virtual Environment for Dynamic AFM (VEDA, nanohub.org/tools/veda) and obtained mean forces of 10nN and peak forces of 600nN. Figure 2-2(a) shows an AFM image taken with one of the LSNT-tip SU8 cantilevers.

To evaluate the tip sharpness, the blind tip estimation algorithm [114] in Gwyddion has been used. The blind tip estimation algorithm is used to estimate the sharpness of the tip from the image of a polycrystalline titanium tip characterizer sample of unknown geometry, with features significantly sharper than the tips under evaluation. The Gwyddion partial blind tip

estimation algorithm iterates over the surface of the image to find high points with the steepest slopes on the image. These points are subsequently used to estimate the radius of the tip 5nm away from its apex by taking the average width of the tip along the two orthogonal axes, using the assumption that the evaluated tip must be sharper than the sharpest feature on the specimen's image. To guarantee that the dilation of the specimen surface results exclusively from the tip geometry, the noise suppression threshold is set at 100pm which is superior to the measured image noise 40pm. Additionally, borders of the image are also excluded from the estimation to prevent edge artifacts. The inset of Figure 2-2(a) shows partial tip estimation, which uses a limited number of the highest points on the image to estimate the sharpness of the tip. For the 20 cantilevers we evaluated we obtained a tip radius of 9nm with the standard deviation of 2nm.

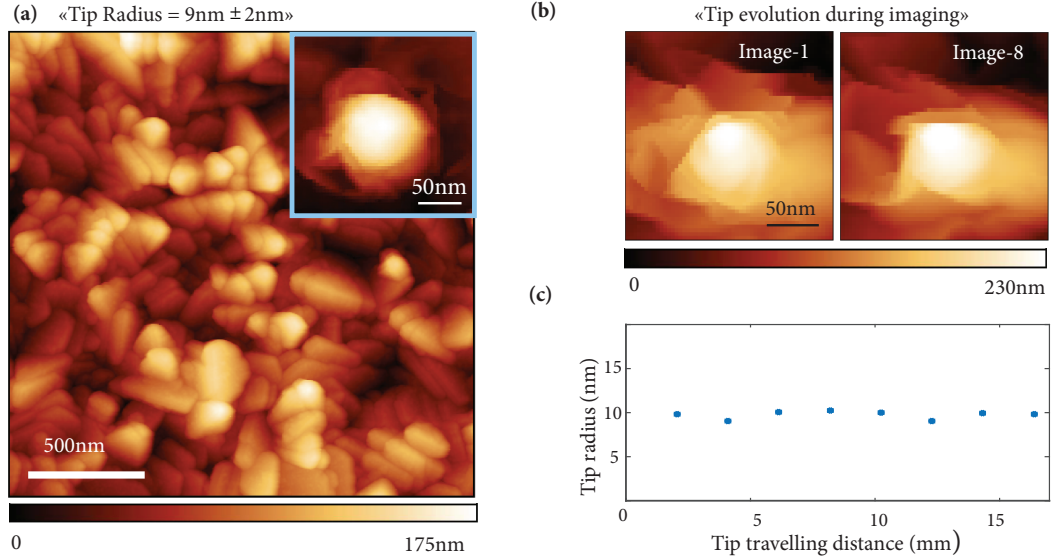


Figure 2-2 Tip sharpness and durability assessment of the LSNT-tip SU8 cantilevers using a polycrystalline titanium roughness sample in tapping mode. (a) The AFM image of the polycrystalline titanium roughness sample, used for the tip radius measurement. The tip radius for 20 randomly chosen cantilevers is 9nm. The image size is $2\mu\text{m} \times 2\mu\text{m}$, pixels 512×512 while the array dimension for tip estimation is 55 by 55 pixels. The inset shows the result of the Gwiddion partial tip blind estimation extracted from the full image. (b) and (c) Tip radius evolution during 16mm travelling distance shows negligible tip degradation.

We evaluated the tip durability in our work by uninterrupted imaging of the polycrystalline titanium roughness sample (tapping mode, scan size $2\mu\text{m}$, pixels 512×512 , and scan rate 1Hz). Figure 2-2(b) shows the partial blind estimation of the tip shape for the first and last images after 16mm tip travel. No obvious degradation occurred. Figure 2-2(c) shows the evolution of the tip radius for more than 16mm of tip travel (8 images).

To investigate the detection speed of the SU8 cantilevers with LSNT-tip, we measured the detection bandwidth of the cantilever in tapping mode by measuring the 3 dB decrease in tracking amplitude similar to protocols described by Kokavecz et al and Sulcheck et al [113][114].

Figure 2-3(a) shows a comparison of the bandwidths of the individual cantilevers, RTESPA (Bruker AFM probes, Camarillo, CA, USA), $f_0=339$ kHz, $k=48$ N/m, $Q=592$, planar dimension $125\text{ }\mu\text{m}$ by $40\text{ }\mu\text{m}$ and thickness $3.4\text{ }\mu\text{m}$, and our LSNT-tip SU8 cantilever, $f_0=328$ kHz, $k=15$ N/m, $Q=23$, planar dimension $80\text{ }\mu\text{m}$ by $20\text{ }\mu\text{m}$ and thickness $7\text{ }\mu\text{m}$. The detection bandwidth is 750 Hz and 50 kHz for the RTESPA and SU8 cantilevers respectively.

Both cantilevers were designed for tapping mode AFM imaging in air. We want to point out that these two cantilevers showed the closest characteristics in terms of resonance frequency based on our choice of planar geometries and thickness of the cantilevers, but their parameters are not an ideal match. Nevertheless, the drastically higher bandwidth of the SU8 cantilever is to be primarily attributed to the change in the materials properties. The LSNT-tip SU8 cantilever is more than 50 times faster than its silicon cantilever counterpart for a given resonance frequency. In order to evaluate the link between tapping bandwidth and image quality, an AFM calibration grating ($1\text{ }\mu\text{m}$ pitch, 100 nm depth) was imaged by a RTESPA ($f_0=331$ kHz, $Q=586$) and a SU8 ($f_0=347$ kHz, $Q=25$) cantilever at scan rates of 1 Hz , 10 Hz , 20 Hz , and 30 Hz . The imaging was conducted with a Bruker Dimension FastScan AFM system, scan size $2\text{ }\mu\text{m}$, and number of pixels 512×512 .

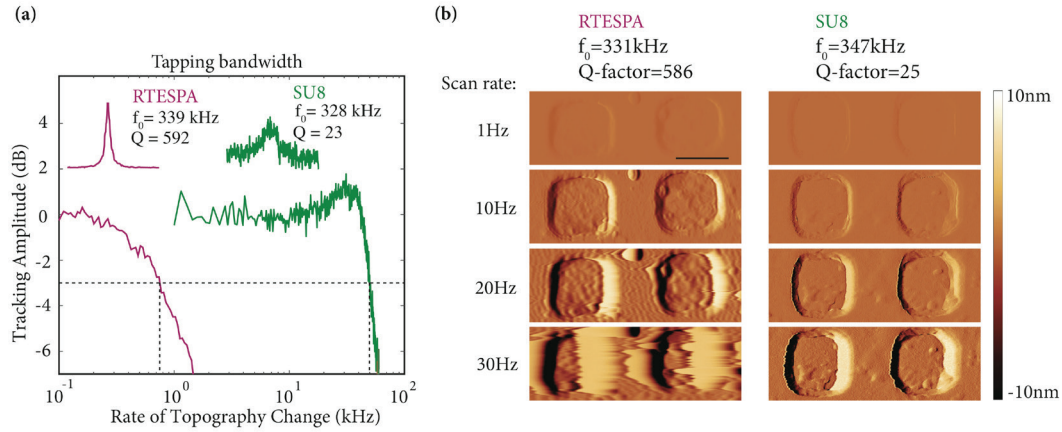


Figure 2-3 Comparison of tapping bandwidth between a tip-integrated SU8 cantilever and a commercial silicon cantilever (RTESPA). (a) The 3dB drop of the surface tracking in tapping mode for RTESPA and the SU8 cantilever happens at 750 Hz and 50 kHz respectively. RTESPA has $f_0=339\text{ kHz}$ and $Q\text{-factor}=592$ whereas the LSNT-tip SU8 cantilever has $f_0=328\text{ kHz}$ and $Q\text{-factor}=23$. (b) Amplitude error images of a $10\text{ }\mu\text{m}$ pitch reference sample taken by RTESPA and the SU8 cantilever at 1 Hz , 10 Hz , 20 Hz , and 30 Hz scan rates. The SU8 cantilever shows better topography tracking ability compared to RTESPA due to its higher tapping bandwidth. The scale bar is 500 nm .

Figure 2-3 (b) shows the amplitude error images taken at different scan rates for these two cantilevers. Lower amplitude error contrast corresponds to better tracking performance. While the silicon cantilever clearly tracks the sample poorly at 30 Hz scan rate, the SU8 cantilever detects the sample topography with lower amplitude error.

2.5 Discussion

A critical feature of any AFM cantilever is the tip. For general imaging, the quality of the tip is primarily determined by the tip radius and the wear rate of the tip. We need to comment that our tips have decent sharpness when it comes to silicon nitride mould tips, but they are less sharp than the typical silicon tips that are commercially available with tip radii less than 2nm. However, even for the ultra sharp tips, the tip wear is an unavoidable mechanism and a great concern for AFM users. We should also mention that our tips have a relatively large opening angle at 35°. While this limits the imaging capabilities on very rough samples, it also presents the advantage of being symmetric and having a clearly defined geometry, which can be beneficial, for example for nanomechanical mapping of biological samples. The tip wear problem has been reported as early as 1991[115]. By assuming that all of the imaging parameters are set correctly, it can still happen due to abrasive wear, fracture and adhesive wear [118], [119]. Tip-integrated polymer cantilevers can fill the gap by providing ca. 10nm radius silicon nitride tips, at a moderate cost and the added value of high tracking ability.

The presented cantilevers have shown good tip sharpness and provide the well-established wear resistance of silicon nitride tips, supplemented with their good tracking bandwidth. However, SU8 cantilevers in general suffer from residual mean stress and residual stress gradients in the beam. The mean stress can be caused by mismatch of the coefficients of thermal expansion (CTE) of cantilever and substrate material. The stress gradient in the polymer is a result of non-uniform processing conditions through the beam thickness. These residual stresses can bend the cantilevers and cause issues with laser alignment and approaching the sample. Keller et al have shown that introducing a long hard bake after SU8 development, and modifying SU8 photolithography baking profile, makes it possible to fabricate 500µm long cantilevers with less than 20µm initial bending for 2µm thick SU8 cantilevers [118]. Although our cantilevers are already relatively straight (due to their shorter length), similar optimization of the process parameters could improve this issue further.

The cantilevers have a somewhat peculiar shape with SU8 residues sticking out in a cross at the SU8 cantilever free end. This is due to the scattering of the light during photolithography of the cantilever patterning. Light travels through SU8 and reaches the bottom surface (LSNT) and then is reflected back to the parts of non-exposed SU8. One way to avoid this problem is adjusting the exposure dose to values not higher than absolutely required.

The increased detection bandwidth of SU8 cantilevers arises from the viscoelastic nature of SU8 resulting in a low Q-factor. This low Q-factor however comes at a price of low mechanical excitation efficiency when shaking the cantilever at resonance with a dither piezo.

Hence the drive amplitude for these cantilevers has to be higher than that of traditional cantilevers. This gives rise to parasitic resonance peaks in the cantilever tune that is well known for tapping mode AFM in low-Q environments such as liquids. As with imaging in fluid, acquiring a thermal tune prior to the mechanical tune helps to find the correct resonance peak to use. The poor mechanical tune caused by the low quality factor of the cantilever is aggravated by the fact that the chip body is also made of SU8 instead of a stiff conventional material. One technique to approach this challenge would be to make the cantilever chip body out of SU8 nanocomposite, with higher Young's modulus, instead of pure SU8. For instance, M. Kandpal et al have shown that embedding ZnO nanoparticles into a pure SU8 matrix increases its Young's modulus from 8GPa to 30GPa [119]. The stiffer cantilever chip body will probably yield better mechanical tuning and hence improved ease of use.

2.6 Conclusion

In this manuscript, a batch fabrication process of LSNT-tip SU8 cantilevers has been presented. The tip sharpness measurement has been performed for 20 cantilevers, which shows a tip sharpness of $9\text{nm} \pm 2\text{nm}$. The tips are made of LSNT, a material known for its wear-resistance, and no clear wear was observed after more than 16mm of tip travel during imaging of a polycrystalline titanium roughness sample. The tip sharpness and wear resistivity have been achieved along with the high tracking bandwidth of SU8 cantilevers. A comparison between a commercial silicon cantilever and LSNT-tip SU8 cantilever shows more than 50 times improvement in the detection speed improvement of the SU8 cantilever over its silicon counterpart.

2.7 Acknowledgment

We thank center of micronanotechnology (CMI) at EPFL for their help during the microfabrication. We also acknowledge funding from the European Union FP7/2007-2013/ERC under Grant Agreement No. 307338-NaMic, the ERC-2017-CoG; InCell; Project number 773091, and Swiss National Science Foundation (Nos.205321_134786, 205320_152675).

Chapter 3

3. Batch fabrication of multilayer polymer cantilevers with integrated hard tips for high-speed atomic force microscopy

As discussed in chapter 2, SU8 cantilevers have great performances for high-speed AFM imaging compared to conventional AFM cantilevers. In chapter 2, we presented a batch fabrication microfabrication process to integrate silicon nitride tips into the SU8 cantilevers. Nevertheless, the performance of those SU8 cantilevers is subjected to low excitation efficiency for AM-AFM applications. One approach to face this problem is making the chip body of the cantilever out of traditional MEMS materials. This requires a higher level of fabrication techniques to have the tip and the chip body out of conventional MEMS materials, while the high tracking ability of the cantilevers is still preserved. In this work, we have overcome the low excitation efficiency of pure polymer cantilevers by introducing multilayer hybrid cantilevers.

In this work, I have developed the fabrication process and did the device fabrication in the clean room. Finally, I have written the paper.

This is a copy of an article:

Hosseini N, Peric O, Neuenschwander M, Andany SH, Adams JD, Fantner GE. Batch fabrication of multilayer polymer cantilevers with integrated hard tips for high-speed atomic force microscopy. Submitted to Proceedings of the IEEE International Conference, *Transducers-2109*.

3.1 Abstract

Increasing the speed of AFM imaging has significant benefits for academic research as well as industrial applications. In many imaging modes, the dynamic response of the cantilever probe dictates the achievable speed. Polymer cantilevers have gained great attention due to their high tracking ability and ease of fabrication. However, polymer cantilevers also have drawbacks. Polymers are not well suitable materials for the tip of the probe due to their high wear rate. This has limited the broader use of polymer cantilevers for AFM imaging. In this work, we combine the advantages of polymer cantilevers with the advantages of tips made of conventional MEMS materials. We demonstrate the batch integration of a hard tip into a polymer-core multilayer cantilever probe, thereby merging speed, high-resolution and durability in a single cantilever.

3.2 Introduction

Cantilever based sensing methods, such as atomic force microscopy (AFM) and related techniques, have become one of the main ways to probe materials in the nanoscale regime [120]. Mechanical properties of the cantilevers significantly influence AFM imaging speed (mechanical bandwidth), image resolution (tip radius) and the analysis of specific samples (cantilever stiffness). The mechanical bandwidth of a cantilever operated in AC mode can be estimated through the ratio $\pi f_0/Q$, where f_0 is the first resonance frequency and Q is the quality factor of the cantilever. Therefore, an increase of the resonance frequency or a decrease of the quality factor will result in higher mechanical bandwidth. Current high-speed AFM (HS-AFM) technology was enabled by the miniaturization of silicon and silicon nitride (SiN) cantilevers to planar dimensions below 10 microns, resulting in cantilevers with resonance frequencies in the MHz range [121], [122]. This approach has been the enabling technology for state of the art, high-speed AFM, producing good-quality, high-speed images even on difficult biological samples. In liquid, viscous damping yields a Q value around 2-4, enabling extremely high imaging speeds. Using small cantilevers immersed in fluid, Ando et al. pioneered video-rate AFM imaging and thereby established the field of HS-AFM in liquid on biological samples [56]. Although such cantilevers may also have a relatively low Q in air, the small spring constants make them primarily intended for imaging in fluid. In air, higher spring constants are often needed to overcome surface adhesion.

We have recently shown that making probes out of polymers yields very fast-responding cantilevers, and polymers are thus excellent structural materials for high-speed AFM probes [62]. By changing the material to a polymer, we can obtain cantilevers with higher intrinsic

damping and hence lower Q-factor, independent of the medium. Pioneering work by Genolet et al [102] has shown that cantilevers with integrated tips can be made out of the polymer SU8 using a silicon mold to form the cantilever tip. These tips can have acceptable radii for various imaging purposes. However, the wear rate of SU8 is very high [63] which makes SU8 and other polymers non-ideal for serving as tip material.

As discussed in chapter 2, previous attempts for making cantilevers as well as the cantilever-carrying chip out of polymer, has shown that mechanical excitation of the cantilever resonance is difficult, and the cantilevers do not show a clean tune required for good tapping mode AFM operation. In this work, we present an alternative strategy to integrate sharp hard tips with acceptable durability into polymer cantilevers. By using non-traditional MEMS materials in combination with traditional materials and fabrication methods, we have fabricated hybrid polymer AFM cantilevers made of a polymer core, sandwiched between two hard thin films. The Q-factor of such hybrid cantilever is higher than pure polymer cantilevers, which facilitates easy excitation of the cantilever resonance when using inertial drive. The reported tri-layer cantilevers maintain high tracking bandwidth, governed by the viscoelastic properties of the polymer core, combined with improved tip durability.

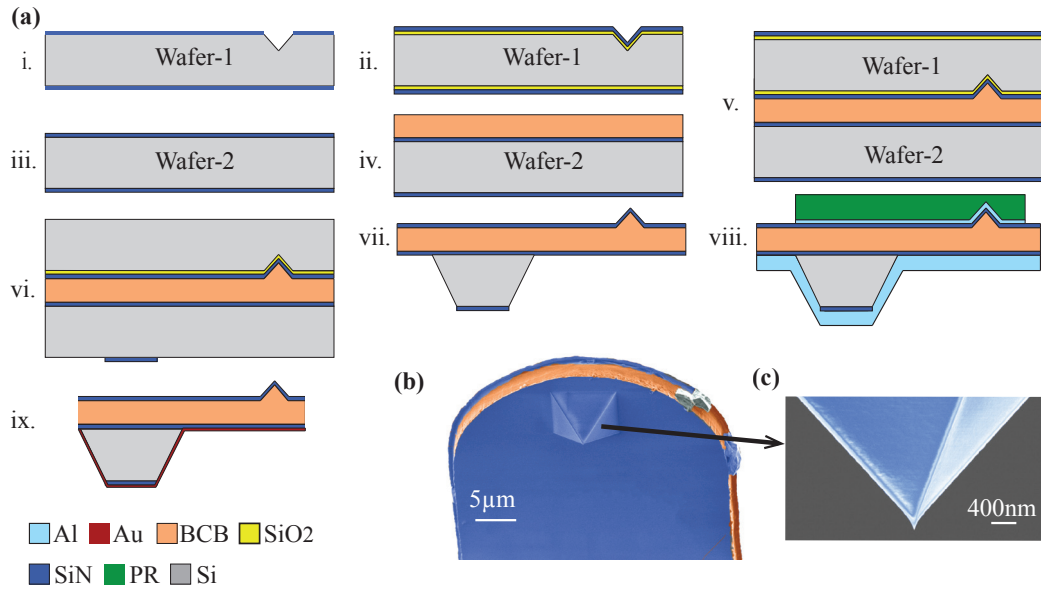


Figure 3-1 Process flow, displaying the most important steps. (a) The process is based on polymer bonding of two pre-processed wafers-1&2. (b), (c) SEM images of a released cantilever and its tip. The BCB polymer core (in orange), is sandwiched between two hard SiN thin films of identical thicknesses (in blue). The hard tip is made of SiN.

3.3 Fabrication

Our approach to fabricate high-speed, hard tip, polymer core cantilevers is to first fabricate the sharp hard-tips on the wafer, which we then bond to a complementary wafer

through polymer bonding. The bonded wafers are then further processed to obtain the final cantilever. The main steps of the process flow are depicted in Figure 3-1(a).

We use a standard four-inch, double-sided polished, silicon (Si) wafer with a thickness of 380 μ m (hereafter called wafer-1). The first step is to deposit a 20-100nm thin layer of low stress silicon nitride (SiN) through LPCVD. Then, we use e-beam lithography to write the circular pattern and DRIE to transfer the pattern onto the SiN layer. The circular patterns for the openings provide maximum symmetry, which after KOH wet etching, results in pyramidal shaped pits. The SiN mask is then removed in diluted HF. We use thermal oxidation to transform silicon layer into silicon oxide (SiO₂), which results in a sharpening of the mold [7]. Next, we deposit low stress SiN through LPCVD. The deposited SiN layer will constitute the outermost layer of the tri-layer cantilever and its thickness can vary from 20nm to 100nm. A complementary double-sided polished silicon wafer (wafer-2) with the same SiN layer thickness is bonded onto wafer-1 (Figure 3-1(a)-v). The bonding material is a viscoelastic polymer responsible for the low quality-factor of the cantilever. We use benzocyclobutene (BCB), with the commercial product named CYCLOTENE 3022 (The Dow Chemical Company) for wafer bonding. BCB is suitable for a polymer layer thickness of 2-11 μ m and can be spin coated on one or both wafers before bonding. For wafer bonding, we use SB6 bonding machine (SüssMicrotech). The bonded wafers are then hard cured under nitrogen atmosphere at 250°C for 60 minutes. Continuing the process flow, we pattern wafer-1 by standard photolithography and dry etching. On wafer-2, we strip the SiO₂ and SiN layers, thus exposing the silicon. Thereafter we etch the wafer assembly in 40% KOH at 60°C overnight with a total etch time of ~ 19h (Figure 3-1(a)-vii). As the BCB layer is covered on both sides with a SiN layer, it resists the hours-long etch. The thermally grown oxide is attacked during the KOH etch and we later completely remove it in buffered HF. Subsequently, we deposit a 2 μ m thick aluminum (Al) layer on the chip body side (wafer -2), which serves as a mechanical support layer for the thin SiN-BCB-SiN membrane. On the cantilever tip side, we deposit a 300nm thin aluminum layer, which acts as a hard mask during consecutive dry etching. To pattern the aluminum on the cantilever tip side of the wafer, we use a 12 μ m thick photoresist (PR) (AZ 9260, MicroChemicals) in order to completely cover the cantilever tips. The patterned aluminum is wet etched (Figure 3-1(a)-viii).

The thick aluminum layer on the chip body side of the wafer is necessary as a structural layer, since the final BCB dry etch defines the cantilever shape and removes the surrounding BCB layer. The BCB dry etch consists of three main etching steps, where the first and the last etch step consist in removing the SiN layer using CHF₃/SF₆ chemistry. During the second etch step, we remove the BCB polymer layer using CHF₃ chemistry. After BCB dry etching, we

remove the aluminum layers on both sides using wet aluminum etchant. The final step is the deposition of a thin reflective layer on the chip body side of the wafer. We first sputter a 5nm layer of titanium (adhesion layer) followed by 20nm of gold (Figure 3-1(a)-ix). The cantilever with the integrated hard tip at the end of the process flow is depicted in Figure 3-1(b) and the close-up of the tip is shown in Figure 3-1(c).

3.4 Results

To evaluate the tip sharpness and wear resistance of the fabricated hard tips, the multilayer hybrid cantilevers are tested through imaging a polycrystalline titanium roughness sample. The results are displayed in Figure 3-2. Tip sharpness is quantified using the blind tip estimation algorithm [112] of the Gwyddion software [123]. The algorithm identifies the sharpest peak in the topography image, which is subsequently used to compute the tip sharpness at 10nm from the apex, as illustrated in Figure 3-2(a). The images are obtained using a Bruker AFM system (Santa Barbara, CA, USA) comprising a Nanoscope-V controller, a MultiMode-V and a J-scanner. Images are taken in tapping mode and imaging parameters are as follows: $2 \times 2 \mu\text{m}$ scan size, $1.95 \times 1.95 \text{ nm}$ pixel size and 1Hz scan rate.

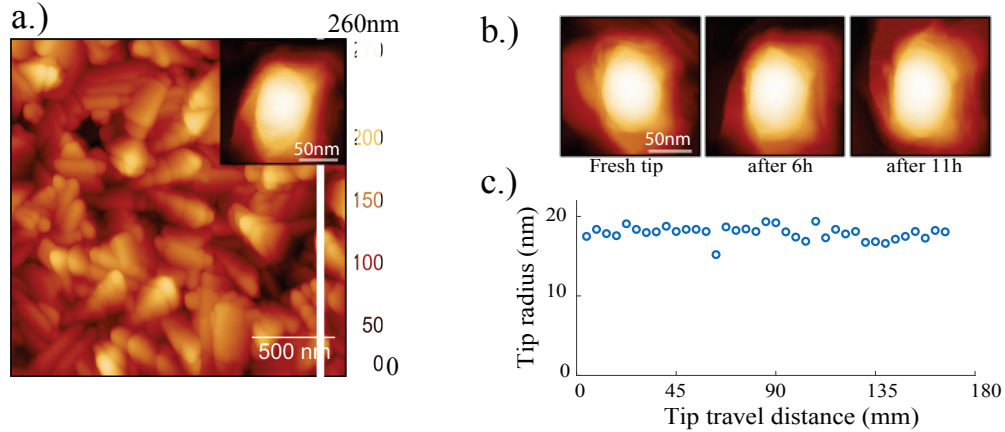


Figure 3-2 Tip sharpness and tip wear characterization through imaging of a titanium polycrystalline roughness sample. (a) Tapping mode image reveals a tip radius of 17nm, at 10nm from the apex. The Inset shows the region used for the Gwyddion blind tip estimation. (b) Evolution of tip sharpness as a function of imaging time and total tip-travel distance shows minimal tip wear, even after 11h of imaging and 170mm of tip travel distance.

Measured tip radii range from 12nm to 20nm and are comparable to commercial cantilevers such as ScanAsyst-Fluid probes (Bruker), and are suitable for most AFM applications. The durability of the fabricated tips was tested during 11 hours of uninterrupted imaging, for a total of 170mm of tip-travel distance. The 37 images obtained were analyzed to detect potential tip degradation issues. Figure 3-2(b) reveal no apparent degradation of the tip, even after prolonged imaging on a demanding sample.

Traditional polymer cantilevers with relatively low Q-factor in air and soft polymer chip bodies suffer from low excitation efficiency. This issue is addressed here by increasing the Q-factor and using silicon chip bodies, drastically improving the mechanical response to excitation during inertial drive as illustrated in Figure 3-3. The tune of two cantilevers with similar first resonance frequencies is compared. The full SU8 lever (red curve, Q-factor=21) shows a more parasitic frequency sweep when compared to the reported tri-layer cantilever (blue curve, Q-factor=58). Extracting the correct first resonance of the cantilever is thus greatly facilitated by using a cantilever with higher Q-factor.

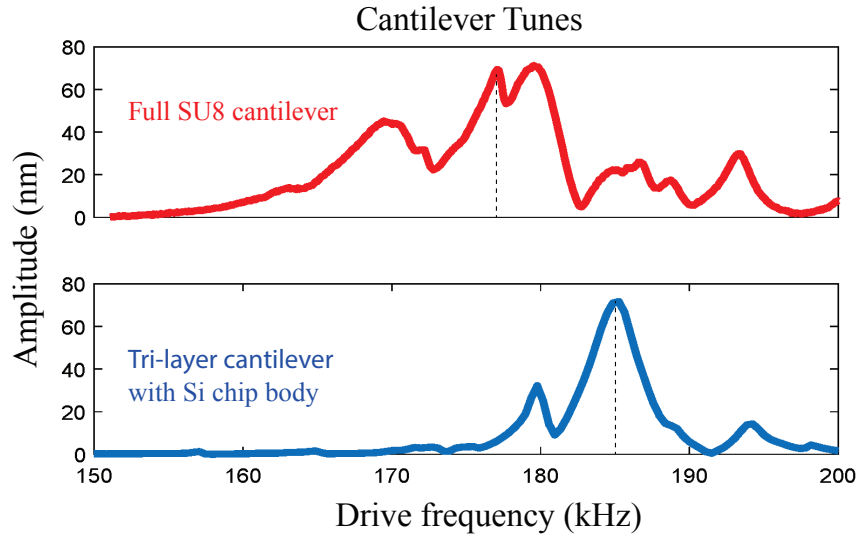


Figure 3-3 Cantilever tunes for an SU8 cantilever (red curve) and for a tri-layer cantilever with a silicon chip body (blue curve). Tri-layer lever characteristics: $Q=58$, $f_0=184\text{kHz}$, length $100\mu\text{m}$, width $50\mu\text{m}$ and thickness $4\mu\text{m}$ BCB core and 20nm LSNT shell. SU8 lever characteristic $Q=21$, $f_0=176\text{kHz}$, length $120\mu\text{m}$, width $30\mu\text{m}$ and thickness $8\mu\text{m}$.

To assess the imaging speed of the tri-layer cantilevers, we measured its detection bandwidth in tapping mode and compared it to a commercial silicon cantilever (RTESPA, Bruker AFM probes, Camarillo, CA, USA). To do so, we defined the tapping bandwidth as the 3dB decrease in tracking amplitude and used a similar protocol in Sulcheck et al [114]. The experiment (Figure 3-4 (a)) showed a more than 10 times higher bandwidth for the tri-layer cantilever ($f_0 = 359\text{kHz}$, $k = 7.2\text{N/m}$, $Q = 55$, planar dimensions $90\mu\text{m}$ by $30\mu\text{m}$ and thickness $2.6\mu\text{m}$) than for its silicon counterpart ($f_0 = 339\text{kHz}$, $k = 48\text{N/m}$, $Q = 592$, planar dimension $125\mu\text{m}$ by $40\mu\text{m}$ and thickness $3.4\mu\text{m}$).

In order to evaluate the correlation between tapping bandwidth and image quality at high speeds, we imaged an AFM calibration grating ($10\mu\text{m}$ pitch, 200nm depth) with the same two cantilevers, at 1Hz and 10Hz scan rate (Figure 3-4(b)). While the silicon cantilever clearly tracks the sample poorly at 10Hz scan rate, the tri-layer cantilever detects the sample topography significantly better.

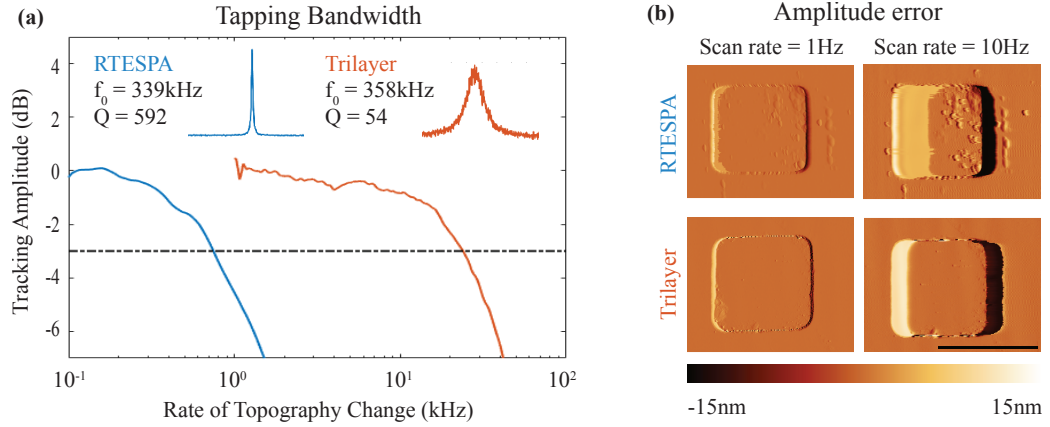


Figure 3-4 Comparison of tapping bandwidth between a tri-layer cantilever and a commercial silicon cantilever (RTESPA). (a) The 3dB drop of the surface tracking in tapping mode for the RTESPA and the tri-layer cantilever occurs at 750Hz and 24kHz, respectively. Both cantilevers have comparable resonance frequencies, but the tri-layer has a 10 times lower Q-factor. The insets show the thermal tune of each cantilever, at identical scale. (b) Amplitude error images of a 10 μ m pitch, 200nm step reference sample taken by RTESPA and the tri-layer cantilever at 1Hz and 10Hz scan rates. The tri-layer cantilever shows better topography tracking ability thanks to its higher tapping bandwidth. The scale bar is 5 μ m.

3.5 Discussion

The present work proposes a way to overcome the primary limitation of polymer AFM cantilevers, which is the poor wear rate of polymer tips and difficult mechanical excitation. By moving from the pure-polymer design to the tri-layer hybrid structure, one can benefit from the high-speed imaging capability of the polymer cantilevers and combine it with the use of tips that are made from the material that is known and accepted in the field as being suitable for high-quality tips. The tri-layer structure was chosen over a bilayer structure (SiN-BCB) to provide symmetry around the neutral axis and thus avoid cantilever bending due to internal stresses in the films. Compared to Si cantilevers, the tri-layer cantilevers have a 10 times higher imaging bandwidth.

However, compared to pure polymer cantilevers (Adams et. Al [62]), the tri-layer cantilevers are slower due to their higher Q-factor. This is due to the over-proportional contribution of the SiN layer to the second moment of area of the cantilever, even for ultra-thin layers. The Young's modulus of the SiN (e.g. 240GPa) is two orders of magnitude higher compared to the BCB (e.g. 2.9GPa) layer, and the contribution of the SiN layer to the second moment of area depends on the distance to the neutral axis squared. It is therefore desirable to keep the SiN layer thickness as low as possible (20nm in our case). In the future we aim to replace SiN with materials with lower stiffness, for instance silicon oxide to obtain hard tip cantilevers with even lower Q-factor and hence even higher tracking speed.

An additional advantage of our proposed process is that all high temperature steps required for fabricating the tip are performed before bonding with the BCB polymer. This allows the integration of other functionalities to the tri-layer cantilevers by adapting the microfabrication recipe. For instance, by pre-patterning the BCB layer, microfluidic devices could be realized with the same technology with inherently sealed channels.

3.6 Conclusion

In this work, we have reported a microfabrication process to resolve the problem of high wear-rate and difficult mechanical excitation in polymer cantilevers by making sharp tips out of thin films with high in-plane stiffness and low out-of-plane stiffness. We have developed high-speed tri-layer AFM cantilevers where the polymer core, e.g. BCB, is sandwiched between two SiN thin films through wafer bonding. The average tip radius for randomly selected cantilevers was measured to be 12nm at a 10nm distance from the tip apex. Long-term imaging showed negligible tip wear, even after 170mm tip traveling distance during 11h of uninterrupted imaging.

The good tip quality combines with the high tracking ability of the tri-layer for a versatile cantilever for AM-AFM. The 3dB decrease in tracking amplitude demonstrates more than one order of magnitude improvement in the tracking ability of the tri-layer cantilevers compared to its traditional silicon counterpart.

3.7 Acknowledgments

We thank the Center of Micronanotechnology (CMI) at EPFL for their help during microfabrication. This work was funded by the European Union FP7/2007-2013/ERC under Grant Agreement No. 307338-NaMic, the ERC-2017-CoG; InCell; Project number 773091, and Swiss National Science Foundation (Nos.205321_134786, 205320_152675).

Chapter 4

4. A novel microfabrication platform for hermetically sealed, hybrid multilayer AFM cantilevers

The flexible microfabrication process of the multilayer hybrid cantilevers described in chapter 3 can be extended to incorporate strain sensors into the cantilevers to realize the hermetically sealed hybrid multilayer self-sensing cantilevers.

This chapter is the core of my PhD research and presents the novelty, the design, the microfabrication, and the performance of such devices in multiple AFM applications. I have been fully dedicated to the development of the microfabrication process as well as the microfabrication, instrumentation development, device assessments, acquiring AFM images, data analysis, and paper writing.

This is a copy of an article:

Hosseini N, Neuenschwander M, Andany SH, Peric O, Adams JD, Fantner GE. A novel microfabrication platform for hermetically sealed, hybrid multilayer self-sensing cantilevers. To be submitted to the peer-reviewed journal, *Nature Nanotechnology*.

4.1 Abstract

This work presents a microengineering platform to develop high-resolution, high-speed, and versatile piezoresistive hybrid multilayer cantilevers, with up to one order of magnitude improvement in force resolution compared to state-of-the art silicon cantilevers. The device performance relies on advanced material engineering and fabrication methods, which brings the self-sensing technique into the required paradigm of low force noise, versatility, and

functionality, for both static and dynamic measurements. The device is composed of a polymer core and strain sensing elements, encapsulated by two hard ultra-thin films. It is shown that the multilayer cantilevers detect the sample topography significantly faster, owing to its low quality factor and hence higher tracking bandwidth. The device has proven great compatibility as it has been used in liquid, air, and vacuum, for different scanning probe microscopy techniques.

4.2 Introduction

Cantilever based sensing is one of the most sensitive measure of force or mass [124], [125]. For example atomic force microscopy (AFM), and related techniques, have become one of the main techniques to probe materials in the nanoscale regime. In AFM, the information about the surface topography is measured by transducing the tip-sample interaction force (F) to an electrically measurable quantity, e.g. primarily voltage (V). However, the currently prevailing method of measuring the cantilever deflection, optical beam deflection (OBD) method, makes the measurement devices complex, requires high level of interaction between the user and the instrument. These restrict a much broader use of the technology in areas such as healthcare and industry. This was already recognized very soon after the invention of AFM, and cantilever sensors have been microfabricated that have self-sensing electrical readout [31][52][126][127]. Compared to the traditional OBD method (shown in Figure 4-1(a)), which measures the change in reflection angle (θ) of a laser beam reflected from the back of the cantilever, self sensing cantilevers directly transduce the cantilever deflection (d) into an electric signal (V_{Elc}), as illustrated in Figure 4-1(b). The self-sensing cantilevers are very attractive for applications where the complex OBD instrumentation is cumbersome or impractical. For example in applications where there is no optical access to the cantilever [128], [129], in-vivo measurements in opaque solutions and for delicate, laser-sensitive biological samples [130], applications requiring multiple parallel sensors[131], [132], or applications in automation that require levels of robustness that are difficult to achieve with the complexity of the OBD method.

However, thus far, self-sensing cantilevers have suffered from two main inconveniences. Firstly, the signal-to-noise ratio of self-sensing cantilevers has been significantly inferior to OBD. Secondly, self-sensing cantilevers were much less versatile than OBD cantilevers, because they are not inherently compatible with measurements in fluids [127] or coatable for advanced measurements requiring additional coatings [133].

In this work, we have overcome these two issues by introducing a fundamentally different approach to fabricating self-sensing cantilevers. In our technology, the AFM cantilevers are

made of a thick polymer core, sandwiched between two thin layers of a hard material in a tri-layer structure. The active electronic parts are embedded between the polymer and the hard layers, and are as such protected from the environment.

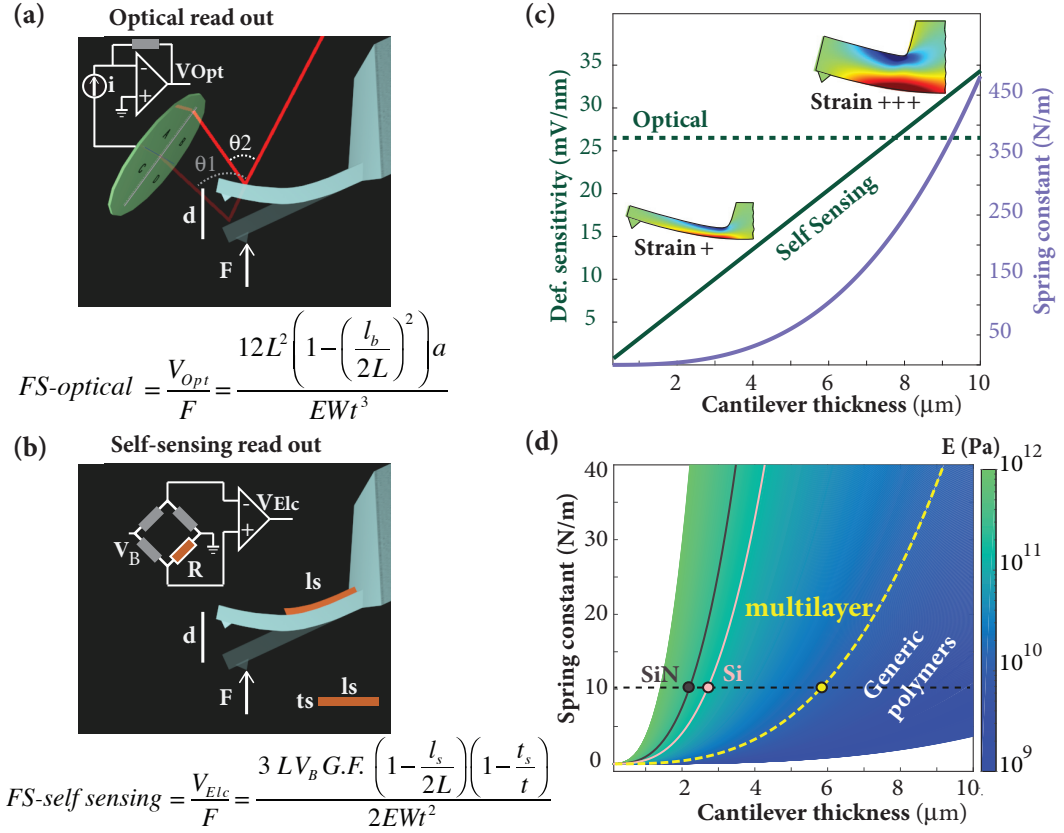


Figure 4-1 From the tip-sample interaction force to the measured voltage, transduction and interdependencies. (a) Optical scheme: The applied force, F , causes deflection at the free end of the cantilever, which consequently changes the beam bending angle (θ) and therefore the position of the reflected laser beam on the quadrant photodiode. The transimpedance amplifier converts the photodiode current (i) into voltage (V_{Opt}). Force sensitivity ($FS-optical$) is defined as V_{Opt}/F where L , W , T and E are length, width, thickness and Young's modulus of the cantilever respectively. l_b is the diameter of the laser beam and a is a constant dependent on standard calibration of the OBD method and is independent of how the cantilever is loaded. (b) Self-sensing scheme: The applied force/deflection induces strain at the base of the cantilever, which can be measured directly by Wheatstone bridge and the instrumentation amplifier. The $FS-self\ sensing$ depends on the gauge factor ($G.F.$) of the sensing element, the bridge bias voltage (V_B), the dimensions of the cantilever and the piezoresistors. (c) The deflection sensitivity is defined as the force sensitivity over the spring constant. The deflection sensitivity of the optical scheme is independent of the cantilever thickness whereas it increases with the cantilever thicknesses for the self-sensing cantilevers. Finite element analysis approves higher strain concentration for a 8um thick cantilever compared to a 2um thick cantilever. The spring constant changes by the cantilever thickness, cubed. (d) Spring constant depends on the cantilever thickness as well as the cantilever material. Soft materials, for example polymers, have the same spring constant for higher thicknesses compared to conventional MEMS materials (e.g. silicon and silicon nitride). Dashed yellow line stands for the multilayer cantilevers.

This makes the cantilevers inherently fluid compatible and allows for multifunctional coatings in the same way as conventional OBD cantilevers. The low Young's modulus of the polymer leads to up to 10 times thicker cantilevers for a given spring constant (k), which increases the sensitivity of the self-sensing devices by up to a factor of 10 compared to traditional self-sensing cantilevers.

In the OBD method, the electrical signal is measured from the change in angle on the cantilever; therefore the deflection sensitivity (V_{Opt}/d) is independent of the cantilever thickness (dashed green line in Figure 4-1(c)). The OBD cantilevers have exceptionally good force sensitivity (V_{Opt}/F), because the force sensitivity, which is obtained by dividing the deflection sensitivity over the spring constant, can be increased by reducing the cantilever thickness and hence the spring constant (see the formula for $FS_{Optical}$ in Figure 4-1(a)). For self-sensing cantilevers that measure the strain in the cantilever, this approach is much less effective since by reducing the thickness, one not only decreases the cantilever stiffness, but also moves the strain sensors closer to the neutral axis. This reduces the output signal of the self-sensing cantilever for a given deflection, i.e. the deflection sensitivity (solid green line in Figure 4-1(c)). As such, the benefit of the lower spring constant is partially counteracted by the reduced deflection sensitivity.

In this work, we have chosen an alternative strategy to reduce the spring constant, while maintaining the thickness and high deflection sensitivity. By making the bulk of the cantilever out of polymer, this multilayer cantilever is much softer (Figure 4-1 (d) dashed line) than conventional AFM cantilevers; see Figure 4-1(d) Si and SiN. We therefore can design our cantilevers to be thick, yet still soft. The increased thickness directly translates to an increased strain at the outer layer of the cantilever where the strain sensors are located (see Figure 4-2(a)).

4.3 Multilayer, polymer-core self sensing cantilevers

The fabrication process of the multilayer cantilevers is based on polymer bonding of two pre-processed wafers, with subsequent release of the multilayer cantilever via KOH wafer through etch (see Figure 4-2(b)). The benefits of this process are that everything is symmetrically sealed and all high temperature processes required for fabricating the sensing elements can be performed before the wafer bonding. The wafer bonding is realized by using Benzocyclobutene (BCB), with the commercial product named CYCLOTENE 3022 (The Dow Chemical Company) polymer. The final product is a hybrid multilayer structure with the sensing elements and electrical connections hermetically sealed inside the cantilever. Figure 4-2(c) displays an SEM image of a released multilayer cantilever where the sensing elements as well as the BCB layer are encapsulated between 20nm low stress silicon nitride (LSNT) thin films.

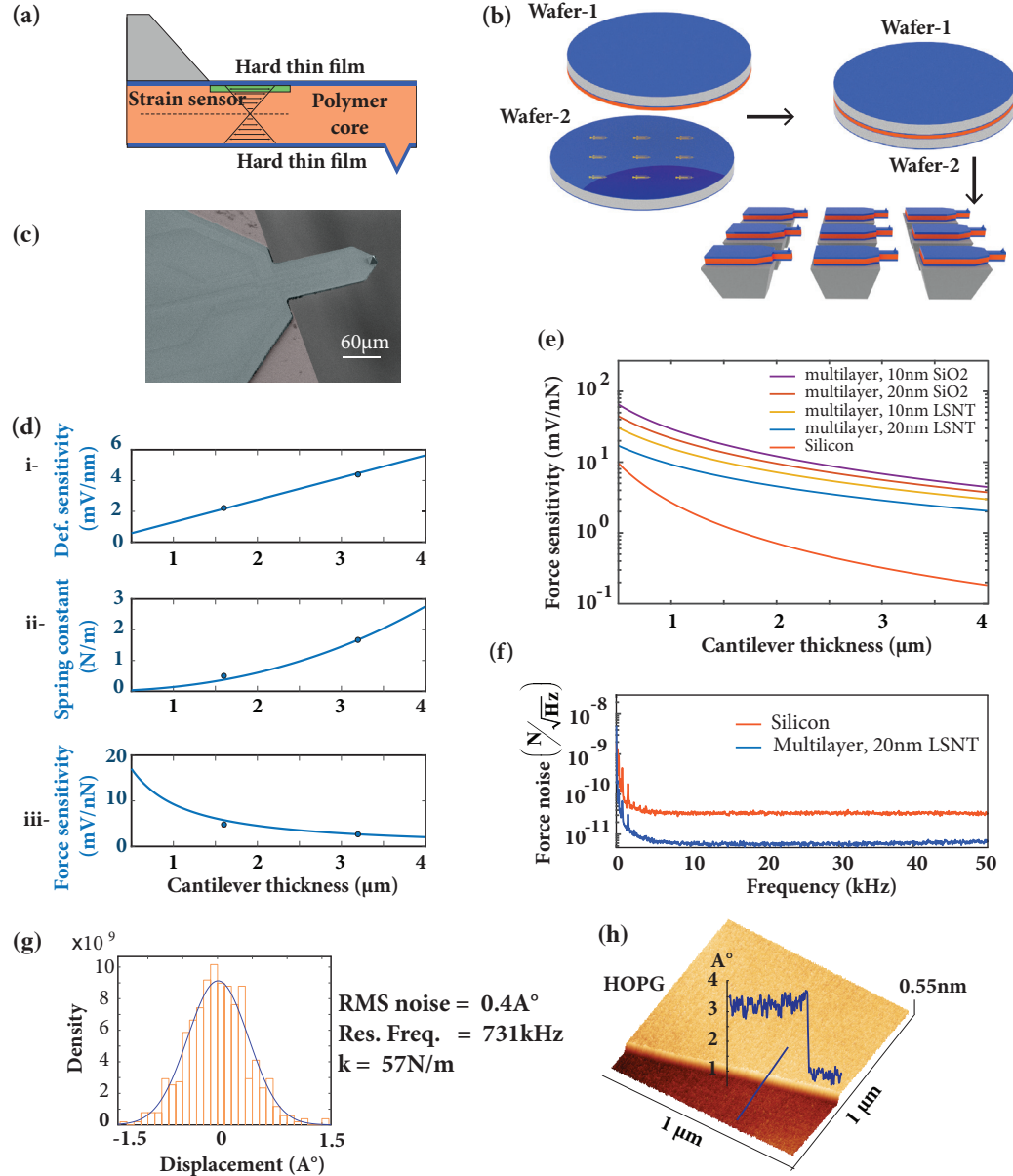


Figure 4-2 The multilayer self-sensing device realization and its basic performance. (a) A schematic of the multilayer cantilever, illustrates a polymer core and self-sensing electronics sandwiched between two hard thin films. Strain/deflection sensitivity increase as the sensing element is placed further away from the neutral axis. (b) The fabrication process is based on polymer bonding of two processed wafers. Wafer-1 has spin coated Cyclotene (BCB in orange) on a thin layer of silicon nitride (blue) and wafer-2 has piezoresistors and interconnections patterned on a silicon nitride layer with the same thickness as the one for wafer-1. Two wafers are bonded together by using BCB as a glue and then silicon chip body (grey) are made through KOH etch. (c) SEM image of a tip integrated multilayer cantilever. Sensing elements are buried under the 20nm silicon nitride thin film. (d) Theoretical and experimental evaluations of the multilayer technology with poly-silicon piezoresistors. Circular points represent two multilayer cantilevers with the same planar dimension (150μm by 50μm) one with 1.6μm BCB and the other with 3.2μm BCB thicknesses. The BCB layer and Wheatstone bridge are encapsulated by 20nm LSNT. i, ii- The deflection sensitivity and the spring constant increase by increasing the thickness. iii- The force sensitivity decreases for stiffer cantilevers. (e) Comparison of different combinations of the multilayer technology with a silicon cantilever with poly-silicon piezoresistors. (f) Experimental data proves better force noise for a multilayer cantilever compared to a silicon cantilever with similar dimensions and similar piezoresistors (e.g. single crystal silicon). (g) Owing to the enhanced deflection sensitivity of the multilayer cantilevers, a RMS noise value of 0.4A° was obtained in AM-AFM in air. (h) Single atomic layer of HOPG is resolved by employing the multilayer cantilever in air.

Figure 4-2(d)-i indicates how the deflection sensitivity of the multilayer cantilever increases linearly with the polymer thickness. The circular data points represent two batches

of cantilevers we fabricated with 1.6 μm and 3.2 μm BCB respectively. The solid lines are theoretically calculated without any fitting parameter.

The spring constant increases with the thickness cubed (Figure 4-2(d)-ii), which follows the conventional wisdom that for improved force sensitivity, the cantilever should be made as thin as possible (Figure 4-2(d)-iii). Comparing different multilayer materials combinations with cantilevers made out of pure silicon, we see that general trend of increased force sensitivity for decreased thicknesses remains true, but the force sensitivity of the multilayer cantilevers is offset compared to that of silicon cantilevers by as much as one order of magnitude as presented in Figure 4-2(e).

The force sensitivity advantage of the multilayer cantilevers over silicon cantilevers disappears when going to very thin cantilevers, because the relative contribution of the polymer decreases compared to the contribution of the silicon nitride. The multilayer geometry is not guaranteed to provide better force sensitivity for all applications. For practical AFM cantilevers having reasonable AC-mode bandwidth (Resonance frequency =10kHz-1MHz, $k=0.1\text{-}60\text{N/m}$), the multilayer geometry provides significantly improved noise performance.

Figure 4-2 (f) represents the noise spectrum of two cantilevers with equal dimensions, and strain sensors (e.g. boron doped silicon), one made of silicon and one using the multilayer geometry. We calculated 6 times better force noise for the multilayer cantilever compared to the silicon cantilever. We measured the achievable 0.4 Angstrom RMS imaging noise with the multilayer cantilevers in AC mode in air (Figure 4-2(g)) and imaged HOPG where one could easily resolve single atomic steps (Figure 4-2(h)). Compared to our measurements of HOPG with silicon self-sensing cantilevers of comparable size [51], we obtained the same image quality with spring constant 3 times lower, leading to a factor of 3 lower tip-sample forces.

4.4 Results and discussion

Self-sensing AFM cantilevers for AFM imaging are of particular interest for applications where OBD measurements are difficult or impossible, such as for in-line process control, low temperature cryostats or inside the vacuum chamber of an SEM. For AM-AFM imaging applications, factors other than force sensitivity also play a vital role for the image quality. A key parameter for the measurement bandwidth is the mechanical quality factor (Q-factor) of the cantilever, especially in vacuum applications. Adams et al. [62] have shown that by making cantilevers out of polymers, the Q-factor is reduced and the imaging bandwidth could be increased by one order of magnitude for identical planar geometries, spring constant and resonance frequencies.

In the case of the multilayer cantilevers, the Q-factor is also dramatically reduced, albeit not as much as for pure polymer cantilevers, because the silicon nitride layers contribute over-proportionally to the stiffness due to the location being far away from the neutral axis. The Q-factor of the multilayer cantilevers in vacuum is a factor of 4 lower than that of comparable silicon cantilevers, which manifests in 4 times faster imaging speed. Figure 4-3(a) shows SEM image of the close packed ommatidium lens surfaces of a wasp eye and the multilayer cantilever on top of the ommatidium lens surfaces in vacuum. One ommatidium was then imaged using the multilayer and the silicon cantilevers at 2 line/sec and 32 lines/sec in vacuum shown in Figure 4-3(b). While the silicon cantilever clearly tracks the sample poorly at 32line/sec scan rate, the multilayer cantilever detects the sample topography significantly better owing to its lower Q-factor and hence higher tracking bandwidth.

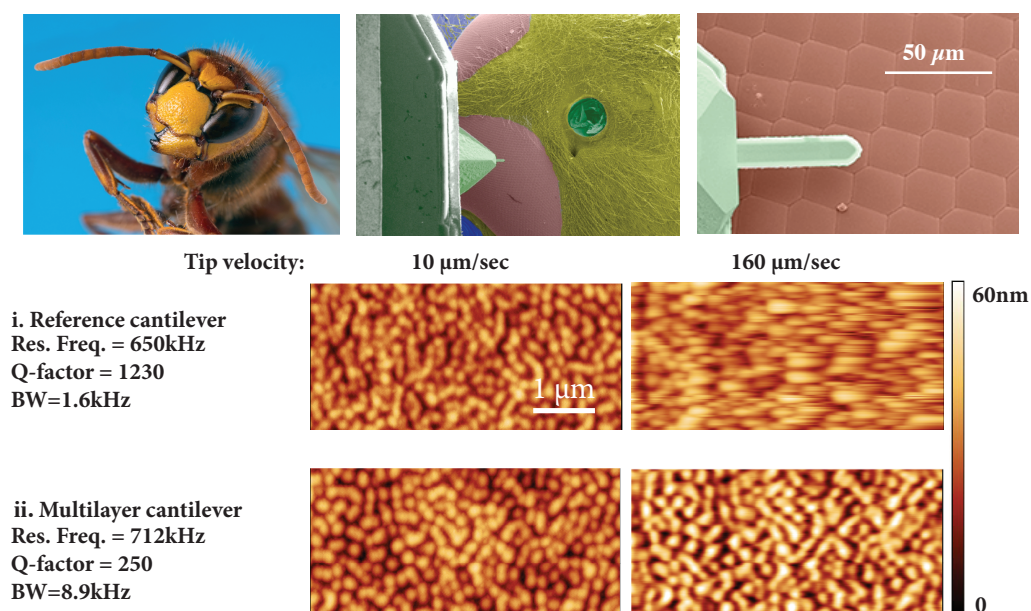


Figure 4-3 High tracking bandwidth of multilayer cantilevers in AM-AFM. (a) i- Wasps has amazing eye cornea (with permission from www.alamy.com). ii- A closer look needs advanced technologies like a SEM-AFM hybrid system. iii- SEM image of the close packed ommatidium lens surfaces of the wasp eye. The multilayer cantilever is placed inside SEM and on top of the ommatidium lens surfaces. (b) Multilayer cantilever has lower Q-factor and therefore higher detection bandwidth. Ommatidium lens surface has been imaged with 2line/sec and 32line/sec scan rates. The multilayer cantilever shows better tracking ability compared to its silicon counterpart.

One of the main benefits of the multilayer geometry is that all sensing elements and electrical connections are safely sealed inside the cantilever. This makes the multilayer cantilevers inherently compatible with AFM imaging in fluid without surface passivation, something that is problematic with conventional self-sensing cantilevers. The combination of the self-sensing and the chemical resistance of the cantilever allows for imaging processes even in opaque and aggressive liquids. Figure 4-4(a) shows the etching process of a polished

nickel surface in ferric chloride (FeCl_3), a brown opaque liquid. Even after 5 hours of imaging, the cantilever showed no sign of degradation.

The fact that in the multilayer cantilevers all sensing elements are sealed inside makes these cantilevers a versatile platform for many other AFM imaging modes that require special coating on the cantilever such as kelvin probe force microscopy (KPFM). KPFM relies on measuring the potential offset between a conductive tip and the sample surface, which reveals the surface work function map. Figure 4-4(b) displays the superposition of the height data and the surface potential measurements of a Polystyrene-Low Density Polyethylene (PS-LDPE) polymer blend, taken by a coated multilayer cantilever. For this measurement, the cantilever bottom side was sputter-coated with a 100nm gold layer.

Another powerful technique that requires functionalized cantilevers is magnetic force microscopy (MFM). We coated the multilayer cantilevers with ca. 70nm evaporated $\text{Ni}_{81}\text{Fe}_{19}$ and performed correlated SEM-AFM-MFM imaging of an artificial spine-ice structure; see Figure 4-4(c). The sample tiling is called Penrose P2 tiling where $\text{Ni}_{81}\text{Fe}_{19}$ nanobars have been fabricated on this tiling [134]. If one looks at the MFM data displayed in Figure 4-4(c)-iii, the intensity of blue and red colors at the vertices is different. The higher intensity of these colors at the vertices implies that these vertices acts as “hotspots” for ferromagnetic switching to begin. Just applying a saturating magnetic field and then reducing the field to zero can essentially program these hotspots.

Self-sensing cantilevers mainly suffer from stiffness, noise performance and fluid compatibility. For dynamic measurements, the resonance frequency of the cantilever, the spring constant, and the minimum thickness of the sensing material creates a limit of how thin the cantilever can be. Roukes et al [46] have shown that extreme miniaturization and impedance matching of the sensor and readout electronics can provide excellent force resolution. Dukic et al [135] have demonstrated nm-range direct printing of nanogranular tunneling strain sensors on sub-micron size devices allows for dynamic AFM measurements. However, scaling down the device sizes creates practical limits on the manufacturability, suitability and functionality in many applications.

In addition to the deflection sensitivity, it is important to have good force sensitivity and measurement bandwidth. Harley et al [52] have shown that exceptionally high force resolution for very thin and long self-sensing cantilevers having spring constant on the order of 10^{-5} N/m. While such soft cantilevers are very well suited for static force measurements, their low resonance frequency makes them ill suited for dynamic measurements such as those in AFM imaging.

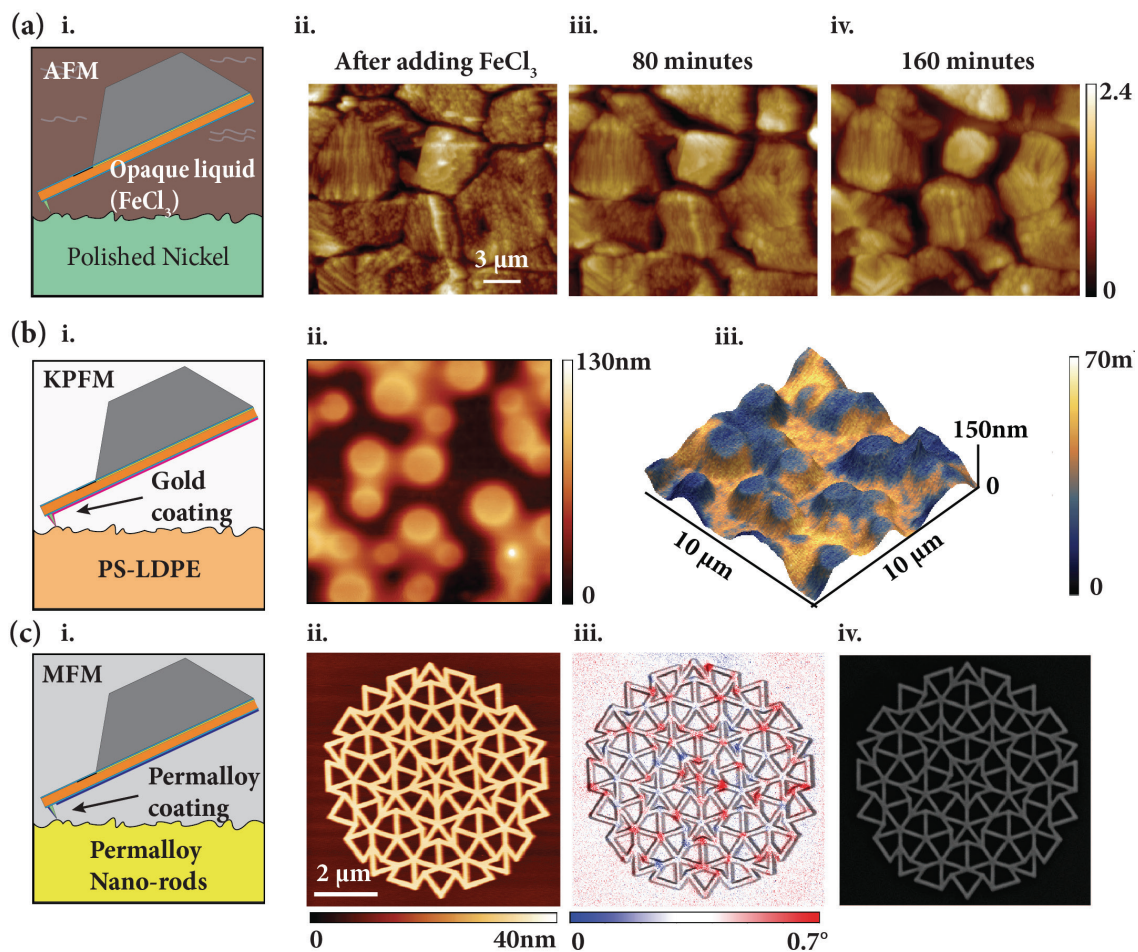


Figure 4-4 Multilayer cantilevers provide a versatile platform for different SPM techniques. (a) A multilayer cantilever is immersed in FeCl₃ to see how a polished nickel surface evolves in times when it is exposed to FeCl₃. (ii),(iii) and (iv) show how nickel grains are shrunk and etched by FeCl₃. (b) A multilayer cantilever can be safely coated with 100nm gold to provide a conductive tip for KPFM applications. PS-LDPE polymer blend is imaged. (ii) Shows the topography and (iii) is the superposition of topography and the work function difference between PS and LDPE. (c) A multilayer cantilever is coated with ca. 70nm Ni₈₁Fe₁₉ to perform MFM in vacuum with our SEM-AFM hybrid system. (ii) Topography image of interconnected Ni₈₁Fe₁₉ nano-rods. (iii) Superposition of topography and phase data. The phase data shows contrasts in the measured stray fields in the Permalloy nano-rods. (iv) SEM image provides visual feedback.

The multilayer technology yields increased force sensitivity, which still meets the practical limits of cantilever size (both minimum and maximum), aspect ratio, resonance frequency and spring constant. For instance, the spring constant must be high enough to overcome surface adhesion, but not too stiff to cause tip-sample damage for AFM purposes.

Due to its adaptable process flow, the multilayer concept does not replace other techniques, but it adds to them. For example, it allows integration of multiple sensor materials (silicon, polysilicon, metal strain gauges, MoS₂, etc.). It also enables having active elements on both sides of the cantilever and further integration of other functionalities such as scanning microwave microscopy. Our technology is expandable beyond AFM cantilevers. For instance same technology can be used for the fabrication of fluid compatible MEMS based biosensors or self-sensing microfluidic MEMS devices by patterning the polymer core.

4.5 Acknowledgment

We thank the Center of Micronanotechnology (CMI) at EPFL for their help during microfabrication. This work was funded by the European Union FP7/2007-2013/ERC under Grant Agreement No. 307338-NaMic, the ERC-2017-CoG; InCell; Project number 773091, and Swiss National Science Foundation (Nos.205321_134786, 205320_152675).

4.6 Methods

4.6.1 Cantilever fabrication

4.6.1.1 Self-sensing multilayer cantilevers based on polysilicon piezoresistors

The key fabrication steps for the multilayer cantilevers with polysilicon piezoresistors are hereby described. First, low stress silicon nitride (LSNT), with a minimum thickness of 20nm, was deposited on silicon wafer-1 (380 μ m-thick double-sided-polished (100)-plane) supported by Low Pressure Chemical Vapour Deposition (LPCVD). LSNT (similar to wafer-1), polysilicon (100nm) and borosilicate glass (BSG, 200nm) were layered by LPCVD onto silicon wafer-2 (380 μ m-thick double-sided-polished (100)-plane), then annealed at 1200°C for 15 minutes. The BSG layer served as a doping source during the annealing process and then as a mask to define the polysilicon piezoresistors. This BSG layer was then patterned by photolithography and then dry etched. The boron doped polysilicon piezoresistors were defined in KOH 40% at room temperature. The BSG layer was then removed in buffered HF (BHF) and aluminum metal traces were deposited by lift-off photolithography and metal evaporation. Wafer-1/wafer-2 (or both) was/were spin coated with Cyclotene 3022-35 Resin (BCB) and bonded in a vacuum bonder; the bonded wafers were then hard baked at 250°C for 1 hour. Cantilever chip bodies were patterned in two steps. First, by employing photolithography and dry etching on the backside of wafer-2, the LSNT mask was patterned. The LSNT on the backside of the wafer-1 was blanket etched. Then, the cantilever chip bodies were patterned by overnight KOH 40% at 60°C by means of the LSNT mask where the bulk silicon of wafer-1 was entirely removed. The cantilevers were then patterned through the use of photolithography and dry etching with aluminum mask. Finally, a reflective coating (titanium-gold, 5nm-10nm) was sputtered onto the backside of the cantilevers.

More details of the process flow are provided in the supplementary information, section 4.7.

4.6.1.2. Self-sensing multilayer cantilevers based on single crystal silicon piezoresistors

In order to adapt the multilayer cantilever process to integrate single crystal silicon piezoresistors, the process was modified to use Silicon On Insulator (SOI) technology where the buried SiO₂ layer functioned as the etch stop layer to protect the silicon piezoresistors during the KOH etch.

The boron doped silicon piezoresistors (BSG source, diffusion at 1200°C for 15 minutes) were patterned through the silicon device layer of the SOI wafer (SOI 725-2-0.13) by photolithography and dry etching. It is important to mention that the SOI wafer was initially mechanically grinded from 725µm to 380µm to match its complementary wafer. The LSNT film was deposited by LPCVD as described in the method section 4.6.1.1. and then punched (photolithography and dry etching) to make two openings for each piezoresistor. These openings acted as via to connect the metal contacts to the silicon piezoresistors. The aluminum metal contacts were then created by lift-off photolithography and metal evaporation. The BCB coating and bonding, and chip release were similar to the one described in the method section 4.6.1.1. The buried SiO₂ was finally removed in 50% diluted HF. For applications where the fluid/coating compatibility is required, we can leave a thin layer (ca. 20nm) of the oxide by timing the HF process. This thin layer of SiO₂ does not compromise the functionality of the multilayer cantilevers because the tensile module of SiO₂ is relatively small compared to LSNT. The reflective metal deposition is similar to the one in the method section 4.6.1.1.

4.6.2 Tip integration

Oxide sharpened [7] silicon nitride tips were created on the wafer composed of the sensing elements (i.e. wafer-2). Silicon wafer-2 was first covered with 20nm LSNT (LPCVD) and circular openings were patterned using e-beam lithography and dry etching. LSNT was chosen over SiO₂ for its high etching resistance in KOH, making it a more suitable mask. The tip moulds were then created by silicon anisotropic KOH (40% at 60°C) etching. The LSNT mask was then removed in 50% HF. This process differs from the non-tip process in the way that 400nm of SiO₂ (for tip sharpening) was deposited prior to the LSNT structural layer. The rest of the process is similar to the recipe described in the method section 4.6.1.1. except that the 400nm SiO₂ layer was removed in BHF after the cantilevers were release in KOH and before reflective metal coating. The best tip radius we achieved with this process was ca. 6nm. We have to state that the tip-integration was attempted only for the polysilicon piezoresistor multilayer cantilevers. For the non tip-integrated cantilevers, carbon Electron Beam Induced Deposition (EBID) tips were made at the free end of the cantilevers.

4.6.3 Cantilever characterization

To calculate the cantilever properties, we used the following values where E stands for the Young's modulus:

$E_{\text{LSNT}}=240\text{GPa}$, $E_{\text{BCB}}=2.9\text{GPa}$, $E_{\text{Silicon}}=130\text{GPa}$, and $E_{\text{SiO}_2}=66\text{GPa}$. Cantilever length= $150\mu\text{m}$, width= $50\mu\text{m}$ and LSNT thickness= 20nm . The BCB thickness changes from 500nm to $4\mu\text{m}$. The piezoresistors length, width and thickness were $40\mu\text{m}$, $8\mu\text{m}$ and 100nm respectively. The gauge factor of polysilicon was measured at 25.

The experimental data were taken by deploying a Bruker NanoscopeV controller and MultiModeV AFM system. The differential signal from the Wheatstone bridge was amplified first by a low noise instrumentation amplifier (AD8429, Analog Devices, USA), and then two operational amplifiers with a total gain of 1000. The electronics output (deflection signal) was then fed into the Bruker Signal Access Module III (channel IN0). The electrical deflection sensitivity for each individual cantilever was obtained in contact mode. The thermomechanical tuning was measured to characterize the resonance frequency and the spring constant of the cantilevers. The force sensitivity was obtained by dividing the deflection sensitivity over the spring constant.

4.6.4 Noise measurement

The noise spectrum in Figure 4-2(f) was acquired with a Zurich Instrument, UHF 600MHz, 1.8GSa/S lock in amplifier for a multilayer cantilever and a silicon cantilever with the same size of $330\mu\text{m}$ by $110\mu\text{m}$ (both were based on boron doped single crystal silicon piezoresistors). The force sensitivity was obtained with the same procedure described in the method section 4.6.3.

The Amplitude Modulation (AM-AFM) imaging noise in Figure 4-2(g) was measured with the system described in the method section 4.6.3 and is as follows: the scan size was set to a very small value (e.g. 0.01nm) and the proportional-integral feedback gains were reduced to very small values. This way, there is no topography change and tracking so all of the fluctuations in the self-sensing deflection signal is contained in the amplitude error signal. The distribution of these fluctuations is used to compute the RMS noise.

4.6.5 Measurements in vacuum

Vacuum measurements (high-speed images of the wasp eye and MFM measurements) were performed with our SEM-AFM hybrid system (GETec, Austria) and Anfatec controller (Anfatec Instrument AG, Germany).

4.6.6 Nickel etch

The experiment was performed using a Bruker NanoscopeV controller and a Dimension Icon AFM scan head with a homebuilt, liquid compatible cantilever holder. The electrical deflection signal was sent to the IN0 port of the Bruker Signal Access Module III. The images were taken in PeakForce Tapping with a 50nN force set point, 1kHz PeakForce frequency and 1Hz scan rate.

4.6.7 MFM

Images were taken with the system described in the method section 4.6.5 using the two-pass technique. This technique allows imaging long-range magnetic interactions while reducing the influence of topography. To collect the MFM data, a tapping self-sensing multilayer cantilever, coated with Permalloy, scanned over the sample surface at 169kHz resonance frequency to obtain topographic information. The tip was then lifted to 30nm above the sample surface. To maintain a constant separation during the second pass, the height data from the first scan was added to the lift height (30nm).

4.6.8 KPFM

The image was taken with a Bruker NanoscopeV controller and MultiModeV AFM system in LiftMode (two-pass technique) with AM-KPFM. The conductive tip of the cantilever was held at ground potential and the sample was biased through the sample holder.

4.6.9 AFM image processing

Images were processed in Gwiddion. We removed line-by-line offset using a median correction method and subtracted the background tilt or bow using first and second order polynomial fittings. The AFM images did not go through any noise filtering corrections. Images of the nickel etch were cropped to compensate for the sample drift.

4.6.10 Sample preparation

The wasp was found dead and the head was removed and then coated with gold and palladium to provide a conductive layer for SEM. The nickel surface was polished with silica suspensions (0.05 μ m) in Interdisciplinary Centre for Electron Microscopy (CIME) at EPFL. The MFM sample was provided by professor Dirk Grunder (Laboratory of Nanoscale Magnetic Materials and Magnonics, EPFL).

4.7 Supplementary information

Process flow. The fabrication process flow of the self-sensing hybrid multilayer cantilevers is illustrated in Figure 4-5, and the corresponding steps are presented in Table 4-1. The detailed run-card is elaborated in Appendix A.

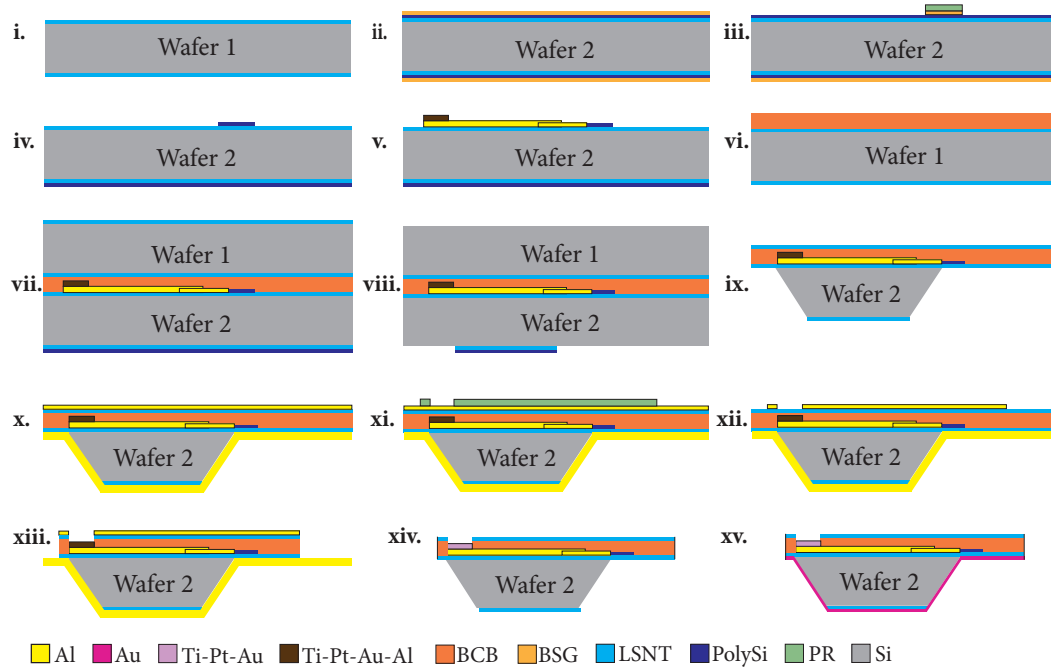


Figure 4-5 Highlights of the process flow to fabricate self-sensing multilayer hybrid cantilevers.

Table 4-1 Highlights of the run-card to fabricate self-sensing multilayer hybrid cantilevers.

Step	Wafer	Process	Material	Target value
i	1	LPCVD	LSNT	20nm-(100nm)
ii	2	LPCVD	LSNT	20nm-(100nm)
			Polysilicon	100nm
			BSG	200nm
		Diffusion		1200°C, 15 minutes
iii	2	Photolithography	AZ1512	1.3μm
		Dry etch	BSG	200nm
		Resist strip	1165 remover	
vi	2	KOH wet etch	Polysilicon	100nm
		BHF wet etch	BSG	200nm
v	2	Photolithography	LOR-AZ1512	480nm-1.1μm
		Metal evaporation	Al	150nm
		Lift off		

		Photolithography	LOR-AZ1512	820nm-1.1 μ m
		Metal evaporation	Al	250nm
		Lift off		
		Photolithography	LOR-AZ1512	820nm-1.1 μ m
		Metal evaporation	Ti-Pt-Au-Al	50nm-50nm-150nm-100nm
		Lift off		
vi	1,(2)	Spin coating	BCB	1.6 μ m-(8 μ m)
vii	1, 2	Wafer bonding		
		Hard bake	BCB	250°C, 1 hour
viii	2	Photolithography	AZ1512	1.3 μ m
		Dry etch	Polysilicon, LSNT	100nm, 20nm-(100nm)
		Resist strip		
	1	Dry etch	LSNT	20nm-(100nm)
ix	1, 2	KOH wet etch	Silicon	380 μ m
x	1	Metal evaporation	Al	300nm
	2	Metal evaporation	Al	2 μ m
xi	1	Photolithography	AZ1512	1.1 μ m
xii	1, 2	ANP wet etch	Al	300nm
xiii	1,2	Dry etch	LSNT-BCB-LSNT	
		Resist strip		
xvi	1, 2	ANP wet etch	Al	2 μ m
xv	2	Metal evaporation	Ti-Au	5nm-10nm

This is the end of the article.

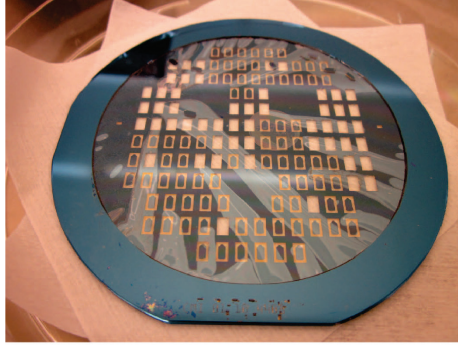
4.8 Microfabrication challenges

4.8.1 Wafer bonding

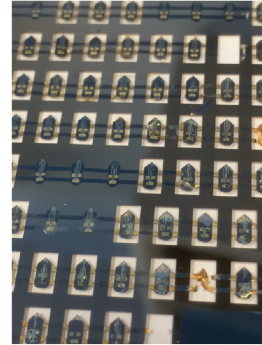
One of the crucial fabrication challenges was the wafer-bonding step. The wafer bonding was based on gluing two wafers together under pressure at moderate-high temperatures where the glue would end up to be the polymer core of the multilayer structure. The quality of the wafer bonding was highly affected by the surface adhesion between the polymer core on one side and the LSNT thin film and the self-sensing components on the other side. Furthermore, to serve the high tracking bandwidth, such a polymer needs to have high

material bandwidth product, defined as $\eta_i \sqrt{E/\rho}$ where E is Young's modulus and ρ the density and η_i the intrinsic loss factor [62]. As a cantilever material, it also has to show low water-uptake when immersed in liquids.

(a) Parylene wafer bonding



(b) BCB wafer bonding, using the wrong bonding parameters



(c) BCB wafer bonding, using the correct bonding parameters

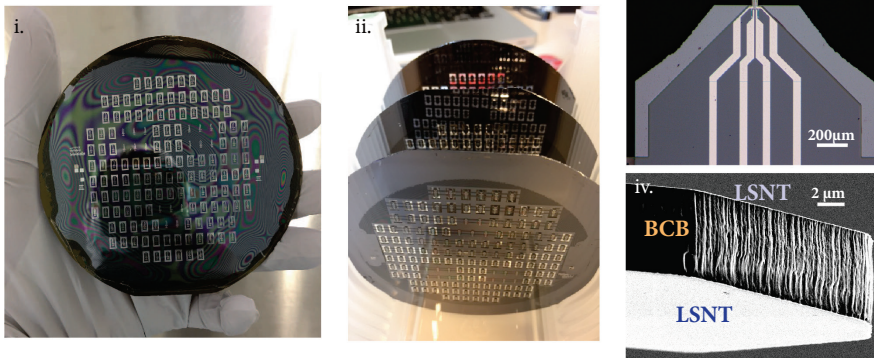


Figure 4-6 Toward successful wafer bonding. (a) An optical photo of a Parylene-bonded wafer (non self-sensing), which shows very clear polymer delamination after overnight KOH. (b) An optical photo of a BCB-bonded wafer (self-sensing) after overnight KOH, which shows how using wrong wafer-bonding parameters results in polymer delamination and damages to the self-sensing elements. (c) Successful BCB wafer bonding (self-sensing cantilevers): i. An Optical photo of a wafer after overnight KOH, ii. An optical photo of three fully processed wafers, iii. An optical Image of an individual self-sensing multilayer hybrid cantilevers, iv. The SEM image of a self-sensing multilayer hybrid cantilever shows the three layers at the free end of the cantilever.

We attempted several polymers with the abovementioned properties. Figure 4-6(a) displays a Parylene-bonded wafer after overnight KOH (step ix in Figure 4-5), with very clear polymer delamination. This unsuccessful wafer bonding happened even without adding the self-sensing components to the process. The next alternative was SU8 as we had fabricated pure SU8 cantilevers. However, we did not find a reliable recipe for SU8 wafer bonding. Finally, Benzocyclobutene (BCB) showed the best credibility as a cantilever and a wafer bonding material. Although, the suitability of BCB wafer bonding was correlated with using the right bonding parameters. For example, Figure 4-6(b) displays the results of the BCB wafer bonding using the wrong bonding parameters. Eventually, we came up with the right

bonding recipe, which is elaborated in Table 4-2. Figure 4-6(c) shows the results of such a BCB wafer bonding.

Table 4-2 BCB wafer bonding parameters, accepted for Süss SB6, vacuum anodic bonder.

Step	Machine action	Chamber Pressure (mbar)	Tool Pressure (mbar)	Temperature (°C)	Time (min)
1	Initialization	1000	0	20	-
2	Pump down	3	0	20	-
3	Top and bottom plates: heat up	3	0	160	-
4	Contact with central spring	3	0	160	-
5	Clamps out	3	0	160	-
6	Spacers out	3	0	160	-
7	Top and bottom plates: in contact with the wafers	3	0	160	-
8	Top and bottom plates: press the wafers together	3	2500	160	3
9	Top and bottom plates: released	3	0	160	-
10	Chamber vent	1000	0	160	-
11	Cool down	1000	0	20	-

4.8.2 Silicon nitride thickness

The thickness of LSNT influences the resonance frequency and the spring constant (hence the force sensitivity) of the cantilevers dramatically. Ideally, to avoid the cantilever stiffening, we would desire to encapsulate the polymer core and the strain sensing elements with ultra-thin layers of LSNT. However, reducing the LSNT thickness from 100nm to 20nm caused a noticeable loss in the metal traces and drop in the fabrication yield (from 85% to 55%). This was attributed to the presence of pinholes and other structural defects in LSNT, combined with several wet-etching (both acid and bases) processes, which potentially damages the Aluminum metal traces. One approach to improve the fabrication yield is replacing the aluminum metal traces with gold, which has principally much better chemical resistance.

Table 4-3 presents a comparison between different cantilever dimensions with different LSNT and BCB thicknesses.

Table 4-3 A set of hybrid multilayer cantilevers characterization.

Thickness	Length (μm)	Width (μm)	Resonance frequency (kHz)	Q-factor	Spring constant (N/m)
20nm LSNT, 4μm BCB	200	50	42	25	0.6
20nm LSNT, 4μm BCB	100	50	182	50	4.5
50nm LSNT, 4μm BCB	200	50	63	41	1.4

50nm LSNT, 4 μ m BCB	100	50	249	78	9.2
50nm LSNT, 8 μ m BCB	200	50	112	65	9
50nm LSNT, 8 μ m BCB	100	50	480	78	46.5
100nm LSNT, 4 μ m BCB	200	50	82	76	3

4.8.3 Photo-mask cleaning

The microfabrication of the self-sensing multilayer cantilevers was engaged with multiple photolithography steps, for instance, patterning the piezoresistors (step iii), metal traces lift-off (steps v), and cantilever patterning (step xi). We noticed that after several mask-wafer alignments, there was some photoresist residues remained on the photomask, which was particularly very problematic for the cantilever patterning. Figure 4-7(a) shows a photomask for cantilever patterning after several uses. The photoresist residues can potentially change the cantilever outline as it is shown in the SEM image of a released cantilever.

To clean the masks, we immersed the contaminated one in sulfuric acid (H_2SO_4) for 2 minutes at room temperature. Figure 4-7(b) displays the photomask after cleansing and a cantilever produced with the use of such a clean mask.

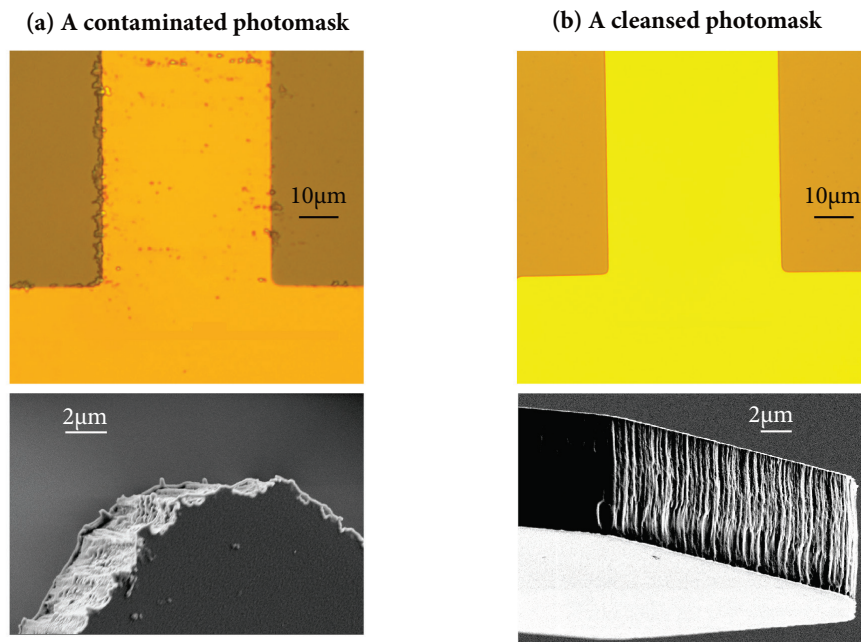


Figure 4-7 Contaminated photomask causes rough patterns and has to be cleansed. (a) A used photomask has photoresist residues, which causes rough outlines. The SEM image shows the free end of a multilayer cantilever, released by using a contaminated photomask. (b) The photo-mask is cleansed by immersing it in H_2SO_4 for 2 minutes. Such a photomask resembles a newly made one. The SEM image displays the free end of a multilayer cantilever, which was released by using the clean photomask, has a very clean edge

4.8.4 Wire bonding issues

In order to connect the electrical signals from/to the self-sensing cantilever (Wheatstone bridge) to/from the read-out electronics, multiple PCBs were designed which were compatible

with our AFM setups. Each PCB had four pads for the Wheatstone bridge, plus one extra pad for the dither piezo. We utilized the ball-wedge wire bonding method, with the use of gold wires. However, the wire bonding of the 20nm-LSNT cantilevers was subjected to some random short-circuit failures, which was merely attributed to the wire bonding process. We realized that the capillary of the wire-bonding machine would break through the 20nm LSNT layer due to ultrasonic forces and would damage the wire-bonding pads of the cantilevers. Therefore, the electrical current could flow from one damaged pad to the next one through the silicon chip body.

We bypassed this problem by gluing the wires manually on the cantilever pads using conductive epoxy. However, this approach is suitable for low-volume research purposes but not for high-volume manufacture of general-purpose AFM cantilevers. One approach to overcome this issue is fortifying the cantilever bonding pads by adding an extra hard layer, for example, 100nm SiO₂, between the LSNT layer and the silicon chip body.

Note:

The concept of the multilayer MEMS devices has been internationally patented which is presented in Appendix B.

Chapter 5

5. Self-sensing SU8 cantilevers based on MoS₂ piezoresistors

As discussed in chapter 2, we showed that the microfabrication process of SU8 cantilevers has promising aspects in terms of the imaging bandwidth and having SU8 as a device material. We can fabricate SU8 devices with thicknesses ranging from hundreds of nanometers to hundreds of micrometers; all by spin coating. Since a high-temperature process is not possible with polymer cantilevers, mostly sputtered metals, polysilicon and carbon composites are used as piezoresistive sensors [47], [136]–[138]. Two-Dimensional (2D) materials are new alternatives for piezoresistive strain sensing [65]. The high mechanical flexibility and low bending stiffness of 2D materials prevent local stiffening of the polymer cantilevers. The local stiffening happens when the elastic modulus of the sensing element is higher than the elastic modulus of the cantilever material and hence the flexural rigidity of the cantilever increases locally where the sensing element is placed. This local stiffening forces the neutral axis to become closer to the sensing element and reduces the deflection sensitivity. Furthermore, the deflection sensitivity depends on the gauge factor of the sensing element. The gauge factor is a unit-less parameter and is defined as the ratio of relative change in electrical resistance R , to the mechanical strain ϵ . For instance the gauge factor of polysilicon is 30 and the gauge factor of thin film gold is 2. For the 2D piezoresistive piezoresistors, the high gauge factor ranging from 10s to 100s further raises the deflection sensitivity [139]–[141]. Based on these advantages of 2D piezoresistive materials, we chose MoS₂ for the piezoresistive readout in our SU8 cantilevers since the in-plane geometric properties of 2D materials provides convenience and flexibility in fabrication and design.

This work has been done in collaboration with Prof. Andras Kis and Dr. Yen-Cheng Kung (lanes.epfl.ch).

5.1 Device design and fabrication process

Rectangular and triangular cantilevers are widely used cantilevers. Triangular cantilevers have the advantage of reducing lateral twisting, so they are preferable in high speed scanning.

In our work, we used a triangular cantilever beam for our study. The analytical formula of

the resonance frequency of a triangular cantilever is $f = \frac{t}{2\pi L^2} \sqrt{\frac{30E}{7\rho}}$. In this formula, t is

the thickness of the cantilever, L is the triangular beam length, E is Young's modulus of the materials and ρ is the mass density. In our design, we chose $t = 10\mu\text{m}$ and $L = 130\mu\text{m}$. The Young's modulus and the mass density of SU8 are 4GPa and 1200kg/m³ respectively. The resulting resonance frequency is 356.6 kHz.

To minimize the complexity of the fabrication, the entire body of the device is made of SU8 through spin coating as presented in Figure 5-1. Sandwiched between the SU8 layers is the Wheatstone bridge readout circuit composed of four pairs of MoS₂ resistors and metal contacts as shown in Figure 5-1(a). One pair of the MoS₂ resistors is on the beam and the resistance changes when the cantilever bends while the other resistors are on the chip body and do not experience any bending. The images of the finalized cantilevers shown in Figure 5-1(b) and (c) prove the successful fabrication.

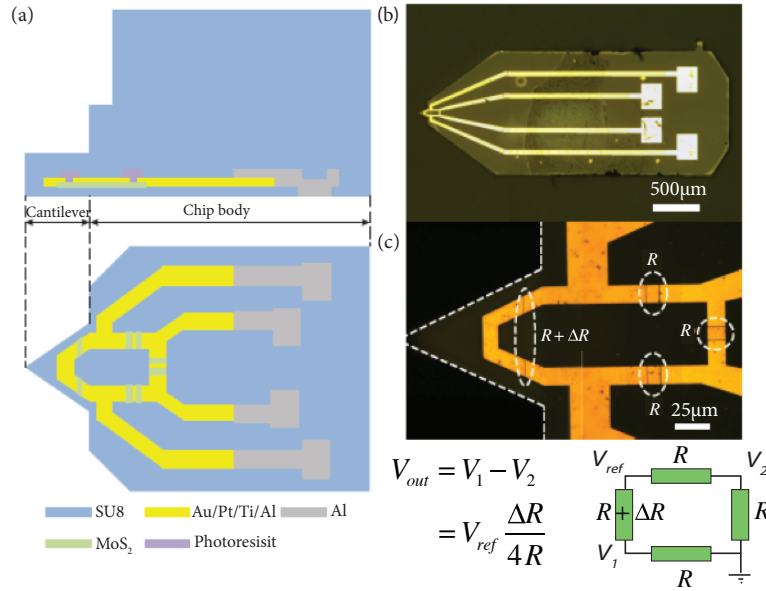


Figure 5-1 SU8 cantilever with MoS₂ piezoresistive readout. (a) Side-view and top-view schematic of the cantilever. (b) An optical image of the entire chip. (c) An optical image and a schematic of the integrated Wheatstone bridge.

The fabrication process flow is shown in Figure 5-2. First, a Cr-Au-Cr sacrificial layer was introduced where 5nm Cr, 50nm Au, and 20nm Cr were deposited sequentially using e-beam evaporation. 1μm SU8 layer was then spin-coated and patterned by photolithography. The MoS₂ flakes were first grown on SiO₂ and then mechanically transferred to the SU8 layer using

PDMS stamp, similar to the protocol described in [142]. Metal traces were formed through e-beam lithography and e-beam evaporation followed by lift-off process. Metal traces were composed of 70nm Au, 15nm Pt, 15nm Ti and 50nm Al. The topmost Al layer was deposited to improve the adhesion between the metal traces and the next SU8 layer. The wire-bonding pads were made through photolithography, 1.5 μ m Al evaporation, and lift off process. Patterning of MoS₂ piezoresistors was performed with photolithography and O₂ plasma to remove the excessive MoS₂. The rest of SU8 structural layers consisting of 9 μ m SU8 cantilever, 30 μ m SU8 chip body-1, and 120 μ m SU8 chip body-2 were then formed through photolithography. Two chip bodies were required to mimic the inclined wall, essential for the laser beam to access the cantilever in the OBD method. Finally, Cr etchant was used to etch the Cr layer and release the cantilevers at the end of the process.

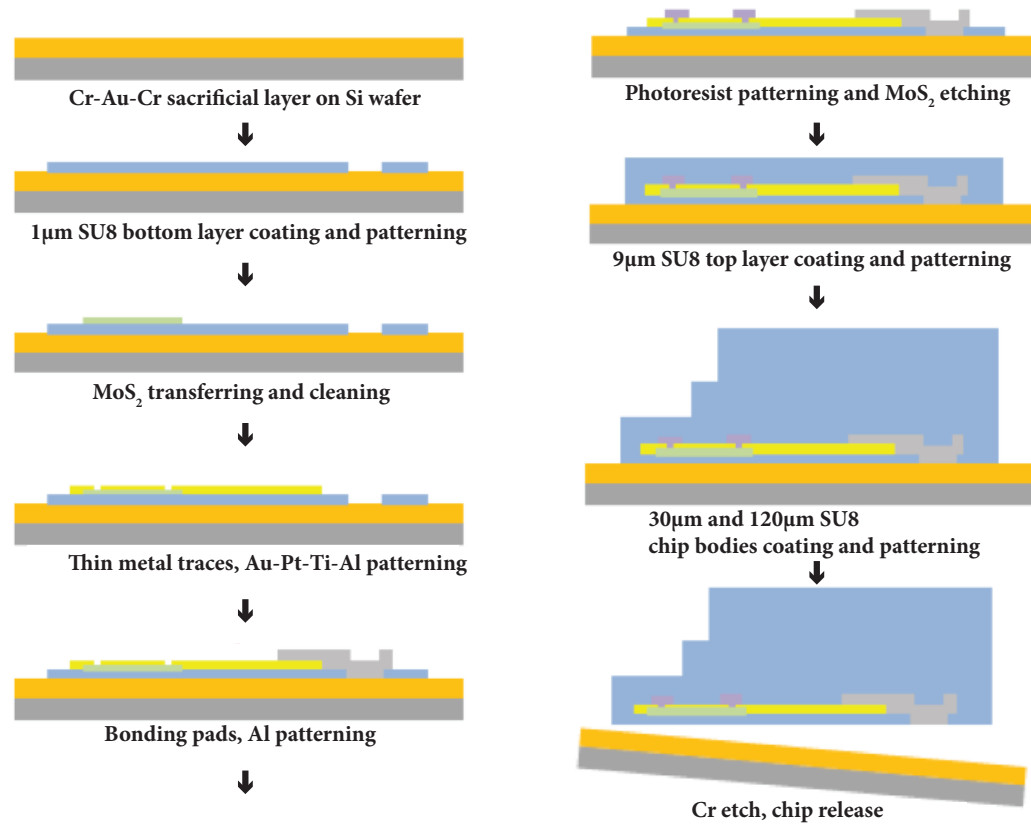


Figure 5-2. The process flow for the fabrication of SU8 cantilevers with MoS₂ piezoresistors.

5.2 Characterization of MoS₂-SU8 cantilevers

The mechanical tuning of the fabricated cantilever was performed using both OBD and piezoresistive readouts. The designed resonance frequency was 356.6kHz, so we have executed the measurement up to 800 kHz. From Figure 5-3, we could see a good overlap of the fundamental resonance frequency between the OBD and the MoS₂ piezoresistive readouts. We confirmed the resonance frequency with the thermal tune measurement where the

fundamental resonance peak is observed. The measured resonance frequency of the cantilever was measured at 332.7kHz. The parasitic peaks discussed in chapter 3 are quite visible in the mechanical tuning.

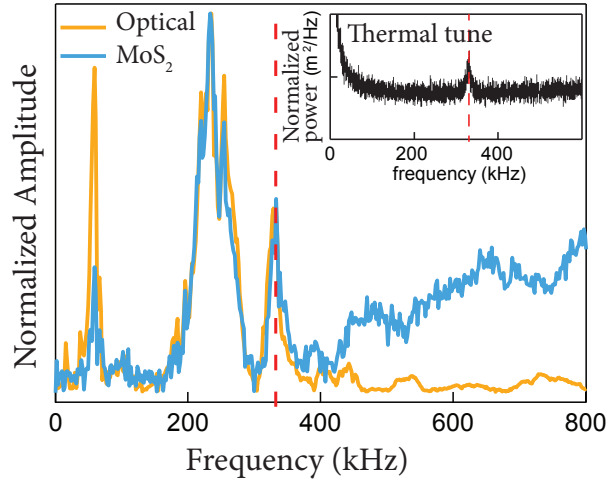


Figure 5-3. The mechanical tuning of the SU8 cantilever with optical and MoS₂ based piezoresistive readouts. The inset is the thermal tuning curve of the cantilever. The red dashed line indicates the position of the resonant frequency located at 332.7kHz.

5.3 Toward successful fabrication

The abovementioned fabrication process is the one that led to functional cantilevers. Plenty of modifications to the process flow have been made in order to optimize the production. Here I discuss some critical steps and the benefits we obtained from the modified process.

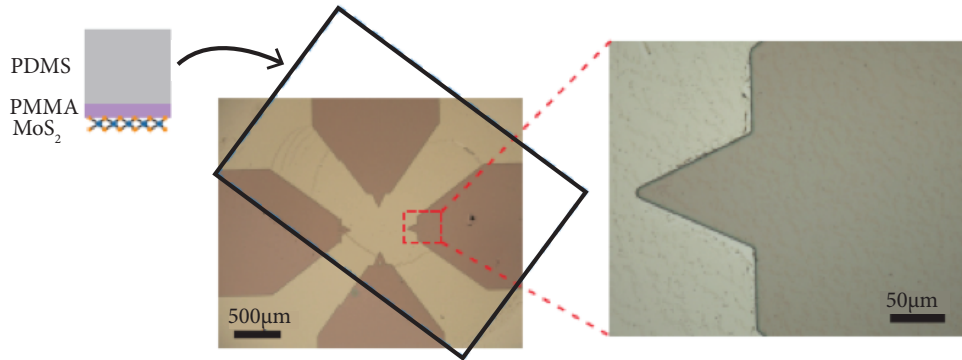


Figure 5-4 MoS₂ transfer on the bottom SU8 layer of the cantilevers. A PDMS/PMMA stack transfers continuous MoS₂ on the bottom SU8 layer. The optical image at the right part of the panel shows the crack-free continuous MoS₂.

For the MoS₂ transfer, the PDMS assisting method is used here for its compatibility for large continuous area transfer. As shown in Figure 5-4, the PDMS/PMMA/MoS₂ covers only the selective area of four cantilevers where the Wheatstone bridges are located, and at the right panel, we could see the transferred MoS₂ showing crack-free uniform coverage on the

first layer of SU8. This method provides a material-saving strategy and could be possibly scaled-up using a robotic machine with precise alignment control.

The entire cantilever with its chip body is composed of several layers of SU8, which is exposed to several thermal cycles. During the development of the fabrication process, the adhesion between SU8 and the silicon wafer, and also the adhesion between the gold metal traces and SU8 layer were the main challenges we faced. In Figure 5-5(a), the optical image shows multiple cantilevers on a silicon wafer after developing the SU8 chip body in PGMEA (SU8 developer) and before the chip release, indicating partial delamination of the SU8 layers mainly above the Wheatstone bridge circuits. We attributed this problem to the internal stresses of the thick SU8 chip body, with a total thickness of $100\mu\text{m} + 200\mu\text{m}$ in this case. Reducing the chip body thickness from $300\mu\text{m}$ to $150\mu\text{m}$ caused an improvement as shown in Figure 5-5(b).

As the total thickness of the chip body was lowered from $300\mu\text{m}$ to $150\mu\text{m}$, the delaminated region significantly diminished, but still remained at the front-end of the devices.

Applying O_2 plasma treatment with MoS_2 channel protected under a photoresist mask could generally make the surface bond with the top SU8 layer better. By implementing this strategy, the delamination issue has been solved as exhibited in Figure 5-5(c), from which no clear color contrast is observed over the entire wafer.

In order to release the devices, first, we attempted top release KOH (40 wt%) silicon etch at a mild temperature of 60°C . Due to the slow lateral etching rate, hours of immersion was required. The long period not only delays the process but also causes damage to the circuit layer due to the penetration of KOH into the interface as shown in Figure 5-6(a). As an alternative, a sacrificial layer composed of 5nmCr, 50nmAu and 20nmCr was deposited on the silicon wafer before the fabrication of cantilevers and Cr etchant (Cr-14), was used to etch the Cr layer to release the cantilevers. The first thin layer of Cr is used to improve the adhesion, and the layers of Au and Cr on top behave as the cathode and the anode in an electrolyte environment due to the big difference in their electronegativity, inducing an internal battery. The induced voltage provides an extra driving force to the reactant at the interface where etching occurs [143]. A Cr-etchant released cantilever is shown in Figure 5-6(b), where there is no damage observed either on the SU8 or the Wheatstone bridge, indicating a superior solution.

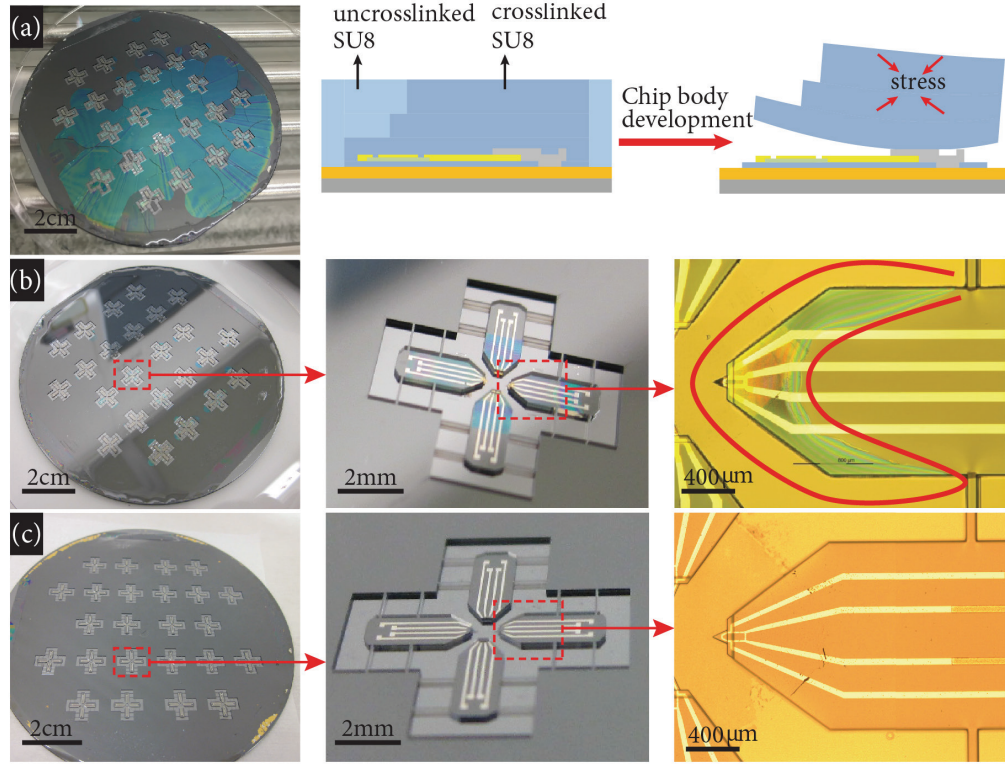


Figure 5-5 Toward fixing the delamination issues. (a) Severe delamination of SU8 mainly due to internal stresses induced during thermal cycles. In the optical image on left, the small gray region is the only part with good adhesion, and the rest is where the delamination occurred. The schematic shows how internal stress causes the delamination. (b) The results after reducing the total thickness of the chip body from 300μm to 150μm where the delaminated region is largely reduced; the red loop in the right picture indicates the still delaminated region of a single device. (c) The results after implementing both strategies of thickness reduction and adhesion enhancement through O₂ plasma activation. No clear delamination is optically observed in this case.

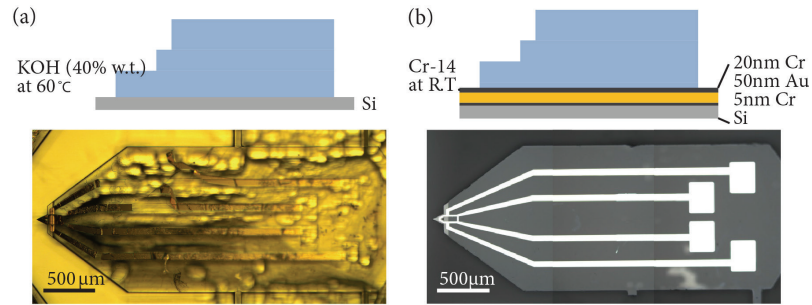


Figure 5-6. Two different release methods for the SU8 cantilevers; the schematics and the optical images of the released cantilevers through (a) KOH and (b) sacrificial layer methods.

5.4 Conclusion

In this work, we integrated MoS₂ piezoresistors with our previously developed SU8 cantilevers. The high mechanical flexibility of atomically thin MoS₂ piezoresistors prevents local stiffening (and hence reducing the deflection sensitivity) at the base of the cantilevers where the sensing elements are placed. In addition, the high gauge factor of the MoS₂

piezoresistors can fundamentally increase the deflection sensitivity of the self-sensing SU8 cantilevers. Although, this high gauge factor is accompanied with the high electrical resistance (in the range of 100s mega ohm) of the MoS₂ piezoresistors. Hence the signal to noise ratio of the deflection signal reduces dramatically.

In order to develop functional MoS₂ based SU8 cantilevers for AFM applications, we are required to reduce the resistance of the MoS₂ piezoresistors, for example by means of surface doping.

Chapter 6

6. Air and water-stable n-type doping and encapsulation of MoS₂ flexible devices with SU8

During the fabrication of self-sensing SU8 cantilevers based on MoS₂ piezoresistors (described in chapter 5), we noticed that the electrical resistance of the MoS₂ piezoresistors was reduced after SU8 coating. This was an appealing behavior since the high electrical resistance of the MoS₂ strain sensors restricts its application in high-resolution MEMS devices. This chapter discusses our performed measurements to study this observation and the achieved results. This work was carried out in collaboration with Prof. Andras Kis group at EPFL (LANES), and my contribution was primarily designing the experiments.

This is a copy of an article:

Kung YC*, Hosseini N*, Dumcenco D, Fantner GE, Kis A. Air and Water-Stable n-Type Doping and Encapsulation of Flexible MoS₂ Devices with SU8. *Advanced Electronic Materials*. 2019 Jan; 5(1):1800492.

*Yen-Cheng Kung and Nahid Hosseini contributed to this equally.

6.1 Abstract

Favorable mechanical and electrical properties motivate the use of 2D semiconductors in flexible electronic devices. One of the main challenges here is the absence of a practical doping strategy which should provide air-stable, tunable doping levels in a process with a low thermal budget. Here, we show that SU8, an epoxy-based photoresist, can be used for non-degenerate n-type doping of monolayer MoS₂. The doping level can be finely tuned via low-temperature annealing. Our doping method exhibits good ambient stability. The high degree of mechanical flexibility and low processing temperature also allows the integration of SU8 coating with flexible MoS₂ FETs, where it can provide both controllable doping and act as an encapsulation layer. The demonstrated stability of the devices to bending and exposure to

water confirms the attractiveness of using SU8 in flexible electronic devices based on 2D semiconductors in a simple, versatile and scalable approach.

6.2 Introduction

Layered transition metal dichalcogenides (TMDCs) are receiving resurgent interest due to their interesting physical and chemical properties [144]. Their potential applications cover a wide range, including electronics [145], optoelectronics, [146], [147] NEMS, [148] spin-valleytronics [149], and catalysis [150]. MoS₂ is the most widely studied semiconducting TMDC, in part due to its high stability. Its semiconducting nature and ultrathin body allow the realization of field-effect transistors with a large on-off ratio [145] while the atomic scale thickness can suppress short-channel effects at aggressively scaled gate lengths [151], [152]. Favorable mechanical properties, with a high fracture strain of at least 10% [153] make MoS₂ and other 2D semiconductors good candidates for applications in flexible electronic devices and circuits [154].

However, several technical challenges need to be overcome before flexible devices based on 2D materials become widely available. Among them, a stable and controllable doping method that is compatible with flexible substrates and low processing temperatures should be developed. Strategies based on exposure to plasma, intercalation and implantation were only demonstrated on multilayer MoS₂ [155]–[157] which is less interesting for optoelectronic applications due to its indirect bandgap. Substitution doping with for example Rhenium or Niobium during CVD growth result in doping levels that cannot be modified after growth and are difficult to implement locally and selectively [158], [159]. Chemical doping on the other hand, can be easily implemented due to the large surface to volume ratio of 2D materials [71]. Various molecular surface doping methods based on wet chemical treatment have been widely explored, but most of them are not air stable and are difficult to control [160]–[163]. While doping strategies based on functionalizing 2D materials with noble metal nanoparticles offer air stability, they do not result in good uniformity [164], [165]. Stable and controllable doping could be achieved using Cs₂CO₃ thin films by varying the film thickness [68] or phosphorus silicate glass (PSG) substrates through thermal and optical activation [166]; however, brittle Cs₂CO₃ films and PSG substrates are not suitable for flexible electronics. So far, a practical technique for achieving air-stable and controllable doping of MoS₂ using materials and processes that are compatible with flexible electronics is missing.

An effective encapsulation layer with good gas barrier performance is another key enabler for flexible devices based on MoS₂ and other 2D semiconductors. It is well known that the performance of MoS₂ FETs degrades in air due to surface adsorption of O₂ and H₂O [167]–

[169]. Al_2O_3 , HfO_2 and other high-k inorganic dielectrics have been commonly used as encapsulation layers for layered 2D devices [170], [145]. However, their brittleness makes them undesirable for applications in flexible electronics, where the encapsulation layer usually experiences the highest strain under bending. Hexagonal boron nitride (h-BN), a layered insulating material, is a promising candidate for encapsulation of other 2D materials due to the clean and smooth interface free of dangling bonds, but encapsulation is performed using a material transfer process which has so far been restricted to laboratory scale [171]–[173].

We propose using SU8 as a solution to these issues. Here, we demonstrate that SU8 can provide air-stable and controllable doping while at the same time acting as a gas and water barrier encapsulations layer, just like in the case of CNT and graphene devices [174], [175]. Its mechanical flexibility and low processing temperature also make it compatible with flexible electronics. We show that the doping level can be easily tuned by simply extending the polymer baking time. We also fabricate flexible MoS_2 transistors that can be submerged in water for extended periods of time thanks to the protective SU8 coating while also being able to withstand bending to over 100 cycles of mechanical deformation.

6.3 Results

6.3.1 Doping of MoS_2 field effect transistors using SU8

We first evaluate the doping effect of SU8 on MoS_2 using bottom-gated field effect transistors fabricated on $\text{SiO}_2/\text{p}^{++}\text{Si}$ substrates, Figure 6-1(a) and (b). Devices were characterized before and after SU8 coating followed by a soft-bake process, with the transfer characteristic shown on Figure 6-1(c). We find a large increase in on-current and a negative shift of the threshold voltage which is the result of n-type doping.

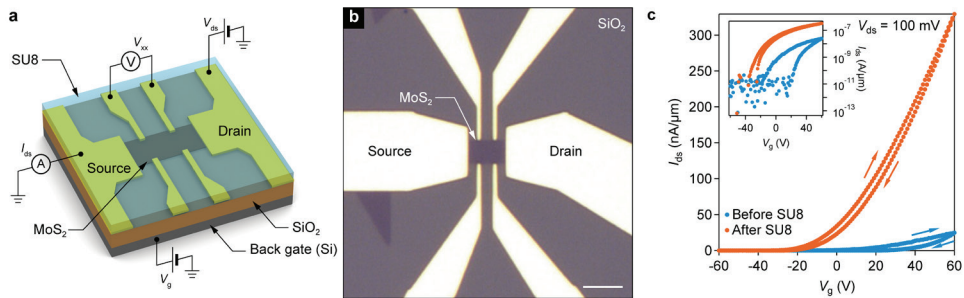


Figure 6-1 Bottom-gated monolayer MoS_2 FET with SU8 coating. (a), Schematic of the device with an SU8 over layer. (b) Optical image of the device before applying SU8, scale bar is 5 μm . (c) Transfer characteristic of the MoS_2 FET before and after SU8 deposition. Inset: logarithmic-scale plot of the transfer characteristic.

The extracted carrier concentration of the doped MoS₂ is $2.4 \times 10^{12} \text{ cm}^{-2}$, which is at a non-degenerate doping level as reflected by the preserved off-state current, Figure 6-1(c) inset. Previous reports of chemical doping of MoS₂ cover a wide range of doping levels, from $\sim 10^{10}$ to $\sim 10^{13} \text{ cm}^{-2}$, with a large variation resulting not only from different doping strategies but also intrinsic MoS₂ properties, the flake thickness and the interface charge state densities [166], [170].

The increased carrier concentration resulting from the n-type doping by SU8 reduces both the sheet resistance (R_s) and the Schottky barrier height between the metal contact and MoS₂, resulting in smaller contact resistance R_c . Measurements on four-terminal devices (Figure 6-2 (a) and (b)), show that both R_s and R_c are reduced by more than one order of magnitude after SU8 doping.

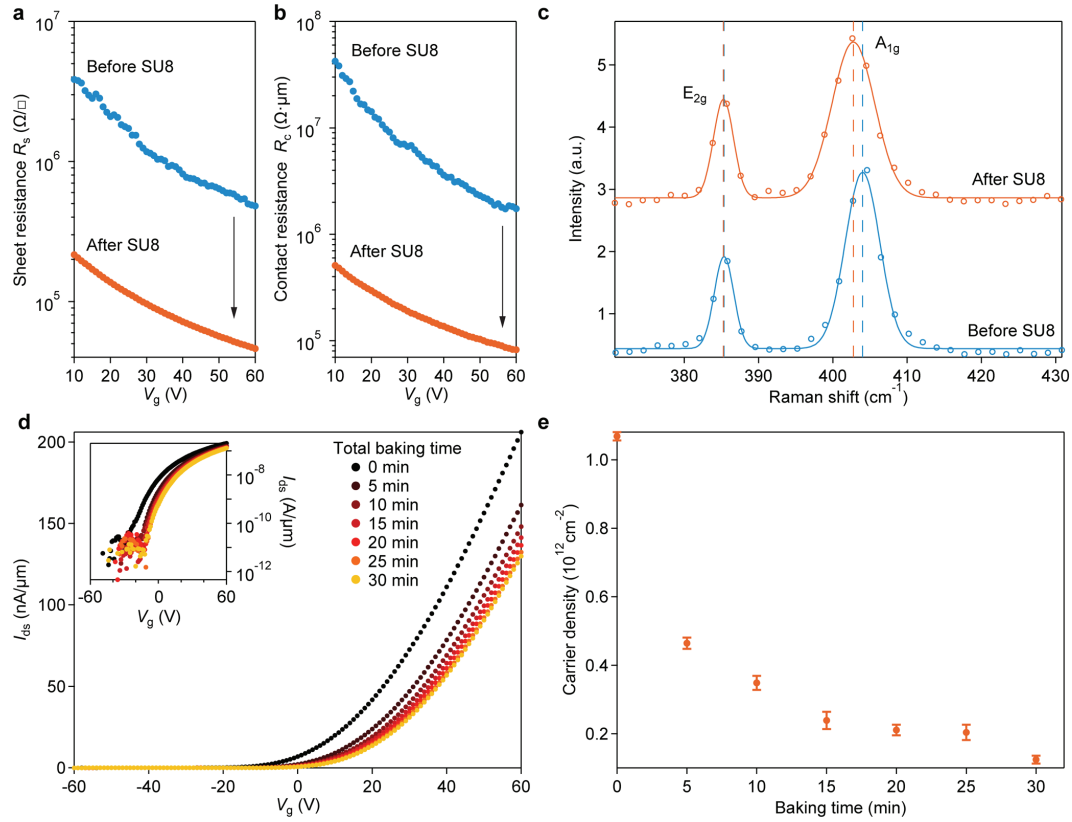


Figure 6-2 Effect of tunable SU8 doping on monolayer CVD-MoS₂. (a) and (b), Sheet resistance and contact resistance of the MoS₂ FET before and after SU8 doping. (c) Raman spectrum of A_{1g} and E_{2g} peaks of a CVD-MoS₂ single crystal before and after SU8 doping. (d) Transfer characteristic of an MoS₂ FET with SU8 doping. The device was annealed at 330 K with different baking times. Inset: log-lin plot of the transfer characteristic. (e), Tuning carrier concentration of the SU8 doped MoS₂ with baking time. The carrier concentration decreases monotonically with increasing baking time.

6.3.2 Raman spectroscopy of monolayer MoS₂ doped using SU8

Raman spectroscopy was performed to observe the effect of SU8 on MoS₂. We have carried out measurements before and after SU8 coating on the same monolayer CVD-MoS₂ single crystal transferred onto a SiO₂/Si substrate. Raman-active A_{1g} and E_{2g} modes are commonly used as indicators of MoS₂ thickness and carrier concentration [176], [177]. The Raman spectrum showing A_{1g} and E_{2g} modes of monolayer MoS₂ before and after SU8 coating is presented in Figure 6-2(c). The Raman shift difference between A_{1g} and E_{2g} peaks is 18.65 cm⁻¹ for our monolayer MoS₂ flake, which matches the reported value for monolayer MoS₂ in the literature [176]. After SU8 doping, the position of the E_{2g} peak does not change and the position of the A_{1g} peak shifts from 404 cm⁻¹ to 402.8 cm⁻¹. The linewidth of the E_{2g} peak does not change while the line-width of the A_{1g} peak increases from 5.5 cm⁻¹ to 6.81 cm⁻¹. The softening and broadening of the A_{1g} peak are the signatures of n-type doping of MoS₂ flakes, consistent with a previous report on the effect of electrostatic doping [177] on the Raman spectrum of MoS₂, further confirming that SU8 induced n-type doping SU8.

6.3.3 Controlling the doping level by low-temperature annealing

Controllable doping methods are essential for practical applications. Various strategies for tuning the doping levels within different ranges of doping have been reported in the literature. For methods based on wet chemistry, typical ways of tuning the doping level are based on controlling the exposure time to the doping agent and using solvents to remove the physisorbed molecules gradually. For example, Kiriya *et al.* reduced the doping from degenerate to non-degenerate levels by using toluene to remove Benzyl Viologen molecules, a process which required two days of immersion in toluene in order to realize the full tuning range [72]. Doping resulting from exposure to (2-Fc-DMBI)₂, potassium, 1,2 dichloroethane, p-toluene sulfonic acid and hydrazine have been tuned by altering the exposure time in the range from seconds to hours [178], [179], [70], [162]. Apart from doping that involves wet chemistry, increasing the thickness of Cs₂CO₃ capping layers was also found to result in the monotonic increase of the doping level in the MoS₂ [68]. Thermal and optical activation of PSG doping on MoS₂ provides a wide range of doping level modulation between 3.6×10¹⁰ and 8.3×10¹² cm⁻², but the process requires high-temperature treatment at up to 900°C [166]. Here, we provide a suitable solution for controllable doping on flexible MoS₂ devices, by taking into consideration that the ideal process should involve low temperatures while preserving mechanical flexibility and air stability. With SU8 treatment, the doping level of MoS₂ can be tuned by low-temperature annealing which does not damage the plastic substrates. We demonstrate the ability to tune the doping level by comparing device characteristics before and after the annealing treatment performed at 330 K for 5 min on SU8-coated MoS₂ FETs.

This annealing treatment was repeated up to a total baking time of 30 min and all the measurements were performed at room temperature, Figure 6-2(d). The transfer characteristic of the device shifts towards positive V_g with increasing baking time, reflecting decreasing electron concentration. The corresponding n-type doping level decreases monotonously from $1.07 \times 10^{12} \text{ cm}^{-2}$ to $1.24 \times 10^{11} \text{ cm}^{-2}$, Figure 6-2(e). Details of the extraction of carrier concentration are described in the supplementary section 1. Our strategy involves a low energy cost and high production efficiency considering the low-temperature treatment and short annealing time used in the tuning process. Furthermore, compared to the chemical treatment methods, thermal activation generally results in a higher degree of process uniformity and simplicity.

6.3.4 Stability of SU8 doping in air and in deionized water

Long-term stability of the doping level is a basic requirement for practical applications. Aging of the doping source itself and the influence of the environment due to O_2 and H_2O adsorbates [178]–[180] are the two main sources of instability. In our case, exposing uncoated monolayer MoS_2 FETs to air, results in a decrease of the on-current by a factor of more than 3 within 35 minutes of devices being removed from vacuum (see supplementary information: 6.7.2, Comparison of device performance with and without SU8 encapsulation). On the other hand, SU8-coated devices demonstrate good gas barrier properties of SU8 by showing nearly no difference in device performance between air and vacuum (Supplementary information, Figure 6-8). Going further, we demonstrate longer-term air stability by exposing the device to air for 233 hours and finding only minor changes in the transfer characteristic, as depicted in Figure 6-3(a) and (b).

Encouraged by the favorable gas barrier properties, we further investigate water resistance of the SU8 layer. Bottom-gated flexible MoS_2 FETs on polyimide substrates were fabricated and coated with a $1 \text{ }\mu\text{m}$ thick SU8 doping and encapsulation layer. The devices were kept in D.I. water for over 65 hours. The device performance was periodically measured after removing the sample from the water and drying it with N_2 . As shown in Figure 6-3(c), both the on and off-state currents remained stable. Future work and optimization of SU8 deposition may result in an even better long-term stability while extending the study to saline-containing solutions could extend the field of applications to flexible electronic implants.

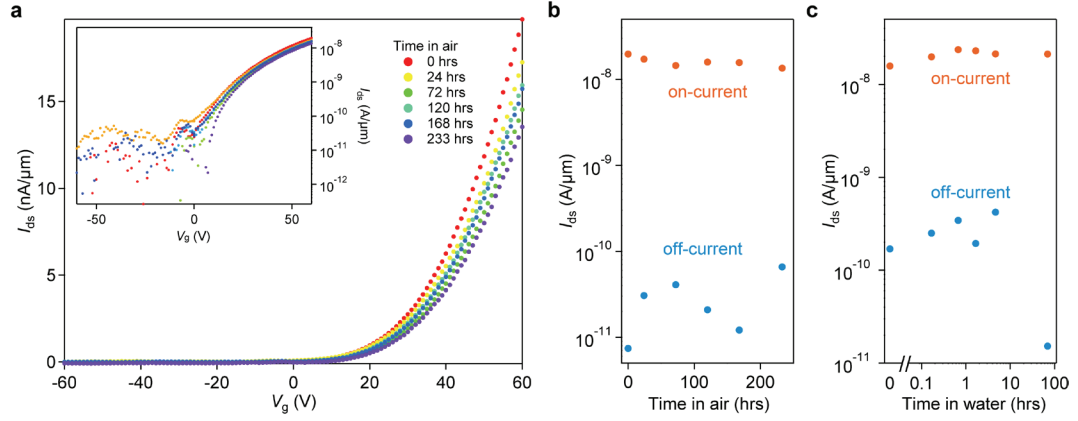


Figure 6-3 Stability of SU8-doped MoS₂ FETs. (a) The evolution of the transfer characteristic for an SU8-doped MoS₂ FET kept in air over 9 days. (b) The variation of on and off currents for the MoS₂ FET with SU8 doping over 9 days in air. (c) The variation of on-current and off-current for a flexible MoS₂ FET with SU8 doping after submersion in D.I. water for over 65 hours. For each measurement, the device was removed from water and dried using an N₂ gun.

6.3.5 Integration of SU8 with flexible MoS₂ field effect transistors

The high degree of mechanical flexibility and favorable electronic properties make MoS₂ and semiconducting TMDCs attractive materials for the realization of flexible FETs [180], [181]. The low glass transition temperature of flexible polymer substrates used for the realization of such devices makes temperature a critical process parameter. SU8 is interesting in this context as a thermally tunable dopant with a relatively low processing temperature of less than 130 °C. There is an additional need to develop a scalable encapsulation method for flexible MoS₂ transistors which could also solve the buckling issue observed in flexible MoS₂ devices under bending [181]. Our promising results on the stability of SU8-coated MoS₂ devices on rigid substrates motivate the integration of SU8 into flexible devices. The simplified process flow and the image of the device are shown in Figure 6-4 (a) and (b). The use of a 10 μm thick polyimide substrate together with a 1 μm SU8 encapsulation layer results in lightweight and easy bendable device (Figure 6-4 (c)). In Figure 6-4 (d) and (e) the consistent shift of the transfer characteristic curves towards the direction of negative gate voltages on multiple devices realized on the same chip reflects the good uniformity of the SU8-based doping method. The resilience of devices to bending was tested by applying strain along the direction of current flow through the channel. We first measure the devices in the flat state, and then bend them to a radius of 10 mm. We electrically characterize the device after releasing the strain and repeat the cycle 50 times. This is followed by an additional test run where we bend the device 50 more times to a radius of 7.5 mm. The uniaxial strain applied onto MoS₂ was estimated to be 0.048% and 0.064% for the bending radius of 10 mm and 7.5 mm respectively.

Figure 6-4 (f) and (g) show the evolution of the transfer characteristic curve of the FET device undergoing the bending test. We observe a positive and saturating shift of the transfer characteristic curve over multiple bending cycles. The off-current remains stable during the mechanical test, while the on-current showed a gradual decrease during the initial part of the test, reaching a stable level later on, Figure 6-4 (h). Overall, the devices show a stable on-off current ratio with changes of less than an order of magnitude over 100 bending cycles, similarly to other reports [182]–[184].

The transfer characteristic of a device under strain is shown in Figure 6-4 (i). The measurement was performed after the multiple bending test in order to guarantee a stable and repeatable reference point for the relaxed state of the device. The data shown for the relaxed state is the average of the values before and after bending. The drain-source current is higher under a smaller bending radius, where a larger strain is applied to MoS₂. While expecting a 7% and 9% increase in current for a bending radius of 10 and 7.5 mm respectively from the piezoresistive effect in MoS₂ [65], we find a stronger increase of 49% and 63% at $V_g = 40V$. This could be explained by different doping levels in our case and also a possible reduction in the contact resistance under strain.

6.4 Conclusion

In conclusion, we demonstrate n-type doping of monolayer CVD-MoS₂ induced by SU8 on monolayer CVD-MoS₂ with four-terminal electrical characterization and Raman spectroscopy.

The doping level can be fine-tuned using low-temperature annealing at 330K. Also, devices with SU8 encapsulation also show good air stability over a period of more than 9 days and good water resistance for more than 65 hours. The low-temperature process and good barrier properties make SU8 an attractive material for encapsulating and doping flexible MoS₂ devices. We have realized flexible MoS₂ FETs with SU8 encapsulation on 10μm polyimide with devices showing only minor changes in performance after 100 cycles of bending. This study paves the way for the end-use of flexible MoS₂ FETs.

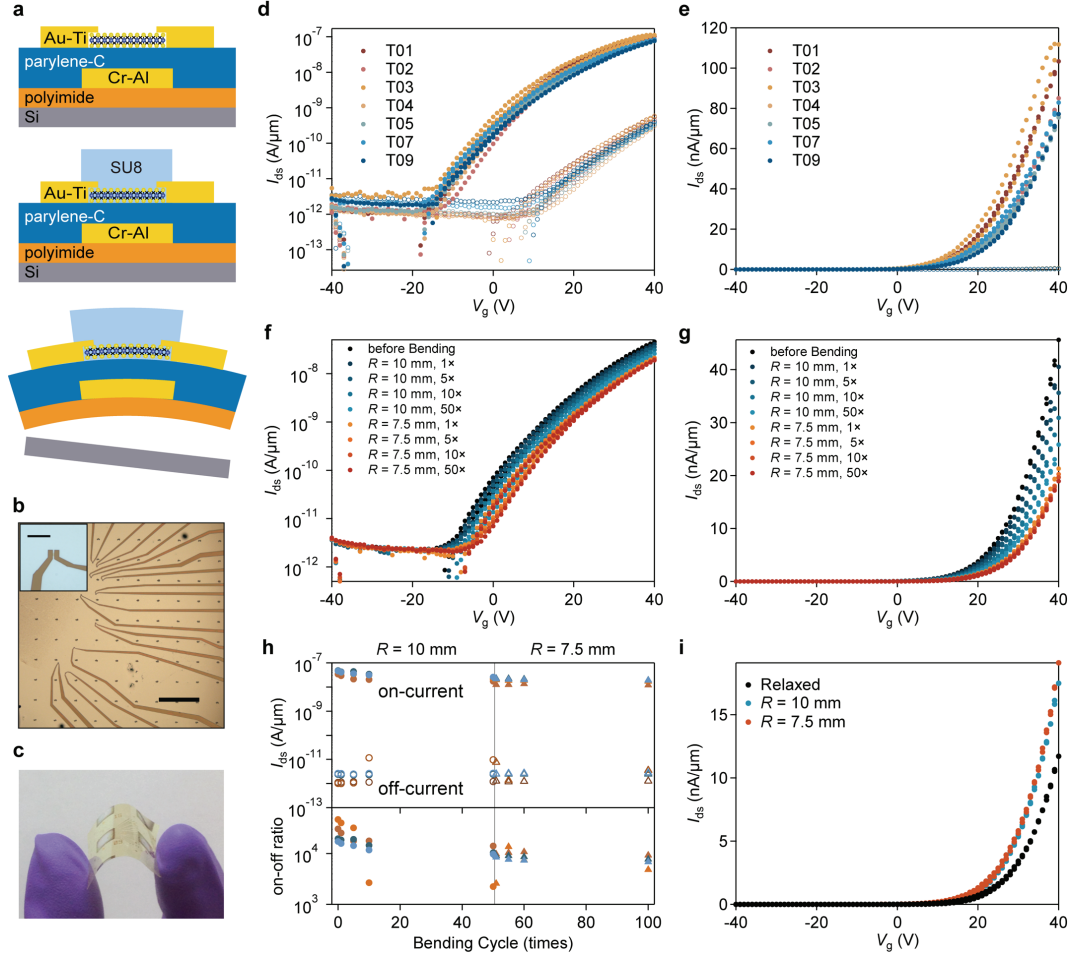


Figure 6-4 Flexible MoS₂ FETs on polyimide substrate with SU8 coating as the doping source and the encapsulation layer. (a) The schematic and the simplified process flow for the fabrication of flexible MoS₂ FETs with an SU8 coating. (b) Optical image of the device. The scale bar is 500 μm. Inset: optical image of a single device. The scale bar is 25 μm. (c) Photograph of flexible devices under bending. (d) and (e) Transfer characteristic for multiple flexible MoS₂ FETs before and after SU8 doping measured in air and shown on logarithmic and linear scales. The drain-source voltage is 100 mV. (f) and (g) The evolution of the change of the transfer curve of a flexible MoS₂ FET over multiple bending cycles in log and linear scale. The device was first bent 50 times to a 10 mm bending radius, followed by bending to a 7.5 mm bending radius for 50 times. (h) The change of on-current, off-current and on-off ratio of four different devices, represented in different colors, over multiple bending cycles. (i) The transfer characteristic curve of a device measured in the relaxed state and under bending. The measurement is performed after the bending test presented in parts f and g.

6.5 Methods

6.5.1 Fabrication of monolayer CVD-MoS₂ FETs on SiO₂/Si substrates

Monolayer CVD-MoS₂ was grown on c-plane sapphire substrate [185]. The film was transferred using PMMA A2 (MW = 950k, MicroChem), which was spin-coated on MoS₂/sapphire sample at 1500 rpm without baking. The coated sample was placed in a vacuum desiccator overnight to remove the solvent. The PMMA/MoS₂ film was released from the sapphire substrate by immersing the sample in 30%w.t. KOH at 75°C for 30 min. The film was then rinsed using D.I. water and picked-up with the SiO₂/Si substrate. The thickness of

SiO₂ is 270 nm. After drying the sample on a hotplate at 75°C, the sample was kept in acetone overnight to remove the PMMA. Annealing in furnace with gas flow of 100 sccm Ar and 10 sccm H₂ at 350°C for 8 hours was used to remove the PMMA residue. Electron beam lithography was used to pattern the metal contact and the etching mask. MMA EL6 (4000 rpm, 180°C, 5 min) and PMMA A2 (1500 rpm, 180°C, 5 min) double layer resist was used as an e-beam resist. 85nm Au and 5nm Ti was deposited by e-beam evaporation and the lift-off was done in acetone. Ti layer was used for improving the adhesion of SU8 to the devices. The sample was annealed for the second time in the furnace under a gas flow of 100 sccm Ar and 10 sccm H₂ at 250°C for 8 hours. MoS₂ channel was defined by O₂ plasma etching followed by acetone cleaning and device annealing with the same recipe to remove the residue of the resist. For devices doped with SU8, the SU8 solution was drop-cast on top of the transistors, followed by soft basing in an oven. Samples were heated up with a ramp rate of 2°C/min from 30°C to 130°C, maintained at 130°C for 5 min and cool-down with the same rate.

6.5.2 Fabrication of flexible CVD-MoS₂ FETs on polyimide substrate

10 μm polyimide (PI2611, HD Microsystems) was spin-coated on an Si wafer at 1200 rpm for 45 s with a ramp rate of 100 rpm/s. The sample was soft-baked on a hotplate at 120°C and hard-baked in an oven with N₂ flow at 300°C. Bottom gate (5nm Cr and 50nm Al) was deposited using an e-beam evaporator through shadow masks. A 200 nm thick parylene-C layer was deposited using chemical vapor deposition and used as the gate insulating layer. CVD-MoS₂ was transferred with the same method as mentioned above onto the parylene-C surface. The sample was immersed in acetone overnight and annealed in a furnace with a 200 sccm Ar flow at 200°C for 4 hours to remove the PMMA residue. Contact electrodes were formed using the same method as in the fabrication of devices on SiO₂/Si substrate mentioned above. SU8 layer 1 μm thick of (GM1040, Gersteltec sàrl) was spin-coated, followed by soft-bake, exposure and post-exposure bake. Finally, the polyimide substrate with fabricated devices on top was peeled-off from the silicon support manually.

6.5.3 Electrical Measurement of MoS₂ FETs

Electrical characterization was carried out using Agilent E5270B, National Instruments DAQ cards, SR570 current preamplifiers and SR560 low noise voltage preamplifiers.

6.5.4 Raman Spectrum Measurement of MoS₂ Flakes

Raman spectrum of CVD monolayer MoS₂ was measured using a Renishaw inVia Reflex Raman Confocal microscope with 532 nm laser source and grating of 1800 gr/mm.

6.5.5 Calculation of Neutral Plane and strain of Flexible Devices

In a multilayer system, there are n layers where the bottom layer is the first layer. Then the distance y between neutral plane and bottom surface of the first layer is given by $y = \frac{\sum_{i=1}^n E_i t_i \left[\sum_{j=1}^i t_j - \frac{t_i}{2} \right]}{\sum_{i=1}^n E_i t_i}$ [186]. E_i and t_i are the Young's moduli and the thickness of each layer. For the flexible MoS₂ FETs, the stack is composed of 10 μm polyimide, 5 nm Cr, 50 nm Al, 200 nm parylene-C, 0.7 nm MoS₂ and 1 μm SU8. The Young's moduli are $E_{\text{polyimide}} = 8.5 \text{ GPa}$, $E_{\text{Cr}} = 279 \text{ GPa}$, $E_{\text{Al}} = 70 \text{ GPa}$, $E_{\text{parylene}} = 2.8 \text{ GPa}$, $E_{\text{MoS}_2} = 270 \text{ GPa}$ and $E_{\text{SU8}} = 2.92 \text{ GPa}$. The calculated y and the distance between MoS₂ and the neutral plane are 5.48 μm and 4.77 μm respectively. The equation $\varepsilon = d/R$ was used to calculate the strain applied onto MoS₂ with ε the applied strain, R the bending radius and d the distance between MoS₂ and the neutral plane of the sample.

6.6 Acknowledgements

We thank Sébastien Jiquet for the discussion on SU8. Devices were fabricated in EPFL Center for Micro/Nanotechnology (CMI). We acknowledge the help of Z. Benes (CMI) with e-beam lithography. Y-C.K, G.F. and A.K. acknowledge support from the CCMX Materials Challenge grant "Large Area Growth of 2D Materials for device integration". Y-C.K and A.K. would like to acknowledge support by the Marie Curie ITN network "MoWSeS" (grant no. 317451) and Swiss National Science Foundation (Grant 157739). A.K. acknowledges funding from the European Union's Horizon 2020 research and innovation program under grant agreement No 696656 (Graphene Flagship).

6.7 Supplementary Information

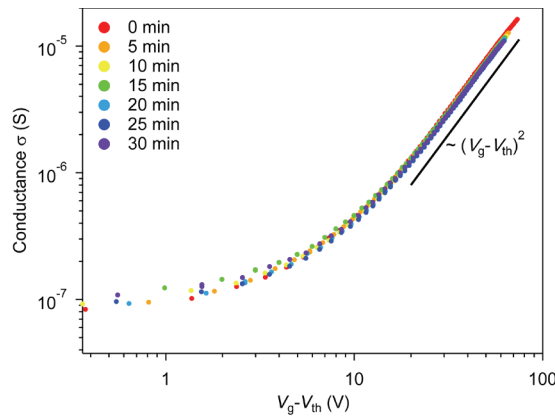


Figure 6-5 MoS₂ FET conductance σ plotted as a function of $(V_g - V_{th})$ for different annealing periods showing a good fit to the expression $\sigma \sim (V_g - V_{th})^2$ at overdrive voltages above 20 V.

The extraction of carrier concentration N_{2D} at zero gate voltage is based on the expression $N_{2D} = C_{ox}(V_g - V_{th})/e$ where C_{ox} is the capacitance per unit area for the 270 nm thick SiO₂ and

V_g is the gate bias voltage. V_{th} is the threshold voltage extracted from the intersect of $\sigma^{0.5}$ vs. V_g since $\sigma \sim (V_g - V_{th})^2$ when scattering from charged impurities is the dominant scattering mechanism. At large carrier concentrations, charged impurities are screened and the conductance is proportional to the charge density n [187]–[189].

6.7.1 The SU8 doping effect in vacuum and inert atmosphere

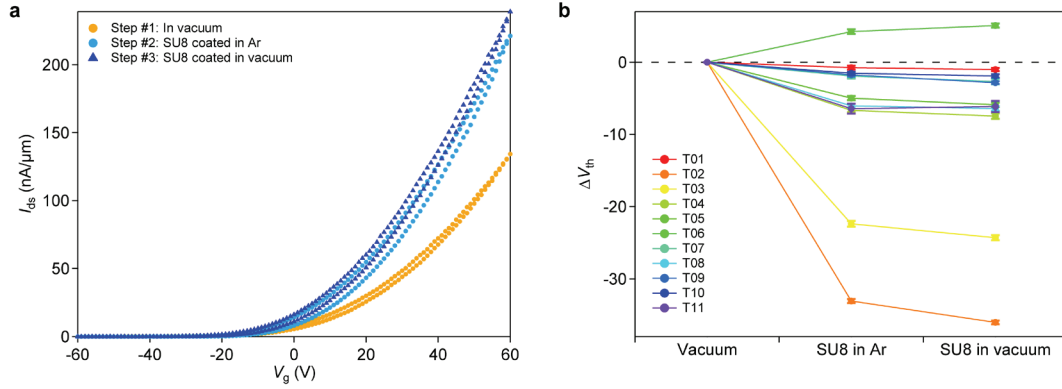


Figure 6-6 The SU8 doping effect under vacuum condition. (a) Transfer characteristics of an MoS₂ FET measured in vacuum after vacuum annealing, in Ar environment after SU8 doping followed by measurement in vacuum. (b) The change of the threshold voltage of multiple devices under different experimental conditions.

In order to remove the influence of water and oxygen adsorbents, which could mask the doping effect of SU8, we have also performed the following experiment using two-terminal bottom-gated MoS₂ FETs. First, we characterize the device in vacuum (5×10^{-7} mbar) after annealing in vacuum at 140°C for 12 hours. The chamber is then sealed with a manual valve, disconnected and transferred into an Ar-filled glovebox. The device is removed from the chamber and doped using SU8. The device is kept in an Ar environment for the second measurement. The device is then transferred back into the vacuum chamber without exposing it to the atmosphere and a third measurement is performed in vacuum. Figure 6-6(a) shows a typical set of transfer characteristics for a device characterized in these three different conditions. We can clearly see the SU8 n-type doping effect by comparing the transfer characteristic curve before and after SU8 coating. On current increased and the threshold voltage shifted to negative voltages after SU8 doping. The same trend was observed in multiple devices as shown on Figure 6-6(b) where we plot the threshold voltage change ΔV_{th} . Ten out of eleven devices we tested showed a clear negative shift of threshold voltage after SU8 doping, indicating the n-type doping effect. The variation of the voltage shift could be caused by variations in the adhesion of SU8 on MoS₂.

6.7.2 Comparison of device performance with and without SU8 encapsulation

The performance degradation of the device without encapsulation under ambient condition is shown in Figure 6-7. The gate voltage sweep started right after the device was exposed to air following annealing in vacuum. With each consecutive sweep, we can clearly see a drop in the current. Within 35 min, the on-current at a gate voltage $V_g = 60$ V decreased by more than a factor of 3 due to adsorption of atmospheric O_2 and H_2O on the MoS_2 surface [167], [190], [191].

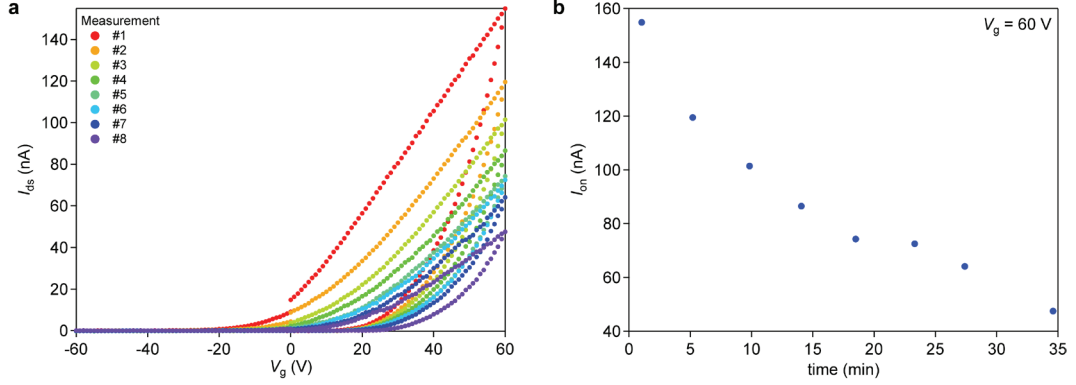


Figure 6-7 The performance degradation of a bottom-gated MoS_2 FET without SU8 encapsulation under ambient condition. (a) Consecutively measured transfer characteristic curves of a MoS_2 FET right after exposure to air from vacuum. (b) The evolution of the on-current recorded in air at $V_g = 60$ V.

The MoS_2 FET coated with SU8 was measured in air and vacuum, and the transfer characteristics show negligible difference between the two conditions, proving that the SU8 layer can effectively block the influence of air on MoS_2 .

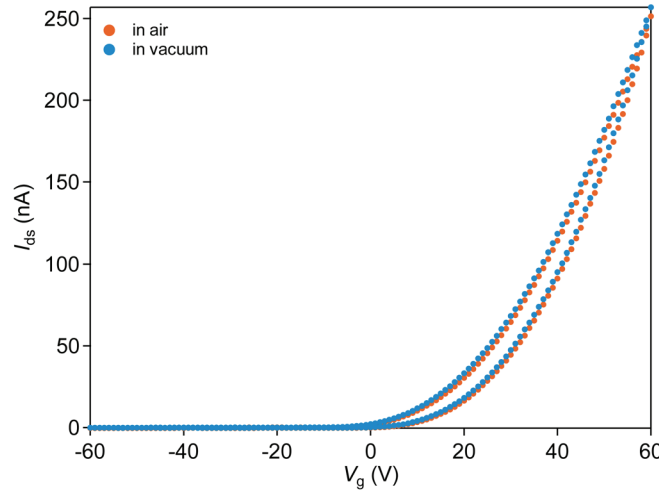


Figure 6-8 The transfer characteristic for an SU8-coated MoS_2 FET measured in air and under vacuum (1×10^{-6} mbar).

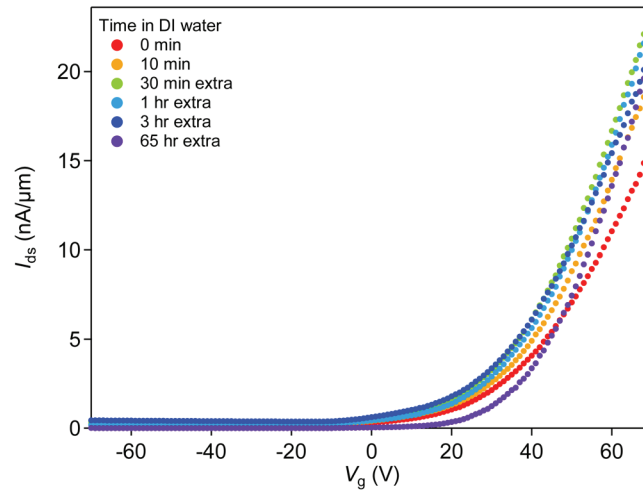


Figure 6-9 Water resistance of flexible MoS₂ FETs encapsulated with SU8. The figure shows the evolution of the transfer characteristics of the flexible device after having been submerged in water for a cumulative duration of over 65 hours. The device was taken out of the water and gently dried with N₂ gun before each measurement, after which it was returned to water.

Chapter 7

7. A monolithic MEMS position sensor for closed-loop high-speed atomic force microscopy

In parallel with my research on the AFM cantilevers, I also worked on the implementation of a closed-loop AFM piezotube scanner based on a monolithic MEMS displacement sensor. Such a closed-loop scanner works based on measuring the real trajectory of the scanner with the displacement sensor and then comparing it with the desired trajectory through a proportional-Integral (PI) controller. Reshaping the drive signal of the piezotube via the PI controller then compensates the nonlinearities of the piezotube scanner. Due to the small mass of our employed displacement sensor, we were able to integrate it into our home-built high-speed scanner.

In this work, I have developed the instrumentation (sensor integration, LABVIEW FPGA code, analog electronics and interfaces) for controlling the closed loop system. I also recovered our home-built high-speed scanner and made the required interfaces. I acquired all of the AFM images and performed all the data analysis. Finally, I have written the paper including the composition of the figures.

This is a copy of an article:

Hosseini N, Nievergelt AP, Adams JD, Stavrov VT, Fantner GE. A monolithic MEMS position sensor for closed-loop high-speed atomic force microscopy. *Nanotechnology*. 2016 Feb 22;27(13):135705.

7.1 Abstract

The accuracy and repeatability of atomic force microscopy (AFM) imaging significantly depend on the accuracy of the piezoactuator. However, nonlinear properties of piezoactuators can distort the image, necessitating sensor-based closed-loop nano-manipulators to achieve high accuracy AFM imaging. The advent of high-speed AFM has made the requirements on the position sensors in such a system even more stringent, requiring higher bandwidths and lower sensor mass than traditional sensors can provide. In this paper, we demonstrate a way for high-speed, high-precision closed-loop AFM nanopositioning using a novel, miniaturized MEMS position sensor in conjunction with a simple PID controller. The sensor was developed to respond to the need for small, lightweight, high-bandwidth, long-range and sub-nm-resolution position measurements in high-speed AFM applications. We demonstrate the use of this sensor for closed-loop operation of conventional as well as high-speed AFM operation to provide distortion-free images. The presented implementation of this closed-loop approach allows for positioning precision down to 2.1\AA (within 22.9kHz measurement bandwidth), reduces the integral nonlinearity to below 0.2% , and allows for accurate closed loop imaging at line rates up to 300 Hz .

7.2 Introduction

Piezoelectric actuators are extensively used in a variety of scanning applications such as scanning tunneling microscopes (STMs) and atomic force microscopes (AFMs) to move a sample or probe with nanometer resolution [192], [193]. However, nonlinear behavior of piezoactuators, such as hysteresis, creep and thermal drift, significantly affects positioning precision and results in image distortion[75], [76].

To account for these nonlinearities, two general types of control approaches are used: open-loop feed-forward input shaping or closed-loop feedback systems. In the first case, the appropriate piezo drive signal to linearize the motion of the scanner is calculated from a mathematical model [194]–[197]. This is a well-known and simple approach to control the drive signal, but linearization is often not perfect, since hysteresis is scan-size and scan-speed dependent.

Closed-loop feedback systems can address hysteresis, creep and drift and have therefore become the preferred method to reduce the nonlinearity of piezoactuators [198]–[202], as thoroughly discussed in a review paper by Fleming [78]. By comparing the real position (measured by a low-noise, precise position sensor) with the demanded position, a closed-loop real-time controller compensates the errors between the two trajectories. However, accurate

and timely measurement of the real position is required for adequate tracking performance. Depending on the performance of the position sensor and the implementation, closed-loop feedback can otherwise add additional noise, introduce additional nonlinearities or cause phase loss. Much work has been done to develop long-range, high-resolution, high-bandwidth, and highly linear position sensors. Nevertheless, combining all these properties in a single sensor is a challenging task [207], and therefore a tradeoff has to be made based on the particular application. Position sensors that have been used for nanopositioning applications include capacitive sensors [81], linear variable differential transformer (LVDT) [204], piezoresistive and piezoelectric strain gauge [205], [206], optical [82], interferometry [83], electrothermal [207] and giant magnetoresistance (GMR) [208] sensors. Each of these sensor types has relative strengths and weaknesses for nanopositioning applications. Optical sensors provide high-resolution and high-bandwidth positioning capability but often require expensive components [78]. Non-optical sensors like capacitive sensors have high bandwidth and good resolution but have internal nonlinearity, which requires additional nonlinearity compensation [78]. Resistive strain gauges are simple and low cost, and can be bonded into the actuator, however the temperature sensitivity and nonlinearity need to be considered [78]. LVDT sensors provide high-resolution, large-range and linear positioning but suffer from a low bandwidth [204]. GMR sensors may provide high-bandwidth and high-resolution position sensing, but cannot be used in applications where magnetic fields can deteriorate imaging accuracy.

While these sensors perform well for normal-speed AFM, most are expensive, require non-negligible forces, and/or add a significant amount of moving mass to the scanner. This added mass is an especially severe problem for high-speed AFMs, since the moving mass determines to a large extent the structural resonances and therefore the maximum achievable scan speed [209]. In this work, we present a small, lightweight and batch-fabricated micro-electro-mechanical system (MEMS) position sensor [210] implemented in closed-loop configuration in a standard as well as a high-speed AFM. This MEMS sensor uses mechanical deamplification flexures to adapt the sensor dynamic range to the scan-range of the scanner. These flexures are fabricated with sidewall-embedded piezoresistors for position sensing. The sidewall-embedded piezoresistors are inherently matched and result in intrinsic thermal stability as well as high sensitivity. These properties, combined with the low stiffness and low mass of the MEMS sensors, are essential to achieving the high resolution, low drift and high bandwidth of the closed-loop AFM scanner presented in this work.

7.3 Experimental setup and controller implementation

7.3.1 Sidewall piezoresistive position sensor

Closed-loop positioning performance depends considerably on the position sensor as the measuring device. To reduce the tracking error, the resolution, bandwidth and linearity of the sensor are primary concerns. Many SPM applications also require a relatively large range of motion (up to hundreds of micrometers), which is often achieved with a reduced resolution of the position sensor. In addition, the sensor should have high mechanical sensitivity and small thermal sensitivity for accurate measurement.

The presented piezoresistive MEMS strain sensor is based on recently developed sidewall-doped piezo-resistive strain sensors with mechanical deamplification for extended ranges [210]. Figure 7-1(a) illustrates the layout of one of the position sensors with 500 μm range of motion;

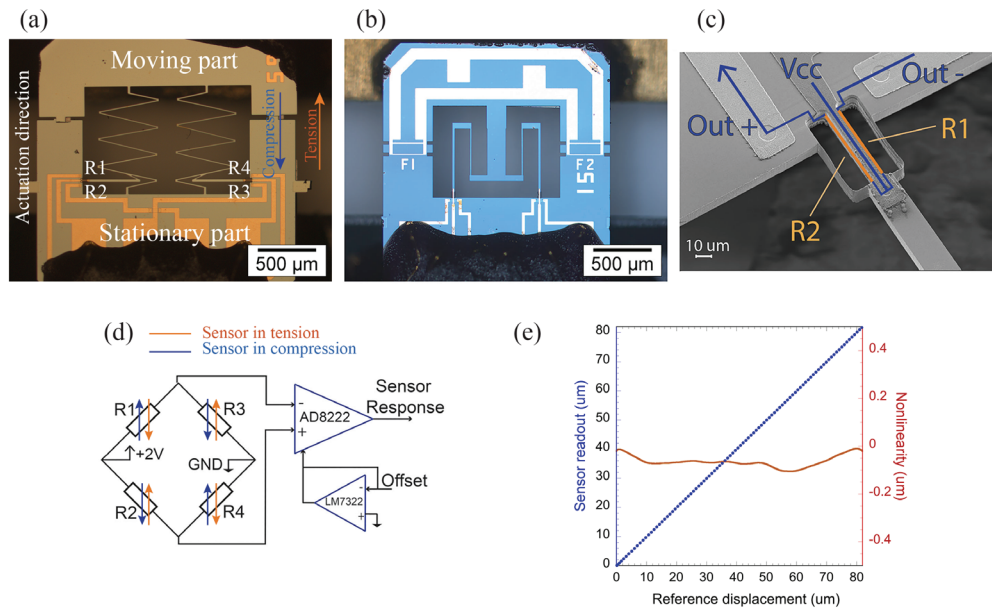


Figure 7-1- (a) Optical image of the 500 μm -range MEMS sensor. When R₁ and R₄ get compressed, R₂ and R₃ get elongated when the moving part moves upwards and vice versa. (b) Optical image of the sidewall piezoresistor 100 μm MEMS sensor. (c) SEM image of one lever and two sidewall piezoresistors. (d) Instrumentation amplifier based readout and compensation offset for the resistor mismatch. The bridge bias voltage is 2 V. (e) Linearity measurement of the 500 μm position sensor.

It comprises an outer frame and two compliant cantilevers with sidewall piezoresistors. Each cantilever is connected to the stationary and moving parts of the frame via a spring, which transduces the displacement of the moving frame to a strain in the area of Boron doped sidewall piezoresistors. Figure 7-1(b) shows an alternative sensor layout with 100 μm motion range, where the linear displacement is transferred to a bending motion of the modified

mechanisms. The sensor with 100 μm scan range has higher sensitivity comparing to 500 μm scan range sensor and provides better nanopositioning resolution.

Four piezo-resistors are pre-wired on chip in a fully active (changes in the resistance of all four resistors cause a change in the output voltage) Wheatstone-bridge configuration, where R_1 and R_4 change equivalently as do R_2 and R_3 . Figure 7-1(c) shows the electrical pathway in one lever with two sidewall piezoresistors. The piezo-resistors are placed at the base of the flexure where they experience maximum strain in the beam. The cantilever beam is narrower there so that additional stress concentration occurs at the points of the piezoresistors.

The resistance change in the sidewall-embedded piezo-resistors is measured using Wheatstone bridge readout electronics based on a low-noise instrumentation amplifier (AD8222, Analog Devices, MA, USA); see Figure 7-1(d). In the case of any temperature change, these four resistors experience the same amount of difference and the Wheatstone bridge configuration compensates this undesired change.

One of the fundamental factors for closed-loop operation is the linearity of the position sensor, as any deviation is mapped onto the controlled position. For instance, capacitive sensors are inherently non-linear, which requires further measurement and calculation to linearize the response [211]. To test the linearity of the 500 μm MEMS position sensor, we compared the sensor response with the motion of a precision, commercial 3D closed-loop positioning stage, having a closed loop range of 82 μm , (TRITOR 102, Piezosystem Jena). The resolution of the positioning stage is specified at 2 nm. Figure 7-1(e) shows that the linearity of our 500 μm position sensor tested over 82 μm (the full range of the reference stage) is better than 0.15% full-scale range.

7.3.2 Closed-loop implementation

Piezotube scanners are very popular for AFM instruments, since they provide a large range of motion, have high resolution and can be easily used as 3D nanopositioners. The drawback of the tube design is its relatively low lateral stiffness, making the tube sensitive to the mass and loads that might be applied by position sensors. Because of their high mass, many types of conventional nanopositioning sensors are therefore not suitable for use with piezo tubes. The sensor presented in this paper is compact and lightweight, with high displacement sensitivity and has a very low stiffness, and thereby does not restrict the motion of the piezo tube.

Here, we retrofitted a commercial 120 μm sample scanner (J scanner, Digital Instruments, Santa Barbara, USA) with 500 μm -range sidewall-embedded MEMS sensors for the X and Y-axes respectively. In order to accurately position the sample, the position sensors are placed on top of the piezotube scanner as close as possible to the scanned sample. The moving part of

the sensor is attached to a PCB that is glued on top of the scanner, and the stationary part is attached to a thin ring that is mounted around the piezo-guard (see Figure 7-2(a)).

Figure 7-2(b) describes the block diagram of the closed-loop implementation. A simple LabVIEW program is implemented on FPGA (NI CRIO 9074 FPGA). This program consists of two main modules, a PI module and a gain-shear correction module. The PI module: The measured sensor's signal is compared with the low voltage drive signal from the AFM controller for each direction and a modified signal is sent to the piezoactuator. The gain-shear module: The two input signals to the PI controller need to have the same amplitudes, and therefore the gain correction is required prior to any subsequent step. Plus, any non-orthogonally between X and Y displacements is corrected by modifying the sensor's signals through shear correction as discussed in methods section 1.

The PID controller is a premade module in LABVIEW FPGA. The controller's gains are set manually and the maximum gain is found by increasing it on the brink of oscillations. For imaging, the gains are then reduced slightly to avoid feedback oscillation in the system.

The PI controller compensates the error between the real position of the tube scanner and the triangular reference signal simultaneously. The output of the feedback is amplified by a high-voltage amplifier and provides linear, drift- and creep-free displacement of the piezo tube scanner. To mechanically protect the sensors and facilitate the imaging, a sample holder was glued on top of the sensors and scanner (see Figure 7-2(a)).

The readout electronics are placed close to the sensors to minimize electrical noise pickup. Figure 7-2(c) displays the Multimode AFM, piezotube and the position sensor readout electronics.

7.3.3 Implementation in a commercial AFM with a piezoelectric tube scanner

In general, the non-ideal behavior of piezoactuators causes several kinds of artifacts in AFM imaging. Figure 7-3(a) demonstrates the position sensor response in open- and closed-loop systems while a triangular trajectory was applied to the piezoactuator. As is clear in the figure, there is a lag between the response and reference signal in open loop. However, in the closed-loop system, the PID controller compensates the position deviation due to inherent hysteresis of the piezoactuator.

To highlight this effect we overlaid two diagonally cropped images, one in open loop and one in closed loop. The nonlinearity caused by hysteresis in the slow scan axis is observable by comparing the image half taken while scanning downward with the one scanning upward in open loop (see Figure 7-3(b)). On the other hand, closed-loop scanning compensates the undesired mismatch between images and provides repeatable scanning (see Figure 7-3(c)).

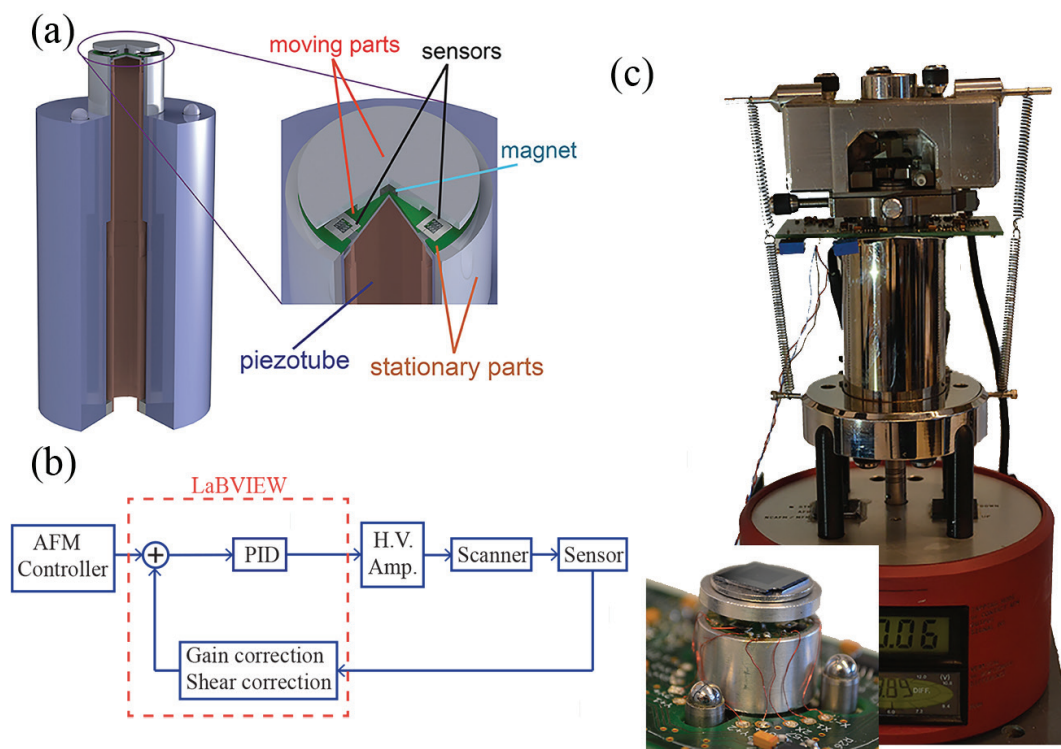


Figure 7-2 (a) Schematic of the piezotube scanner and two position sensors. (b) Schematic of the closed-loop system. (c) Multi Mode AFM scanner retrofitted with position sensors and readout electronics.

In comparison with capacitive sensors, there is no inherent nonlinearity in the presented sensor [78]. Another problem with open-loop piezo actuation is creeping, in which the piezo responds to a rapid positioning step by moving only a certain percentage quickly and then approaches slowly the rest of the way to the desired position.

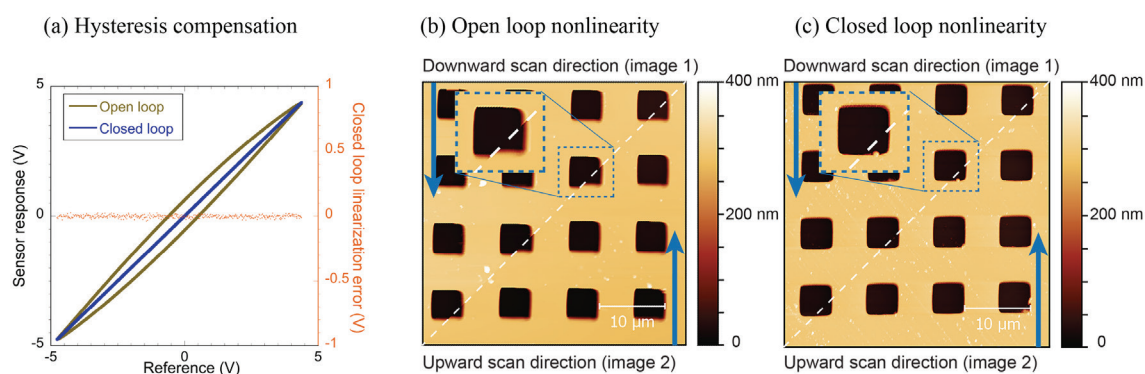


Figure 7-3 Nonlinearity in open loop compared with closed-loop scanning. (a) Open-loop hysteresis and closed-loop linear displacement of the piezotube scanner measured with the position sensor. (b) Two diagonally-stitched AFM images of a silicon calibration grating in open-loop scanning where the mismatch between two images is observed. (c) Two diagonally stitched calibration-grating images in closed-loop scanning where the mismatch between two images is removed.

Creep in nanopositioners prevents accurate positioning when a sharp displacement is required, such as a scan offset. Figure 7-4(a) shows the creep in open-loop operation for a step

offset. We imaged a $10\mu\text{m}$ pitch square silicon grating while the slow scanning axis was disabled (resulting in a repeated scanning of the same line, visible in the image as vertical stripes). We then added a $56\mu\text{m}$ offset to the fast scan axis. The open-loop scanner only performs part of the desired offset directly and then approaches the full offset very slowly, resulting in the bent stripes in the image Figure 7-4(a). Closed-loop operation eliminates such image distortion arising from creep, but only as far as the sensor does not exhibit any creep by itself. Strain-gauge-based nanopositioning sensors are known in particular to suffer from creep due to the required adhesion layer between the strain gauge and its substrate. While our position sensor also operates on a strain gauge, the sensing element and the flexure substrate are one monolithic silicon MEMS device, and therefore only the flexure substrate is glued onto the moving/stationary parts (and not the sensing element). The stiffness of the flexure is also very low (3N/m), thereby adding no appreciable load to the piezo or its glue joints. Our closed-loop implementation therefore performs the $56\mu\text{m}$ -offset step without exhibiting any detectable creep (see Figure 7-4(b)).

The lack of creep and the improved linearity of the closed-loop scanner allows for accurate zooming during AFM operation. Figure 7-4(c) demonstrates a $50\mu\text{m}$ scan size overview image with a dotted square depicting the chosen zoom area. The inset shows the zoomed in image showing exactly the chosen zoom area.

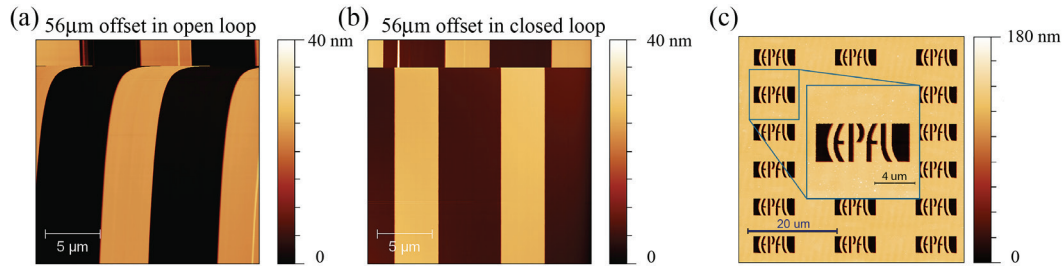


Figure 7-4 Creep removal using a closed-loop system. (a) Nonlinear displacement of the piezoactuator according to $56\mu\text{m}$ applied offset in open loop due to creep. (b) Linear displacement of the piezoactuator according to $56\mu\text{m}$ applied offset in closed loop. (c) Creep compensation permits accurate zooming in AFM imaging.

The achievable resolution of the positioning feedback system is influenced by the total noise of the position sensor over a given bandwidth [212]. The closed-loop resolution determines the distance between two distinguishable adjacent points and is defined in terms of the standard deviation of the positioning noise [213]. Nevertheless, there is a tradeoff between the positioning range, bandwidth and resolution of the position sensor [196]. To compare the lateral resolution in open- and closed-loop systems, we performed noise measurements in amplitude modulation AFM on a scanner equipped with the $100\mu\text{m}$ -travel-range MEMS sensor.

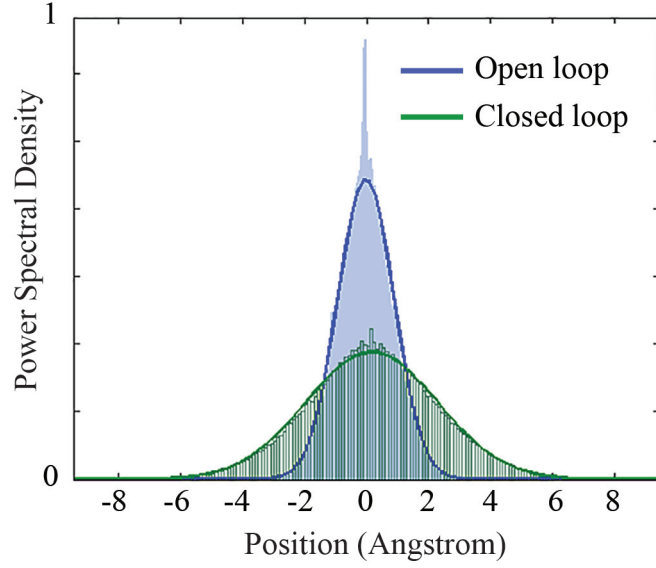


Figure 7-5 Normal distribution of the lateral noise in open- and closed-loop systems. The 1σ resolutions are 0.9\AA and 2.1\AA in open and closed loop respectively.

We used a sample of tilted mica, with the projected lateral noise calculated from the vertical amplitude signal in tapping mode (see Methods, section 2). The RMS values of the lateral noise in open loop and closed loop are 0.9\AA and 2.1\AA respectively. Figure 7-5 illustrates the normal distribution of the lateral noise in open and closed-loop systems. The measurement used a 1 kHz bandwidth of the closed-loop system.

7.3.4 Implementation in a custom high-speed AFM

Much progress has been made in the area of high-speed AFM in recent years, with improvements for example in cantilevers [214]–[216], detection systems [61], controllers and scanner designs [77], [217]. Obtaining high scanner resonance frequencies often requires very small and compact scanner designs. Operating such high-speed scanners in closed-loop faces two additional challenges over conventional scanners: 1) a high sensor bandwidth with low noise density is necessary to maintain high-resolution closed-loop imaging over a larger frequency spectrum. 2) The size and mass of the sensor should not significantly increase the overall scanned mass, in order to not reduce the resonance frequency of the whole system [218].

We upgraded our homebuilt piezo-stack high-speed scanner [216] with two $100\mu\text{m}$ -range position sensors to measure the lateral displacement (see Figure 7-6(a)). The scanner is operated using a high-speed AFM controller (Anfatec AFT-MMC50, Germany) with a high-speed piezo amplifier (Techproject, Austria). We used the same FPGA as for the tube scanner implementation for closed-loop feedback. Figure 7-6(b) displays the X-axis frequency response of our home-built high-speed scanner measured with the MEMS sensor. The lateral

resonance frequency of the scanner is 11.5 kHz, which is sufficiently high to image at several hundred lines/second. In order to minimize residual scanner vibrations at the turn around, a butterworth lowpass filter with a cut off frequency of 10 kHz was implemented on the controller.

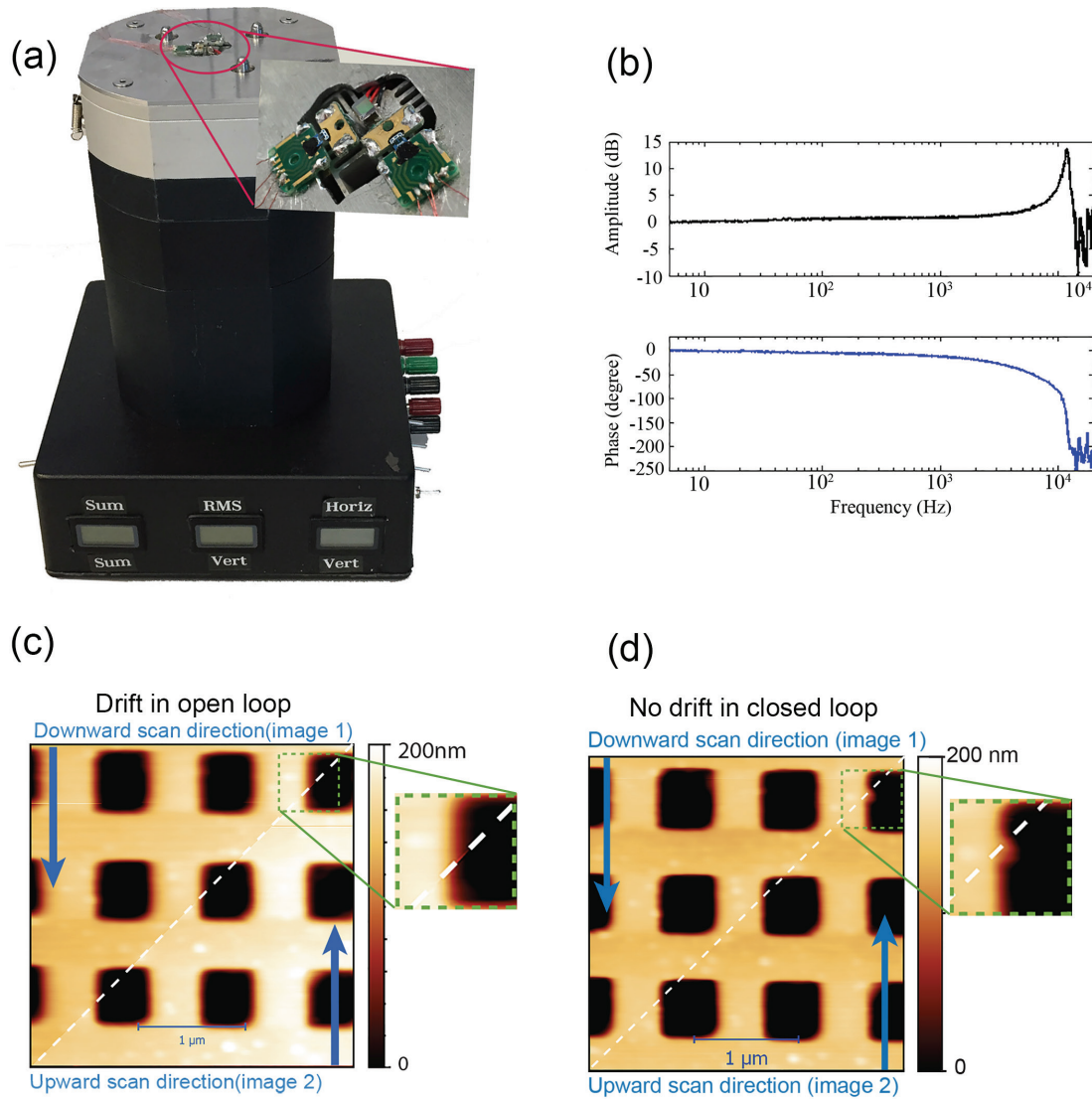


Figure 7-6 High-speed closed-loop system. (a) Custom designed high-speed scanner and position sensors. (b) Frequency response of the high-speed scanner. (c) Drift in open loop (d) No nonlinearity at 300 Hz scan rate in closed-loop operation.

In order to measure the performance of the closed-loop high-speed system, we used the same down-up measurement as discussed earlier. To compare the implementation, images in open loop and closed loop are taken. Figure 7-6(c) displays two images taken in open loop where drift is visible between two images. Figure 7-6(d) includes two images in closed loop captured at 300 Hz scan rate and cut diagonally. The square pits have the correct regular spacing and the downward scanned image is well matched with the upward scanned image. At present, the sensors on our high-speed, closed-loop system are not fluid sealed, which

limits the imaging-in-fluid capabilities of this instrument for imaging biological samples. In order to provide a high-speed, closed loop scanner for biological samples, these sensors would need to be sealed or protected from potential fluid leaks.

7.4 Discussion

The performance of the sidewall piezoresistive position sensor shows great promise for lateral closed-loop AFM applications. The inherent linearity of the sensor simplifies implementation for electronics and signal processing. The position sensor's size and ease of use make it possible to install it in close proximity to the sample without impeding the scanner motion. The AFM images demonstrate adequate hysteresis, creep and drift removal in the implemented closed-loop system.

A drawback of our implementation is the need for crosstalk compensation between the X, Y, and to some extent Z-axis. Both the tube and flexure-based scanner implementations are parallel kinematic designs in the XY plane [219]. Therefore any motion in X will also lead to a motion in the Y-axis, and vice versa. Additional cross coupling will occur in the sensors (coupling strength ca. 1:20 for X-Y and 1:100 for Z-X or Y) in addition to inherent cross coupling of the scanners. This cross coupling depends on the exact design of the differential spring for the mechanical deamplification. We minimize this effect by aligning the sensor measurement axis very well with the scanner motion axis. Nevertheless, the crosstalk correction as well as the sensitivity correction can be easily implemented using standard shear transformations. For the tube scanner implementation, we implemented a cross-coupling correction for the Z-X and Z-Y signals using the low voltage actuation signal, which reduced any cross coupling below the measurement limit.

The presented sensor obtains its high sensitivity and linearity from the fact that it is a monolithic structure fabricated from single crystal silicon. However, this architecture, combined with the low spring constant of the MEMS flexures, also makes the sensor fragile. Therefore, great care must be taken not to break the lightweight, small and fragile sensor during mounting. In operation, we have not observed any fatigue failure or nonlinearity at the ends of the dynamic range. The sensor behaves linearly until it passes its allowed dynamic range, after which failure occurs in the form of brittle fracture in the silicon flexure. While we have not observed any failure of the sensors during months of operation, the sensors can become damaged when stretched beyond their dynamic range, for example when the closed-loop controller becomes unstable and the scanner is excited at resonance.

The high bandwidth, small size, and low mass of the MEMS sensor make it well suited for high-speed AFM. The capacitive sensors often used in high-resolution closed-loop piezo

stages are problematic for high-speed AFM applications, since they are comparatively large to the size of high-speed scanners and generally do not operate beyond a few kHz. Optical methods such as interferometry can easily operate at high frequencies and implementations are available in small form factors, but their high price limits their practical use. The advantage of the presented feedback system is the stability and high bandwidth due to small mass of the position sensors (combined with the scalability of batch fabrication). This performance enabled high-speed closed-loop imaging of our scanner with 300 Hz without instability in the system. Larger scan rates could be achieved by model-based filtering of the mechanical resonances of the home-built HS-scanner. We predict that further improvement of the readout electronics and direct implementation of the feedback in the AFM controller will reduce the closed-loop imaging noise to levels equal to the open-loop imaging noise.

7.5 Conclusion

In this work, we have presented a lateral feedback implementation using monolithic, sidewall-embedded, MEMS-based nanopositioning sensors for both conventional piezo tube scanners as well as high-speed, flexure-based piezo scanners. Experimental results show distortion free, repeatable imaging with accurate zoom and offset operation. The small size, low noise and high bandwidth of the sensor combined with the simplicity of the readout electronics makes such a MEMS based closed-loop system ideally suited for integration into piezo-tube scanners as well as compact, high-speed, flexure-based AFM scanners.

7.6 Methods

7.6.1 Closed loop implementation

Shear and gain corrections are required before feeding the sensor's signal to PI controller. The gain correction is performed by comparing the sensor's signal with the low voltage drive signal from the AFM controller, and amplifying the sensor signal to have the same amplitude as the low voltage drive signal. The linearity of the sensor guarantees that once the gain is set there is no need to change it again. The gain correction is implemented by using high throughput multipliers in LABVIEW FPGA.

The shear correction is implemented as follows:

$$X_{\text{Sensor}} = X_{\text{Sensor, Shear}} - (\alpha \times Y_{\text{Sensor, Shear}})$$

$$Y_{\text{Sensor}} = Y_{\text{Sensor, Shear}} - (\beta \times X_{\text{Sensor, Shear}})$$

Where $X_{\text{Sensor, Shear}}$ and $Y_{\text{Sensor, Shear}}$ are the sensor signals before shear correction, X_{Sensor} and Y_{Sensor} are sensor signals after shear correction. α and β are the shear correction factors, which

are defined to get orthogonal sensor's signals. The shear correction is performed by using high throughput multiplier and subtraction modulus in LABVIEW FPGA.

Afterwards the sensor signal is compared with the low voltage drive signal from the AFM controller. The PID module is chosen from "PID and fuzzy logic toolkit" in LABVIEW FPGA.

The PID gains are adjustable on the front panel of the LABVIEW code. The output of the PID is amplified with home built high voltage piezo amplifiers and then applied to the scanner.

7.6.2 Lateral noise measurement

The additional lateral noise in the closed-loop AFM image originates from the readout electronics, FPGA setup, the position sensor itself, as well as the existing position noise of the open-loop system. To characterize the total lateral noise in closed-loop imaging we recorded the amplitude variation on a tilted mica sample with a slope of 30° in amplitude modulation mode, with a scan size of 0nm while holding the position constant and using very low Z-feedback gains (just sufficient not to drift off the surface). The total noise consists of the vertical noise in Z and the lateral noise for each X and Y directions scaled by the 30° angle. The lateral noise has been projected given the fact that the sample was tilted and has been compared for both open and closed-loop systems.

7.6.3 Conventional AFM imaging

We used a Bruker multimode in contact mode with retrofitted J scanner (digital instruments, Santa Barbara, USA). The low-voltage signals for X and Y scanning were outputs from the controller and reshaped through our closed-loop system. The compensated low voltage signals were then input to the controller.

7.6.4 High-speed AFM imaging

For high-speed AFM imaging we used an Anfatec controller (Anfatec AFT-MMC50, Germany) in high-speed contact mode. Our home built small lever head [27] was placed on our custom designed high-speed scanner using a Bruker FastScan-C cantilever. Having the position sensors on the scanner, we implemented the closed-loop system on a LabVIEW FPGA as discussed in the main text.

7.7 Acknowledgment

The authors would like to thank Maja Dukic Pjanic and Pat McPhail from Bruker Nano Surfaces for helpful discussions, as well as the Atelier de l'institut de production et robotique at EPFL for fabrication of research equipment. This work has been funded by the European

Union's Seventh Framework Programme FP7/2007-2011 under grant agreement 286146 and the European Union's Seventh Framework Programme FP7/2007-2013/ERC grant agreement 307338, Eurostars E!8213 – Triple-S, and the Swiss National Science Foundation through grants 205321 134786 and 205320 152675.

This is the end of the article.

7.8 Toward further extension of the closed-loop scanner

Due to lightweight and a small package of the employed displacement sensors, we aimed to place them inside the piezotube scanner (Model J, Bruker Nano Surfaces), so the sensors are protected from the environment and mechanical disturbances. Besides, the displacement sensors are then in direct contact with the piezotube so they can read the real trajectory even with higher accuracy. In order to locate the sensors safely inside, we modified our piezotube scanner to be able to glue the stationary side of the sensor onto the scanner guard and the moving part of the sensor onto the piezotube.

First, we cut the top part of the X, Y piezotube in a crown shape, and then we made a metallic fixture which can be placed among the piezotube crown and hold the sensors. This fixture also allows for sensor orthogonality correction. We managed to fit the first amplification stage next to the sensors, inside the piezotube. This readout PCB has a dual channel instrumentation amplifier (AD8222, Analog Devices, MA, USA) for both sensors. Figure 7-7(a) shows the cross-sectional view and the top view of the modified piezotube scanner with the sensors, the fixture and the electronics. Figure 7-7(b) displays the closed loop scanner with the displacement sensors inside at different stages of the implementation.

The wires containing signals from/to the instrumentation amplifier were then connected to an external electronic box for further amplification and offset adjustment. The LABVIEW FPGA code, including the PI controller and the shear/gain corrections, was similar to the one discussed in section 7.6.1. As a proof of concept, we imaged a reference-grating sample, shown in Figure 7-8, where the nonlinearity of the piezotube scanner was successfully removed thanks to the displacement sensors and the PI controller.

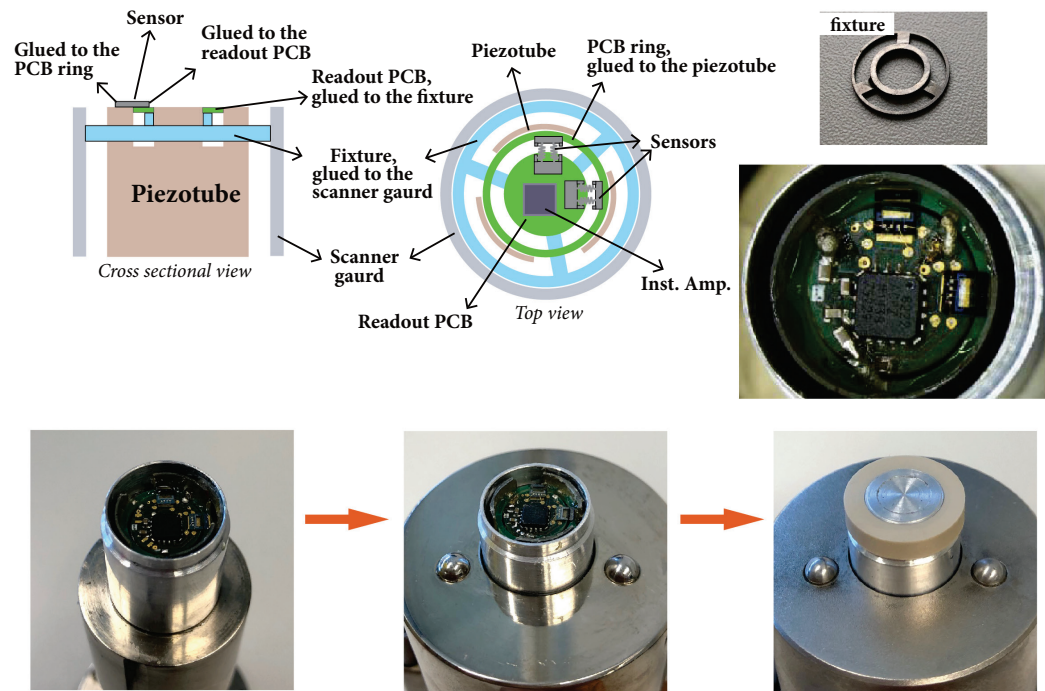


Figure 7-7 Implementation of the closed loop scanner with the displacement sensors inside the scanner. (a) The top part of the piezotube is cut into a crown shape so the fixture can be fitted. The sensors are glued onto the readout PCB and the PCB ring. The readout PCB is glued onto the fixture (stationary part) and the PCB ring is glued to the piezotube (moving part). The fixture is glued to the scanner guard so the scanner guard via the fixture supports the readout PCB. The instrumentation amplifier is placed next to the sensors. (b) The implementation steps toward a functional closed loop scanner where the displacement sensors are protected safely inside.

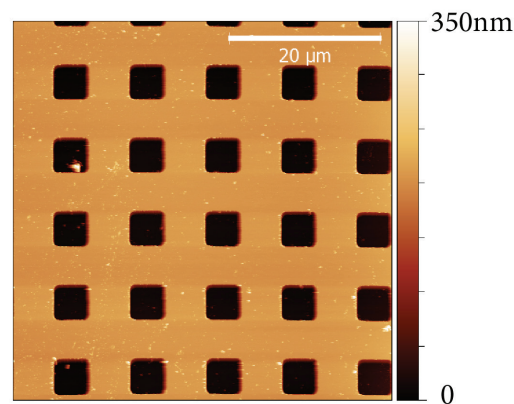


Figure 7-8 An AFM image of a reference-grating sample, imaged by employing the developed closed-loop scanner where the displacement sensors were embedded safely inside the scanner.

8. Conclusion and outlook

8.1 Tip-integrated SU8 cantilevers

8.1.1 Achieved results

One of the primary research goals in AFM manufacturing is developing cantilevers with sharp and long-lasting tips. It becomes particularly important for high-speed polymer cantilevers since the tips made of polymers are subject to high wear-rates. These high wear-rates prevent the polymer cantilevers from being exploited for high-speed AFM applications.

In this thesis, the integration of sharp silicon nitride tips into SU8 cantilevers was presented. The critical aspects of the process were mechanical anchoring of moulded silicon nitride tips and two-step cantilever release. By imaging a polycrystalline titanium roughness sample, the tip sharpness was measured at $9\text{nm} \pm 2\text{nm}$ for 20 individual cantilevers, and no visible wear was observed after more than 16mm of tip travel. The introduced tip-integrated SU8 cantilevers preserve their high tracking bandwidth. The 3dB drop of the surface tracking in tapping mode has been measured, and it confirmed more than 50 times faster response for the tip-integrated SU8 cantilevers compared to a silicon cantilever with the same resonance frequency.

8.1.2 Outlook

Tip integrated SU8 cantilevers are yet far from a product for every-day use. We showed a batch fabrication recipe to integrate durable tips with descent tip sharpness, but still AFM users would find it challenging to deal with the parasitic peaks during the cantilever tuning. We attributed this issue mainly to the low Q-factor of polymer cantilever itself, but we still need to investigate other sources and try to fix them. For instance, we need to consider if the commercial cantilever holders designed for silicon and silicon nitride cantilevers, are a proper choice for polymer cantilevers or not.

In terms of the microfabrication, we observed some diffusion patterns from the first SU8 chip body to the silicon substrate and the SU8 beam. This diffusion is a known problem in SU8 microfabrication processes and happens due to the diffusion of photo-acids into a non-exposed area of SU8 when it goes to several thermal cycles after the UV exposure. In the past, we used to develop all three SU8 chip body layers once, so the first SU8 chip body layer had to

go through several baking steps. We can solve this problem by separating the first SU8 chip body patterning from the next SU8 layers.

8.2 Tip-integrated, hybrid multilayer cantilevers

8.2.1 Achieved results

Pure polymer cantilevers suffer from low excitation efficiency when they are actuated with the dither piezo. To promote excitation efficiency, a multilayer design was presented. The process was based on sandwiching the polymer core with two hard thin films (with high in-plane stiffness). The multilayer devices were realized through covering two silicon wafers with a thin layer of silicon nitride, then bonding them together using Benzocyclobutene (BCB) as both a glue for wafer bonding and a structural layer for the cantilever core. This microfabrication recipe enabled fabricating hybrid multilayer (silicon nitride-BCB-silicon nitride) cantilevers with silicon chip bodies, and oxide sharpened silicon nitride tips. It was shown that the mechanical tuning of a multilayer cantilever (Q -factor=58) was significantly improved compared to a SU8 cantilever (Q -factor=21). The 3dB decrease in tracking amplitude demonstrated more than 30 times faster response for the multilayer cantilevers compared to its traditional silicon counterpart. It was also shown that the silicon nitride tip showed minimal tip wear, even after 11h of imaging and 170mm of tip travel distance.

8.2.2 Outlook

The microfabrication process of the hybrid multilayer cantilevers includes an adhesive wafer-bonding step, which potentially let us further explore new fabrication recipes to make even better tips. For instance making a sharp corner-tip, which protrudes out from the very end of the cantilever helps to have a more accessible approach to the sample surface. Such a corner-tip can be designed by combining anisotropic dry and isotropic wet etching procedures, similar to Nanosensors AdvancedTEC and Nanoworld Arrow commercial cantilevers.

8.3 Self-sensing, hybrid multilayer cantilevers

8.3.1 Achieved results

The design and the adaptable microfabrication recipe of the introduced multilayer cantilevers make an ideal platform to integrate strain sensors and fabricate self-sensing hybrid multilayer cantilevers. In this thesis, it was shown that the piezoresistive strain sensors could be formed on the silicon nitride thin film before the wafer bonding, and were safely embedded afterwards. By incorporating a polymer (BCB) as the structural cantilever material we

fabricated thick, but soft cantilevers. It means that one can make cantilevers with high deflection sensitivity and low spring constant, and consequently high force sensitivity. The high force sensitivity is a significant advance for dynamic AFM applications, where the suitability of the self-sensing method over OBD has been primarily limited by inferior force resolution of the self-sensing cantilevers. It was shown that a multilayer self-sensing cantilever has 6 times lower force noise compared to a silicon cantilever with similar dimensions and sensing elements. We measured an achievable 0.4 Angstrom RMS noise with the self-sensing multilayer cantilevers (spring constant=57N/m) in AC mode in air and imaged HOPG, efficiently resolving the single atomic steps. The exciting aspect of the self-sensing hybrid multilayer cantilevers is that the high deflection/force sensitivity is achieved while the cantilever characteristics (resonance frequency, spring constant and planar dimension) remain within the practical limits for both static and dynamic measurements.

It has been demonstrated that the polymer-core multilayer cantilevers are capable of tracking topography changes faster than cantilevers made of traditional MEMS materials. In this scope, it was shown that the quality factor of the multilayer cantilevers in a vacuum was 4 times lower than that of comparable silicon cantilevers, which manifested in 400% faster imaging speeds. The ommatidium lens surface of a wasp eye was scanned in a vacuum with a self-sensing multilayer cantilever and a silicon cantilever. It was shown that while the silicon cantilever tracks the sample poorly at 160 μ m/s tip velocity, the self-sensing multilayer cantilever detects the sample topography significantly better thanks to its high tracking bandwidth.

The hermetically sealed self-sensing multilayer cantilevers have been employed in multiple AFM techniques. For instance, the topography change of polished nickel surface was observed in dark, corrosive, ferric chloride liquid where the cantilever showed no sign of degradation even after 5 hours of continuous imaging. It has been verified that the self-sensing multilayer cantilevers can be supplemented with additional coatings. In this regard, the surface potential measurements of a PS-LDPE polymer blend were presented, for which the cantilever bottom side was sputter-coated with a 100nm gold layer. Besides, we coated a self-sensing multilayer cantilever with 70nm evaporated Ni₈₁Fe₁₉ and performed correlated SEM-AFM-MFM imaging on Ni₈₁Fe₁₉ Penrose P2 tiling in a vacuum where the phase contrasts at the vertices in MFM measurements were clearly observed.

8.3.2 Outlook

The idea of having hermetically sealed piezoresistive multilayer MEMS devices is not limited merely to AFM cantilevers. For example, we have designed and fabricated piezoresistive multilayer membranes to be employed as a surface stress sensor in liquids.

While we were able to release the self-sensing multilayer membranes successfully, such devices need further design optimization to reach practical sensitivities. We can also consider patterning the polymer core to realize encapsulated microfluidics devices. By integrating the sensing elements and the electrodes inside the channel, one can measure the resistance of fluids or even apply an electric field inside the channel, along with self-sensing mass (frequency shift) measurements.

We have demonstrated how the hybrid multilayer structure improves the force sensitivity; nevertheless, we were not satisfied with the low GF of doped polysilicon (20-25 in our case). In an effort to increase the deflection sensitivity, we modified our fabrication process to integrate doped silicon (which has higher GF) through using an SOI wafer and performing some critical steps. However, the process was pricy, and the silicon piezoresistors were not encapsulated between the LSNT film and the polymer core as discussed in the method section 4.6.1.2. .

As an alternative to improve the GF of polysilicon, one approach would be performing laser processing, which can initiate the recrystallization process of polysilicon by removing grain boundaries. This process has been attempted in the past for SOI wafers [220]. The polysilicon recrystallization on LSNT film requires an in-depth study to provide the right profile for laser annealing. In another effort, we have contacted researchers in Australia who have reported polysilicon piezoresistors that are fabricated using Aluminum-induced-crystallization (AIC) of evaporated silicon, with GF as high as 62 [50].

Furthermore, in collaboration with Prof. Alexandra Radovich and Prof. Andras Kis, we are working on the integration of MoS₂ piezoresistors into our multilayer cantilevers. With recent achievements of our collaborators in producing wafer-scale MoS₂, we have targeted to have an acceptable fabrication yield. The MoS₂ based multilayer devices have the inherent advantage that the MoS₂ piezoresistors are fully encapsulated.

8.4 Self-sensing SU8 cantilevers based on MOS₂ piezoresistors

8.4.1 Achieved results

SU8 cantilevers have shown promising aspects due to the ease of fabrication and high detection speed. In the scope of my research, it was revealed that highly flexible, high gauge factor MoS₂ piezoresistors could be incorporated into the SU8 cantilevers. The microfabrication was based on the mechanical transfer of monolayer CVD-grown MoS₂ to the first SU8 layer, followed by patterning MoS₂ piezoresistors and metal traces. The rest of the process was mainly similar to the microfabrication of pure SU8 cantilevers except that the chip release was based on etching a Cr-Au-Cr sacrificial layer rather than silicon KOH

etching. The cantilever tuning was attempted electrically and optically where the self-sensing measurements showed very good agreement with the optical results.

8.4.2 Outlook

So far, we have proven that MoS₂-SU8 cantilever fabrication is feasible and follows the design rule by successfully fabricating the device and measuring the resonance frequency with piezoresistive readout. However, up to this moment, further characterization and application of the cantilevers are hindered because of the low yield of successful devices. With the recent progress on wafer-scale growth of MoS₂, we can fabricate MoS₂ based SU8 cantilever with an improved fabrication yield.

8.5 SU8, a simple and stable doping and encapsulation approach for MoS₂ devices

8.5.1 Achieved results

It was noticed that SU8 could play three roles in cantilever fabrication. It can act as a structural device layer, as an encapsulation layer and finally as an n-type doping source for CVD grown monolayer MoS₂ devices. Evaluating the Raman spectroscopy and the transfer characteristic of SU8-coated MoS₂ based FETs confirmed a large increase in on-current and a negative shift of the threshold voltage, which was the result of n-type doping. The mechanical flexibility of SU8, combined with its good air and water stability, made it possible to realize flexible MoS₂ FETs with SU8 encapsulation on 10 μ m polyimide. Such a device showed only minor changes after going through 100 cycles of bending, which marks SU8 as a practical strategy to encapsulate and dope MoS₂ based flexible devices.

8.5.2 Outlook

We have proven that SU8 is a promising doping and encapsulation strategy for MoS₂ based devices. However, we cannot explain yet what the physical/chemical explanation of this effect is. In a back-engineering approach, we tried to rule out multiple factors. For example, we coated the MoS₂ devices with SU8 without photo-acid generator (PAG) and realized that the doping effect was still preserved. We also covered the MoS₂ devices only with Gamma-Butyrolactone (GBL), SU8 solvent, and saw no sign of doping. We believe that understanding the physics behind this phenomenon needs a higher level of knowledge in chemistry and then the results can be possibly further applied to other 2D materials.

8.6 Nonlinearity compensation of the AFM piezo scanners using a monolithic MEMS position sensor in a closed loop scheme

8.6.1 Achieved results

A monolithic, sidewall-embedded piezoresistive displacement sensor has been employed in a closed loop design to compensate the nonlinearities of the AFM piezotube scanner, such as hysteresis, creep and drift. The closed loop controller was developed and implemented on an FPGA using the PID and fuzzy logic toolkit of LABVIEW. It was shown that by measuring the real trajectory of the scanner (through the displacement sensors) and then reshaping the drive signal of the piezotube scanner (through the PI controller), one could counterbalance the associated nonlinearities of the piezotube scanner with precise zoom and offset control in AFM imaging. The lateral RMS noise of the piezotube scanner was measured at 2.1 Angstrom in the closed loop design. Also, we combined the introduced closed loop design with our home-built high-speed scanner. Subsequently, we were able to image a reference-grating sample at 300Hz scan rate with the closed loop scheme.

8.6.2 Outlook

The fundamental problem associated with using closed loop control in piezotube scanners is the need for a displacement sensor. Every piezoresistive displacement sensor has its inherent noise, which will affect the nanopositioning resolution. Combining an iterative learning control with our introduced piezoresistive displacement sensor can significantly improve the nano-manipulation resolution.

8.7 Overall outlook

Using AFM for nanocharacterization is making the transition from laboratories to research centers and production environments. Although, the user interaction needed for acquiring trustworthy results requires a specially trained operator and thus limits the automat-ability of AFM. Self-sensing cantilevers have improved the ease of use of AFM, but they lack a universal platform to be employed with commercial AFM setups. For example, each research group, who has developed self-sensing cantilevers, has a customized cantilever holder, read-out electronics and interfaces. It restricts the use of newly developed self-sensing cantilevers to internal users to a large extent. Along with producing high-performance self-sensing cantilevers, developing a comprehensive platform for self-sensing cantilevers can genuinely expand their use in AFM field.

9. Bibliography

- [1] G. Binnig and H. Rohrer, "Scanning tunneling microscopy," *Surf. Sci.*, vol. 126, no. 1–3, pp. 236–244, Mar. 1983.
- [2] G. Binnig, C. F. Quate, and C. Gerber, "Atomic Force Microscope," *Phys. Rev. Lett.*, vol. 56, no. 9, pp. 930–933, Mar. 1986.
- [3] Y. Martin, C. C. Williams, and H. K. Wickramasinghe, "Atomic force microscope-force mapping and profiling on a sub 100-Å scale," *J. Appl. Phys.*, vol. 61, p. 4723, 1987.
- [4] E. Meyer, "Atomic force microscopy," *Prog. Surf. Sci.*, vol. 41, pp. 3–49, 1992.
- [5] T. R. Albrecht, S. Akamine, T. E. Carver, and C. F. Quate, "Microfabrication of cantilever styli for the atomic force microscope," *J. Vac. Sci. Technol. A Vacuum, Surfaces, Film.*, vol. 8, no. 4, pp. 3386–3396, Jul. 1990.
- [6] R. A. Buser, J. Brugger, and N. F. de Rooij, "Micromachined silicon cantilevers and tips for bidirectional force microscopy," *Ultramicroscopy*, vol. 42–44, pp. 1476–1480, Jul. 1992.
- [7] T. S. Ravi, R. B. Marcus, and D. Liu, "Oxidation sharpening of silicon tips," *J. Vac. Sci. Technol. B Microelectron. Nanom. Struct.*, vol. 9, no. 6, p. 2733, Nov. 1991.
- [8] P. Walke, Y. Fujita, W. Peeters, S. Toyouchi, W. Frederickx, S. De Feyter, and H. Uji-i, "Silver nanowires for highly reproducible cantilever based AFM-TERS microscopy: towards a universal TERS probe," *Nanoscale*, vol. 10, no. 16, pp. 7556–7565, Apr. 2018.
- [9] X. Ma, Y. Zhu, S. Kim, Q. Liu, P. Byrley, Y. Wei, J. Zhang, K. Jiang, S. Fan, R. Yan, and M. Liu, "Sharp-Tip Silver Nanowires Mounted on Cantilevers for High-Aspect- Ratio High-Resolution Imaging," *Nano Lett.*, vol. 16, no. 11, pp. 6896–6902, 2016.
- [10] M. Behzadizad, M. Nami, A. K. Rishinaramagalam, D. F. Feezell, and T. Busani, "GaN nanowire tips for nanoscale atomic force microscopy," *Nanotechnology*, vol. 28, no. 20, p. 20LT01, 2017.
- [11] J. H. Hafner, C. L. Cheung, and C. M. Lieber, "Growth of nanotubes for probe microscopy tips," *Nature*, vol. 398, no. 6730, pp. 761–762, Apr. 1999.
- [12] A. Zakhurdaeva, P.-I. Dietrich, H. Hölscher, C. Koos, J. Korvink, and S. Sharma, "Custom-Designed Glassy Carbon Tips for Atomic Force Microscopy," *Micromachines*, vol. 8, no. 9, p. 285, Sep. 2017.
- [13] S. Zheng, C. Zhu, R. K. Dey, and B. Cui, "Batch fabrication of AFM probes with direct positioning capability," *J. Vac. Sci. Technol. B, Nanotechnol. Microelectron. Mater. Process. Meas. Phenom.*, vol. 35, no. 6, p. 06GC02, Nov. 2017.
- [14] O. A. Ageev, A. S. Kolomyitsev, A. V. Bykov, V. A. Smirnov, and I. N. Kots, "Fabrication of advanced probes for atomic force microscopy using focused ion beam," *Microelectron. Reliab.*, vol. 55, no. 9–10, pp. 2131–2134, Aug. 2015.
- [15] H. Ximen and P. E. Russell, "Microfabrication of AFM tips using focused ion and electron beam techniques," *Ultramicroscopy*, vol. 42, pp. 1526–1532, 1992.
- [16] K. Miyazawa, H. Izumi, T. Watanabe-Nakayama, H. Asakawa, and T. Fukuma, "Fabrication of electron beam deposited tip for atomic-scale atomic force microscopy in liquid," *Nanotechnology*, vol. 26, no. 10, p. 105707, Mar. 2015.
- [17] M. Huth, F. Porriati, C. Schwalb, M. Winhold, R. Sachser, M. Dukic, J. Adams, and G. Fantner, "Focused electron beam induced deposition: A perspective.,", *Beilstein J. Nanotechnol.*, vol. 3, pp. 597–619, 2012.
- [18] A. Temiryazev, S. I. Bozhko, A. E. Robinson, and M. Temiryazeva, "Fabrication of sharp atomic force microscope probes using in-situ local electric field induced deposition under ambient conditions," *Rev. Sci. Instrum.*, vol. 87, no. 11, p. 113703, 2016.
- [19] A. B. H. Tay and J. T. L. Thong, "Fabrication of super-sharp nanowire atomic force microscope probes using a field emission induced growth technique," *Rev. Sci. Instrum.*, vol. 75, no. 10, pp. 3248–3255, 2004.
- [20] G. Meyer and N. M. Amer, "Novel optical approach to atomic force microscopy," *Appl. Phys.*

- Lett*, vol. 53, p. 1045, 1988.
- [21] D. Rugar, H. J. Mamin, and P. Guethner, "Improved fiber-optic interferometer for atomic force microscopy," *Appl. Phys. Lett*, vol. 55, p. 2588, 1989.
 - [22] J. Brugger, R. A. Buser, and N. F. de Rooij, "Micromachined atomic force microprobe with integrated capacitive read-out," *J. Micromechanics Microengineering*, vol. 2, no. 3, pp. 218–220, Sep. 1992.
 - [23] N. Blanc, J. Brugger, N. F. de Rooij, and U. Dürig, "Scanning force microscopy in the dynamic mode using microfabricated capacitive sensors," *J. Vac. Sci. Technol. B Microelectron. Nanom. Struct.*, vol. 14, no. 2, p. 901, Mar. 1996.
 - [24] E. Forsen, G. Abadal, S. Ghatnekar-Nilsson, J. Teva, J. Verd, R. Sandberg, W. Svendsen, F. Perez-Murano, J. Esteve, E. Figueras, F. Campabadal, L. Montelius, N. Barniol, and A. Boisen, "Ultrasensitive mass sensor fully integrated with complementary metal-oxide-semiconductor circuitry," *Appl. Phys. Lett.*, vol. 87, no. 4, p. 43507, Jul. 2005.
 - [25] S.-J. Kim, T. Ono, and M. Esashi, "Capacitive resonant mass sensor with frequency demodulation detection based on resonant circuit," *Appl. Phys. Lett.*, vol. 88, no. 5, p. 53116, Jan. 2006.
 - [26] J. Verd, A. Uranga, G. Abadal, J. Teva, F. Torres, F. Pérez-Murano, J. Fraxedas, J. Esteve, and N. Barniol, "Monolithic mass sensor fabricated using a conventional technology with attogram resolution in air conditions," *Appl. Phys. Lett.*, vol. 91, no. 1, p. 13501, Jul. 2007.
 - [27] G. E. Fantner, W. Schumann, R. J. Barbero, A. Deutschinger, V. Todorov, D. S. Gray, A. M. Belcher, I. W. Rangelow, and K. Youcef-Toumi, "Use of self-actuating and self-sensing cantilevers for imaging biological samples in fluid," *Nanotechnology*, vol. 20, no. 43, p. 434003, Oct. 2009.
 - [28] J. Chu, T. Itoh, C. Lee, T. Suga, and K. Watanabe, "Frequency modulation detection high vacuum scanning force microscope with a self-oscillating piezoelectric cantilever," *J. Vac. Sci. Technol. B Microelectron. Nanom. Struct.*, vol. 15, no. 5, p. 1647, Sep. 1997.
 - [29] S. Puri, T. Aegerter-Wilmsen, A. Jazwińska, and C. M. Aegerter, "In vivo quantification of mechanical properties of caudal fins in adult zebrafish.," *J. Exp. Biol.*, vol. 221, no. Pt 4, p. jeb171777, Feb. 2018.
 - [30] J. D. Adams, G. Parrott, C. Bauer, T. Sant, L. Manning, M. Jones, B. Rogers, D. Mccorkle, and T. L. Ferrell, "Nanowatt chemical vapor detection with a self-sensing, piezoelectric microcantilever array," *Cit. Appl. Phys. Lett*, vol. 83, p. 3428, 2003.
 - [31] M. Tortonese, R. C. Barrett, and C. F. Quate, "Atomic resolution with an atomic force microscope using piezoresistive detection," *Appl. Phys. Lett.*, vol. 62, no. 8, pp. 834–836, Feb. 1993.
 - [32] R. Linnemann, T. Gotszalk, L. Hadjiiski, and I. W. Rangelow, "Characterization of a cantilever with an integrated deflection sensor," *Thin Solid Films*, vol. 264, no. 2, pp. 159–164, Aug. 1995.
 - [33] R. Jumpertz, A. v. d. Hart, O. Ohlsson, F. Saurenbach, and J. Schelten, "Piezoresistive sensors on AFM cantilevers with atomic resolution," *Microelectron. Eng.*, vol. 41–42, pp. 441–444, Mar. 1998.
 - [34] J. Thaysen, A. Boisen, O. Hansen, and S. Bouwstra, "Atomic force microscopy probe with piezoresistive read-out and a highly symmetrical Wheatstone bridge arrangement," *Sensors Actuators A Phys.*, vol. 83, no. 1–3, pp. 47–53, May 2000.
 - [35] X. Yu, J. Thaysen, O. Hansen, and A. Boisen, "Optimization of sensitivity and noise in piezoresistive cantilevers," *J. Appl. Phys.*, vol. 92, no. 10, pp. 6296–6301, 2002.
 - [36] G. Yoshikawa, H.-P. Lang, T. Akiyama, L. Aeschimann, U. Staufer, P. Vettiger, M. Aono, T. Sakurai, and C. Gerber, "Sub-ppm detection of vapors using piezoresistive microcantilever array sensors," *Nanotechnology*, vol. 20, no. 1, p. 15501, Jan. 2009.
 - [37] J. C. Doll and B. L. Pruitt, "High-bandwidth piezoresistive force probes with integrated thermal actuation," *J. Micromechanics Microengineering*, vol. 22, no. 9, p. 95012, Sep. 2012.
 - [38] G. Tosolini, F. Scarponi, S. Cannistraro, and J. Bausells, "Biomolecule recognition using piezoresistive nanomechanical force probes," *Appl. Phys. Lett.*, vol. 102, no. 25, p. 253701, Jun. 2013.
 - [39] J. Bausells, "Microelectronic Engineering Piezoresistive cantilevers for nanomechanical sensing," *Microelectron. Eng.*, vol. 145, pp. 9–20, 2015.
 - [40] T. Itoh and T. Suga, "Development of a force sensor for atomic force microscopy using piezoelectric thin films," *Nanotechnology*, vol. 4, no. 4, pp. 218–224, Oct. 1993.
 - [41] J. H. Lee, K. S. Hwang, J. Park, K. H. Yoon, D. S. Yoon, and T. S. Kim, "Immunoassay of

- prostate-specific antigen (PSA) using resonant frequency shift of piezoelectric nanomechanical microcantilever," *Biosens. Bioelectron.*, vol. 20, no. 10, pp. 2157–2162, Apr. 2005.
- [42] R. B. Karabalin, M. H. Matheny, X. L. Feng, E. Defaÿ, G. Le Rhun, C. Marcoux, S. Hentz, P. Andreucci, and M. L. Roukes, "Piezoelectric nanoelectromechanical resonators based on aluminum nitride thin films," *Appl. Phys. Lett.*, vol. 95, no. 10, p. 103111, Sep. 2009.
 - [43] P. Ivaldi, J. Abergel, M. H. Matheny, L. G. Villanueva, R. B. Karabalin, M. L. Roukes, P. Andreucci, S. Hentz, and E. Defaÿ, "50 nm thick AlN film-based piezoelectric cantilevers for gravimetric detection," *J. Micromechanics Microengineering*, vol. 21, no. 8, p. 85023, Aug. 2011.
 - [44] A. N. Cleland and M. L. Roukes, "Fabrication of high frequency nanometer scale mechanical resonators from bulk Si crystals," *Appl. Phys. Lett.*, vol. 69, no. 18, pp. 2653–2655, Oct. 1996.
 - [45] K. L. Ekinci, X. M. H. Huang, and M. L. Roukes, "Ultrasensitive nanoelectromechanical mass detection," *Appl. Phys. Lett.*, vol. 84, no. 22, pp. 4469–4471, May 2004.
 - [46] M. Li, H. X. Tang, and M. L. Roukes, "Ultra-sensitive NEMS-based cantilevers for sensing, scanned probe and very high-frequency applications," *Nat. Nanotechnol.*, vol. 2, no. 2, pp. 114–120, Feb. 2007.
 - [47] A. Johansson, G. Blagoi, and A. Boisen, "Polymeric cantilever-based biosensors with integrated readout," *Appl. Phys. Lett.*, vol. 89, no. 17, p. 173505, Oct. 2006.
 - [48] J. A. Harley and T. W. Kenny, "1/f noise consideration for the design and process optimization of piezoresistive cantilevers," *J. Microelectromechanical Syst.*, vol. 9, no. 2, pp. 226–235, 2000.
 - [49] J. C. Doll, S. J. Park, and B. L. Pruitt, "Design optimization of piezoresistive cantilevers for force sensing in air and water," *J. Appl. Phys.*, vol. 106, no. 6, pp. 1–12, 2009.
 - [50] I. Chuang, A. Michael, and C. Y. Kwok, "High Gauge Factor Piezoresistors Using Aluminium Induced Crystallisation of Silicon at Low Thermal Budget," *Proceedings*, vol. 1, no. 5, p. 354, 2017.
 - [51] M. Dukic, J. D. Adams, and G. E. Fantner, "Piezoresistive AFM cantilevers surpassing standard optical beam deflection in low noise topography imaging," *Sci. Rep.*, vol. 5, no. 1, p. 16393, Dec. 2015.
 - [52] J. A. Harley and T. W. Kenny, "High-sensitivity piezoresistive cantilevers under 1000 Å thick," *Appl. Phys. Lett.*, vol. 75, no. 289, pp. 289–291, 1999.
 - [53] H.-J. Butt, P. Siedle, K. Seifert, K. Fendler, T. Seeger, E. Bamberg, A. L. Weisenhorn, K. Goldie, and A. Engel, "Scan speed limit in atomic force microscopy," *J. Microsc.*, vol. 169, no. 1, pp. 75–84, Jan. 1993.
 - [54] M. Hilbert, A. Noga, D. Frey, V. Hamel, P. Guichard, S. H. W. Kraatz, M. Pfreundschuh, S. Hosner, I. Flückiger, R. Jaussi, M. M. Wieser, K. M. Thieltges, X. Deupi, D. J. Müller, R. A. Kammerer, P. Gönczy, M. Hirono, and M. O. Steinmetz, "SAS-6 engineering reveals interdependence between cartwheel and microtubules in determining centriole architecture," *Nat. Cell Biol.*, vol. 18, no. 4, pp. 393–403, 2016.
 - [55] G. E. Fantner, G. Schitter, J. H. Kindt, T. Ivanov, K. Ivanova, R. Patel, N. Holten-Andersen, J. Adams, P. J. Thurner, I. W. Rangelow, and P. K. Hansma, "Components for high speed atomic force microscopy," *Ultramicroscopy*, vol. 106, no. 8, pp. 881–887, 2006.
 - [56] N. Kodera, D. Yamamoto, R. Ishikawa, and T. Ando, "Video imaging of walking myosin V by high-speed atomic force microscopy," *Nature*, vol. 468, no. 7320, pp. 72–76, 2010.
 - [57] G. E. Fantner, R. J. Barbero, D. S. Gray, and A. M. Belcher, "Kinetics of antimicrobial peptide activity measured on individual bacterial cells using high-speed atomic force microscopy," *Nat. Nanotechnol.*, vol. 5, no. 4, pp. 280–285, Apr. 2010.
 - [58] J. Mertz, O. Marti, and J. Mlynek, "Regulation of a microcantilever response by force feedback," *Appl. Phys. Lett.*, vol. 62, no. 19, pp. 2344–2346, 1993.
 - [59] T. Sulchek, R. Hsieh, J. D. Adams, G. G. Yaralioglu, S. C. Minne, C. F. Quate, J. P. Cleveland, A. Atalar, and D. M. Adderton, "High-speed tapping mode imaging with active Q control for atomic force microscopy," *Appl. Phys. Lett.*, vol. 76, no. 11, pp. 1473–1475, 2000.
 - [60] M. W. Fairbairn and S. O. R. Moheimani, *A new approach to active Q control of an atomic force microscope micro-cantilever operating in tapping mode*, vol. 46, no. 5. IFAC, 2013.
 - [61] J. D. Adams, A. Nievergelt, B. W. Erickson, C. Yang, M. Dukic, and G. E. Fantner, "High-speed imaging upgrade for a standard sample scanning atomic force microscope using small cantilevers," *Rev. Sci. Instrum.*, vol. 85, no. 9, p. 93702, Sep. 2014.
 - [62] J. D. Adams, B. W. Erickson, J. Grossenbacher, J. Brugger, A. Nievergelt, and G. E. Fantner, "Harnessing the damping properties of materials for high-speed atomic force microscopy," *Nat. Nanotechnol.*, vol. 11, no. 2, pp. 147–151, Feb. 2016.

- [63] K. Sidler, "Fabrication and Characterization of SU-8 Cantilevers with Integrated Tips Designed for Dip-Pen Nanolithography," p. Master's thesis, mechanical engineering, ETH, 2006.
- [64] J. D. Adams, C. H. Schwalb, M. Winhold, M. Đukić, M. Huth, and G. E. Fantner, "Analysis of local deformation effects in resistive strain sensing of a submicron-thickness AFM cantilever," vol. 8763, p. 876327, May 2013.
- [65] S. Manzeli, A. Allain, A. Ghadimi, and A. Kis, "Piezoresistivity and Strain-induced Band Gap Tuning in Atomically Thin MoS₂," *Nano Lett.*, vol. 15, no. 8, pp. 5330–5335, Aug. 2015.
- [66] S. Bertolazzi, J. Brivio, and A. Kis, "Stretching and Breaking of Ultrathin MoS₂," *ACS Nano*, vol. 5, no. 12, pp. 9703–9709, Dec. 2011.
- [67] M. Park, Y. J. Park, X. Chen, Y.-K. Park, M.-S. Kim, and J.-H. Ahn, "MoS₂-Based Tactile Sensor for Electronic Skin Applications," *Adv. Mater.*, vol. 28, no. 13, pp. 2556–2562, Apr. 2016.
- [68] J. D. Lin, C. Han, F. Wang, R. Wang, D. Xiang, S. Qin, X.-A. Zhang, L. Wang, H. Zhang, A. T. S. Wee, and W. Chen, "Electron-Doping-Enhanced Trion Formation in Monolayer Molybdenum Disulfide Functionalized with Cesium Carbonate," *ACS Nano*, vol. 8, no. 5, pp. 5323–5329, May 2014.
- [69] A. T. Neal, R. Pachter, and S. Mou, "P-type conduction in two-dimensional MoS₂ via oxygen incorporation," *Appl. Phys. Lett.*, vol. 110, no. 19, p. 193103, May 2017.
- [70] H. Fang, M. Tosun, G. Seol, T. C. Chang, K. Takei, J. Guo, and A. Javey, "Degenerate n-Doping of Few-Layer Transition Metal Dichalcogenides by Potassium," *Nano Lett.*, vol. 13, no. 5, pp. 1991–1995, May 2013.
- [71] V. P. Pham and G. Y. Yeom, "Recent Advances in Doping of Molybdenum Disulfide: Industrial Applications and Future Prospects," *Adv. Mater.*, vol. 28, no. 41, pp. 9024–9059, Nov. 2016.
- [72] D. Kiriya, M. Tosun, P. Zhao, J. S. Kang, and A. Javey, "Air-Stable Surface Charge Transfer Doping of MoS₂ by Benzyl Viologen," *J. Am. Chem. Soc.*, vol. 136, no. 22, pp. 7853–7856, 2014.
- [73] A. P. Nievergelt, B. W. Erickson, N. Hosseini, J. D. Adams, and G. E. Fantner, "Studying biological membranes with extended range high-speed atomic force microscopy," *Sci. Rep.*, vol. 5, p. 11987, Jul. 2015.
- [74] C.-F. Yen and S. Sivasankar, "Minimizing open-loop piezoactuator nonlinearity artifacts in atomic force microscope measurements," *J. Vac. Sci. Technol. B, Nanotechnol. Microelectron. Mater. Process. Meas. Phenom.*, vol. 35, no. 5, p. 53201, Sep. 2017.
- [75] D. Croft, G. Shed, and S. Devasia, "Creep, Hysteresis, and Vibration Compensation for Piezoactuators: Atomic Force Microscopy Application," *J. Dyn. Syst. Meas. Control*, vol. 123, no. 1, p. 35, Mar. 2001.
- [76] J. Peng and X. Chen, "A Survey of Modeling and Control of Piezoelectric Actuators," *Mod. Mech. Eng.*, vol. 3, no. 1, pp. 1–20, Feb. 2013.
- [77] S. O. R. Moheimani, "Invited review article: accurate and fast nanopositioning with piezoelectric tube scanners: emerging trends and future challenges," *Rev. Sci. Instrum.*, vol. 79, no. 7, p. 71101, Jul. 2008.
- [78] A. J. Fleming, "A review of nanometer resolution position sensors: Operation and performance," *Sensors Actuators A Phys.*, vol. 190, pp. 106–126, Feb. 2013.
- [79] B. Mokaberi and A. A. G. Requicha, "Drift compensation for automatic nanomanipulation with scanning probe microscopes," *IEEE Trans. Autom. Sci. Eng.*, vol. 3, no. 3, pp. 199–207, 2006.
- [80] G. Zhang, C. Zhang, and C. Wang, "Iterative Learning Control of Hysteresis in Piezoelectric Actuators," *Math. Probl. Eng.*, vol. 2014, pp. 1–6, May 2014.
- [81] U. Pinsopon, S. Cetinkunt, and S. Nakajima, "Design, fabrication, and real-time neural network control of a three-degrees-of-freedom nanopositioner," *IEEE/ASME Trans. Mechatronics*, vol. 5, no. 3, pp. 273–280, 2000.
- [82] Y. Shan, J. E. Speich, and K. K. Leang, "Low-Cost IR Reflective Sensors for Submicrolevel Position Measurement and Control," *IEEE/ASME Trans. Mechatronics*, vol. 13, no. 6, pp. 700–709, Dec. 2008.
- [83] J. Schneir, "Design of an atomic force microscope with interferometric position control," *J. Vac. Sci. Technol. B Microelectron. Nanom. Struct.*, vol. 12, no. 6, p. 3561, Nov. 1994.
- [84] G. Binnig, H. Rohrer, C. Gerber, and E. Weibel, "Surface Studies by Scanning Tunneling Microscopy," *Phys. Rev. Lett.*, vol. 49, no. 1, pp. 57–61, Jul. 1982.
- [85] L. Montelius and J. O. Tegenfeldt, "Direct observation of the tip shape in scanning probe microscopy," *J. Vac. Sci. Technol. B Microelectron. Nanom. Struct. Process.*, vol. 62, no. 2628, p. 1518, 1993.

- [86] U. D. Schwarz, P. Haefke, Reimann, and H.-J. Güntherodt, "Tip artefacts in scanning force microscopy," *J. Microsc.*, vol. 173, no. 3, pp. 183–197, Mar. 1994.
- [87] M. Leitner, G. E. Fantner, E. J. Fantner, K. Ivanova, T. Ivanov, I. Rangelow, A. Ebner, M. Rangel, J. Tang, and P. Hinterdorfer, "Increased imaging speed and force sensitivity for bio-applications with small cantilevers using a conventional AFM setup," *Micron*, vol. 43, no. 12, pp. 1399–1407, 2012.
- [88] M. Shibata, T. Uchihashi, T. Ando, and R. Yasuda, "Long-tip high-speed atomic force microscopy for nanometer-scale imaging in live cells," *Sci. Rep.*, vol. 5, p. 8724, 2015.
- [89] M. R. Nellist, Y. Chen, A. Mark, S. Gödrich, C. Stelling, J. Jiang, R. Poddar, C. Li, R. Kumar, G. Papastavrou, M. Retsch, B. S. Brunschwig, Z. Huang, C. Xiang, and S. W. Boettcher, "Atomic force microscopy with nanoelectrode tips for high resolution electrochemical, nanoadhesion and nanoelectrical imaging," *Nanotechnology*, vol. 28, no. 9, p. 95711, Mar. 2017.
- [90] J. Velmurugan, A. Agrawal, S. An, E. Choudhary, and V. A. Szalai, "Fabrication of Scanning Electrochemical Microscopy-Atomic Force Microscopy Probes to Image Surface Topography and Reactivity at the Nanoscale," *Anal. Chem.*, vol. 89, no. 5, pp. 2687–2691, Mar. 2017.
- [91] I. Maouli, A. Taguchi, Y. Saito, S. Kawata, and P. Verma, "Optical antennas for tunable enhancement in tip-enhanced Raman spectroscopy imaging," *Appl. Phys. Express*, vol. 8, no. 3, p. 32401, Mar. 2015.
- [92] R. Suriano, T. Zandrini, C. De Marco, R. Osellame, S. Turri, and F. Bragheri, "Nanomechanical probing of soft matter through hydrophobic AFM tips fabricated by two-photon polymerization," *Nanotechnology*, vol. 27, no. 15, p. 155702, Apr. 2016.
- [93] Y. Yan, Y. Geng, and Z. Hu, "Recent advances in AFM tip-based nanomechanical machining," *Int. J. Mach. Tools Manuf.*, vol. 99, pp. 1–18, Dec. 2015.
- [94] T. Umakoshi, Y. Saito, and P. Verma, "Highly efficient plasmonic tip design for plasmon nanofocusing in near-field optical microscopy," *Nanoscale*, vol. 8, no. 10, pp. 5634–5640, 2016.
- [95] A. Sanders, L. Zhang, R. W. Bowman, L. O. Herrmann, and J. J. Baumberg, "Facile Fabrication of Spherical Nanoparticle-Tipped AFM Probes for Plasmonic Applications," *Part. Part. Syst. Charact.*, vol. 32, no. 2, pp. 182–187, Feb. 2015.
- [96] K. Kawashima, T. Mineta, E. Makino, T. Kawashima, and T. Shibata, "Self-Align Fabrication of Narrow-Gapped Dual AFM Tip Using Si Trench Refilling with SOG and Magnetostrictive Film Stacked Dual Cantilever Formation," *Electron. Commun. Japan*, vol. 98, no. 12, pp. 30–36, Dec. 2015.
- [97] V. Seena, A. Fernandes, P. Pant, S. Mukherji, and V. Ramgopal Rao, "Polymer nanocomposite nanomechanical cantilever sensors: Material characterization, device development and application in explosive vapour detection," *Nanotechnology*, vol. 22, no. 29, p. 295501, 2011.
- [98] V. Seena, A. Nigam, P. Pant, S. Mukherji, and V. R. Rao, "Organic CantiFET: A nanomechanical polymer cantilever sensor with integrated OFET," *J. Microelectromechanical Syst.*, vol. 21, no. 2, pp. 294–301, 2012.
- [99] A. Johansson, M. Calleja, P. A. Rasmussen, and A. Boisen, "SU-8 cantilever sensor system with integrated readout," *Sensors Actuators, A Phys.*, vol. 123–124, pp. 111–115, 2005.
- [100] X. Wang, K. S. Ryu, D. A. Bullen, J. Zou, H. Zhang, C. A. Mirkin, and C. Liu, "Scanning Probe Contact Printing," *Langmuir*, vol. 19, no. 21, pp. 8951–8955, 2003.
- [101] A. W. McFarland, M. A. Poggi, L. A. Bottomley, and J. S. Colton, "Production and characterization of polymer microcantilevers," *Rev. Sci. Instrum.*, vol. 75, no. 8, pp. 2756–2758, 2004.
- [102] G. Genolet, J. Brugger, M. Despont, U. Drechsler, P. Vettiger, N. F. de Rooij, and D. Anselmetti, "Soft, entirely photoplastic probes for scanning force microscopy," *Rev. Sci. Instrum.*, vol. 70, no. 5, pp. 2398–2401, May 1999.
- [103] M. Despont, G. Genolet, N. F. de Rooij, D. Anselmetti, and P. Vettiger, "All-photoplastic, soft cantilever cassette probe for scanning force microscopy," *J. Vac. Sci. Technol. B Microelectron. Nanom. Struct.*, vol. 18, no. 2, p. 617, 2002.
- [104] S. Mouaziz, G. Boero, R. S. Popovic, and J. Brugger, "Polymer-based cantilevers with integrated electrodes," *J. Microelectromechanical Syst.*, vol. 15, no. 4, pp. 890–895, 2006.
- [105] C. Martin-Olmos, H. I. Rasool, B. H. Weiller, and J. K. Gimzewski, "Graphene MEMS: AFM Probes Performance Improvement," *ACS Nano*, no. 5, pp. 4164–4170, 2013.
- [106] J. S. Lee, J. Song, S. O. Kim, S. Kim, W. Lee, J. A. Jackman, D. Kim, N.-J. Cho, and J. Lee, "Multifunctional hydrogel nano-probes for atomic force microscopy," *Nat. Commun.*, vol. 7, p. 11566, May 2016.

- [107] S. Kim, J. Song, S.-J. Cho, and J. Lee, "Facile Batch Fabrication of Hydrogel Atomic Force Microscope Cantilevers via Capillary Filling and Ultraviolet Curing in an Aligned Elastomeric Mold Pair," *J. Microelectromechanical Syst.*, vol. 26, no. 3, pp. 504–506, Jun. 2017.
- [108] A. Boisen, J. P. Rasmussen, O. Hansen, and S. Bouwstra, "Indirect tip fabrication for Scanning Probe Microscopy," *Microelectron. Eng.*, vol. 30, no. 1–4, pp. 579–582, Jan. 1996.
- [109] R. B. Marcus and T. T. Sheng, "The Oxidation of Shaped Silicon Surfaces," *J. Electrochem. Soc.*, vol. 129, no. 6, p. 1278, Jun. 1982.
- [110] D.-B. Kao, J. P. McVittie, W. D. Nix, and K. C. Saraswat, "Two-dimensional thermal oxidation of silicon. II. Modeling stress effects in wet oxides," *IEEE Trans. Electron Devices*, vol. 35, no. 1, pp. 25–37, 1988.
- [111] J. Mertz, O. Marti, and J. Mlynek, "Regulation of a microcantilever response by force feedback," *Cite as Appl. Phys. Lett.*, vol. 62, p. 2344, 1993.
- [112] J. S. Villarrubia, "Algorithms of Scanned Probe Microscope Image," *J. Res. Natl. Inst. Stand. Technol.*, vol. 102, no. 4, pp. 425–454, 1997.
- [113] J. Kokavecz, O. Marti, P. Heszler, and Á. Mechler, "Imaging bandwidth of the tapping mode atomic force microscope probe," *Phys. Rev. B*, vol. 73, no. 15, p. 155403, Apr. 2006.
- [114] T. Sulchek, G. G. Yaralioglu, C. F. Quate, and S. C. Minne, "Characterization and optimization of scan speed for tapping-mode atomic force microscopy," *Rev. Sci. Instrum.*, vol. 73, no. 8, pp. 2928–2936, Aug. 2002.
- [115] L. Hellemans, K. Waeyaert, F. Hennau, L. Stockman, I. Heyvaert, and C. Van Haesendonck, "Can atomic force microscopy tips be inspected by atomic force microscopy?," *J. Vac. Sci. Technol. B Microelectron. Nanom. Struct.*, vol. 9, no. 2, p. 1309, Mar. 1991.
- [116] M. L. Bloo, H. Haitjema, and W. O. Pril, "Deformation and wear of pyramidal, silicon-nitride AFM tips scanning micrometre-size features in contact mode," *Meas. Sci. Technol.*, vol. 25, no. 3, pp. 203–211, 1999.
- [117] H. Bhaskaran, B. Gotsmann, A. Sebastian, U. Drechsler, M. A. Lantz, M. Despont, P. Jaroenapibal, R. W. Carpick, Y. Chen, and K. Sridharan, "Ultralow nanoscale wear through atom-by-atom attrition in silicon-containing diamond-like carbon," *Nat. Nanotechnol.*, vol. 5, no. 3, pp. 181–185, Mar. 2010.
- [118] S. Keller, D. Haefliger, and A. Boisen, "Fabrication of thin SU-8 cantilevers: Initial bending, release and time stability," *J. Micromechanics Microengineering*, vol. 20, no. 4, p. 45024, 2010.
- [119] M. Kandpal, C. Sharan, P. Poddar, K. Prashanthi, P. R. Apte, and V. Ramgopal Rao, "Photopatternable nano-composite (SU-8/ZnO) thin films for piezo-electric applications," *Appl. Phys. Lett.*, vol. 101, no. 10, p. 104102, Sep. 2012.
- [120] R. García, R. Magerle, and R. Perez, "Nanoscale compositional mapping with gentle forces," *Nat. Mater.*, vol. 6, no. 6, pp. 405–411, Jun. 2007.
- [121] D. A. Walters, J. P. Cleveland, N. H. Thomson, P. K. Hansma, M. A. Wendman, G. Gurley, and V. Elings, "Short cantilevers for atomic force microscopy," *Rev. Sci. Instrum.*, vol. 67, no. 10, pp. 3583–3590, 1996.
- [122] T. Ando, N. Kodera, E. Takai, D. Maruyama, K. Saito, and A. Toda, "A high-speed atomic force microscope for studying biological macromolecules," *Proc. Natl. Acad. Sci.*, vol. 98, no. 22, pp. 12468–12472, 2001.
- [123] D. Nečas and P. Klapetek, "Gwyddion: An open-source software for SPM data analysis," *Cent. Eur. J. Phys.*, vol. 10, no. 1, pp. 181–188, 2012.
- [124] O. Wolter, T. Bayer, and J. Greschner, "Micromachined silicon sensors for scanning force microscopy," *J. Vac. Sci. Technol. B Microelectron. Nanom. Struct.*, vol. 9, no. 2, p. 1353, Mar. 1991.
- [125] G. Longo, L. Alonso-Sarduy, L. Marques Rio, A. Bizzini, A. Trampuz, J. Notz, G. Dietler, and S. Kasas, "Rapid detection of bacterial resistance to antibiotics using AFM cantilevers as nanomechanical sensors," vol. 8, no. 7, p. 522, 2013.
- [126] A. Boisen, J. Thaysen, H. Jensenius, and O. Hansen, "Environmental sensors based on micromachined cantilevers with integrated read-out," *Ultramicroscopy*, vol. 82, no. 1–4, pp. 11–16, Feb. 2000.
- [127] G. Tosolini, F. Scarponi, S. Cannistraro, and J. Bausells, "Biomolecule recognition using piezoresistive nanomechanical force probes," *Appl. Phys. Lett.*, vol. 102, no. 25, p. 253701, Jun. 2013.
- [128] J. Kreith, T. Strunz, E. J. Fantner, G. E. Fantner, and M. J. Cordill, "A versatile atomic force microscope integrated with a scanning electron microscope," *Rev. Sci. Instrum.*, vol. 88, no. 5,

- p. 53704, May 2017.
- [129] U. Stahl, C. W. Yuan, A. L. de Lozanne, and M. Tortonese, "Atomic force microscope using piezoresistive cantilevers and combined with a scanning electron microscope," *Appl. Phys. Lett.*, vol. 65, no. 22, pp. 2878–2880, Nov. 1994.
 - [130] A. L. Eastwood, A. Sanzeni, B. C. Petzold, S.-J. Park, M. Vergassola, B. L. Pruitt, and M. B. Goodman, "Tissue mechanics govern the rapidly adapting and symmetrical response to touch," *Proc. Natl. Acad. Sci.*, vol. 112, no. 50, pp. E6955–E6963, Dec. 2015.
 - [131] Q. Yang, Q. Ma, K. M. Herum, C. Wang, N. Patel, J. Lee, S. Wang, T. M. Yen, J. Wang, H. Tang, Y.-H. Lo, B. P. Head, F. Azam, S. Xu, G. Cauwenberghs, A. D. Mcculloch, S. John, Z. Liu, R. Lal, and D. A. Weitz, "Array atomic force microscopy for real-time multiparametric analysis," *PNAS*, vol. 116, no. 13, pp. 5872–5877, 2019.
 - [132] Y.-S. Kim, H.-J. Nam, S.-M. Cho, J.-W. Hong, D.-C. Kim, and J. U. Bu, "PZT cantilever array integrated with piezoresistor sensor for high speed parallel operation of AFM," *Sensors Actuators A Phys.*, vol. 103, no. 1, pp. 122–129, 2003.
 - [133] N. Harjee, A. Haemmerli, D. Goldhaber-Gordon, and B. L. Pruitt, "Coaxial tip piezoresistive scanning probes with sub-nanometer vertical displacement resolution," in *2010 IEEE Sensors*, 2010, pp. 1962–1966.
 - [134] V. S. Bhat, J. Sklenar, B. Farmer, J. Woods, J. T. Hastings, S. J. Lee, J. B. Ketterson, and L. E. De Long, "Controlled Magnetic Reversal in Permalloy Films Patterned into Artificial Quasicrystals," *Phys. Rev. Lett.*, vol. 111, no. 7, p. 77201, Aug. 2013.
 - [135] M. Dukic, M. Winhold, C. H. Schwalb, J. D. Adams, V. Stavrov, M. Huth, and G. E. Fantner, "Direct-write nanoscale printing of nanogranular tunnelling strain sensors for sub-micrometre cantilevers," *Nat. Commun.*, vol. 7, p. 12487, Sep. 2016.
 - [136] J. Thaysen, A. D. Yal inkaya, P. Vettiger, and A. Menon, "Polymer-based stress sensor with integrated readout," *J. Phys. D: Appl. Phys.*, vol. 35, no. 21, pp. 2698–2703, Nov. 2002.
 - [137] N. S. Kale, S. Nag, R. Pinto, and V. R. Rao, "Fabrication and Characterization of a Polymeric Microcantilever With an Encapsulated Hotwire CVD Polysilicon Piezoresistor," *J. Microelectromechanical Syst.*, vol. 18, no. 1, pp. 79–87, Feb. 2009.
 - [138] L. Gammelgaard, P. A. Rasmussen, M. Calleja, P. Vettiger, and A. Boisen, "Microfabricated photoplastic cantilever with integrated photoplastic/carbon based piezoresistive strain sensor," *Appl. Phys. Lett.*, vol. 88, no. 11, p. 113508, Mar. 2006.
 - [139] J. Tong and Y. Sun, "Toward Carbon Nanotube-Based AFM Cantilevers," *IEEE Trans. Nanotechnol.*, vol. 6, no. 5, pp. 519–523, Sep. 2007.
 - [140] M. A. Cullinan and M. L. Culpepper, "Carbon nanotubes as piezoresistive microelectromechanical sensors: Theory and experiment," *Phys. Rev. B*, vol. 82, no. 11, p. 115428, Sep. 2010.
 - [141] C. Stampfer, A. Jungen, R. Linderman, D. Obergfell, A. S. Roth, and C. Hierold, "Nano-Electromechanical Displacement Sensing Based on Single-Walled Carbon Nanotubes," *Nano Lett.*, vol. 6, no. 7, pp. 1449–1453, 2006.
 - [142] Y.-C. Kung, "Stretchable and Highly Bendable Thin Film Transistors Based on Atomically Thin Chemical Vapor Deposited Molybdenum Disulfide," *École polytechnique fédérale de Lausanne EPFL*, 2018.
 - [143] G. Genolet, "New photoplastic fabrication techniques and devices based on high aspect ratio photoresist." Thèse École polytechnique fédérale de Lausanne EPFL, p. no. 2421, 2001.
 - [144] Q. H. Wang, K. Kalantar-Zadeh, A. Kis, J. N. Coleman, and M. S. Strano, "Electronics and optoelectronics of two-dimensional transition metal dichalcogenides," *Nat. Nanotechnol.*, vol. 7, no. 11, pp. 699–712, Nov. 2012.
 - [145] B. Radisavljevic, A. Radenovic, J. Brivio, V. Giacometti, and A. Kis, "Single-layer MoS2 transistors," *Nat. Nanotechnol.*, vol. 6, no. 3, pp. 147–150, Mar. 2011.
 - [146] O. Lopez-Sanchez, D. Lembke, M. Kayci, A. Radenovic, and A. Kis, "Ultrasensitive photodetectors based on monolayer MoS2," *Nat. Nanotechnol.*, vol. 8, no. 7, pp. 497–501, Jul. 2013.
 - [147] F. H. L. Koppens, T. Mueller, P. Avouris, A. C. Ferrari, M. S. Vitiello, and M. Polini, "Photodetectors based on graphene, other two-dimensional materials and hybrid systems," *Nat. Nanotechnol.*, vol. 9, no. 10, pp. 780–793, Oct. 2014.
 - [148] A. Castellanos-Gomez, R. van Leeuwen, M. Buscema, H. S. J. van der Zant, G. A. Steele, and W. J. Venstra, "Single-Layer MoS2 Mechanical Resonators," *Adv. Mater.*, vol. 25, no. 46, pp. 6719–6723, 2013.

- [149] D. Xiao, G.-B. Liu, W. Feng, X. Xu, and W. Yao, "Coupled Spin and Valley Physics in Monolayers of MoS_2 and Other Group-VI Dichalcogenides," *Phys. Rev. Lett.*, vol. 108, no. 19, p. 196802, May 2012.
- [150] H. Li, C. Tsai, A. L. Koh, L. Cai, A. W. Contryman, A. H. Fragapane, J. Zhao, H. S. Han, H. C. Manoharan, F. Abild-Pedersen, J. K. Nørskov, and X. Zheng, "Activating and optimizing MoS_2 basal planes for hydrogen evolution through the formation of strained sulphur vacancies," *Nat. Mater.*, vol. 15, no. 1, pp. 48–53, Jan. 2016.
- [151] Y. Yoon, K. Ganapathi, and S. Salahuddin, "How Good Can Monolayer MoS_2 Transistors Be?," *Nano Lett.*, vol. 11, pp. 3768–3773, 2011.
- [152] S. B. Desai, S. R. Madhvapathy, A. B. Sachid, J. P. Llinas, Q. Wang, G. H. Ahn, G. Pitner, M. J. Kim, J. Bokor, C. Hu, H.-S. P. Wong, and A. Javey, " MoS_2 transistors with 1-nanometer gate lengths," *Science* (80-.), vol. 354, no. 6308, pp. 99–102, Oct. 2016.
- [153] S. Bertolazzi, J. Brivio, and A. Kis, "Stretching and Breaking of Ultrathin MoS_2 ," *ACS Nano*, vol. 5, no. 12, pp. 9703–9709, 2011.
- [154] D. Akinwande, N. Petrone, and J. Hone, "Two-dimensional flexible nanoelectronics," *Nat. Commun.*, vol. 5, Dec. 2014.
- [155] S. Wi, H. Kim, M. Chen, H. Nam, L. J. Guo, E. Meyhofer, and X. Liang, "Enhancement of Photovoltaic Response in Multilayer MoS_2 Induced by Plasma Doping," *ACS Nano*, vol. 8, no. 5, pp. 5270–5281, May 2014.
- [156] J. Guo, F. Li, Y. Sun, X. Zhang, and L. Tang, "Oxygen-incorporated MoS_2 ultrathin nanosheets grown on graphene for efficient electrochemical hydrogen evolution," *J. Power Sources*, vol. 291, pp. 195–200, Sep. 2015.
- [157] A. Nipane, D. Karmakar, N. Kaushik, S. Karande, and S. Lodha, "Few-Layer MoS_2 p-Type Devices Enabled by Selective Doping Using Low Energy Phosphorus Implantation," *ACS Nano*, vol. 10, no. 2, pp. 2128–2137, Feb. 2016.
- [158] J. Suh, T.-E. Park, D.-Y. Lin, D. Fu, J. Park, H. J. Jung, Y. Chen, C. Ko, C. Jang, Y. Sun, R. Sinclair, J. Chang, S. Tongay, and J. Wu, "Doping against the Native Propensity of MoS_2 : Degenerate Hole Doping by Cation Substitution," *Nano Lett.*, vol. 14, no. 12, pp. 6976–6982, Dec. 2014.
- [159] J. Gao, Y. D. Kim, L. Liang, J. C. Idrobo, P. Chow, J. Tan, B. Li, L. Li, B. G. Sumpter, T.-M. Lu, V. Meunier, J. Hone, and N. Koratkar, "Transition-Metal Substitution Doping in Synthetic Atomically Thin Semiconductors," *Adv. Mater.*, vol. 28, no. 44, pp. 9735–9743, Nov. 2016.
- [160] Y. Li, C.-Y. Xu, P. Hu, and L. Zhen, "Carrier Control of MoS_2 Nanoflakes by Functional Self-Assembled Monolayers," *ACS Nano*, vol. 7, no. 9, pp. 7795–7804, Sep. 2013.
- [161] Y. Du, H. Liu, A. T. Neal, M. Si, and P. D. Ye, "Molecular Doping of Multilayer MoS_2 Field-Effect Transistors: Reduction in Sheet and Contact Resistances," *IEEE Electron Device Lett.*, vol. 34, no. 10, pp. 1328–1330, Oct. 2013.
- [162] A. Tarasov, S. Zhang, M.-Y. Tsai, P. M. Campbell, S. Graham, S. Barlow, S. R. Marder, and E. M. Vogel, "Controlled Doping of Large-Area Trilayer MoS_2 with Molecular Reductants and Oxidants," *Adv. Mater.*, vol. 27, no. 7, pp. 1175–1181, Feb. 2015.
- [163] D.-H. Kang, M.-S. Kim, J. Shim, J. Jeon, H.-Y. Park, W.-S. Jung, H.-Y. Yu, C.-H. Pang, S. Lee, and J.-H. Park, "High-Performance Transition Metal Dichalcogenide Photodetectors Enhanced by Self-Assembled Monolayer Doping," *Adv. Funct. Mater.*, vol. 25, no. 27, pp. 4219–4227, Jul. 2015.
- [164] D. Sarkar, X. Xie, J. Kang, H. Zhang, W. Liu, J. Navarrete, M. Moskovits, and K. Banerjee, "Functionalization of Transition Metal Dichalcogenides with Metallic Nanoparticles: Implications for Doping and Gas-Sensing," *Nano Lett.*, vol. 15, no. 5, pp. 2852–2862, May 2015.
- [165] T. S. Sreeprasad, P. Nguyen, N. Kim, and V. Berry, "Controlled, Defect-Guided, Metal-Nanoparticle Incorporation onto MoS_2 via Chemical and Microwave Routes: Electrical, Thermal, and Structural Properties," *Nano Lett.*, vol. 13, no. 9, pp. 4434–4441, Sep. 2013.
- [166] H.-Y. Park, M.-H. Lim, J. Jeon, G. Yoo, D.-H. Kang, S. K. Jang, M. H. Jeon, Y. Lee, J. H. Cho, G. Y. Yeom, W.-S. Jung, J. Lee, S. Park, S. Lee, and J.-H. Park, "Wide-Range Controllable n-Doping of Molybdenum Disulfide (MoS_2) through Thermal and Optical Activation," *ACS Nano*, vol. 9, no. 3, pp. 2368–2376, Mar. 2015.
- [167] D. Jariwala, V. K. Sangwan, D. J. Late, J. E. Johns, V. P. Dravid, T. J. Marks, L. J. Lauhon, and M. C. Hersam, "Band-like transport in high mobility unencapsulated single-layer MoS_2 transistors," *Appl. Phys. Lett.*, vol. 102, no. 17, p. 173107, Apr. 2013.
- [168] B. Baugher, H. O. H. Churchill, Y. Yang, and P. Jarillo-Herrero, "Intrinsic Electronic Transport

- Properties of High Quality Monolayer and Bilayer MoS₂,” *Nano Lett.*, vol. 13, no. 9, pp. 4212–4216, 2013.
- [169] D. Lembke, A. Allain, and A. Kis, “Thickness-dependent mobility in two-dimensional MoS₂ transistors,” *Nanoscale*, vol. 7, no. 14, pp. 6255–6260, Mar. 2015.
 - [170] D. Kufer and G. Konstantatos, “Highly Sensitive, Encapsulated MoS₂ Photodetector with Gate Controllable Gain and Speed,” *Nano Lett.*, vol. 15, no. 11, pp. 7307–7313, Nov. 2015.
 - [171] L. Wang, I. Meric, P. Y. Huang, Q. Gao, Y. Gao, H. Tran, T. Taniguchi, K. Watanabe, L. M. Campos, D. A. Muller, J. Guo, P. Kim, J. Hone, K. L. Shepard, and C. R. Dean, “One-Dimensional Electrical Contact to a Two-Dimensional Material,” *Science* (80-.), vol. 342, no. 6158, pp. 614–617, Nov. 2013.
 - [172] A. Avsar, I. J. Vera-Marun, J. Y. Tan, K. Watanabe, T. Taniguchi, A. H. Castro Neto, and B. Özyilmaz, “Air-Stable Transport in Graphene-Contacted, Fully Encapsulated Ultrathin Black Phosphorus-Based Field-Effect Transistors,” *ACS Nano*, vol. 9, no. 4, pp. 4138–4145, Apr. 2015.
 - [173] H. C. P. Movva, A. Rai, S. Kang, K. Kim, B. Fallahazad, T. Taniguchi, K. Watanabe, E. Tutuc, and S. K. Banerjee, “High-Mobility Holes in Dual-Gated WSe₂ Field-Effect Transistors,” *ACS Nano*, vol. 9, no. 10, pp. 10402–10410, Oct. 2015.
 - [174] H. Al-Mumen, L. Dong, and W. Li, “SU-8 doped and encapsulated n-type graphene nanomesh with high air stability,” *Appl. Phys. Lett.*, vol. 103, no. 23, p. 232113, Dec. 2013.
 - [175] H. Al-Mumen, “Characterisation of SU-8 n-doping carbon nanotube-based electronic devices,” *Micro Nano Lett.*, vol. 10, no. 12, pp. 670–673, Dec. 2015.
 - [176] C. Lee, H. Yan, L. E. Brus, T. F. Heinz, J. Hone, and S. Ryu, “Anomalous Lattice Vibrations of Single- and Few-Layer MoS₂,” *ACS Nano*, vol. 4, no. 5, pp. 2695–2700, May 2010.
 - [177] B. Chakraborty, A. Bera, D. V. S. Muthu, S. Bhowmick, U. V. Waghmare, and A. K. Sood, “Symmetry-dependent phonon renormalization in monolayer MoS₂ transistor,” *Phys. Rev. B*, vol. 85, no. 16, p. 161403, Apr. 2012.
 - [178] S. Andleeb, A. Kumar Singh, and J. Eom, “Chemical doping of MoS₂ multilayer by p-toluene sulfonic acid,” *Sci. Technol. Adv. Mater.*, vol. 16, no. 3, p. 35009, Jun. 2015.
 - [179] D. Lim, E. S. Kannan, I. Lee, S. Rathi, L. Li, Y. Lee, M. A. Khan, J. Park, and G.-H. Kim, “High performance MoS₂ -based field-effect transistor enabled by hydrazine doping,” *Nanotechnology*, vol. 27, no. 22, p. 225201, 2016.
 - [180] J. Pu, Y. Zhang, Y. Wada, J. T.-W. Wang, L.-J. Li, Y. Iwasa, and T. Takenobu, “Fabrication of stretchable MoS₂ thin-film transistors using elastic ion-gel gate dielectrics,” *Appl. Phys. Lett.*, vol. 103, no. 2, p. 23505, 2013.
 - [181] H.-Y. Chang, S. Yang, J. Lee, L. Tao, W.-S. Hwang, D. Jena, N. Lu, and D. Akinwande, “High-Performance, Highly Bendable MoS₂ Transistors with High-K Dielectrics for Flexible Low-Power Systems,” *ACS Nano*, vol. 7, no. 6, pp. 5446–5452, Jun. 2013.
 - [182] J. Yoon, W. Park, G.-Y. Bae, Y. Kim, H. S. Jang, Y. Hyun, S. K. Lim, Y. H. Kahng, W.-K. Hong, B. H. Lee, and H. C. Ko, “Highly Flexible and Transparent Multilayer MoS₂ Transistors with Graphene Electrodes,” *Small*, vol. 9, no. 19, pp. 3295–3300, Oct. 2013.
 - [183] H.-Y. Chang, M. N. Yogeesh, R. Ghosh, A. Rai, A. Sanne, S. Yang, N. Lu, S. K. Banerjee, and D. Akinwande, “Large-Area Monolayer MoS₂ for Flexible Low-Power RF Nanoelectronics in the GHz Regime,” *Adv. Mater.*, vol. 28, no. 9, pp. 1818–1823, Dec. 2015.
 - [184] M.-Y. Tsai, A. Tarasov, Z. R. Hesabi, H. Taghinejad, P. M. Campbell, C. A. Joiner, A. Adibi, and E. M. Vogel, “Flexible MoS₂ Field-Effect Transistors for Gate-Tunable Piezoresistive Strain Sensors,” *ACS Appl. Mater. Interfaces*, vol. 7, no. 23, pp. 12850–12855, Jun. 2015.
 - [185] D. Dumcenco, D. Ovchinnikov, K. Marinov, P. Lazić, M. Gibertini, N. Marzari, O. L. Sanchez, Y.-C. Kung, D. Krasnozhan, M.-W. Chen, S. Bertolazzi, P. Gillet, A. Fontcuberta i Morral, A. Radenovic, and A. Kis, “Large-Area Epitaxial Monolayer MoS₂,” *ACS Nano*, vol. 9, no. 4, pp. 4611–4620, Apr. 2015.
 - [186] M. Kaltenbrunner, T. Sekitani, J. Reeder, T. Yokota, K. Kuribara, T. Tokuhara, M. Drack, R. Schwödiauer, I. Graz, S. Bauer-Gogonea, S. Bauer, and T. Someya, “An ultra-lightweight design for imperceptible plastic electronics,” *Nature*, vol. 499, no. 7459, pp. 458–463, Jul. 2013.
 - [187] S. Adam and S. Das Sarma, “Boltzmann transport and residual conductivity in bilayer graphene,” *Phys. Rev. B*, vol. 77, no. 11, p. 115436, Mar. 2008.
 - [188] S. Ghatak, A. N. Pal, and A. Ghosh, “Nature of Electronic States in Atomically Thin MoS₂ Field-Effect Transistors,” *ACS Nano*, vol. 5, no. 10, pp. 7707–7712, Oct. 2011.
 - [189] Y. Guo, X. Wei, J. Shu, B. Liu, J. Yin, C. Guan, Y. Han, S. Gao, and Q. Chen, “Charge trapping at the MoS₂-SiO₂ interface and its effects on the characteristics of MoS₂ metal-oxide-

- semiconductor field effect transistors,” *Appl. Phys. Lett.*, vol. 106, no. 10, p. 103109, Mar. 2015.
- [190] H. Qiu, L. Pan, Z. Yao, J. Li, Y. Shi, and X. Wang, “Electrical characterization of back-gated bilayer MoS₂ field-effect transistors and the effect of ambient on their performances,” *Appl. Phys. Lett.*, vol. 100, no. 12, p. 123104, Mar. 2012.
 - [191] D. Lembke, A. Allain, and A. Kis, “Thickness-dependent mobility in two-dimensional MoS₂ transistors,” *Nanoscale*, vol. 7, no. 14, pp. 6255–6260, Apr. 2015.
 - [192] T. R. Albrecht and C. F. Quate, “Atomic resolution imaging of a nonconductor by atomic force microscopy,” *J. Appl. Phys.*, vol. 62, no. 7, p. 2599, Oct. 1987.
 - [193] G. Binnig and D. P. E. Smith, “Single-tube three-dimensional scanner for scanning tunneling microscopy,” *Rev. Sci. Instrum.*, vol. 57, no. 8, p. 1688, Aug. 1986.
 - [194] G. M. Clayton, S. Tien, K. K. Leang, Q. Zou, and S. Devasia, “A Review of Feedforward Control Approaches in Nanopositioning for High-Speed SPM,” *J. Dyn. Syst. Meas. Control*, vol. 131, no. 6, p. 61101, Nov. 2009.
 - [195] B. J. Kenton and K. K. Leang, “Design and Control of a Three-Axis Serial-Kinematic High-Bandwidth Nanopositioner,” *IEEE/ASME Trans. Mechatronics*, vol. 17, no. 2, pp. 356–369, Apr. 2012.
 - [196] S. Devasia, E. Eleftheriou, and S. O. R. Moheimani, “A Survey of Control Issues in Nanopositioning,” *IEEE Trans. Control Syst. Technol.*, vol. 15, no. 5, pp. 802–823, Sep. 2007.
 - [197] C.-Y. Su, Y. Stepanenko, J. Svoboda, and T. P. Leung, “Robust adaptive control of a class of nonlinear systems with unknown backlash-like hysteresis,” *IEEE Trans. Automat. Contr.*, vol. 45, no. 12, pp. 2427–2432, 2000.
 - [198] T. Tuma, A. Pantazi, D. R. Sahoo, P. Eib, G. Salis, H. Pozidis, and A. Sebastian, “A high-bandwidth spintronic position sensor,” *Nanotechnology*, vol. 25, no. 37, p. 375501, Sep. 2014.
 - [199] A. J. Fleming, A. G. Wills, and S. Moheimani, “Sensor Fusion for Improved Control of Piezoelectric Tube Scanners,” *IEEE Trans. Control Syst. Technol.*, vol. 16, no. 6, pp. 1265–1276, Nov. 2008.
 - [200] M. S. Rana, H. R. Pota, and I. R. Petersen, “Nonlinearity Effects Reduction of an AFM Piezoelectric Tube Scanner Using MIMO MPC,” *IEEE/ASME Trans. Mechatronics*, vol. 20, no. 3, pp. 1458–1469, Jun. 2015.
 - [201] A. Esbrook, X. Tan, and H. K. Khalil, “Control of Systems With Hysteresis Via Servocompensation and Its Application to Nanopositioning,” *IEEE Trans. Control Syst. Technol.*, vol. 21, no. 3, pp. 725–738, May 2013.
 - [202] X. Liu, J. Tong, and Y. Sun, “Millimeter-sized nanomanipulator with sub-nanometer positioning resolution and large force output,” *Smart Mater. Struct.*, vol. 16, no. 5, pp. 1742–1750, Oct. 2007.
 - [203] T. Tuma, A. Sebastian, J. Lygeros, and A. Pantazi, “The Four Pillars of Nanopositioning for Scanning Probe Microscopy: The Position Sensor, the Scanning Device, the Feedback Controller, and the Reference Trajectory,” *IEEE Control Syst.*, vol. 33, no. 6, pp. 68–85, Dec. 2013.
 - [204] S. Salapaka, A. Sebastian, J. P. Cleveland, and M. V. Salapaka, “High bandwidth nanopositioner: A robust control approach,” *Rev. Sci. Instrum.*, vol. 73, no. 9, p. 3232, Aug. 2002.
 - [205] A. A. Barlian, W.-T. Park, J. R. Mallon, A. J. Rastegar, and B. L. Pruitt, “Review: Semiconductor Piezoresistance for Microsystems,” *Proc. IEEE*, vol. 97, no. 3, pp. 513–552, Mar. 2009.
 - [206] Y. K. Yong, A. J. Fleming, and S. O. Moheimani, “A Novel Piezoelectric Strain Sensor for Simultaneous Damping and Tracking Control of a High-Speed Nanopositioner,” *IEEE/ASME Trans. Mechatronics*, vol. 18, no. 3, pp. 1113–1121, Jun. 2013.
 - [207] Y. Zhu, S. O. R. Moheimani, and M. R. Yuce, “Simultaneous Capacitive and Electrothermal Position Sensing in a Micromachined Nanopositioner,” *IEEE Electron Device Lett.*, vol. 32, no. 8, pp. 1146–1148, Aug. 2011.
 - [208] V. Kartik, A. Sebastian, T. Tuma, A. Pantazi, H. Pozidis, and D. R. Sahoo, “High-bandwidth nanopositioner with magnetoresistance based position sensing,” *Mechatronics*, vol. 22, no. 3, pp. 295–301, Apr. 2012.
 - [209] J. H. Kindt, G. E. Fantner, J. A. Cutroni, and P. K. Hansma, “Rigid design of fast scanning probe microscopes using finite element analysis,” *Ultramicroscopy*, vol. 100, no. 3–4, pp. 259–65, Aug. 2004.
 - [210] V. T. Stavrov, V. M. Todorov, A. A. Shulev, and C. M. Hardalov, “MEMS sensors for mm-range displacement measurements with sub-nm resolution,” *Smart sensors and actuators*, vol. 8763, p. 87632G, May 2013.

- [211] M. Kim, W. Moon, E. Yoon, and K.-R. Lee, "A new capacitive displacement sensor with high accuracy and long-range," *Sensors Actuators A Phys.*, vol. 130–131, pp. 135–141, Aug. 2006.
- [212] A. Mohammadi, M. R. Yuce, and S. O. R. Moheimani, "Dealing with 1/f noise in MEMS electrothermal sensing," in *IECON 2011 - 37th Annual Conference of the IEEE Industrial Electronics Society*, 2011, pp. 4054–4058.
- [213] A. J. Fleming and K. K. Leang, *Design, Modeling and Control of Nanopositioning Systems*. Cham: Springer International Publishing, 2014.
- [214] J. D. Adams, A. Nievergelt, B. W. Erickson, C. Yang, M. Dukic, and G. E. Fantner, "High-speed imaging upgrade for a standard sample scanning atomic force microscope using small cantilevers," *Rev. Sci. Instrum.*, vol. 85, no. 9, p. 93702, Sep. 2014.
- [215] T. Ando, "High-speed atomic force microscopy coming of age.," *Nanotechnology*, vol. 23, no. 6, p. 62001, Feb. 2012.
- [216] G. E. Fantner, G. Schitter, J. H. Kindt, T. Ivanov, K. Ivanova, R. Patel, N. Holten-Andersen, J. Adams, P. J. Thurner, I. W. Rangelow, and P. K. Hansma, "Components for high speed atomic force microscopy.," *Ultramicroscopy*, vol. 106, no. 8–9, pp. 881–7, Jan. 2006.
- [217] S. S. Aphale and S. O. Reza Moheimani, "Design, Identification, and Control of a Flexure-Based XY Stage for Fast Nanoscale Positioning," *IEEE Trans. Nanotechnol.*, vol. 8, no. 1, pp. 46–54, Jan. 2009.
- [218] S. P. Wadikhaye, Y. K. Yong, B. Bhikkaji, and S. O. Reza Moheimani, "Control of a piezoelectrically actuated high-speed serial-kinematic AFM nanopositioner," *Smart Mater. Struct.*, vol. 23, no. 2, p. 25030, Feb. 2014.
- [219] B. Dasgupta and T. S. Mruthyunjaya, "Force redundancy in parallel manipulators: theoretical and practical issues," *Mech. Mach. Theory*, vol. 33, no. 6, pp. 727–742, Aug. 1998.
- [220] R. Buchner, W. Van Der Wel, K. Habberger, and P. Seegebrecht, "Substrate-damage-free laser recrystallization of polycrystalline silicon," *Mater. Sci. Eng. B*, vol. 4, no. 1–4, pp. 197–200, Oct. 1989.

10. Appendix A

The following table elaborates the process flow to fabricate the self-sensing hybrid multilayer cantilevers. This run-card is developed for CMI facilities.

Table 10-1 The process run card to fabricate the multilayer cantilevers.

Step N°	Description	Equipment	Program / Parameters	Target	Time of Step
0	WAFER PREPARATION				
	Substrates: 100/P/DS/1-10 Si				
1	Low stress nitride, polysilicon, BSG depositon and diffusion - sensor wafer				
1.1	RCA1 clean	RCA request	H2O:NH4OH:H2O2 (5:1:1)	15min 75°C	
1.2	HF dip	RCA request	HF:H2O (1:10)	15s	
1.3	RCA2 clean	RCA request	H2O:HCl:H2O2 (6:1:1)	15min 75°C	
1.4	Fast fill rinse	RCA request		15min	
1.5	Trickle tank	RCA request		15min	
1.6	SRD	RCA request	prog 1		
1.7	Nitride deposition	RCA request	Low stress nitride	20-100 nm	
1.8	Polysilicon deposition	RCA request	polysilicion	100 nm	
1.9	BSG deposition	RCA request	Wet oxide std process	200 nm	
1.10	Diffusion	RCA request	1200 deg C 15 min		
2	Photolithography - "Backside registry"				
2.1	Surface activation / Clean	Tepla GigaBatch	3min @ 600W O2 plasma		10min
2.2	Spin on	ACS200	CMi_0104_1.1um_AZ1512_HMDS	1.1um	30min
2.3	Expose	MA6	Hard contact, CP mode	3.0s	1h
2.4	PR develop	ACS200	CMi_Dev_0904_2um_AZ1512		30min
2.5	Plade solvent	SRD	prog 1		10min
3	Oxide/poly/nitride dry etch backside registry				
3.1	Dry etch	SPTS	SiN smooth	2min45s	1h30min
3.2	Inspection	Microscope			
4	Resist strip				
4.1	O2 plasma	Tepla GigaBatch	7 min @ 600W		10min
4.2	Inspection	Microscope	Visual inspection for resist residue		
5	Photolithography - "Polysilicon"				
5.1	Surface activation	Tepla GigaBatch	1min @ 200W		
5.2	Spin on	ACS200	CMi_0145_2um_AZ9221_HMDS	2um	40min

5.3	Expose	MA6	Hard contact, CI mode	9.5s	1h15min
5.4	PR develop	ACS200	CMi_Dev_0945_2um_AZ9221		30min
5.5	Plade solvent	SRD	prog 1		10min
5.6	Inspection	Microscope	Visual inspection for pattern		
6	BSG mask dry etch				
6.1	Descum	Tepla GigaBatch	10s @ 200W		10min
6.2	Oxide dry etch	SPTS	SiO2 PR 3:1	200nm	1h30min
6.3	Inspection	Microscope	Visual inspection for pattern		
6.4	Resist strip	Tepla GigaBatch	7min @ 600W		10min
6.5	Inspection	Visual	Visual inspection for resist residue		
7	KOH wet etching of polysilicon				
7.1	HF dip	Plade Six Sigma	1% HF, 1min30sec		
7.2	FFR	Plade Six Sigma			10min
7.3	KOH Etching	Plade Six Sigma	40%, 20°C (ambient), about 6min	100nm	1h
7.4	FFR	Plade Six Sigma			10min
7.5	Neutralization	Plade Six Sigma	HCL room temp	2h	2h
7.6	FFR	Plade Six Sigma			10min
7.7	Air dry	Plade Six Sigma			half-day
8	BSG strip				
8.1	BHF oxide etch	Plade oxide	BHF clean, 10min	200nm	10min
8.2	FFR	Plade oxide			10min
8.3	Trickle tank	Plade oxide			5min
8.4	SRD	Plade oxide	prog 1		5min
9	Photolithography - "Thin metal" - thin metal for polysilicon contacting - sensor wafer				
9.1	Spin on	ACS200	0171-CMi.AZ1512onLOR.0um48	1.1um	1h30min
9.2	Expose	MA6	Hard contact, CP mode	2.0 s	
9.3	Develop	ACS200	0971-CMiDev.AZ1512onLOR.0um48		
9.4	SRD	Plade solvent	prog 1		
9.5	Descum	Tepla GigaBatch	10s @ 200W	10 s	
9.6	Inspection	Microscope	Lithography resolution and alignment		
10	Metal deposition and liftoff - thin metal for polysilicon contacting - sensor wafer				
10.1	BHF oxide etch	Plade oxide	BHF clean	1 min	
10.2	FFR	Plade oxide			
10.3	TT	Plade oxide			
10.4	SRD	Plade oxide	prog 2		
10.5	Al deposition	EVA760	450_Al_50	150 nm	
10.6	Liftoff	Plade solvent	Room temp 1165 bath overnight		
10.7	IPA rinse	Plade solvent	Isopropanol bath	2 min	
10.8	FFR	Plade solvent			
10.9	TT	Plade solvent			

10.10	SRD	Plade solvent	prog 2		
11	Photolithography - "Thick metal" - thick metal for polysilicon contacting - sensor wafer				
11.1	Spin on	ACS200	0172-CMi.AZ1512onLOR.0um82	820nm/1.1 um	
11.2	Expose	MA6	Hard contact, CP mode	3.3 s	
11.3	Develop	ACS200	0972-CMiDev.AZ1512onLOR.0um82		
11.4	SRD	Plade solvent	prog 1		
11.5	Descum	Tepla GigaBatch	strip low 10 sec	10 s	
11.6	Inspection	Microscope	Visual inspection for lithography resolution and alignment		
12	Metal deposition and liftoff - thick metal for polysilicon contacting - sensor wafer				
12.1	Al deposition	EVA760	450_Al_50	250 nm	
12.2	Liftoff	Plade solvent	Room temp 1165 bath overnight		
12.3	IPA rinse	Plade solvent	Isopropanol bath	2 min	
12.4	FFR	Plade solvent			
12.5	TT	Plade solvent			
12.6	SRD	Plade solvent	prog 1		
12.7	Inspection	Microscope	Visual inspection for resolution and alignment		
13	Photolithography - "Bond pad caps" mask - sensor wafer				
13.1	Spin on	ACS200	0172-CMi.AZ1512onLOR.0um82	820nm/1.1 um	
13.2	Expose	MA6	Hard contact, CP mode	3.3 s	
13.3	Develop	ACS200	0972-CMiDev.AZ1512onLOR.0um82		
13.4	SRD	Plade solvent	prog 1		
13.5	Descum	Tepla GigaBatch	strip low 10 sec	10 s	
13.6	Inspection	Microscope	Visual inspection for lithography resolution and alignment		
14	Metal deposition and liftoff - bond pad caps - sensor wafer				
14.1	Ti/Pt/Au deposition	EVA760	450_Ti_Pt_Au_50	50/50/150 nm	
14.2	Al deposition	EVA760	450_Al_50	100nm	
14.3	Liftoff	Plade solvent	Room temp 1165 bath overnight		
14.4	IPA rinse	Plade solvent	Isopropanol bath	2 min	
14.5	FFR	Plade solvent			
14.6	TT	Plade solvent			
14.7	SRD	Plade solvent	prog 1		
14.8	Inspection	Microscope	Visual inspection for resolution and alignment		
15	Resistance measurement				
15.1	Measurement	PM8	2 point resistance (in TP micro folder)		
16	BCB coating and bonding				
16.1	Surface activation	Tepla	strip high 3min 500rpm for 10s & 3000rpm for 30s (w/ N2)		
16.2	BCB primer coating	Wet bench			
16.3	BCB coating	RC8 mid zone	700rpm for 9s & 4000rpm for 30s		
16.4	BCB pre-baking 1	RC8 mid zone	80s @80°C		

16.5	BCB pre-baking 2	RC8 entrance zone	20min@150°C		
16.6	Relaxation	in wafer box	1-2h minimum		
16.7	BCB bonding	SB6	prog Operic_BCB-final / G_T220_340		
16.8	Relaxation	in wafer box	overnight		
16.9	BCB hard baking	Heraeus T6060	30min ramp to 250°C + 1h @250°C (+ down ramp to RT)		2h
17	Photolithography - chip body openings on sensor wafer				
17.1	Surface activation	Tepla	Strip high 1 min (GigaBatch)		
17.2	Spin on	SSE SB20	AZ1512HS, STD-4000-RPM	1.3 um	
17.3	PR bake	SSE SB20	100°C on hotplate	1 min	
17.4	Expose	MA6	Hard contact, CP mode	2.1 s	
17.5	PR develop	Develop bench	MFC26	30 sec	
17.6	DI Rinse	Develop bench			
17.7	N2 dry	Develop bench			
17.8	Inspection	Microscope			
18	Dry etch - chip body openings on sensor wafer				
18.1	Poly/LSNT dry etch	SPTS	Si3N4 Smooth		
18.2	Inspection	Z2/microscope			
18.3	O2 plasma	Tepla GigaBatch	Strip high 7 min @ 600W		
18.4	Inspection	Visual	Visual inspection for resist residue		
19	Dry etch - opening on complementary wafer				
19.1	Nitride dry etch	SPTS	SiO2 PR 3:1		
19.2	Inspection	Visual			
20	KOH wet etching - Si bulk removal and membrane release				
20.1	KOH Etching	Plade Six Sigma	40%, 60°C, control density to 1.37 at 60°C	380 um	
20.2	FFR	Plade Six Sigma			
20.3	Neutralization	Plade Six Sigma	HCL room temp	2h	
20.4	FFR	Plade Six Sigma			
20.5	Air dry	Plade Six Sigma		3h	
21	Aluminum deposition				
21.1	Etch stop Al coating	EVA760	250_Al_160	2 um	1h30m
21.2	Hard mask Al coating	EVA760	450_Al_50	300 nm	1h
22	Photolithography - onto top side				
22.1	Surface activation	SSE SB20	Dehydration, 105°	5 min	
22.2	Spin on	SSE SB20	AZ1512, STD-4000-RPM	1.3 um	
22.3	PR bake	SSE SB20	105 °C on hotplate	1 min	
22.4	Expose	MJB4		2.5 s	
22.5	PR develop	Develop bench	AZ developer	40 s	
22.6	DI Rinse	Develop bench			
22.7	air dry	Develop bench			
22.8	Inspection	Microscope			

23	Aluminum wet etch (3min in ANP)				
23.1	Alu wet etch	Plade metal	ANP 35 degrees	300 nm	
23.2	DI rinse	Plade metal	TT only, or manual beaker rinse	3 times	
23.3	Air dry	Plade metal			
24	Dry etch - sandwich etch for cantilever shape definition				
24.1	Nitride dry etch	SPTS	LBNI-BCB custom process	100 nm	
24.2	BCB dry etch	SPTS	LBNI-BCB custom process	4-8 um	
24.3	Nitride dry etch	SPTS	LBNI-BCB custom process	100 nm	
25	Aluminum wet etch				
25.1	Alu wet etch	Plade metal	ANP 35 degrees	2 um	
25.2	DI rinse	Plade metal	TT only, or manual beaker rinse	3 times	
25.3	Air dry	Plade metal			
26	Metal reflective coating deposition				
26.1	Ti/Au evap	EVA760 or DP650	450-lift-off_Ti-Au_50-50 / RTU_Ti-Au	5 nm/20 nm	
26.2	Inspection	SEM Merlin			

11. Appendix B

(12) INTERNATIONAL APPLICATION PUBLISHED UNDER THE PATENT COOPERATION TREATY (PCT)

(19) World Intellectual Property
Organization
International Bureau

(43) International Publication Date
1 December 2016 (01.12.2016)



(10) International Publication Number
WO 2016/189451 A1

- (51) International Patent Classification:
G01Q 60/38 (2010.01) *B81C 1/00* (2006.01)
B81B 3/00 (2006.01) *G01Q 70/14* (2010.01)
- (21) International Application Number: PCT/IB2016/053013
- (22) International Filing Date: 23 May 2016 (23.05.2016)
- (25) Filing Language: English
- (26) Publication Language: English
- (30) Priority Data: PCT/IB2015/053769 22 May 2015 (22.05.2015) IB
- (71) Applicant: **ECOLE POLYTECHNIQUE FEDERALE DE LAUSANNE (EPFL)** [CH/CH]; EPFL Innovation Park J, 1015 Lausanne (CH).
- (72) Inventors: **FANTNER, Georg Ernest**; Allée du Tilleul 2/52, 1022 Chavannes-renens (CH). **ADAMS, Jonathan David**; Chemin du Levant 14, 1005 Lausanne (CH). **HOSSEINI, Nahid**; Avenue du Tir-Fédéral 48, 1024 Ecublens (CH).
- (74) Agent: **BYRNE, Declan**; c/o Andre Roland S.A., P.O. Box 5107, 1002 Lausanne (CH).
- (81) Designated States (unless otherwise indicated, for every kind of national protection available): AE, AG, AL, AM, AO, AT, AU, AZ, BA, BB, BG, BH, BN, BR, BW, BY, BZ, CA, CH, CL, CN, CO, CR, CU, CZ, DE, DK, DM, DO, DZ, EC, EE, EG, ES, FI, GB, GD, GE, GH, GM, GT, HN, HR, HU, ID, IL, IN, IR, IS, JP, KE, KG, KN, KP, KR, KZ, LA, LC, LK, LR, LS, LU, LY, MA, MD, ME, MG, MK, MN, MW, MX, MY, MZ, NA, NG, NI, NO, NZ, OM, PA, PE, PG, PH, PL, PT, QA, RO, RS, RU, RW, SA, SC, SD, SE, SG, SK, SL, SM, ST, SV, SY, TH, TJ, TM, TN, TR, TT, TZ, UA, UG, US, UZ, VC, VN, ZA, ZM, ZW.
- (84) Designated States (unless otherwise indicated, for every kind of regional protection available): ARIPO (BW, GH, GM, KE, LR, LS, MW, MZ, NA, RW, SD, SL, ST, SZ, TZ, UG, ZM, ZW), Eurasian (AM, AZ, BY, KG, KZ, RU, TJ, TM), European (AL, AT, BE, BG, CH, CY, CZ, DE, DK, EE, ES, FI, FR, GB, GR, HR, HU, IE, IS, IT, LT, LU, LV, MC, MK, MT, NL, NO, PL, PT, RO, RS, SE, SI, SK, SM, TR), OAPI (BF, BJ, CF, CG, CI, CM, GA, GN, GQ, GW, KM, ML, MR, NE, SN, TD, TG).

[Continued on next page]

(54) Title: MULTILAYER MEMS CANTILEVERS

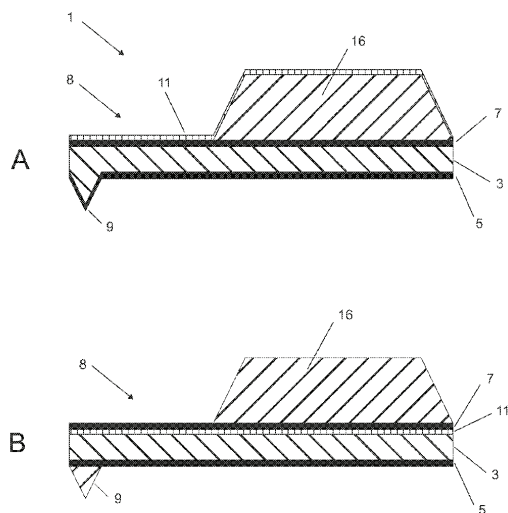


Figure 4a

(57) Abstract: The present invention relates to a cantilever or membrane comprising a body and an elongated beam attached to the body. The elongated beam includes a first layer comprising a first material, a second layer comprising a second material having an elastic modulus different to that of the first material, a third layer comprising a third material having an elastic modulus different to that of the first material, where the first layer is sandwiched between the second layer and the third layer.

MULTILAYER MEMS CANTILEVER

CROSS-REFERENCE TO RELATED APPLICATIONS

The present application claims the priority of international PCT Application PCT/IB2015/053769 that was filed on May 22nd 2015, the entire contents thereof being herewith incorporated by reference.

5 FIELD OF THE INVENTION

The present application generally relates to a cantilever or membrane, and more particularly a multilayer ATM cantilever or membrane. The present application also concerns a method for producing an elongated beam of the cantilever or membrane as well as a method for producing a cantilever or membrane.

10 DISCUSSION OF THE BACKGROUND ART

High bandwidth AFM cantilevers for operation in air or vacuum

In comparison with other AFM (atomic force microscopy) imaging modes, increasing the imaging speed of AFM in dynamic modes in air or vacuum has proven especially difficult. These dynamic modes include non-contact AFM, intermittent contact AFM (tapping mode), and pulsed force or peak force modes. The reason for this difficulty is the slow dynamic response of the cantilever oscillation amplitude. When subject to a change in boundary condition, the transient response of the cantilever decays with a time constant related to its resonance frequency, f_0 , and quality factor, Q . This time constant directly impacts the imaging bandwidth, B , of the cantilever, which is a measure of how quickly the AFM cantilever can track surface topography changes. For example, in tapping mode, in the case of a linear tip sample interaction and a cantilever driven at resonance, B takes the numerical value $B = \pi f_0 / Q$.

The row marked "Low f_0 , high Q " of Figure 1 shows on the left a schematic of a driven oscillating cantilever with a steady state oscillation amplitude subject to a sudden increase in tip-sample distance. After some time, the cantilever reaches a new steady-state oscillation amplitude according to the new boundary conditions. The response time is linked to the cantilever resonance frequency and Q -factor, which are represented in the amplitude versus frequency drawing. Immediately to the right, we see experimental data of the deflection response time of a typical tapping-mode-in-air AFM cantilever (RTESPA, Bruker AFM Probes) subject to a sudden step increase in the drive amplitude. The corresponding resonance frequency and quality factor were measured for this cantilever with the thermal tune method. The numerical values, $f_0 = 347$ kHz and $Q = 500$, yield a response time of order one millisecond, and a corresponding imaging bandwidth of order 1 kHz. Finally, on the right, we see an SEM image of the cantilever showing its dimensions.

Thus far, efforts to increase the cantilever bandwidth have focused on increasing the resonance frequency by reducing the cantilever dimensions (so called 'small cantilevers'). This approach, shown in the row marked "High f_0 , high Q " in Figure 1, has by and large been the enabling technology for state of the art high-speed AFM, producing good-quality, high-speed images even on difficult biological samples.

The higher resonance frequency reduces the response time, even with largely unchanged Q , as shown schematically on the left and experimentally on the right of the second row in Figure 1 using a commercially-available small cantilever (FastScan A, Bruker AFM Probes). Cantilevers with widths

approaching the optical diffraction limit and lengths of a few micrometres are now usable in specialized high-speed AFMs.

- 5 The fastest AFM imaging in dynamic modes has been, however, uniformly performed in a liquid environment, where the Q of the cantilever is decreased substantially by the large amount of fluid damping in liquid (in fluid, most AFM cantilevers have $Q \approx 3$). However, reaching equivalent speed performance using dynamic modes in air or vacuum, where the fluid damping is substantially lower, has yet to be shown.

- 10 The work of the inventors leading to this invention has focused on an alternate cantilever construction approach to enable cantilevers with inherently low Q . Intrinsically, Q is related to the damping of the resonator. Sources of damping include fluid (air or water), mechanical clamping losses, and internal friction --- which includes both surface effects and volume effects such as thermoelastic damping or viscoelastic damping. Each of these sources contribute to the overall Q of the system, which can be expressed as a combination of the Q_i associated with each individual damping source:

$$\frac{1}{Q} = \sum \frac{1}{Q_i} = \frac{1}{Q_{medium}} + \frac{1}{Q_{material}} + \frac{1}{Q_{support}} + \dots$$

- 15 Optimizing the cantilever bandwidth through Q reduction therefore translates in practice to increasing the damping mechanisms present in the system.

- AFM cantilevers that are commercially available are made out of materials with low intrinsic damping, such as crystalline silicon or silicon nitride. The intrinsic damping coefficient (or loss coefficient) of a material η_i is defined as the ratio of the imaginary component of the dynamic modulus E'' to the real component of the dynamic modulus E' , $\eta_i = \frac{E''}{E'}$. Figure 2 shows some potential cantilever materials classified by their intrinsic damping coefficient on the horizontal axis, and the square root of the ratio of the elastic modulus E to the density ρ , $\sqrt{E/\rho}$, on the vertical axis. This factor E/ρ is also known as the stiffness to weight ratio. Here, the square root in this ratio $\sqrt{E/\rho}$ comes from the expression for the fundamental resonance frequency of a cantilever beam $f_0 = \frac{0.56}{l^2} \sqrt{\frac{I}{A}} \sqrt{\frac{E}{\rho}}$ factored into geometrical and materials properties terms. In the expression, l is the cantilever length, I is the second moment of area and A is the cross-sectional area of the cantilever beam. Three different classes of materials are given: crystalline or ceramic materials, metals, and polymers or elastomers. The dashed lines show constant values of the product $\eta_i \sqrt{E/\rho}$, which is a measure of the bandwidth ratio f_0/Q expressed in terms of materials properties. Higher values trend towards the upper left corner of the plot. By this metric, the polymers and elastomers as a class of material are roughly 3 orders of magnitude better than the crystals and ceramics.
- 25 materials properties terms. In the expression, l is the cantilever length, I is the second moment of area and A is the cross-sectional area of the cantilever beam. Three different classes of materials are given: crystalline or ceramic materials, metals, and polymers or elastomers. The dashed lines show constant values of the product $\eta_i \sqrt{E/\rho}$, which is a measure of the bandwidth ratio f_0/Q expressed in terms of materials properties. Higher values trend towards the upper left corner of the plot. By this metric, the polymers and elastomers as a class of material are roughly 3 orders of magnitude better than the crystals and ceramics.
- 30

For cantilevers made of materials with very low damping coefficient, such as silicon or silicon nitride, the primary damping source is thus the air damping, which leads to cantilever with $Q \approx 500$ in air as shown in the row marked "Low f_0 , high Q " of Figure 1.

- 35 If the cantilever is made out of a material that exhibits large intrinsic damping, the material damping dominates the cantilever response. The total number of oscillation cycles needed to reach steady state in this case is decreased, and so the response time is decreased, even though the frequency of oscillation may be unchanged.

Of the various classes of materials that can be used to microfabricate cantilevers, polymers in particular can exhibit large intrinsic damping through viscoelastic effects, making them ideal materials for this application. Shown in the row “Low f_0 , low Q ” in Figure 1 is a cantilever designed to maintain similar resonance frequency and spring constant as a standard tapping mode in air cantilever, but with a drastically lower Q . The cantilever is made out of a photosensitive polymer (SU-8), which has previously been demonstrated as a promising low-cost, low spring constant cantilever microfabrication material for both AFM imaging and cantilever-based biosensing. The experimental data show that the cantilever, which has a $Q = 21$, has a similar response to a change in boundary condition to the commercial small cantilever (row marked “High f_0 , high Q ” of Figure 1), even though the size and resonance frequency of the SU-8 cantilever is comparable to a standard cantilever (and is useable in standard AFM systems).

These two approaches, high resonance frequency and low quality factor, can be combined by reducing the dimensions of the cantilever and making a small cantilever out of a viscoelastic material. The row marked “High f_0 , low Q ” in Figure 1 illustrates this combination. The resulting cantilever, which has a resonance frequency similar to the commercial small cantilever and a Q similar to the large SU-8 cantilever, has a response time that appears almost instantaneous on the timescale shown.

The inventors performed high-speed AFM imaging using these small SU-8 cantilevers in a customized AFM for high-speed operation. The scratched mica surface we imaged has sharp step edges, which are a difficult feature for topography feedback.

Figure 3a shows images of the same imaging area at line scan rates from 43 Hz up to 166 Hz. The highest scan rate corresponds to scan speeds in excess of 1 image/s and a linear tip speed over the surface of 1953 $\mu\text{m/s}$. The height images (left of Figure 3a) appear identical at all scan rates, apart from more pixelation at higher speed due to system data-rate limits. Notable in the amplitude error images (right of Figure 3a) is the absence of imaging artefacts such as overshoot, parachuting or ringing. Taken together, these images show good tracking behaviour even at the highest scan rates.

Faster AFM imaging also enables the ability to take a high-resolution overview image and digitally investigate regions at higher magnification. This task presents a challenge to AFM systems because at large scan areas, the surface speed remains high even for low line scan rates. As a demonstration of how the SU-8 cantilevers enable this feature, large areas of a Celgard sample were imaged.

Celgard is a standard sample for assessing the speed performance of AFM imaging due to the challenge of tracking the freely-suspended fibrils in the material. On a standard MultiMode AFM system using large SU-8 cantilevers, we found that we could image Celgard with acceptable quality at line scan rates of 10 Hz, corresponding to a tip velocity of 100 $\mu\text{m/s}$. At this scan rate, the large silicon cantilever tracked very poorly and was unable to resolve the fibrils at all. On an unmodified commercial high-speed AFM system (FastScan, Bruker Nano Surfaces) we used our small SU-8 cantilevers to scan a 30 \times 30 μm area of Celgard at a line scan rate of 4 Hz at 8192 \times 3200 pixels, corresponding to a surface speed of 261 $\mu\text{m/s}$ (Figure 3b upper left image).

In comparison, the highest previously reported surface scan speeds we were able to find regarding Celgard using standard small AFM cantilevers was 56 $\mu\text{m/s}$. The upper right part of Figure 3b presents a 2.4 μm digital zoom of the overall image corresponding to 656 \times 256 pixels, showing the individual fibrils of the Celgard are still well resolved. The amplitude error and phase images in Figure 3b show further evidence that the AFM tracks the surface well.

Electronic readout of AFM cantilevers

The optical beam detection technique is the most common method to detect the deflection of AFM cantilevers. It is easily implemented and very sensitive, however it requires a number of components, such as lasers, objectives, and photodetectors, which require both space and the ability to align them with the cantilever. Furthermore, optical diffraction sets the minimum width of the cantilever to a practical lower limit of about 2 μm . For these reasons, there has been much interest in the development of cantilevers with integrated deflection sensing elements (so-called self-sensing cantilevers). Cantilevers using resistive or piezoresistive, piezoelectric, thermal and capacitive detection techniques have been developed. Thus far, the performance of the current self-sensing cantilevers still lags behind the optical beam detection performance, and so these cantilevers are generally only used in situations where having optical beam detection is not possible.

SUMMARY

The present invention addresses the inconveniences and problems of the background art and concerns a cantilever or membrane according to claim 1, an Atomic force microscope, molecule detector, biosensor or multi-cantilever array including at least one such cantilever or membrane. The present application also concerns a method for producing an elongated beam of the cantilever or membrane according to claim 24 as well as a method for producing a cantilever or membrane according to claim 28.

Other advantageous features can be found in the dependent claims.

BRIEF DESCRIPTION OF THE FIGURES

The above object, features and other advantages of the present invention will be best understood from the following detailed description in conjunction with the accompanying drawings, in which:

Figure 1 is a Schematic of the transient response of a cantilever and its relation to the resonance frequency and quality factor, a standard AFM cantilever (top row) has a low resonance frequency and high Q; experimentally, this leads to a long amplitude response time; small cantilevers designed for high-speed imaging have thus far focused on increasing the resonance frequency only (second row), which decreases the response time but requires special instrumentation for use of the cantilevers; alternately, lowering the Q of the cantilever by using a cantilever material with inherent dampening characteristics can yield a similar benefit without the need to reduce the cantilever dimensions (3rd row); a high resonance frequency, low Q cantilever optimized for short response time can be created by reducing the dimensions of the large, low Q cantilever (bottom row);

Figure 2 shows potential cantilever materials, classified according to the square root of the stiffness to weight ratio $\sqrt{E/\rho}$ and the intrinsic loss coefficient η_i ;

Figure 3 shows HS-AFM AM-mode imaging in air using small SU-8 cantilevers where a) shows imaging of sharp step edges in sanded mica, the maximum scan rate achieves over 1 frame per second while maintaining good surface tracking; and b) shows a high-resolution overview imaging of a Celgard sample at a tip surface speed of 261 $\mu\text{m/s}$, 6 times faster than previous reports, the overview image is 8192x3200 pixels and the digital zoom-ins are 656x256 pixels;

Figures 4a and 4b show a cantilever structure according to an aspect of the present invention, where A and B show a schematic of the cantilever architecture for optical deflection readout, the most critical

- aspect is the multilaminar nature of a thick core separating outer layers with higher elastic modulus, the tip may be integrated in the outer layer or adhered to that layer, an optically-reflective layer may be included on an outer or inner layer (or multiple layers); where C to E show three possible architectures of the cantilever for self-sensing deflection detection; the strain sensing element is integrated onto an
- 5 outer layer, the strain sensor can either be a strain-sensing material deposited over a portion of the cantilever (C) or a full layer of a strain-sensing material (D); the strain-sensing element is preferably located as far as possible from the neutral axis, and can either be shielded from the outer surface of the cantilever such that it is inherently protected from the outside environment (C) or exposed to the environment when shielding is unnecessary (E);
- 10 Figure 5 presents the influence of the elastic modulus of the core layer on the mechanical properties and resonance behaviour of the cantilever;
- Figures 6a and 6b: illustrate, according to another aspect of the invention, a basic process flow for fabrication of the cantilever with core separating outer layers with higher elastic modulus;
- Figure 7a is an Image of a fabricated cantilever;
- 15 Figure 7b presents a Frequency spectrum of several fabricated cantilevers, where the upper numbers refer to the nominal planar dimensions of the cantilever;
- Figure 7c is an image of a $1 \times 1 \mu\text{m}$, 200 nm depth calibration grating taken with a fabricated cantilever;
- Figure 7d presents a measurement of the tapping-mode imaging bandwidth for a cantilever with $f_0 = 392 \text{ kHz}$, $k=24 \text{ N/m}$ and $Q=73$, the bandwidth defined at the -3 dB point corresponds to 11 kHz;
- 20 Figures 8a and 8b present an overview of a cantilever fabrication process incorporating a batch-fabricated silicon nitride sharp tip according to another aspect of the present invention;
- Figures 9a and 9b shows an approach towards integration of self-sensing elements into the cantilever fabrication process according to yet another aspect of the present invention;
- 25 Figures 10a and 10b illustrate a fabrication process towards integration of self-sensing elements onto an external surface of the cantilever according to another aspect of the present invention;
- Figures 11a and 11b show a fabrication process towards integration of self-sensing elements onto both upper and lower internal surfaces of the cantilever according to yet another aspect of the present invention;
- 30 Figures 12a and 12b illustrate a fabrication process towards integration of a sharp silicon tip into a self-sensing cantilever according to further aspect of the present invention;
- Figures 13a and 13b illustrate a fabrication process towards a self-sensing cantilever with of piezoelectric self-sensing elements according to yet another aspect of the present invention;
- Figures 14a and 14b illustrate a fabrication process for a membrane-based multilayer device according to yet another aspect of the present invention;
- 35 Figures 14c illustrates a plurality of different membranes having different forms, such as a doubly-clamped beam, a crossed beam, or a full membrane;

Figure 15 shows an alternate configuration for a composite sandwich cantilever, a layer of high elastic modulus forms the core of the cantilever, with layers of low elastic modulus and high loss coefficient surrounding this core;

5 Figures 16a and 16b show a fabrication process for tip integration into the alternate cantilever configuration of Figure 15;

Figures 17a, 17b, 17c and 17d show a process for fabrication a cantilever using a layer-by-layer process according to yet another aspect of the present invention; and

Figure 18 illustrates a process for cantilever fabrication using a layer-by-layer process with integrated tip according to further another aspect of the present invention.

10 DETAILED DESCRIPTION OF THE INVENTION

The present disclosure may be more readily understood by reference to the following detailed description presented in connection with the accompanying drawing figures, which form a part of this disclosure. It is to be understood that this disclosure is not limited to the specific conditions or parameters described and/or shown herein, and that the terminology used herein is for the purpose of
15 describing particular embodiments by way of example only and is not intended to be limiting of the claimed disclosure.

Motivating factors

The concept of material damping for high bandwidth AFM probes is demonstrated with a prototype SU-8 cantilevers. This probe architecture, however, has some limitations:

- 20 • SU-8 and other polymers are poor materials for making sharp and wear-resistant tips. Although reasonably sharp tips can be made via molding, the tips suffer from very high wear rates and blunt quickly. In contrast, according to the present invention, the tip can be made out of much harder materials such as silicon or silicon nitride, two materials that are used commercially to make good quality tips for AFM imaging.
- 25 • SU-8 and other polymers are poor materials for the chip body (to which the cantilever is fixed). Resonances of the chip structure near or below the cantilever resonance lead to loss of drive efficiency and an unclear drive signal when using a piezo to excite the cantilever. A polymer chip body has resonances at lower frequency than a silicon chip body of the same dimensions. Given the industry has adopted a set of standard chip body dimensions, compensating the poor
30 performance of a polymer chip body by changing the dimensions is not easily achievable.

Furthermore, for self-sensing cantilevers, the limitations of current self-sensing architectures are noted as well as the use of a relatively soft material such as a polymer for a self-sensing cantilever:

- The signal of the self-sensing cantilever is directly related to the distance the sensor is located away from the neutral axis of the cantilever. For cantilevers made from hard materials, however,
35 increasing the thickness quickly leads to an unusably stiff cantilever.
- A common requirement in self-sensing cantilevers is that the cantilever is able to operate in liquid. In traditional cantilever designs, this often means that a thick protective coating over the strain sensing element is applied, which leads to difficulty with tip integration and negatively impacts the sensitivity through a shift in the neutral axis.

- Adding a strain sensor onto a cantilever can perturb the behaviour of the cantilever, which locally can experience a reduction in strain around the sensing element; thus, making a self-sensing cantilever out of a soft material and adding on a stiff strain-sensing element can reduce the expected signal based on the geometry of the designed cantilever.

5 Major features and aspects of the cantilever architecture according to the present invention
 In order to both optimize the ratio f_0/Q and to overcome the issues described above, one aspect of the present invention concerns a composite, multilayered cantilever structure that includes layers of high loss coefficient (but low elastic modulus and low density) with layers of high elastic modulus (but high density and low loss coefficient). Here, high loss coefficient refers to values above 10^{-2} , high elastic modulus refers to values above 10 GPa, and high density refers to values about 1500 kg/m³. Suitable methods for measuring elastic modulus of thin layers include methods such as nanoindentation (see for example reference 26), bulge testing (see for example reference 27), or microbeam deflection (see for example reference 28). Measurement of intrinsic loss coefficient may be performed using dynamic mechanical analysis or nanoindentation (see for example reference 29), or using a reference beam coated with the material of interest, as in ASTM E756 and also applied to microscale systems (see for example reference 30). This architecture of the present invention has a number of benefits to the issues described above, including:

- In air and vacuum, the quality factor of the cantilever will be substantially determined by the material properties of the layer(s) with high loss modulus.
- The layer(s) of high elastic modulus provide a suitable support for tip and/or strain-sensor integration. In certain cases, these layers could be themselves a multi-lamellar structure.

In one embodiment of the invention, the cantilever is made up of a three layer structure, with an inner core made up of a layer with high loss modulus sandwiched between two layers of high elastic modulus. This embodiment has a number of advantages compared with cantilevers made of a uniform material:

- The structure is overall substantially symmetric, which reduces thermally-induced or residual stress-induced bending of the cantilever. However, if an asymmetry is desirable, the structure may be also made intentionally asymmetric.
- Strain-sensing elements can be integrated within the multilayer structure, inherently protected from the outside environment.
- The distance of the strain sensor from the neutral axis can be increased relative to a uniform cantilever, without increasing the spring constant of the cantilever.
- The cantilever performance metric f_0^2/k may be increased. For equivalent cantilever spring constant, the cantilever can have a higher resonance frequency than a cantilever made out of a uniform material while maintaining the same spring constant. This result is achieved by reducing the mass of the cantilever in the core, where the elastic modulus has less influence on the bending stiffness of the cantilever.

Part A of Figure 4a shows a schematic of an exemplary multilayer cantilever design intended for optical deflection readout and the major features of this design. The cantilever 1 maintains a core 3 substantially made up of a material with high loss coefficient, sandwiched between two layers 5, 7 of high elastic modulus. The core 3 and the two outer layers 5, 7 form a beam 8 of the cantilever. A tip 9 is

integrated into the lower layer 5 (in this depicted embodiment, the tip is made via moulding the hard material in a pit with a sharp point).

A thin metal layer 11 can be deposited on the outside of the upper cantilever surface 15 to provide an optically reflective surface.

- 5 The cantilever further includes body 16 for supporting the beam 8.

An alternative embodiment, shown in part B of Figure 4a, comprises the trilayer structure with the optically-reflective coating on the interior surface 17 of the upper layer 11, and a sharp tip 19 made of a different hard material (such as silicon) to that of layers 5, 7 and that is attached to the outer surface of the lower layer 5. A second metal coating can be applied to the top or bottom side of layer 5. Any such combination can be performed with either a moulded tip or an attached tip.

- 10

Figure 4b shows three different embodiments for integrating self-sensing elements into the trilayer cantilever. A self-sensing cantilever needs to maximize the strain at the base of the cantilever, without making the cantilever undesirably stiff.

Part C of Figure 4b shows a self-sensing cantilever where the strain sensor 21 is deposited over only a small portion of the cantilever. This strain sensor 21 could be metal traces, a piezoresistive material like doped crystalline silicon or polysilicon or a nanogranular metal or a 2D material like graphene or molybdenum disulfide, and could be deposited as a full or partial layer and subsequently patterned via lithography, or deposited via a direct-write technique like electron beam-induced deposition. This sensor 21 can be deposited onto an inner surface 33 of the upper layer 7 such that it is located within the multilayer structure and hence inherently protected from the outside environment.

- 15

- 20

Part D of Figure 4b shows a full-layer strain sensor, as would be implemented for piezoelectric materials like for example aluminum nitride or lead zirconate titanate (PZT). In this implementation, the strain sensor layer 21 is itself sandwiched between two electrically conducting contact layers 23, 25, and an upper layer 7 that provides a substrate on which the layer 7 attaches to a chip body 16 and also shields the upper metal contact layer 23 from the outside environment. This multi-layer structure comprising or consisting of layers 23 and 7 forms the upper layer with high elastic modulus 31 of the trilayer structure. The lower layer of high elastic modulus 5 may be a simple single layer of silicon nitride or other material, in which a tip 9 is integrated or attached to. Access to bonding pads 37 could be made by etching at appropriate points through the multilayer structure, stopping on the conducting layers.

- 25

Part E of Figure 4b shows a self-sensing cantilever similar to that of parts C or D of Figure 4b, except the strain sensor is located on the outer surface 41 of the multilayer structure. For use in environments where the strain sensor and contact traces do not need to be shielded, this can provide an additional route to fabrication and the benefit that the strain sensor 21 is located further from the neutral axis of the cantilever. The strain sensor 21 in this implementation could be made of the same material as described above in part C of Figure 4b or with a piezoelectric layer as shown in part D of Figure 4b.

- 30

- 35

The present invention thus relates to a cantilever comprising the body 16 and the elongated beam 8 attached to the body 16. The elongated beam 8 includes a first layer 3 comprising a first material, a second layer 5 comprising a second material having an elastic modulus different to that of the first material, and a third layer 7 comprising a third material having an elastic modulus different to that of the first material. The first layer 3 is sandwiched between the second layer 5 and the third layer 7.

- 40

The first material can have an elastic modulus inferior to that of the second and third material; and/or the first material can have a loss coefficient superior to that of the second and third material; and/or the first material can have a density inferior to that of the second and third material.

- 5 The first material may have an elastic modulus superior to that of the second and third material; and/or the first material may have a loss coefficient inferior to that of the second and third material.

The first material can be a viscoelastic material.

- 10 The second layer 5 and the third layer 7 may have a smaller layer thickness than that of the first layer 3.

- 15 The cantilever may include the optically reflective layer 11 for determining movement of the cantilever and the optically reflective layer 11 can be deposited on the first layer or is sandwiched between the first layer 3 and the second layer 7. The optically reflective layer 11 can be deposited on an inner or outer surface of the first or second layer.

- 20 The beam 8 can include the sensing tip 9, 19 formed by the second layer 5, or formed of a material different to that of the second 5 and third 7 layers. The beam 8 can also include the sensing element 21 to detect the deflection of the beam 8. The sensing tip can be integrated into or be integral with the second layer 5.

The sensing element 21 can extend substantially along a full length of the beam 8. The sensing element 21 may alternatively extend partially along a length of the beam 8.

- 25 The cantilever can include a first 23 and a second 25 metal layer sandwiching the sensing element 21 to measure a deflection of the beam 8.

- 30 The first metal layer 23 can be located between the sensing element 21 and the third layer 7, and the second metal layer 25 can be located between the sensing element 21 and the first layer 3.

- The cantilever can further include a first metal layer 23 contacting a first portion of the sensing element 21 and a second metal layer 25 contacting a second portion of the sensing element 21 to measure a deflection of the beam 8.

- 35 The sensing element 21 and the first 23 and second 25 metal layers can be attached to the third layer 7.

The sensing element 21 and the first 23 and second 25 metal layers may be attached to an inner surface 33 of the third layer 7.

- 40 The sensing element 21 and the first 23 and second 25 metal layers may alternatively be attached to the second layer 5. The sensing element 21 and the first 23) and second 25 metal layers are attached to an outer surface 41 of the second layer 5.

- 45 According to another aspect of the present invention, a method for producing the elongated beam 8 of the cantilever comprises the steps of providing the first layer 3 comprising a first material, providing the second layer 5 comprising a second material having an elastic modulus different to that of the first material, providing a third layer 7 comprising the third material having an elastic modulus different to that of the first material, and enclosing the first layer 3 between the second layer 5 and the third layer 7.

Targeted application of the invention and extension to other domains

Atomic force microscopy is one exemplary targeted application area of this cantilever structure according to the present invention, specifically imaging using dynamic modes (such as tapping mode or peak force tapping), however the architecture may find wide use in other application areas. For example, in cantilever-based or membrane-based detection of small molecules. Using the self-sensing architecture, one can create a multi-cantilever array structure or membrane structure, such as those used in biosensing applications (see for example reference 31), without the need for a cumbersome multi-cantilever optical readout system. Another technological extension is to introduce microfluidic channels within the polymer layer 3. This can, for example, enable cantilever-based liquid or cell dispensing, biomolecule detection or other types of applications.

The first layer 3 may thus include a microfluidic channel.

According to another aspect, the present invention relates to an atomic force microscope, a molecule detector, a biosensor, or multi-cantilever array including at least one such cantilever.

Influence of core layer mechanical properties

Materials suitable for use as the core layer in the exemplary cantilevers described above may span a wide range of elastic modulus. For example, Polydimethylsiloxane PDMS has a lower elastic modulus of order 10^6 Pa, and SU-8 can have an elastic modulus of nearly 10^{10} Pa. Incorporating these different polymers into the central layer 3 of the cantilever can have significant influence on the overall mechanical properties of the cantilever.

Figure 5 shows the variation in expected spring constant and resonance frequency for a 100 μm long cantilever with 500 nm silicon nitride outer layers and a 5 μm thickness polymer layer with a varying elastic modulus, based on a 2D FEM simulation (Comsol). As the elastic modulus is varied over 8 orders of magnitude, the spring constant varies by 4 orders of magnitude and the resonance frequency by 2 orders of magnitude (Figure 5(a)). In addition, the resonance mode shape changes from a shearing motion at low elastic modulus, to a complex hybrid motion at a mid-range elastic modulus to a bending motion similar to a uniform beam at high elastic modulus.

This variation lends a large capacity for tuning cantilever mechanical properties to achieve a desired behaviour. In particular, a low elastic modulus polymer would be suitable for softer, optically-detected cantilevers (the stress on the outer layers remains low in the shearing mode). A higher elastic modulus would be desirable for a self-sensing cantilever or a stiffer, optically-detected cantilever.

Cantilever fabrication and performance evaluation

The outline of a process flow that has been successfully implemented according to another aspect of the present invention is shown in Figures 6a and 6b. This process is only one approach towards achieving the desired end structure. This process is designed for cantilevers to be used with optical deflection detection, hence there is no integration of a strain sensing element into the structure.

It is noted that one novel aspect of this process flow is the use of two separate wafers that are bonded together using the polymer layer. Other processes have used two wafers along with wafer bonding (including polymer wafer bonding) in the fabrication process, however one important difference with the process of the present invention is that elements of both wafers form an integral component of the

cantilever. In this manner, the structure of the hard outer layers, including processing of the tip structure and processing of the strain-sensing element, in the case of a self-sensing cantilever, could proceed independently on standard wafers before being combined into a multilayer sandwich structure.

As shown in Figures 6a and 6b, in step A, layers **47c** and **47d** are grown or deposited or doped on the top and bottom surface of a silicon wafers **43b**. The same step is performed on second similar wafer. Preferred materials for layers **47c** and **47d** are silicon dioxide or silicon nitride; other options could be doped silicon, polysilicon, gallium nitride, silicon carbide, tungsten carbide, titanium dioxide, a metal like tungsten, etc. The range of thickness for these layers could be from 10 nm up to about 2 μm . The range of elastic modulus of this layer could be from 10 GPa up to 600 GPa. Suitable deposition processes include CVD, MBE, sputtering, thermal oxidation, ALD, etc. The current process uses low-stress silicon nitride with thickness of 100 nm, deposited by LPCVD. The elastic modulus of this material is approximately 250 GPa.

In step B, by way of layer **45**, bond together wafers **43a** and **43b**. The thickness of layer **45** ranges from about 100 nm up to 20 μm . Layer **45** is ideally a polymer with elastic modulus in the range from about 0.5 MPa up to about 10 GPa, and intrinsic loss coefficient greater than 10^{-2} . Layer **45** could be deposited using processes like CVD, spin-coating, spray coating, screen printing, or transfer printing, etc. The deposition could be onto layer **47a**, layer **47c**, or partially on layer **47a** and partially on layer **47b**. Suitable polymers include parylene, polyimide, PDMS, SU-8, BCB, polyurethane, and many others. The current process uses parylene-C deposited by CVD with 2 μm thickness deposited onto both layers **47a** and **47c**. The elastic modulus of parylene-C is about 2.8 GPa and density about 1289 kg/m³. An adhesion promoter may be necessary to enhance adhesion of the polymer layer. The current process uses parylene adhesion promoter A-174. The bonding is performed by bringing wafers **43a** and **43b** together under a combination of applied pressure and temperature, along with possible surface pre-treatments, dependent upon the particular polymer used. The current process uses a 20 second pre-treatment of 200W oxygen plasma, followed by bonding under vacuum environment, with a tool pressure of 100 kPa at a temperature of 280 °C for 30 minutes.

In step C, layers **47b** and **47d** are removed or partially removed through lithography and etching. The etch could be a dry or wet etch depending on the composition of the layers. The current process uses a dry etch and photolithography.

In step D, silicon wafers **43a** and **43b** are etched using KOH or similar anisotropic wet etchant like TMAH in order to release a multilayered membrane **48**. The lower wafer **43b** is etched such that part of the wafer forms a remaining support structure **42** and part of the wafer forms the chip body **44**. An important aspect of this etch is that the chip body forms an inclined surface to provide access for optical deflection detection onto the cantilever. The current process uses KOH, which forms an inclined surface at 54.7°. Alternatively, the wafers **43a** and **43b** could be etched using a dry etch process like DRIE, which could be tuned to achieve an inclined surface or through a technique like greyscale lithography.

In step E the shape of the cantilever **8** is defined from the membrane formed in the previous step via lithography and etching through layers **47a**, **45** and **47c**. This etch could be a wet etch or dry etch and may need an additional hard mask, and/or a mechanical support layer or etch stop layer. In the current process, a 2 μm thick aluminum mechanical support and etch stop layer is evaporated onto the bottom side of the membrane. The current process uses either a photoresist mask, or a photoresist mask in combination with a 300 nm evaporated aluminum hard mask. The layers are etched in a sequential dry

etch process, first etching the hard mask, using a photoresist mask, and subsequently layers **47a**, **45** and **47c**.

- 5 In step F, a reflective coating layer **49** is deposited onto the cantilever. This layer could be either evaporated or sputtered, and be composed of any number of reflective materials, ideally being either aluminum or chrome/gold or titanium/gold. In the current process, 5 nm of Cr and 50 nm of Au are evaporated onto the cantilever.

According to another aspect, the present invention thus relates to a method for producing a cantilever comprising the steps of:

- 10 providing a first wafer 43a including a first layer 47a deposited on a first external surface of the wafer and a second layer 47b deposited on a second external surface of the wafer,

providing a second wafer 43b including a first layer 47c deposited on a first external surface of the wafer and a second layer 47d deposited on a second external surface of the wafer,

forming a first structure by depositing a third layer 45 comprising a material having an elastic modulus inferior to that of the first 47a and second layer 47b on the first layer 47a of the first wafer 43a,

- 15 forming a second structure by depositing a third layer 45 comprising a material having an elastic modulus inferior to that of the first 47c and second layer 47d on the first layer 47c of the second wafer 43b,

wafer bonding the first and second structures together by combining the third layer 45 of the first structure with the third layer 45 of the second structure,

- 20 partially removing the exposed second layer 47b on a first external surface of the bonded structure to expose the first wafer material 43a and create a first etch mask window, and partially removing the exposed second layer 47d on a second external surface of the bonded structure to expose the second wafer material 43b and create a second etch mask window,

- 25 etching the exposed first wafer material 43a and the exposed second wafer material 43b to remove part of the first and second wafer material and expose a beam 48 including the combined third layers 45 sandwiched between the first layers 47a, 47c,

depositing an etch stop and support layer on the second wafer material 43b and the first layer 47c of the second wafer 43b, etching through the beam 48 to divide the beam 48 in two parts, and removing the etch stop and support layer.

- 30 A reflective coating may be deposited on the second wafer material 43b and the first layer 47c of the second wafer 43b.

- 35 The step of providing a second wafer 43b including a first layer 47c deposited on a first external surface of the wafer and a second layer 47d deposited on a second external surface of the wafer further includes a step of depositing a metal layer 51 to measure cantilever deflection on the first layer 47c to partially cover the first layer 47c, and a step of depositing a metal bonding pad 53 on the metal layer 51 to partially cover the metal layer 51, wherein the third layer 45 comprising a viscoelastic material is deposited on the first layer 47c, the metal bonding pad 53 and the metal layer 51.

The first layer 47a and the third layer (45) of the beam (48) can be etched to expose the metal bonding pad 53.

During the step of wafer bonding, the third layer 45 flows to adapt to the extra topography presented by the metal bonding pad 53 and the metal layer 51.

- 5 Using the above process flow, several trilayer MEMS cantilevers have been fabricated and tested. Figure 7(a) shows a SEM image of one cantilever. These cantilevers have 100 nm silicon nitride layers 47, and a 4 μ m parylene layer 45, made of two, 2 μ m parylene layers 45 bonded together. Of note, the cantilever shows no residual stress bending. Two-layer nitride-parylene cantilevers were also fabricated, which showed substantial residual stress bending.
- 10 Figure 7(b) shows measurement of the power spectrum of the thermal deflections for several trilayer cantilevers. This measurement characterises the principle mechanical properties of the cantilever, namely the resonance frequency, spring constant and quality factor. Two features are evident based on this measurement: first, the Q factors are significantly lower than standard AFM cantilevers, and vary little across a wide range of spring constants and resonance frequencies, suggesting that the viscoelastic
- 15 properties of the cantilever are indeed dominant. Second, the resonance frequency of the cantilever with spring constant 38 N/m is 600 kHz, which is double the resonance frequency of order 300 kHz one would expect for a silicon cantilever with spring constant around 40 N/m (e.g. Bruker model MPP-1123-10).

- 20 Figure 7(c) shows an AFM image of a calibration grating taken with a trilayer cantilever, using an unmodified commercial Bruker MultiMode VIII AFM system. Figure 7(d) shows the tapping mode imaging bandwidth of a cantilever with $f_0 = 394$ kHz, $k = 24$ N/m and $Q = 73$. The imaging bandwidth, defined as the -3 dB frequency of the tracking amplitude, corresponds to 11 kHz. In comparison, a silicon cantilever with $f_0 \approx 300$ kHz has a bandwidth of order 1 kHz.

Tip integration

- 25 Integrating a sharp tip onto the end of the cantilever may be accomplished in a number of different ways. For cantilevers without a batch-fabricated sharp tip, such as those presented above, a tip may be grown (e.g. via electron beam-induced deposition) or glued onto the cantilever.

- 30 A more desirable solution is to integrate a tip in the batch-fabrication process. The simplest process for accomplishing this tip integration is to mould a tip in one of the hard layers; this process is an industry standard for creating silicon nitride tips. An overview of the process is shown below in Figures 8a and 8b. A detailed process run card is given later herein in Appendix A.

Step A in Figure 8a is performed for layers 53c and 53d on wafer 51b as is described in step A from Figure 6a.

- 35 For Figure 8 step B, on silicon wafer 51a, etch mask layers 55a and 55b are grown or deposited on the top and bottom surface of the wafer. The current process uses 500 nm of thermally grown silicon dioxide. Layer 55b is partially removed using lithography and etching. The current process uses photolithography and dry etching. Wafer 51a, masked by layers 55a and 55b, is then etched in order to create a tip-like indentation 57. The current process uses KOH as an anisotropic etchant to form a pyramidal structure where the resulting planes of the silicon surface in the indentation are <111> planes.

As one alternative, the tip-like indent could be etched using an isotropic wet or dry etch to form a hemispherical-like indentation.

- 5 In Figure 8 step C, layers **55a** and **55b** are removed (using a dry or wet etch, for example, using BOE as in the current process). Optionally, thermally grow oxide layer **59a** and **59b**, which serves to reduce the radius of the bottom of the indent **59**. In the current process, layers **59a** and **59b** are grown using steam at 950 °C. Layers **53a** and **53b** are then added, ideally using the same material and processes as for wafer **51b** from step A.

In Figure 8 step D, layer **61** is used to bond together wafers **51a** and **51b** as described in step B of Figure 6.

- 10 In Figure 8 step E, layers **53b**, **53d** and **59a** are removed or partially removed through lithography and etching. The etch could be a dry or wet etch depending on the composition of the layers. The current process uses a dry etch and photolithography.

Figure 8 step F is performed according to the description of step D of Figure 6. Layer **59b** must be removed, as part of the wet etch process, or through an additional wet or dry etch step.

- 15 Figure 8 step G is performed according to the description of step E of Figure 6.

Figure 8 step H is performed according to the description of step F of figure 6.

Self-sensing integration

- 20 As discussed earlier, three advantages of this architecture for self-sensing integration are that the processing of the tip and self-sensing elements may be performed on separate wafers, that the self-sensing elements may be inherently insulated from the exterior environment, and that the thickness of the cantilever is larger than that of a standard silicon or silicon nitride cantilever for similar spring constant, thus increasing the strain at the sensor (for cantilevers that behave in a bending motion as shown in Figure 5).

- 25 A basic process overview towards integrating thin metal self-sensing elements is shown in Figures 9a and 9b. It adopts the basic process flow shown in Figure 8.

- 30 In Figure 9a step A, layers **53c** and **53d** are grown or deposited or doped on wafer **51b** as is described in step A of Figure 6. Subsequently, strain sensor element **67** and electrical connections **69** and **71** are deposited (or deposited and patterned). Only one set of sensor element and electrical connections is shown, but actual devices may include a plurality of sensors and connections, in locations both on the cantilever and off of the cantilever. In the current process, the sensor element is made from evaporated Cr/Au with thickness 5/50 nm and the electrical connections are made from evaporated Cr/Au with thickness 20/200 nm. Other potential sensor elements include any kind of piezoresistive material, for example doped crystalline silicon or polysilicon, granular metals or 2D materials.

Figure 9 steps B-F follow the description given for steps B-F of Figure 8.

- 35 Figure 9b step G follows the description given for step G of Figure 8, with the addition of etching openings **73** in order to make electrical connection between the electrical connections **67** and **71**, and further instrumentation off of the cantilever chip. These openings would be etched either during the same step as the cantilever release as described in Figure 6 step F (if the electrical contact layer acts as a

suitable etch stop for the etch process), or with a similar etch only in the opening region before the cantilever release step.

Figures 10a and 10b present an overview of a process for integrating both a moulded sharp tip and electrical deflection sensing elements onto the upper outer surface of the cantilever device.

- 5 Figure 10, steps A-F follow the description given for steps A-F of Figure 8.

In Figure 10 step G, strain sensor element **75** and electrical connections **77** and **79** are deposited (or deposited and patterned) as described in Figure 9 step A. An area to make electrical connections **73** to further instrumentation off the cantilever chip can be included as part of the definition of the electrical connection **79**.

- 10 Figure 10 step H follows the description from step G in Figure 8.

Figures 11a and 11b present an overview of a process for integrating both a moulded sharp tip and electrical deflection sensing elements onto two inner surfaces of the composite sandwich cantilever device.

Figure 11 step A is performed according to the description in step A of Figure 9.

- 15 Figure 11 steps B-C follow the description given for steps B-C of Figure 8.

In Figure 11 step D, on wafer **51a** from step C, strain sensor element **81** and electrical connections **83** and **85** are deposited (or deposited and patterned) according to the description in Figure 9 step A.

Figure 11 steps E-G are performed according to the description in steps D-F of Figure 8.

- 20 Figure 11 step H is performed according to the description in Figure 9, step G. Opening **87** to connection **85** as well as opening **73** to connection **71** must both be made, according to description in Figure 9 step G. These openings may be created serially or as part of one etching process step.

Alternative tip integration strategies beyond a moulded tip are desirable. Figures 12a and 12b present an overview of a process for integrating both an etched sharp silicon tip and electrical deflection sensing elements onto one inner surface of the composite sandwich cantilever device.

- 25 Figure 12 step A is performed as is described in step A of Figure 8.

- In Figure 12 step B, the process is shown using an SOI wafer consisting of two silicon layers **89** and **91** separated by a silicon dioxide layer **93**. The thickness of layer **89** is from about 5 μm up to 50 μm , and is related to the desired final height of the silicon tip. On the SOI wafer, a layer **95** is grown or deposited according to the description in Figure 8, step A. An SOI wafer is not strictly necessary for this process, but is a matter of convenience for defining the thickness of layer **89**. On this wafer, layers **53a** and **53b** are grown or deposited according to the description in Figure 8, step A.
- 30

In Figure 12 step C, the wafer from step A and step B are bonded together using an intermediate polymer layer **61** according to Figure 8, step D.

Figure 12 step D is performed as is described in Figure 8, step E.

- 35 In Figure 12 step E, an etch is performed according to the description of Figure 6 step C, in order to remove or partially remove layer **91** and wafer **51b**. Layer **93** in the SOI wafer serves as an etch stop in

this process to help define the thickness of layer **89**. If not using an SOI wafer, the etch could be timed in order to leave a layer **89** of desired thickness, and subsequently, a layer **93** that serves subsequently as a wet etch mask could be deposited on the wafer using any low-temperature process, for example using PECVD to deposit silicon oxide or nitride, or evaporated Cr/Au. The remaining sections of wafer **51b** form a remaining support structure **52** and the chip body **54**.

In Figure 12 step F, layer **93** is partially removed using lithography and a dry or wet etch.

In Figure 12 step G, layer **89** is etched using the patterned layer **93** as a mask, in order to leave a sharp tip structure **95** on the released composite membrane **56**. This etch can be, for example a wet etch using KOH or other anisotropic etchant as is commonly done (e.g. using a triangular mask) for the fabrication of sharp tip structures in silicon.

Figure 12 step H is performed according to Figure 9, step G.

As described in relation to Figure 4, different types of self-sensing strategies can be integrated into the cantilever. Figures 13a and 13b presents an overview of a process for integrating both a moulded sharp tip and piezoelectric deflection sensing elements onto one inner surface of the composite sandwich cantilever device.

Figure 13a, step A is performed according to the description in Figure 8, step A to create on wafer **51b** layers **53c** and **53d**. Subsequently, electrical contact layer **97**, piezoelectric layer **99** and electrical contact layer **101** are grown or deposited successively. The piezoelectric layer could be made of a material like AlN, or PZT, or others. The thickness of this layer would depend upon the material but could range from a few hundred nm up to about 2 μm . The electrical contact layers would be typically made of a metal like gold, silver, platinum, aluminum, molybdenum, etc. or an alloy and would have a thickness from about 20 nm up to 200 nm.

In Figure 13a step B, electrical contact layers **97** and **101** and piezoelectric layer **99** are lithographically patterned and etched in order to expose part of layer **97**. In addition, the layers could be partially removed across the wafer if desired (for example, such that the layers do not extend completely across the planar area of the cantilever beam. The etch could be a dry or wet etch.

Figure 13 steps C-D are performed according to the description of Figure 8, steps B-C.

In Figure 13 step E, wafers from step D and step B are bonded according to description of Figure 8 step D.

Figure 13 steps F-G are performed as is described for Figure 8, steps E-F.

Figure 13 step H follows the description of Figure 9, step G. Openings **103** and **105** to both electrical contact layers **97** and **101** must be made.

Membrane devices

In addition to cantilever-based devices, an alternative embodiment of the invention concerns membrane devices, or structured membranes such as doubly- or multiply-clamped beams, etc.

Figures 14a and 14b present an overview of a process for fabricating a device with electrical deflection sensing elements, where the device is a membrane instead of a cantilever. In the figure, no tip-like structure is shown in the process, although one could be incorporated into the membrane following a

process like that shown in Figure 9, along the description below in order to make a membrane and not a cantilever.

In Figure 14a step A, layers **47c** and **47d** are created on wafer **43a** according to figure 6, step A. In addition, deflection sensing elements **67a** and **67b** with electrical contacts **69a**, **69b**, **71a** and **71b** are included as is described for Figure 9, step A. Two elements are shown in the figure, but more or fewer could be included as part of the process.

Figures 14a and 14b steps B-D are performed according to the description in Figure 6 steps B-D, in order to release the composite membrane **90**.

In Figure 14b step E, an etch is performed in order to define the (optionally) structured membrane **92** as is described in Figure 9 step G. At minimum, openings **111** to the electrical contacts must be made during this etch. The membrane can be structured into a number of different shapes, such as a doubly-clamped beam, a crossed beam, or a full membrane as shown in Figure 14c.

Alternative layer configurations

Figure 15 presents an overview of an alternate configuration for a composite sandwich cantilever. In this embodiment of the invention, a layer of high elastic modulus forms the core of the cantilever, with layers of low elastic modulus and high loss coefficient surrounding this core. The core layer can for example include or be formed of any of the materials previously mentioned for the surrounding or sandwiching layers. The surrounding or sandwiching layers can for example include or be formed of any of the materials previously mentioned for the core layer. The advantage of this construction over the earlier-described embodiments is the relative simplicity of the fabrication process. This architecture would retain a benefit to the bandwidth ratio f_0/Q through a reduction in the Q factor of the cantilever over a uniform cantilever, due to the inclusion of damping layers. However, the cantilever performance metric f_0^2/k would not be improved through this architecture, because the layers with highest elastic modulus are close to the neutral axis.

In Figure 15 step A, layers **153a** and **153b** on wafer **151** are created according to the description for Figure 6 step A.

In Figure 15 step B, layer **153b** is partially removed through lithography and a wet or dry etch. Wafer **151** is then etched, using KOH or other etch process as described in Figure 6 step D, in order to release the membrane **156** and define support structure **152** and chip body **150**.

In Figure 15 step C, layers **155** and **157** with low elastic modulus and high loss coefficient are deposited in order to define the composite membrane **158**. These layers are ideally made of material and thickness as described in Figure 6, step B for layer **45**. The deposition process could be any number of conformal deposition processes, for example CVD or spray coating.

In Figure 15 step D, layers **153a**, **155** and **157** are etched in order to define the cantilever **160**. This etch process is performed according to the description in Figure 6, step E.

Figure 15 step E is performed as is described for Figure 6, step F.

Figures 16a and 16b present an overview for the addition of a sharp tip on the cantilever architecture shown in figure 15. In step A, layers **153a** and **153b** are grown or deposited on silicon wafer **151**. These

layers could be silicon nitride or silicon oxide, with thickness from 100 nm up to 2 μ m, depending on the layer material and the desired etch depth of the silicon wafer (in step B).

- 5 In Figure 16a step B, layer **153b** is patterned using lithography and a dry or wet etch. Subsequently, the wafer **151** is exposed to KOH or similar anisotropic etchant until the desired thickness of silicon wafer remains. This thickness is between about 5 and 50 μ m depending on the specific tip geometry. Alternatively, an SOI wafer could be used to define the desired thickness of the remaining silicon wafer, stopping on the buried oxide layer (which may need to be subsequently removed).

- 10 In Figure 16a step C, layers **153a** and **153b** are removed using a dry or wet etch. Layers **161a** and **161b** are then grown or deposited following the description of Figure 6 step A. Layer **161a** is patterned using lithography and a dry or wet etch to form a mask for the subsequent tip etch.

Figure 16a step D is performed according to the description of Figure 12, step G, to create sharp silicon tip structure **163** on released membrane **156**, with remaining silicon wafer forming a support structure **152** and chip body **150**.

Figure 16b step E follows the description for Figure 15, step C.

- 15 In Figure 16b step F, layer **155** is removed in the region covering the tip using lithography combined with a dry or wet etch. The layer could be patterned using a photoresist or a hard mask.

Figure 16b step G follows the description for figure 15, step D.

Figure 16b step H is performed as is described for Figure 6, step F.

Alternative fabrication process – layer by layer deposition

- 20 Figures 17a, 17b, 17c and 17d present an overview of a process to create the cantilever using layer-by-layer deposition, as opposed to wafer bonding.

In Figure 17 step A, layers **183a** and **183b** are grown or deposited on silicon wafer **181** as described for Figure 6, step A.

- 25 In Figure 17 step B, layer **185** is grown or deposited as described for Figure 6, step B. Subsequently, layer **187** is grown or deposited. Layer **187** would have similar properties and thickness to layer **183a** (ideally the same material and thickness). The process used to deposit layer **187** is dependent on the maximum temperature that the underlying layers (**183a**, most importantly **185**) can withstand. Some polymers are able to withstand processes above 200-300 °C, which would permit using deposition processes like PECVD, ALD, evaporation, sputtering, etc. in order to deposit layer **187**.

- 30 In Figure 17 step C, layer **183b** is patterned using lithography and a dry or wet etch.

In Figure 17 step D, silicon wafer **181** is exposed to KOH or similar anisotropic etchant to release composite membrane **184**, leaving support structure **180** and chip body **182**. Alternatively, a dry etch like DRIE could be used (see Figure 6, step D for reference).

Figure 17, steps E-F are performed following the description for Figure 6, steps E-F.

- 35 Layer by layer deposition implementation

The process has been carried out by deposition of thin films with ALD (Atomic Layer Deposition) shown in Figures 17c and 17d. The advantages of ALD over other deposition processes like CVD, sputtering and

thermal evaporation are low deposition temperature, convenient thin film quality, thickness control and material variety like SiO₂, TiO₂, HfO₂, Al₂O₃ and TiN. These advantages enable us to tune the quality factor of the cantilevers, however other deposition or growth methods can be used as well.

- 5 Figure 17c step G demonstrates wafer **201** which consists of wafer **181** and layer **183b** where layer **183a** is stripped off by dry etching. Layer **98** is an etch stop layer like Al or Ti to protect the deposited thin film from KOH shown in Figure 17 step D.

In Figure 17c step H, layer **202a** is deposited by ALD followed by coating layer **185** and then deposition of layer **202b** by ALD.

Figure 17 steps I and J are carried out as described previously in relation to steps C and D of Figure 17.

- 10 In Figure 17 step K the sandwich structure and layer **98** are etched followed by step L which is carried out as described in relation to step F of Figure 17b.

Figure 18 presents an overview of a process to create the cantilever including a sharp tip structure using a layer-by-layer deposition.

The structure shown in Figure 18 step A is achieved following the description for Figure 16 steps A-D.

- 15 In Figure 18 step B, layers **195** and **197** are deposited as described for Figure 17, step B, forming the composite membrane **184**.

In Figure 18 step C, layers **195** and **197** are removed in the region covering the tip using lithography and a dry or wet etch, exposing the tip structure **191**. The layers could be patterned using a photoresist or hard mask.

- 20 Figure 18 steps D-E are performed following the description of Figure 6, steps E-F.

Having described preferred embodiments of this invention, it will be apparent to one of skill in the art that other embodiments incorporating its concept may be used. This invention should not be limited to the disclosed embodiments, but rather should be limited only by the scope of the appended claims.

- 25 While the invention has been disclosed with reference to certain preferred embodiments, numerous modifications, alterations, and changes to the described embodiments, and equivalents thereof, are possible without departing from the sphere and scope of the invention. Accordingly, it is intended that the invention not be limited to the described embodiments, and be given the broadest reasonable interpretation in accordance with the language of the appended claims.

References

- 30 1. Mertz, J., Marti, O. & Mlynek, J. Regulation of a microcantilever response by force feedback. *Appl. Phys. Lett.* **62**, 2344–2346 (1993).
2. Walters, D. A. *et al.* Short cantilevers for atomic force microscopy. *Rev. Sci. Instrum.* **67**, 3583–3590 (1996).
- 35 3. Ando, T. *et al.* A high-speed atomic force microscope for studying biological macromolecules. *Proc. Natl. Acad. Sci.* **98**, 12468–12472 (2001).

4. Fantner, G. E. *et al.* Components for high speed atomic force microscopy. *Ultramicroscopy* **106**, 881–887 (2006).
5. Viani, M. B. *et al.* Probing protein-protein interactions in real time. *Nat. Struct. Biol.* **7**, 644–647 (2000).
- 5 6. Fantner, G. E., Barbero, R. J., Gray, D. S. & Belcher, A. M. Kinetics of antimicrobial peptide activity measured on individual bacterial cells using high-speed atomic force microscopy. *Nat. Nanotechnol.* **5**, 280–285 (2010).
7. Uchihashi, T., Iino, R., Ando, T. & Noji, H. High-speed atomic force microscopy reveals rotary catalysis of rotorless F1-ATPase. *Science* (80-.). **333**, 755–758 (2011).
- 10 8. Casuso, I. *et al.* Characterization of the motion of membrane proteins using high-speed atomic force microscopy. *Nat. Nanotechnol.* **7**, 525–529 (2012).
9. Genolet, G. *et al.* Soft, entirely photoplastic probes for scanning force microscopy. *Rev. Sci. Instrum.* **70**, 2398–2401 (1999).
- 10 10. Thaysen, J., Yalçinkaya, A., Vettiger, P. & Menon, A. Polymer-based stress sensor with integrated readout. *J. Phys. D: Appl. Phys.* **35**, 2698–2703 (2002).
- 15 11. Calleja, M. *et al.* Highly sensitive polymer-based cantilever-sensors for DNA detection. *Ultramicroscopy* **105**, 215–222 (2005).
12. Nordström, M. *et al.* SU-8 Cantilevers for Bio/chemical Sensing; Fabrication, Characterisation and Development of Novel Read-out Methods. *Sensors* **8**, 1595–1612 (2008).
- 20 13. Mangonov, S. N. & Whangbo, M.-H. *Surface analysis with STM and AFM: experimental and theoretical aspects of image analysis. Surface analysis with STM and AFM: experimental and theoretical aspects of image analysis* (VCH, 1996).
14. Li, M., Tang, H. X. & Roukes, M. L. Ultra-sensitive NEMS-based cantilevers for sensing, scanned probe and very high-frequency applications. *Nat. Nanotechnol.* **2**, 114–20 (2007).
- 25 15. Gotszalk, T., Grabiec, P., Tomerov, E. & Rangelow, I. W. Thermally driven micromechanical beam with piezoresistive deflection readout. **68**, 550–556 (2003).
16. Ivanov, T., Gotszalk, T., Sulzbach, T., Chakarov, I. & Rangelow, I. W. A FM cantilever with ultra-thin transistor-channel piezoresistor : quantum confinement. **68**, 534–541 (2003).
17. Linnemann, R. Characterization of a cantilever with an integrated. **264**, (1995).
- 30 18. Manalis, S. R., Minne, S. C. & Quate, C. F. Atomic force microscopy for high speed imaging using cantilevers with an integrated actuator and sensor. *Appl. Phys. Lett.* **68**, 871 (1996).

19. Lee, C., Itoh, T. & Suga, T. Self-excited piezoelectric PZT microcantilevers for dynamic SFM - with inherent sensing and actuating capabilities. *Sensors Actuators A* **72**, 179–188 (1999).
20. Watanabe, S. & Fujii, T. Micro-fabricated piezoelectric cantilever for atomic force microscopy. *Rev. Sci. Instrum.* **67**, 3898 (1996).
- 5 21. Lee, J. & King, W. P. Liquid Operation of Silicon Microcantilever Heaters. *IEEE Sens. J.* **8**, 1805–1806 (2008).
22. King, W. P. Improved All-Silicon Microcantilever Heaters With Integrated Piezoresistive Sensing. *J. Microelectromechanical Syst.* **17**, 432–445 (2008).
- 10 23. Lee, J. *et al.* Electrical, Thermal, and Mechanical Characterization of Silicon Microcantilever Heaters. *J. Microelectromechanical Syst.* **15**, 1644–1655 (2006).
24. Brugger, J., Blamf, N., Renaudb, P. & Rooija, N. F. De. Microlever with combined integrated sensor / actuator functions for scanning force microscopy. **43**, 339–345 (1994).
- 15 25. Adams, J. D. *et al.* Analysis of local deformation effects in resistive strain sensing of a submicron-thickness AFM cantilever. in *Proceedings of SPIE Microtechnologies, Smart Sensors, Actuators, and MEMS IV* **8763**, 876327 (2013).
26. Pharr, G. M. & Oliver, W. C. Measurement of Thin Film Mechanical Properties Using Nanoindentation. (1992).
27. Xiang, Y., Chen, X. & Vlassak, J. J. Plane-strain Bulge Test for Thin Films. *J. Mater. Res.* **20**, 2360–2370 (2011).
- 20 28. Weihs, T. P., Hong, S., Bravman, J. C. & Nix, W. D. Mechanical deflection of cantilever microbeams: A new technique for testing the mechanical properties of thin films. *J. Mater. Res.* **3**, 931–942 (1988).
- 25 29. Le Rouzic, J., Delobelle, P., Vairac, P. & Cretin, B. Comparison of three different scales techniques for the dynamic mechanical characterization of two polymers (PDMS and SU8). *Eur. Phys. J. Appl. Phys.* **48**, 11201 (2009).
- 30 30. Ayala, C., Heinrich, S. M., Josse, F. & Dufour, I. Resonant microcantilevers for the determination of the loss modulus of thin polymer films. *J. Microelectromechanical Syst.* **20**, 788–790 (2011).
31. Huber, F., Lang, H. P., Backmann, N., Rimoldi, D. & Gerber, C. Direct detection of a BRAF mutation in total RNA from melanoma cells using cantilever arrays. *Nat. Nanotechnol.* **8**, 125–9 (2013).
- 30 32. Yang, Y. *et al.* Batch-fabricated cantilever probes with electrical shielding for nanoscale dielectric and conductivity imaging. *J. Micromechanics Microengineering* **22**, 115040 (2012).
33. Albrecht, T. R., Akamine, S., Carver, T. E. & Quate, C. F. Microfabrication of cantilever styli for the atomic force microscope. *J. Vac. Sci. Technol. A* **8**, 3386–3396 (1990).

34. Burt, D. P., Dobson, P. S., Donaldson, L. & Weaver, J. M. R. A simple method for high yield fabrication of sharp silicon tips. *Microelectron. Eng.* **85**, 625–630 (2008).

Appendix A

5 The table below presents a detailed runcard for parylene/nitride trilayer cantilevers with moulded nitride tip.

Projet :
Parylene/nitride AFM
cantilevers
Substrates : silicon <100>, 100mm, 380um, double side, Prime, p type, 1-10
Ohmcm. 2 wafers

Step N°	Description	Equipment	Program / Parameters	Target	Actual	Remarks	Name	Date
1	Oxide deposition - tip wafer							
1.1	RCA1 clean	Z3/WB_PreOx_Clean	H2O:NH4OH:H2O2 (5:1:1)	15min 75°C		CMI staff to perform		
1.2	HF dip	Z3/WB_PreOx_Clean	HF:H2O (1:10)	15s		CMI staff to perform		
1.3	RCA2 clean	Z3/WB_PreOx_Clean	H2O:HCl:H2O2 (6:1:1)	15min 75°C		CMI staff to perform		
1.4	Fast fill rinse	Z3/WB_PreOx_Clean		15min		CMI staff to perform		
1.5	Trickle tank	Z3/WB_PreOx_Clean		15min		CMI staff to perform		
1.6	Spin rinser dryer	Z3/Semitoil	Prog. 1			CMI staff to perform		
1.7	Wet oxidation	Z3/Centrotherm LPCVD	Wet oxide std process	500 nm		CMI staff to perform		
1.8	Oxide thickness meas.	Z3/Nanospec/AFT6100		500 nm				
2	Photolithography - Backside registry mask - tip wafer							
2.1	Surface activation	Z11/Tepla 300 or Z2/Tepla GigaBatch	Program 4 (300) or Strip high 5 min (GigaBatch)					
2.2	Spin on	Z13/SSE SB20	AZ1512HS, STD-4000-RPM	1.2 um		Dispense ~3 mL resist		
2.3	PR bake	Z13/SSE SB20	100 °C on hotplate	1 min				
2.4	Expose	Z13/MJB4	Hard contact, CP mode	3 sec		for 20 mW/cm2 i-line intensity		
2.5	PR develop	Z13/Develop bench	MFCD26	30 sec				
2.6	DI Rinse	Z13/Develop bench	3 fill-exchanges					
2.7	N2 dry	Z13/Develop bench						
2.8	Inspection	Z13/microscope						
2.9	Descum	Z11/Tepla 300 or Z2/Tepla GigaBatch	Program 44 (300) or Strip low 20 sec (GigaBatch)					
3	Oxide dry etch backside registry - tip wafer							
3.1	Oxide dry etch	Z2/SPTS	SiO2 PR 5:1	500 nm		Stop after EPD		
3.2	Inspection	Z2/microscope						
4	Resist strip - tip wafer							
4.1	O2 plasma	Z2/Tepla GigaBatch	Strip high 5 min					
4.2	1165	Z2/UFT resist	5 min bath 1, 5 min bath 2, QDR, TT					

WO 2016/189451

PCT/IB2016/053013

4.3	Spin rinser dryer	Z2/UFT resist	prog 1					
4.4	Inspection	Z2/Visual	Visual inspection for resist residue					
5	Photolithography - Tip openings mask - tip wafer							
5.1	Surface activation	Z11/Tepla 300 or Z2/Tepla GigaBatch	Program 4 (300) or Strip high 5 min (GigaBatch)					
5.2	Spin on	Z13/SSE SB20	AZ1512HS, STD-4000-RPM	1.2 um		Dispense ~3 mL resist		
5.3	PR bake	Z13/SSE SB20	100 °C on hotplate	1 min				
5.4	Expose	Z6/MA6	Hard contact, CP mode	2.4 s		for 10 mW/cm2 broadband		
5.5	PR develop	Z13/Develop bench	MFCD26	30 sec				
5.6	DI Rinse	Z13/Develop bench	3 fill-exchanges					
5.7	N2 dry	Z13/Develop bench						
5.8	Inspection	Z13/microscope						
5.9	Descum	Z11/Tepla 300 or Z2/Tepla GigaBatch	Program 44 (300) or Strip low 20 sec (GigaBatch)					
6	Oxide dry etch tip openings - tip wafer							
6.1	Oxide dry etch	Z2/SPTS	SiO2 PR 5:1	500 nm		Stop after EPD		
6.2	Inspection	Z2/microscope						
7	Resist strip - tip wafer							
7.1	O2 plasma	Z2/Tepla GigaBatch	Strip high 5 min					
7.2	1165	Z2/UFT resist	5 min bath 1, 5 min bath 2, QDR, TT					
7.3	Spin rinser dryer	Z2/UFT resist	prog 1					
7.4	Inspection	Z2/Visual	Visual inspection for resist residue					
8	KOH Etching - tip pits - tip wafer							
8.1	HF dip	Z5/ Plade Six Sigma	1% HF, 30 sec					
8.2	FFR	Z5/ Plade Six Sigma	3 fill-exchanges					
8.3	KOH Etching	Z5/ Plade Six Sigma	40%, 60°C, control density to 1.37 at 60°C	3.5 um		perform 100% overetch		
8.4	FFR	Z5/ Plade Six Sigma	3 fill-exchanges					
8.5	Neutralization	Z5/ Plade Six Sigma	HCL room temp	2h				
8.6	FFR	Z5/ Plade Six Sigma	3 fill-exchanges					
8.7	Air dry	Z5/ Plade Six Sigma						
9	Oxide strip - tip wafer							
9.1	BHF oxide etch	Z2/Plade oxide	BHF clean	500 nm		perform 50% overetch		
9.2	FFR	Z2/Plade oxide	3 fill-exchanges			check for hydrophobicity		
9.3	TT	Z2/Plade oxide						
9.4	SRD	Z2/Plade oxide	prog 1					
10	Wet oxidation and low-stress nitride deposition - tip wafer							
10.1	RCA1 clean	Z3/WB_PreOx_Clean	H2O:NH4OH:H2O2 (5:1:1)	15min 75°C		CMi staff to perform		
10.2	HF dip	Z3/WB_PreOx_Clean	HF:H2O (1:10)	15s		CMi staff to perform		
10.3	RCA2 clean	Z3/WB_PreOx_Clean	H2O:HCl:H2O2 (6:1:1)	15min 75°C		CMi staff to perform		
10.4	Fast fill rinse	Z3/WB_PreOx_Clean		15min		CMi staff to perform		
10.5	Trickle tank	Z3/WB_PreOx_Clean		15min		CMi staff to perform		

10.6	Spin rinser dryer	Z3/Semitool	Prog. 1			CMi staff to perform		
10.7	Oxide deposition	Z3/Centrotherm wet oxide	wet oxide 950°C	4000 A		CMi staff to perform		
10.8	Nitride deposition	Z3/Centrotherm LPCVD	Low stress nitride	200 nm		CMi staff to perform		
10.9	Nitride thickness meas.	Z3/Nanospec/AFT6100		200 nm				
11 Nitride deposition - chip wafer								
11.1	RCA1 clean	Z3/WB_PreOx_Clean	H2O:NH4OH:H2O2 (5:1:1)	15min 75°C		CMi staff to perform		
11.2	HF dip	Z3/WB_PreOx_Clean	HF:H2O (1:10)	15s		CMi staff to perform		
11.3	RCA2 clean	Z3/WB_PreOx_Clean	H2O:HCl:H2O2 (6:1:1)	15min 75°C		CMi staff to perform		
11.4	Fast fill rinse	Z3/WB_PreOx_Clean		15min		CMi staff to perform		
11.5	Trickle tank	Z3/WB_PreOx_Clean		15min		CMi staff to perform		
11.6	Spin rinser dryer	Z3/Semitool	Prog. 1			CMi staff to perform		
11.7	Nitride deposition	Z3/Centrotherm LPCVD	Low stress nitride	200 nm		CMi staff to perform		
11.8	Nitride thick. meas.	Z3/Nanospec/AFT6100						
12 Parylene deposition - chip and tip wafers								
12.1	Piranha clean	Z2/UFT piranha	5 min bath 1, 5 min bath 2, QDR, TT					
12.2	Spin rinser dryer	Z2/UFT piranha	Prog. 1					
12.3	Silanization	Z14/Solvent bench	Std process, instructions posted at bench					
12.4	UV tape protect	Z11/Powatec	Manual mounting. Avoid touching wafer surface					
12.5	Package for transfer	Material transfer zone	Fill out form and place wafers in parylene cabinet			use dedicated parylene I/O box		
12.6	Parylene deposition	Z10/Comelec		2 um		CMi staff to perform		
12.7	Wafers back to cleanroom	Material transfer zone						
13 Parylene-Parylene bonding - chip and tip wafers								
13.1	UV tape removal	Z11/Powatec	std process avoid touching parylene surface					
13.2	O2 plasma	Z11/Tepla 300 or Z2/Tepla GigaBatch	prog 44 (15 sec) or Strip low 20 sec (GB)					
13.3	HF dip	Z2/Plade oxide	HF:H2O (1:4) room temp	20 s		HF dip and oven dry untested, may improve bonding		
13.4	FFR	Z2/Plade oxide						
13.5	TT	Z2/Plade oxide						
13.6	SRD	Z2/Plade oxide						
13.7	Oven dry	Z6/Heraus	150 deg C 15 min			12.2-12.7 done individually right before bonding		
13.8	Parylene bonding	Z6/SB6	prog adams_parylene_v1 (280 deg c vac 30 min)			align flats by eye		
14 Photolithography - chip body openings - backside alignment								
14.1	Surface activation	Z11/Tepla 300 or Z2/Tepla GigaBatch	Program 3 (300) or Strip high 1 min (GigaBatch)					
14.2	Spin on	Z13/SSE SB20	AZ1512HS, STD-4000-RPM	1.2 um		Dispense ~3 mL resist		

WO 2016/189451

PCT/IB2016/053013

14.3	PR bake	Z13/SSE SB20	100 °C on hotplate	1 min				
14.4	Expose	Z6/MA6	Hard contact, CP mode, backside align	2.4 s		for 10 mW/cm2 broadband		
14.5	PR develop	Z13/Develop bench	MFCD26	30 sec				
14.6	DI Rinse	Z13/Develop bench	3 fill-exchanges					
14.7	N2 dry	Z13/Develop bench						
14.8	Inspection	Z13/microscope						
15	Dry etch - chip body openings							
15.1	Nitride dry etch	Z2/SPTS	SiO2 PR 5:1	200 nm		Use EPD, overetch is ok		
15.2	Inspection	Z2/microscope						
16	Resist strip - chip side							
16.1	O2 plasma	Z2/Tepla GigaBatch	Strip high 1 min					
16.2	1165	Z2/UFT resist	5 min bath 1, 5 min bath 2, QDR, TT					
16.3	Spin rinser dryer	Z2/UFT resist	prog 1					
16.4	Inspection	Z2/Visual	Visual inspection for resist residue					
17	Photolithography - usable disk - tip side							
17.1	Surface activation	Z11/Tepla 300 or Z2/Tepla GigaBatch	Program 3 (300) or Strip high 1 min (GigaBatch)					
17.2	Spin on	Z13/SSE SB20	AZ1512HS, STD-4000-RPM	1.2 um		Dispense ~3 mL resist		
17.3	PR bake	Z13/SSE SB20	100 °C on hotplate	1 min				
17.4	Expose	Z6/MA6	Hard contact, CP mode, backside align	2.4 s		for 10 mW/cm2 broadband		
17.5	PR develop	Z13/Develop bench	MFCD26	30 sec				
17.6	DI Rinse	Z13/Develop bench	3 fill-exchanges					
17.7	N2 dry	Z13/Develop bench						
17.8	Inspection	Z13/microscope						
18	Dry etch - usable disk opening							
18.1	Nitride/oxide dry etch	Z2/SPTS	SiO2 PR 5:1	400nm/200 nm		Use EPD, overetch is ok		
18.2	Inspection	Z2/microscope						
19	KOH etching - Si bulk removal and membrane release							
19.1	SS Chuck mounting	Z5/ Plade Six Sigma		150 um				
19.2	KOH Etching	Z5/ Plade Six Sigma	40%, 60°C, control density to 1.37 at 60°C	380 um		overnight etch approx 18 h		
19.3	FFR	Z5/ Plade Six Sigma	3 fill-exchanges					
19.4	Neutralization	Z5/ Plade Six Sigma	HCL room temp	2h				
19.5	FFR	Z5/ Plade Six Sigma	3 fill-exchanges					
19.6	Air dry	Z5/ Plade Six Sigma				dry overnight		
20	Aluminum etch stop and hard mask deposition							

20.1	Etch stop al coating	Z11/EVA760	250 mm height prog AL 160?	2 um				
20.2	Hard mask al coating	Z11/EVA760	250 mm height prog AL 160?	300 nm				
21	Photolithography - Cantilever definition							
21.1	Surface activation	Z6/Heraus	150 deg C 15 min			Or alternate thermal dehydration		
21.2	Spin on	Z13/SSE SB20	AZ9260, STD-1200-RPM	12 um		dispense resist over all wafer		
21.3	PR bake	Z13/SSE SB20	115 °C on hotplate	6 min				
21.4	Rehydration delay	Z13/wafer carrier	1 h delay in ambient					
21.5	Expose	Z13/MJB4	Hard contact, CH1 mode, 1900 mJ/cm ²	95 sec		20 mW/cm ² i-line		
21.6	PR develop	Z13/Develop bench	AZ developer full conc.	5 min?		photolitho params to be refined		
21.7	DI Rinse	Z13/Develop bench	3 fill-exchanges			careful with fragile membrane		
21.8	air dry	Z13/Develop bench				dry overnight ideally		
21.9	Inspection	Z13/microscope						
22	Dry etch - sandwich							
22.1	Al dry etch	Z2/STS	Al_etch	300 nm (~1 min)		Use EPD, signal difficult to see. Also observe visually		
22.2	Oxide + nitride dry etch	Z2/STS	Oxyde	400nm/ 200 nm		Use EPD, signal difficult to see. Also observe visually		
22.3	pyralene dry etch	Z2/STS	pyralin	4 um		Use EPD, signal difficult to see. Also observe visually		
22.4	Nitride dry etch	Z2/STS	Oxyde	200 nm		Use EPD, signal difficult to see. Also observe visually		
23	Resist strip							
23.1	1165	Z2/UFT resist	5 min bath 1, 5 min bath 2, QDR, TT	12 um				
23.2	Air dry	Z2/UFT resist						
23.3	Inspection	Z2/Visual	Visual inspection for resist residue					
24	Aluminum wet etch							
24.1	Alu wet etch	Z2/Plade metal or Z14/Arias acid	ANP 35 degrees	2 um				
24.2	DI rinse	Z2/Plade metal or Z14/Arias acid	TT only, or manual beaker rinse	3 times				
24.3	Air dry	Z2/Plade metal or Z14/Arias acid				no need for extensive drying		
25	Oxide strip - tip wafer							
25.1	BHF oxide etch	Z2/Plade oxide or Z14/Arias acid	BHF contaminated	400 nm		perform 50% overetch		
25.2	DI rinse	Z2/Plade oxide or Z14/Arias acid	3 fill-exchanges					
25.3	Air dry	Z2/Plade oxide or Z14/Arias acid				dry overnight		
25	Metal reflective coating deposition							
25.1	Ti/Au evap	Z11/EVA760	450 mm height Ti/Al for liftoff	5 nm/30 nm				

CLAIMS

1. Cantilever or membrane comprising:
 - 5 - a body (16),
 - an elongated beam (8) attached to the body (16),
 wherein the elongated beam (8) includes:
 - 10 - a first layer (3) comprising a first material,
 - a second layer (5) comprising a second material having an elastic modulus different to that of the first material,
 - a third layer (7) comprising a third material having an elastic modulus different to that of the first material,
 the first layer (3) being sandwiched between the second layer (5) and the third layer (7).
- 15 2. Cantilever or membrane according to claim 1, wherein the first material has an elastic modulus inferior to that of the second and third material; and/or the first material has a loss coefficient superior to that of the second and third material; and/or the first material has a density inferior to that of the second and third material.
- 20 3. Cantilever or membrane according to claim 1, wherein the first material has an elastic modulus superior to that of the second and third material; and/or the first material has a loss coefficient inferior to that of the second and third material.
- 25 4. Cantilever or membrane according to any previous claim, wherein the first material is a viscoelastic material.
5. Cantilever or membrane according to any previous claim, wherein the second layer (5) and the third layer (7) have a smaller layer thickness than that of the first layer (3).
- 30 6. Cantilever or membrane according to any previous claim, further including an optically reflective layer (11) for determining movement of the cantilever.
7. Cantilever or membrane according to the previous claim, wherein the optically reflective layer (11) is deposited on the first layer (7).
- 35 8. Cantilever or membrane according to claim 6, wherein the optically reflective layer (11) is sandwiched between the first layer (3) and the second layer (7).
9. Cantilever or membrane according to the previous claim, wherein the optically reflective layer (11) is deposited on an inner or outer surface of the first or second layer.
- 40 10. Cantilever according to any one of the previous claims, wherein the beam (8) includes a sensing tip (9, 19) formed by the second layer (5), or formed of a material different to that of the second (5) and third (7) layers.
- 45 11. Cantilever or membrane according to any one of previous claims 1 to 5 or 10, wherein the beam (8) further includes a sensing element (21) to detect the deflection of the beam (8).

12. Cantilever or membrane according to the previous claim, wherein the sensing element (21) extends substantially along a full length of the beam (8).
- 5 13. Cantilever or membrane according to the previous claim, wherein the cantilever further includes a first (23) and a second (25) metal layer sandwiching the sensing element (21) to measure a deflection of the beam (8).
- 10 14. Cantilever or membrane according to the previous claim, wherein the first metal layer (23) is located between the sensing element (21) and the third layer (7), and the second metal layer (25) is located between the sensing element (21) and the first layer (3).
- 15 15. Cantilever or membrane according to claim 11, wherein the sensing element (21) extends partially along a length of the beam (8).
- 16 16. Cantilever or membrane according to the previous claim, wherein the cantilever further includes a first metal layer (23) contacting a first portion of the sensing element (21) and a second metal layer (25) contacting a second portion of the sensing element (21) to measure a deflection of the beam (8).
- 20 17. Cantilever or membrane according to the previous claim, wherein the sensing element (21) and the first (23) and second (25) metal layers are attached to the third layer (7).
- 25 18. Cantilever or membrane according to the previous claim, wherein the sensing element (21) and the first (23) and second (25) metal layers are attached to an inner surface (33) of the third layer (7).
- 30 19. Cantilever or membrane according to claim 16, wherein the sensing element (21) and the first (23) and second (25) metal layers are attached to the second layer (5).
- 35 20. Cantilever or membrane according to the previous claim, wherein the sensing element (21) and the first (23) and second (25) metal layers are attached to an outer surface (41) of the second layer (5).
21. Cantilever or membrane according to claim 10, wherein the sensing tip is integrated into or integral with the second layer (5).
22. Cantilever or membrane according to any previous claim, wherein the first layer (3) includes a microfluidic channel.
- 40 23. Atomic force microscope, molecule detector, biosensor or multi-cantilever array including at least one cantilever or membrane according to any one of the previous claims.
- 45 24. Method for producing an elongated beam (8) of a cantilever or membrane comprising the steps of:
 - providing a first layer (3) comprising a first material;
 - providing a second layer (5) comprising a second material having an elastic modulus different to that of the first material;

- providing a third layer (7) comprising a third material having an elastic modulus different to that of the first material; and
- enclosing the first layer (3) between the second layer (5) and the third layer (7).

- 5 25. Method according to the previous claim, wherein the first material has an elastic modulus inferior to that of the second and third material; and/or the first material has a loss coefficient superior to that of the second and third material; and/or the first material has a density inferior to that of the second and third material.
- 10 26. Method according to claim 24, wherein the first material has an elastic modulus superior to that of the second and third material; and/or the first material has a loss coefficient inferior to that of the second and third material.
- 15 27. Method according to any one of previous claims 24 to 26, wherein the first material is a viscoelastic material.
28. Method for producing a cantilever or membrane comprising the steps of:
- providing a first wafer (43a) including a first layer (47a) deposited on a first external surface of the wafer and a second layer (47b) deposited on a second external surface of the wafer;
 - 20 - providing a second wafer (43b) including a first layer (47c) deposited on a first external surface of the wafer and a second layer (47d) deposited on a second external surface of the wafer;
 - forming a first structure by depositing a third layer (45) comprising a material having an elastic modulus inferior to that of the first (47a) and second layer (47b) on the first layer (47a) of the first wafer (43a);
 - 25 - forming a second structure by depositing a third layer (45) comprising a material having an elastic modulus inferior to that of the first (47c) and second layer (47d) on the first layer (47c) of the second wafer (43b);
 - wafer bonding the first and second structures together by combining the third layer (45) of the first structure with the third layer (45) of the second structure,
 - 30 - partially removing the exposed second layer (47b) on a first external surface of the bonded structure to expose the first wafer material (43a) and create a first etch mask window, and partially removing the exposed second layer (47d) on a second external surface of the bonded structure to expose the second wafer material (43b) and create a second etch mask window;
 - etching the exposed first wafer material (43a) and the exposed second wafer material (43b) to remove part of the first and second wafer material and expose a beam (48) including the combined third layers (45) sandwiched between the first layers (47a, 47c);
 - 35 - depositing an etch stop and support layer on the second wafer material (43b) and the first layer (47c) of the second wafer (43b);
 - etching through the beam (48) to divide the beam (48) in two parts; and
 - 40 - removing the etch stop and support layer.
29. Method according to claim 28, further including the step of depositing a reflective coating on the second wafer material (43b) and the first layer (47c) of the second wafer (43b).
- 45 30. Method according to claim 29, wherein in the step of providing a second wafer (43b) including a first layer (47c) deposited on a first external surface of the wafer and a second layer (47d) deposited on a second external surface of the wafer further includes a step of depositing a metal layer (51) to measure cantilever deflection on the first layer (47c) to partially cover the first layer

(47c), and a step of depositing a metal bonding pad (53) on the metal layer (51) to partially cover the metal layer (51), wherein the third layer (45) comprising a viscoelastic material is deposited on the first layer (47c), the metal bonding pad (53) and the metal layer (51).

- 5 31. Method according to claim 30, further including the step of etching the first layer (47a) and the third layer (45) of the beam (48) to expose the metal bonding pad (53).
- 10 32. Method according to claim 30 or 31, wherein during the step of wafer bonding, the third layer (45) flows to adapt to the extra topography presented by the metal bonding pad (53) and the metal layer (51).

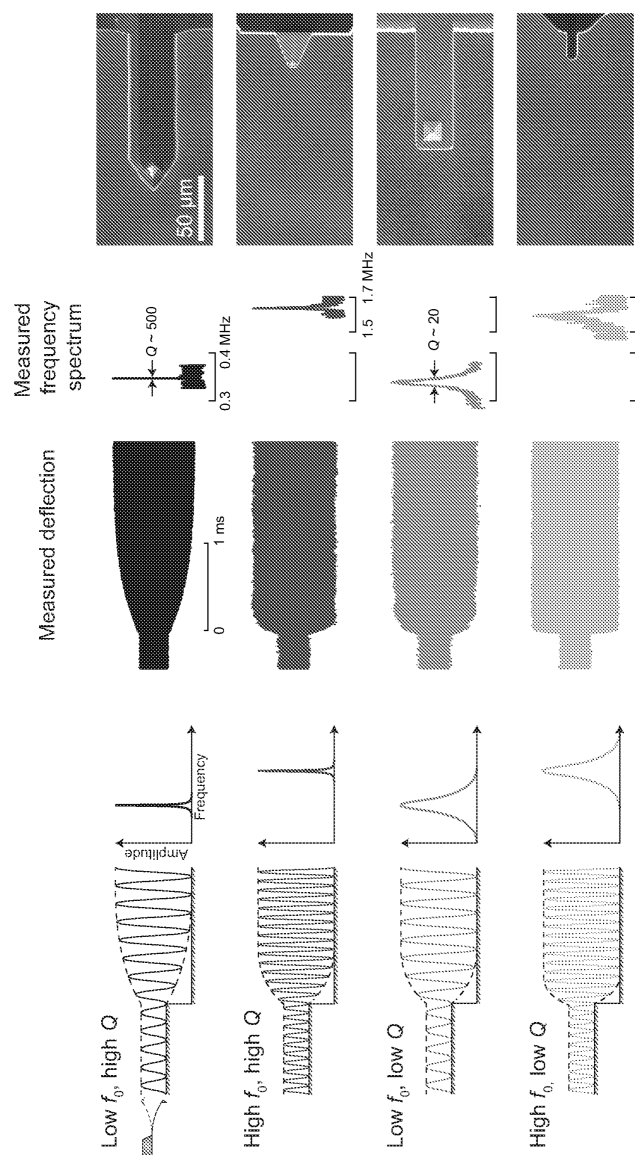


Figure 1

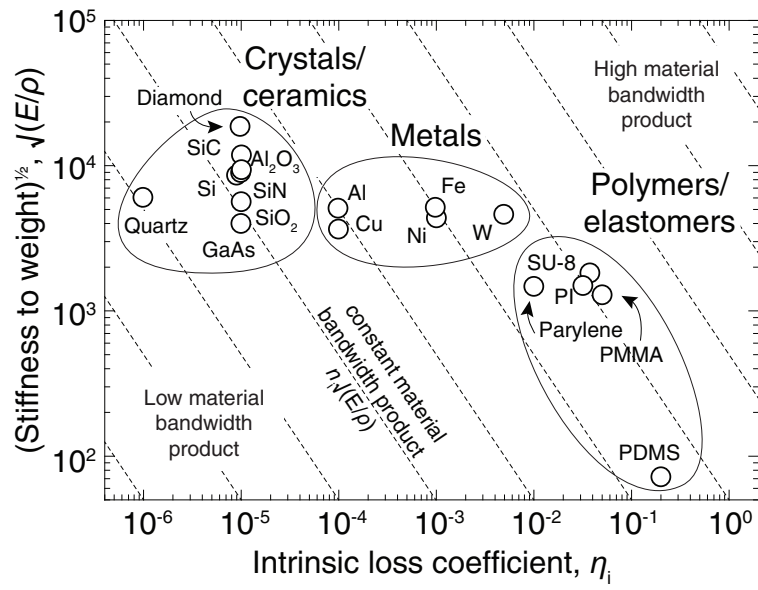


Figure 2

WO 2016/189451

PCT/IB2016/053013

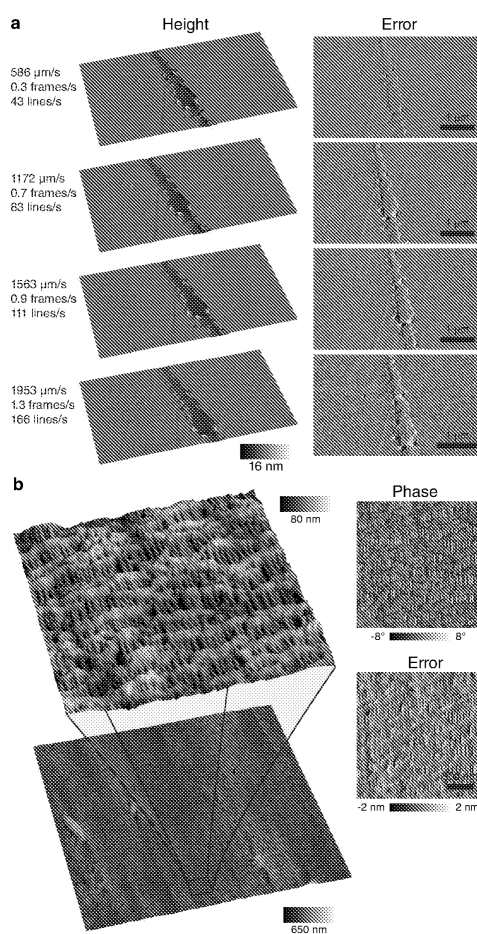


Figure 3

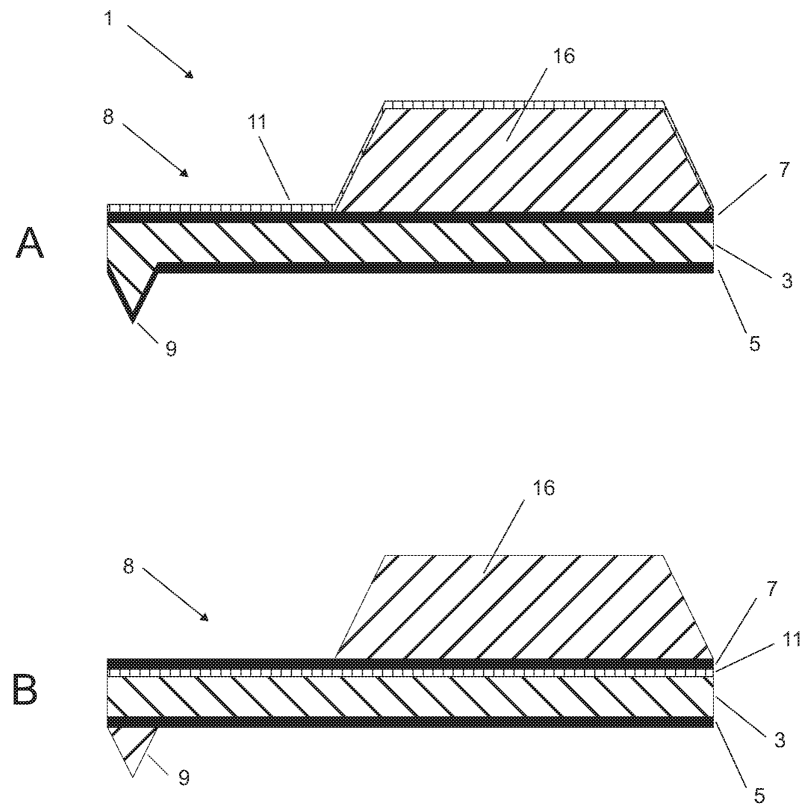


Figure 4a

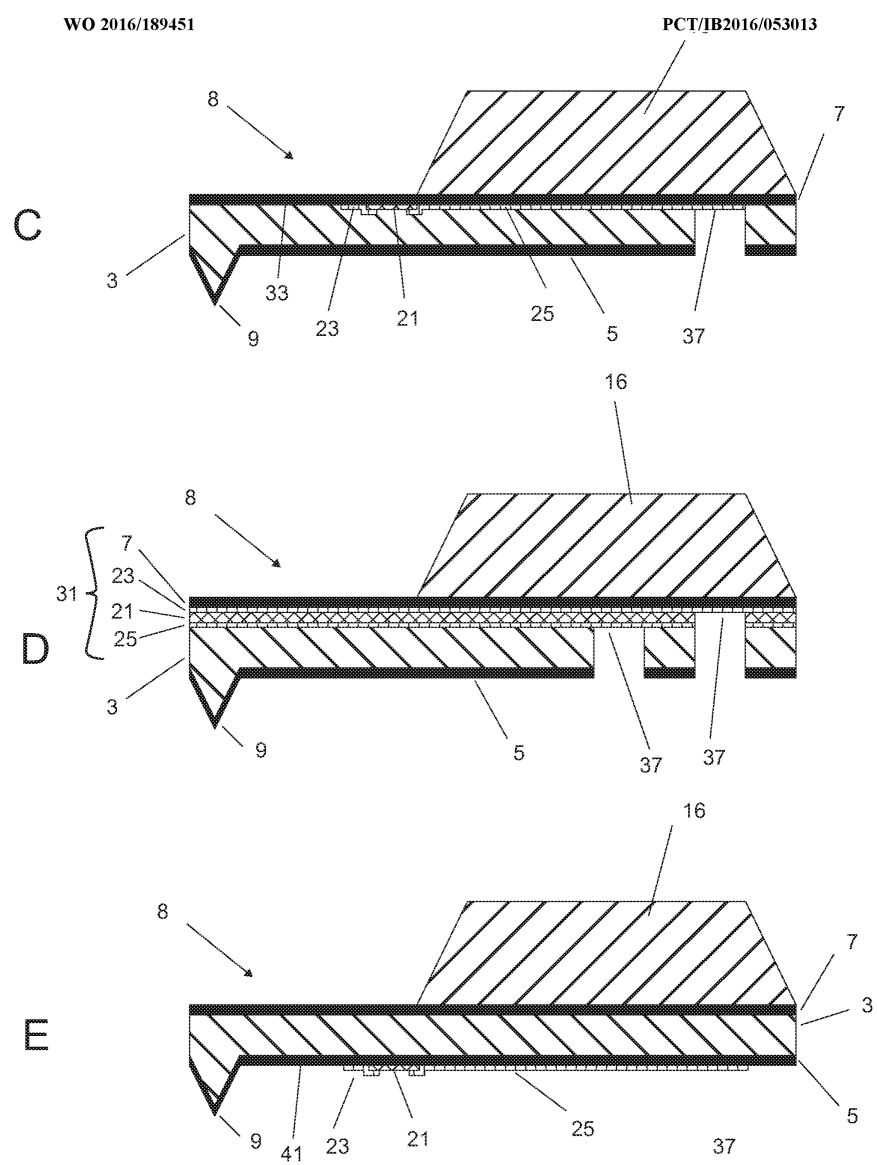


Figure 4b

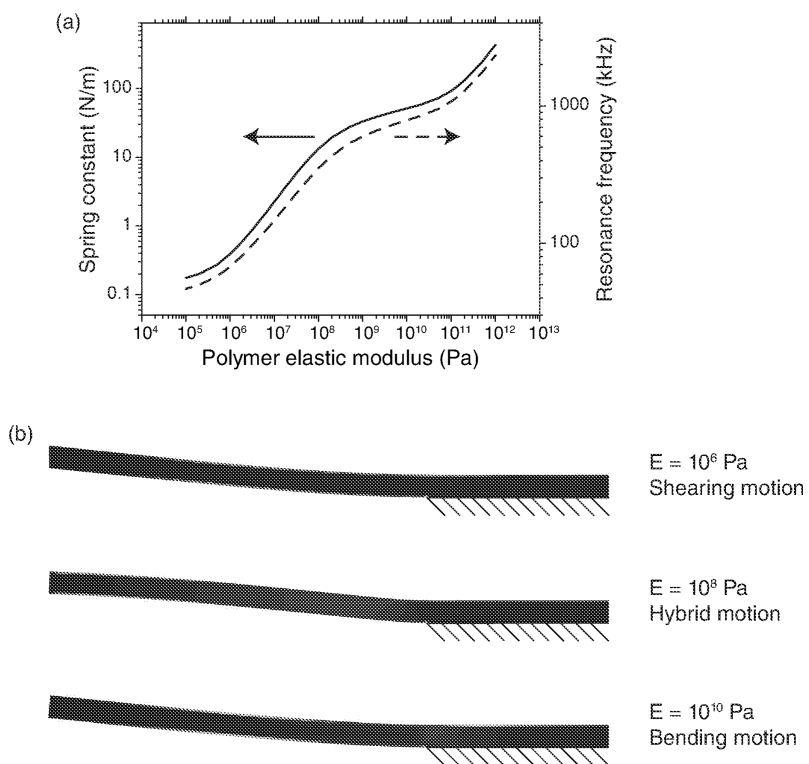


Figure 5

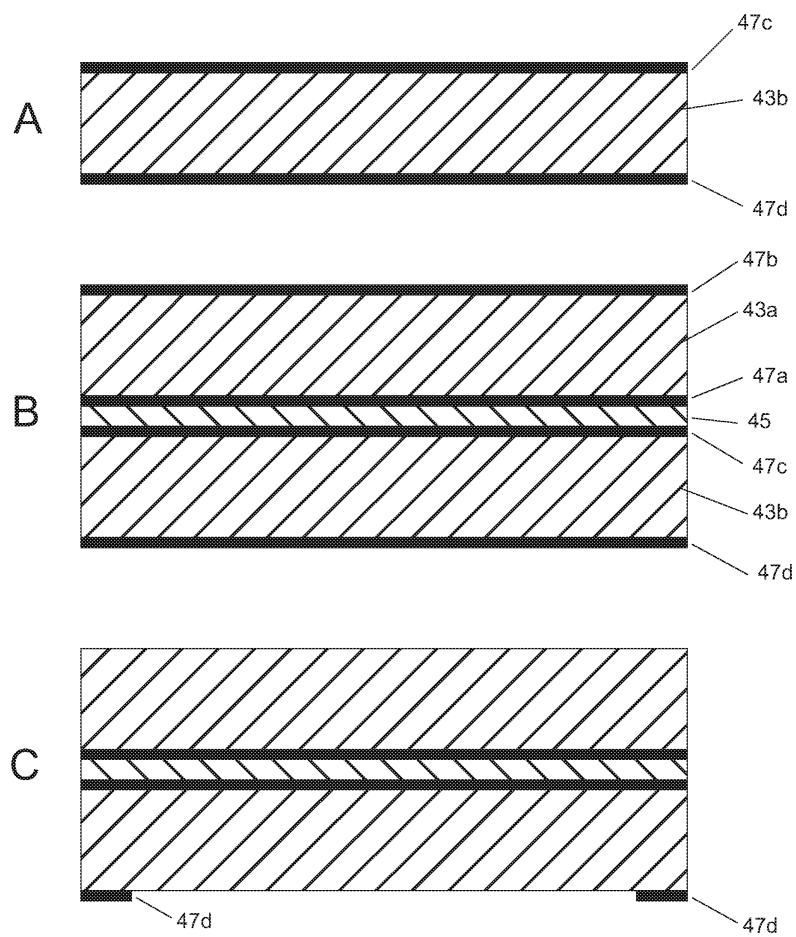


Figure 6a

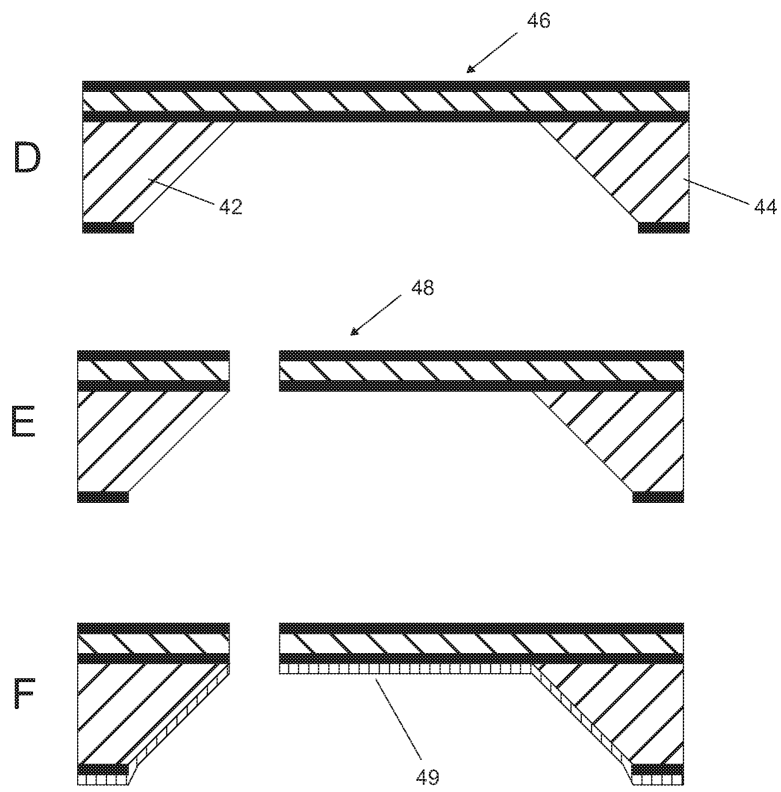


Figure 6b

WO 2016/189451

PCT/IB2016/053013

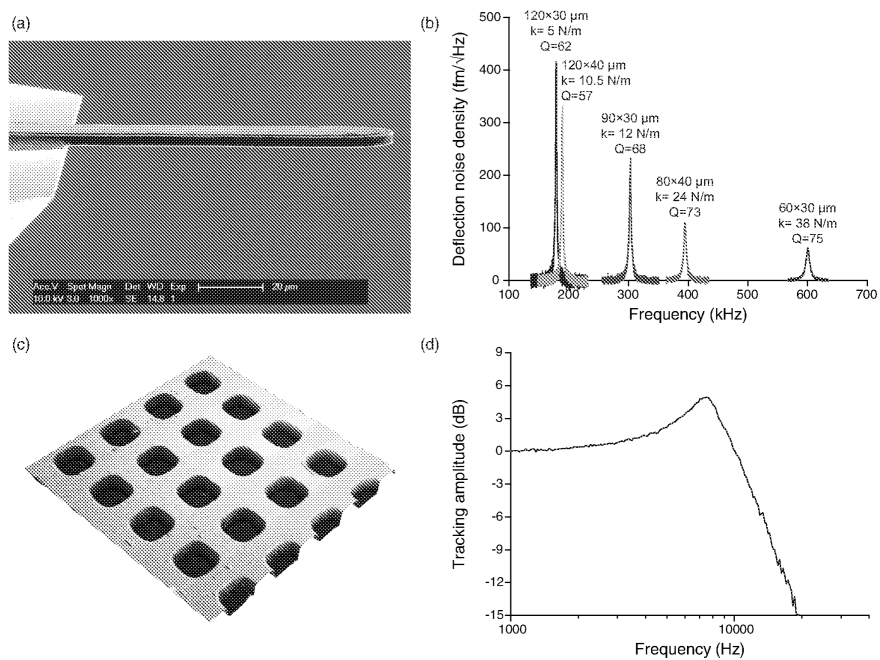


Figure 7

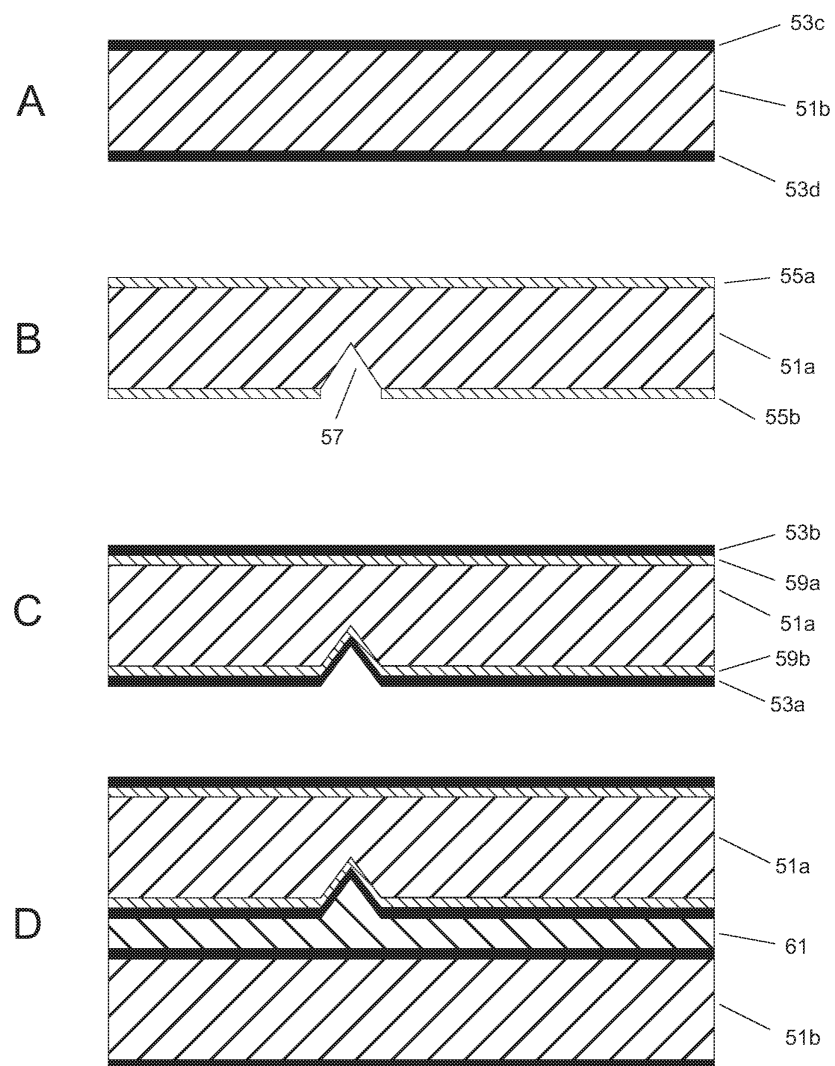


Figure 8a

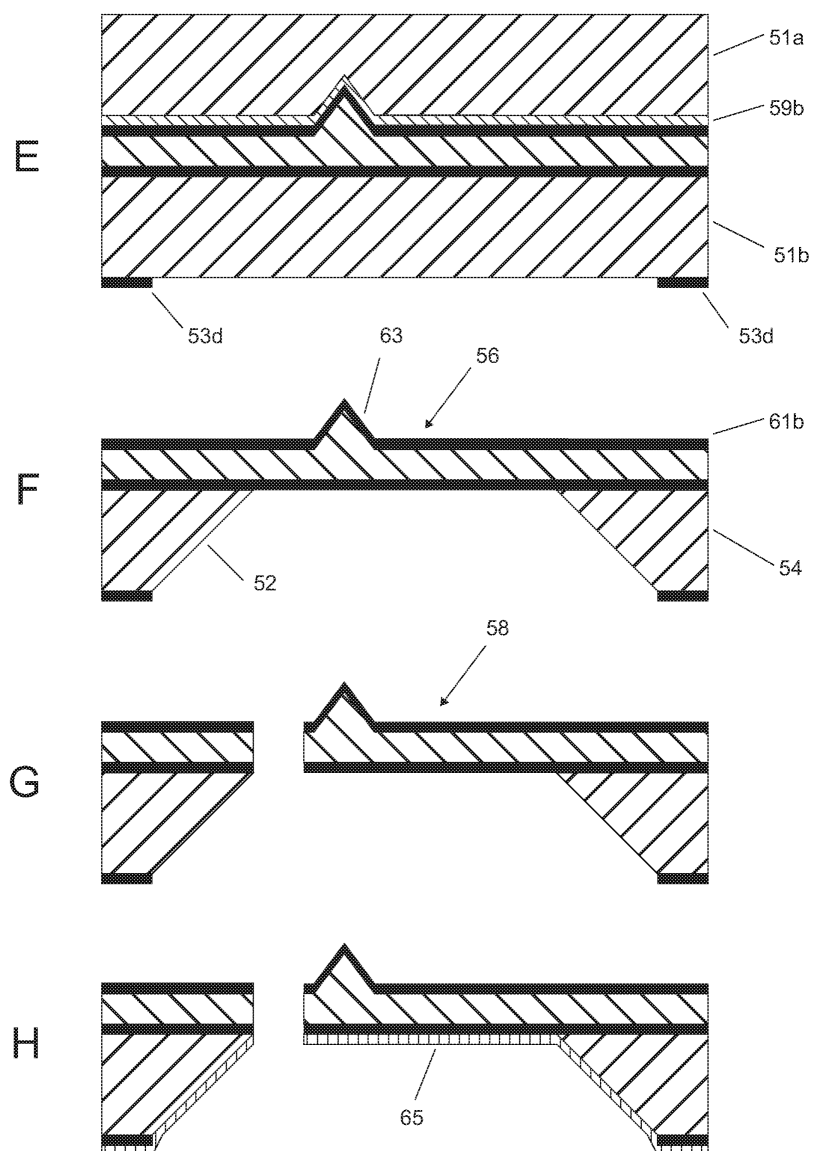


Figure 8b

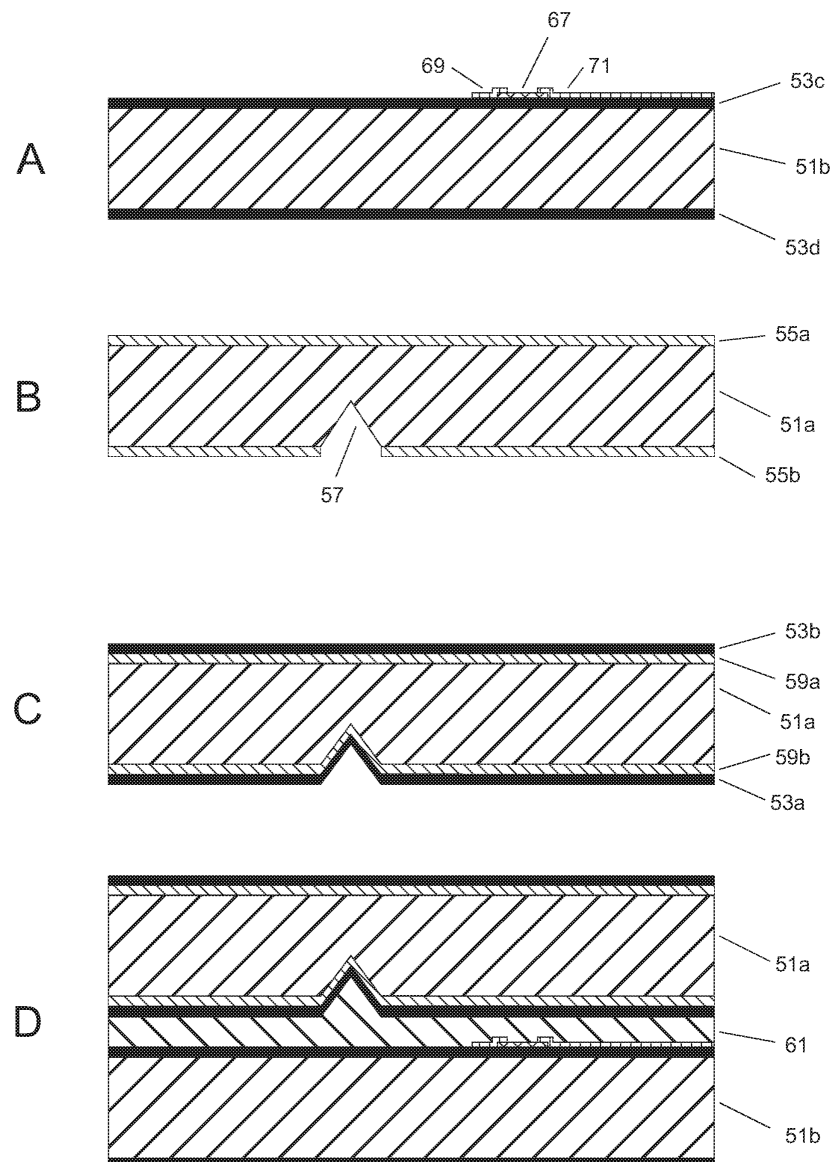


Figure 9a

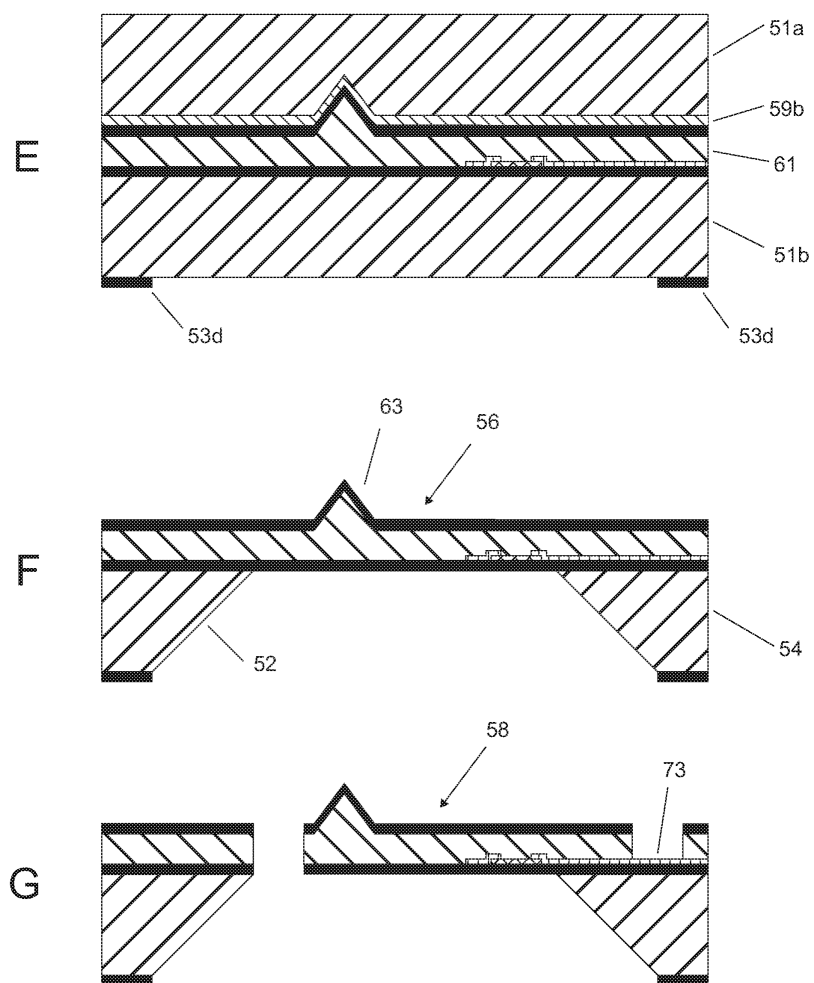


Figure 9b

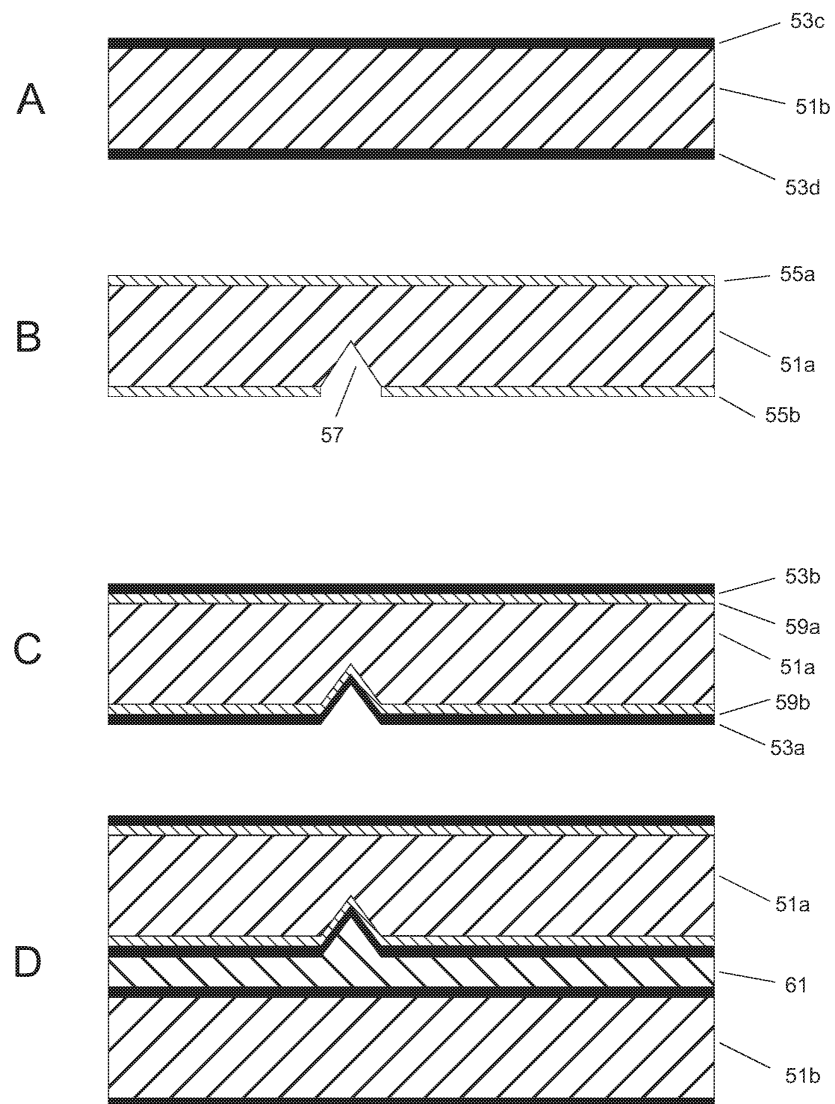


Figure 10a

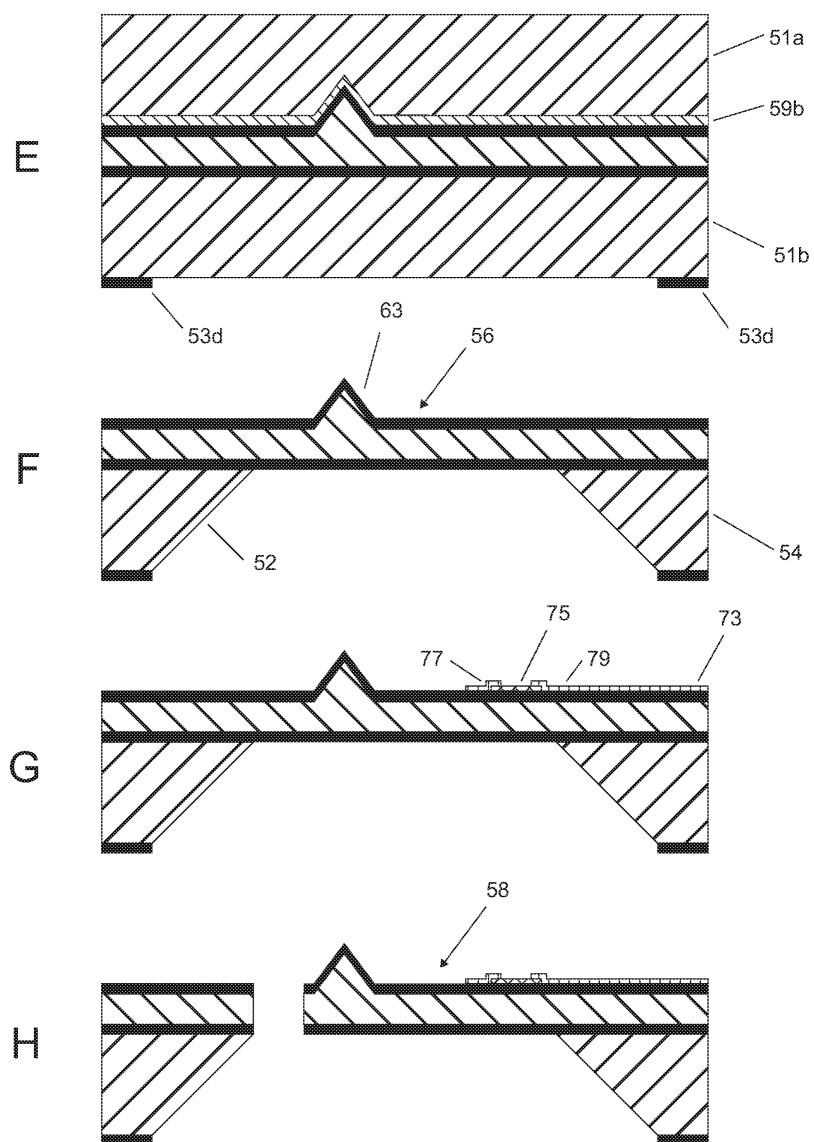


Figure 10b

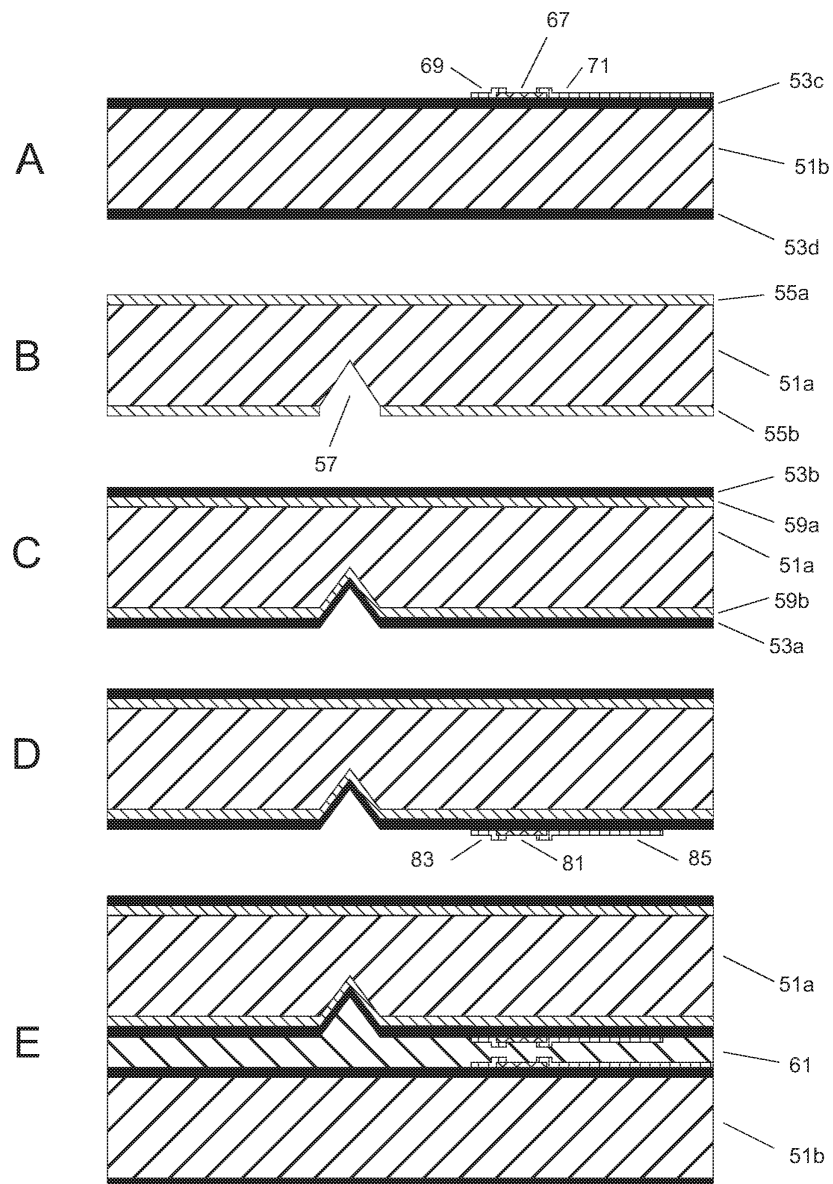


Figure 11a

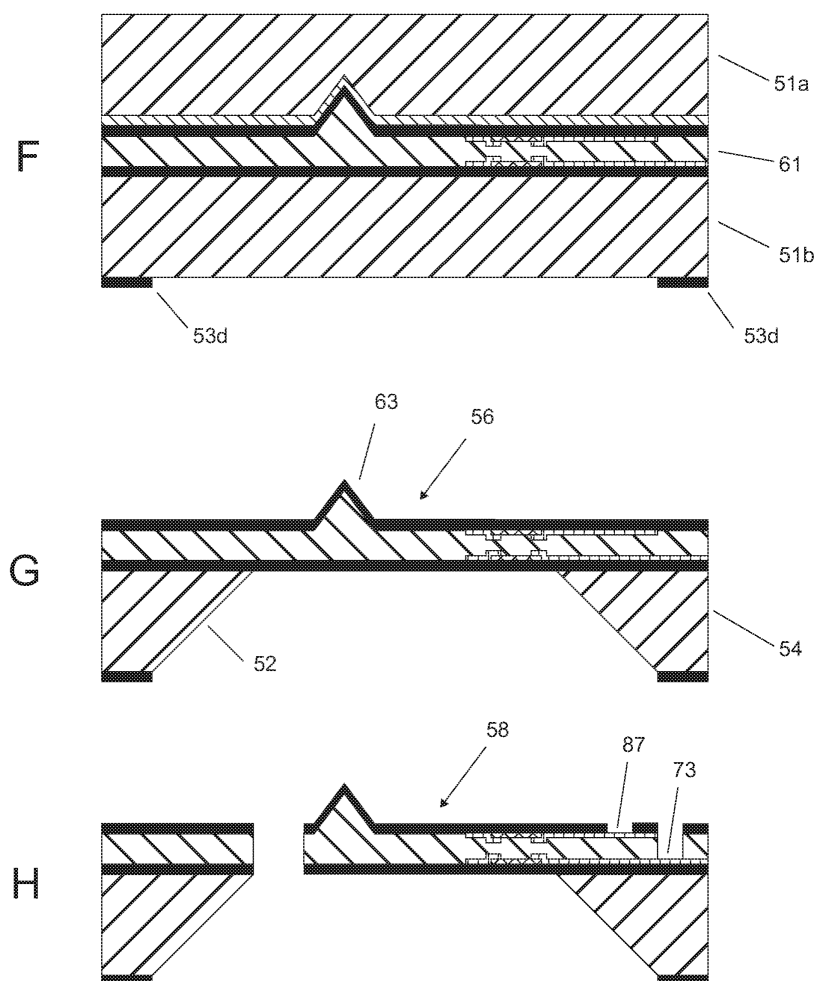


Figure 11b

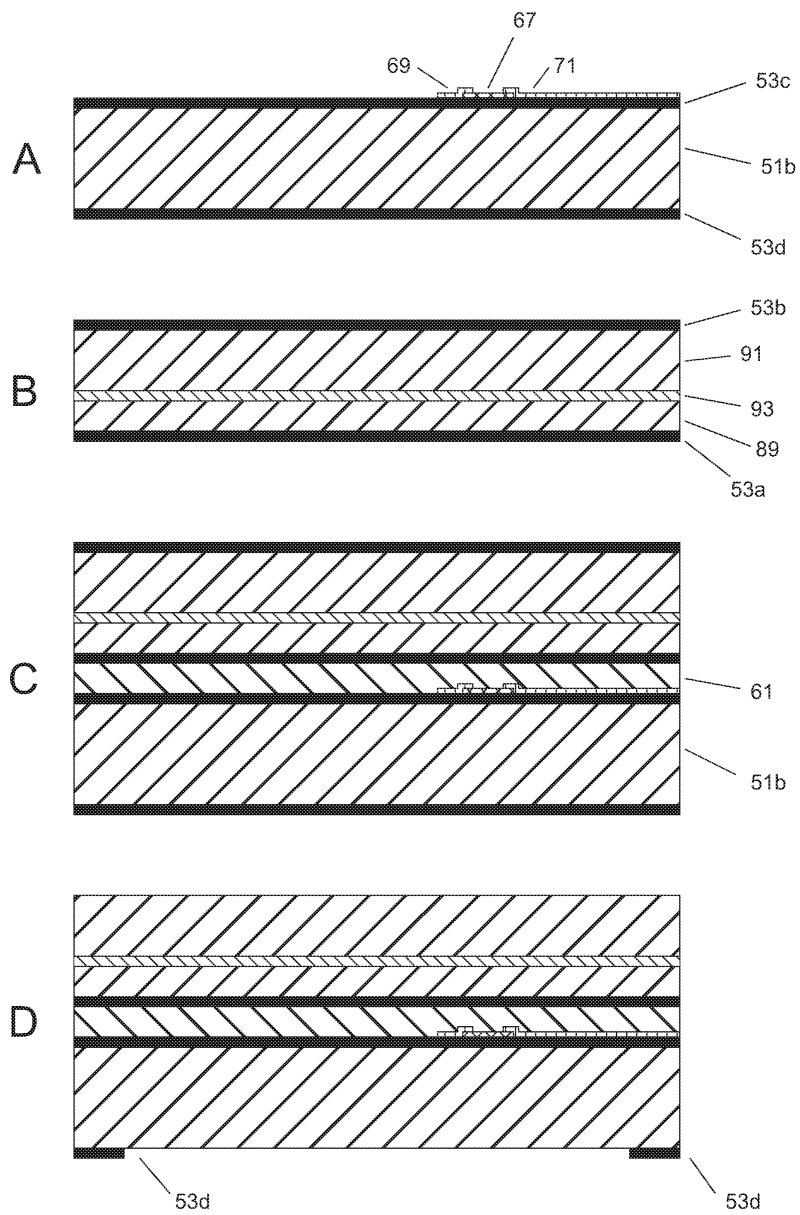


Figure 12a

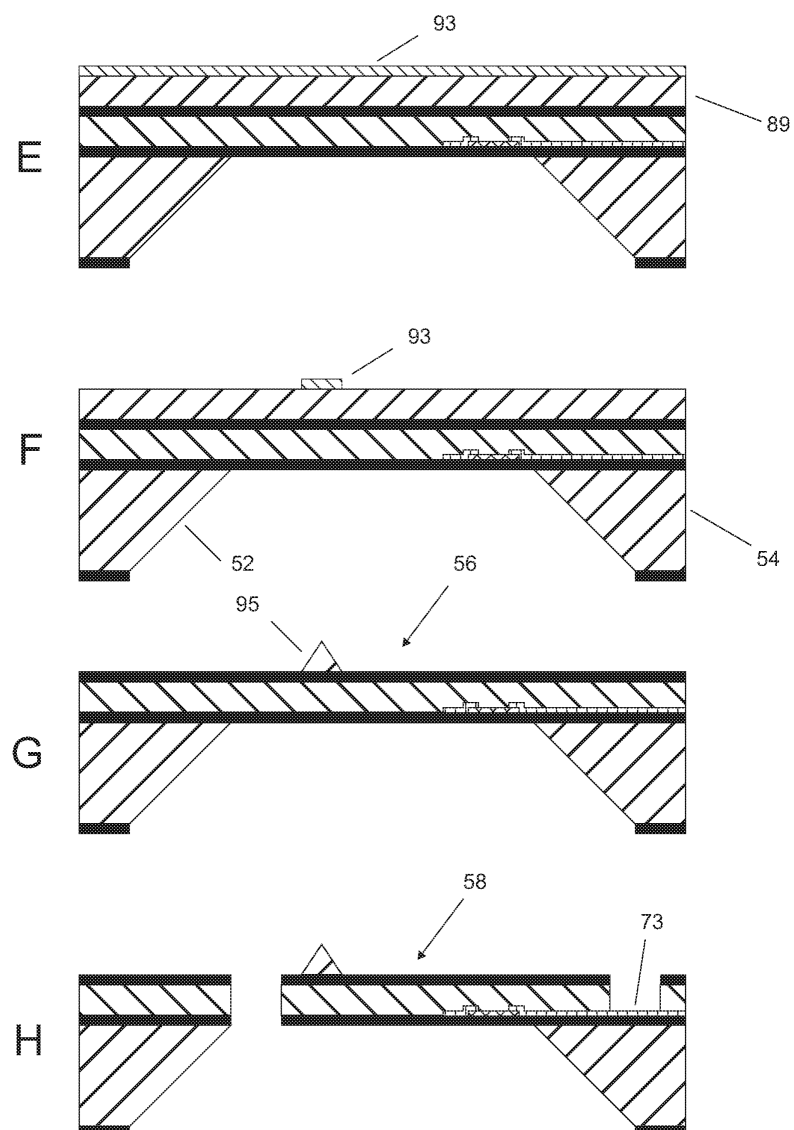


Figure 12b

WO 2016/189451

PCT/IB2016/053013

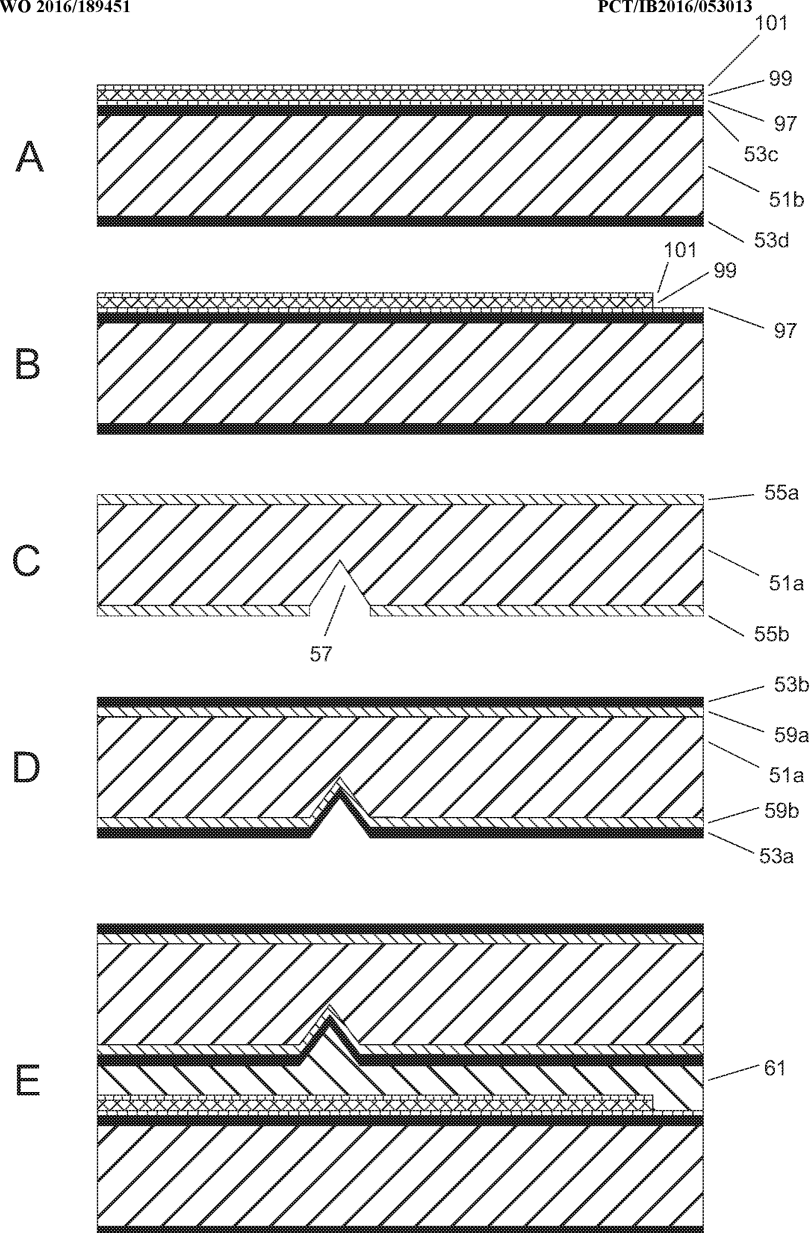


Figure 13a

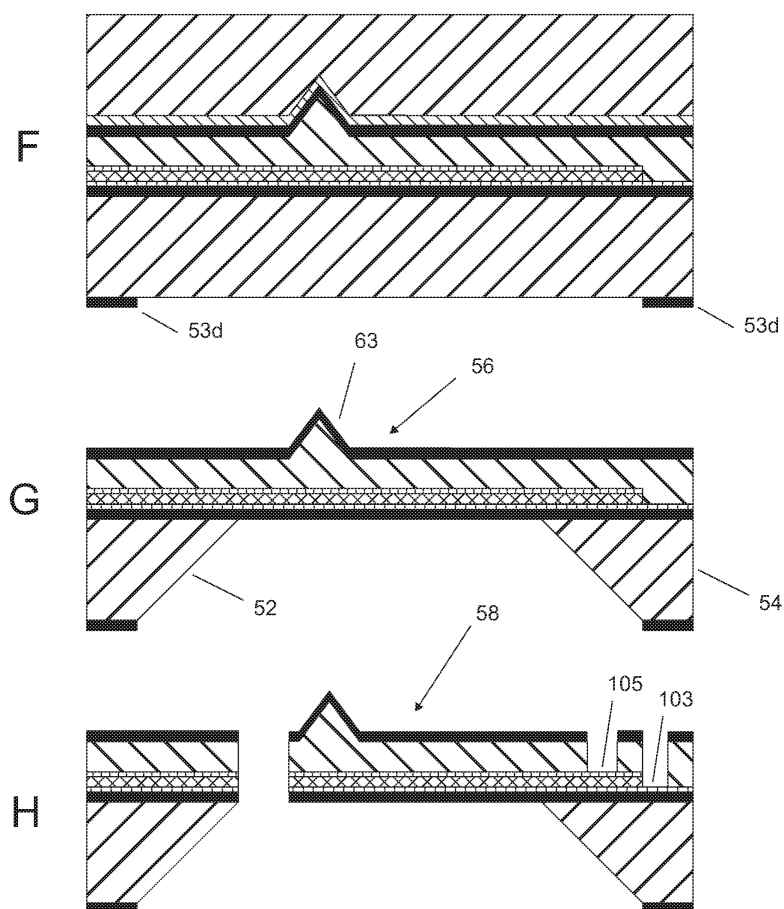


Figure 13b

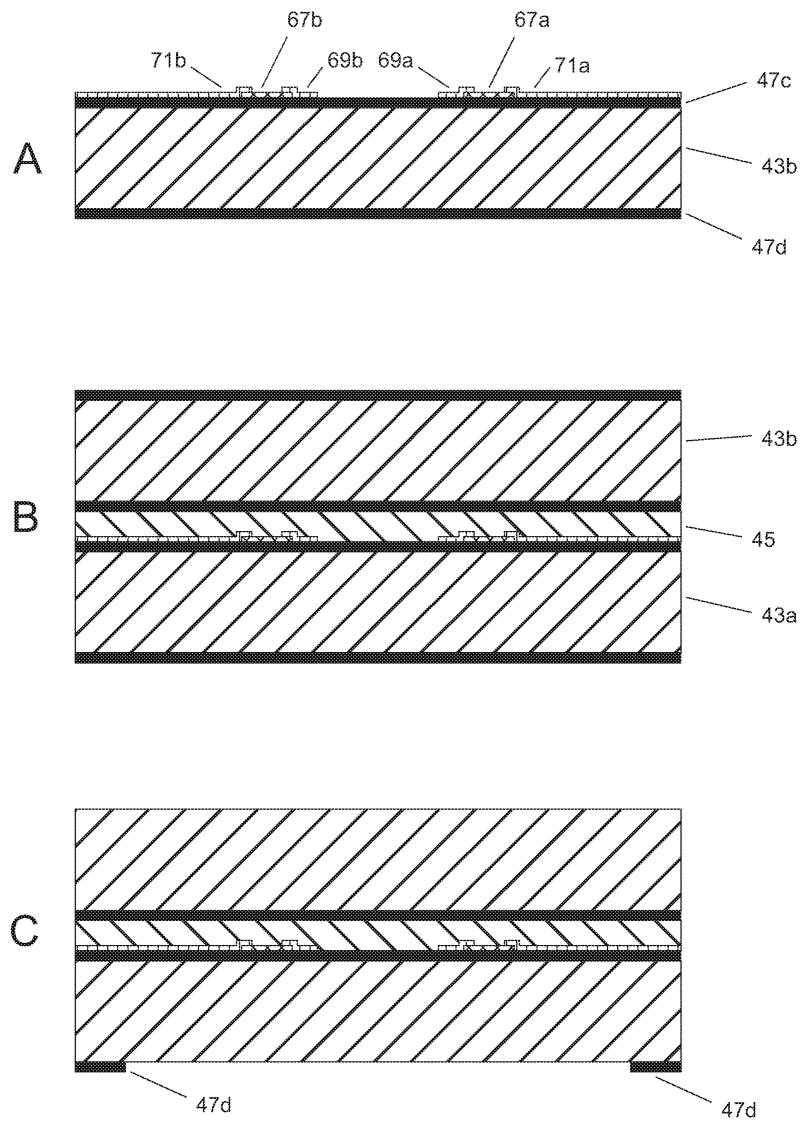


Figure 14a

WO 2016/189451

PCT/IB2016/053013

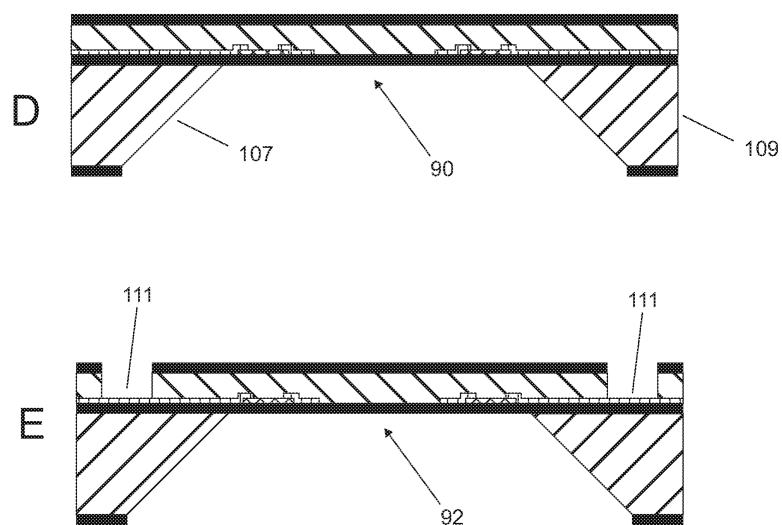


Figure 14b

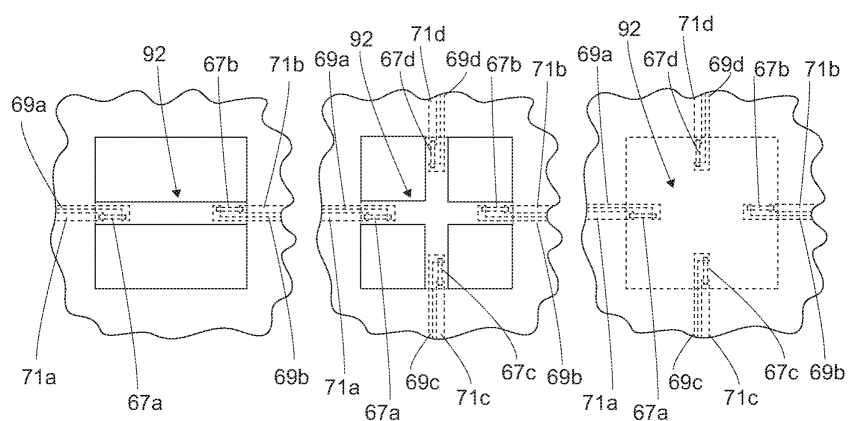


Figure 14c

WO 2016/189451

PCT/IB2016/053013

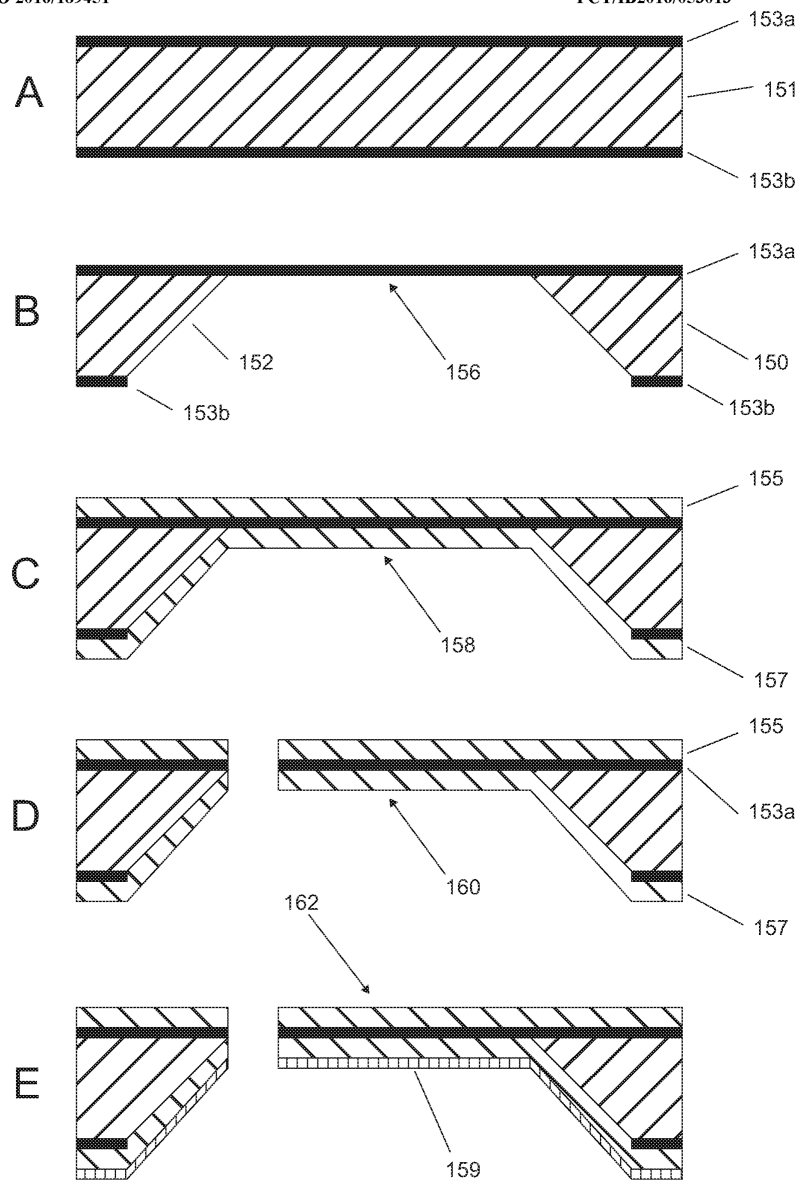


Figure 15

WO 2016/189451

PCT/IB2016/053013

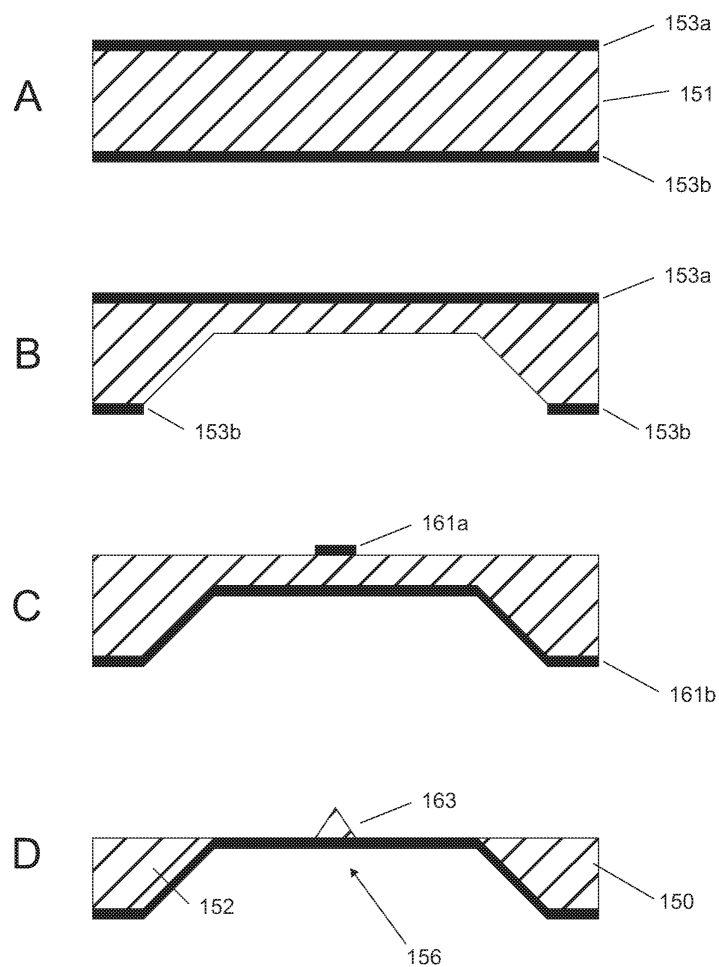


Figure 16a

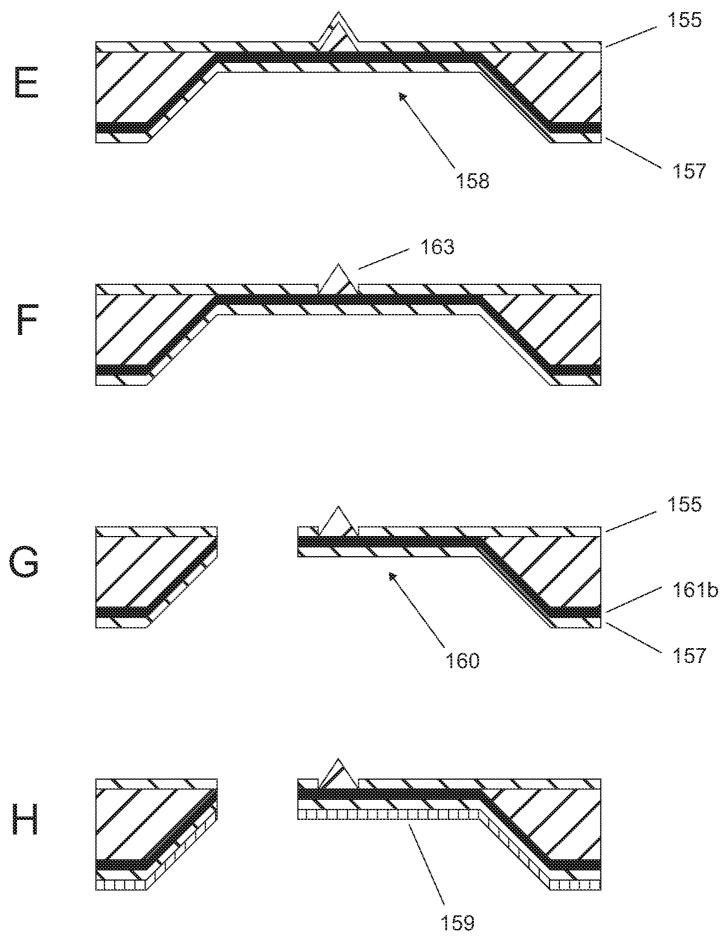


Figure 16b

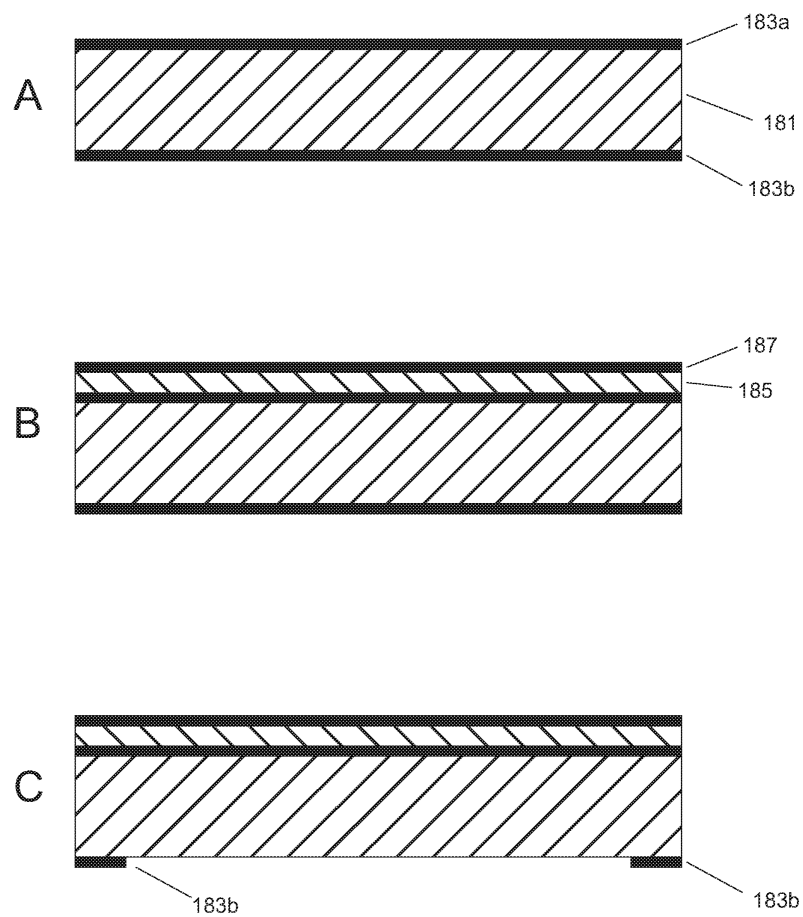


Figure 17a

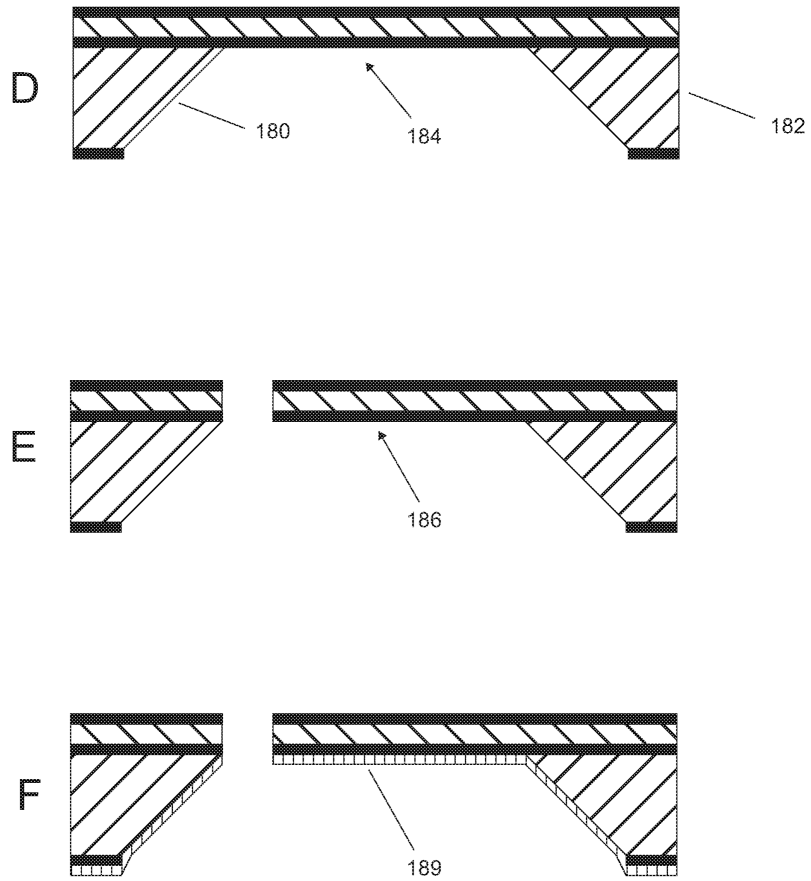


Figure 17b

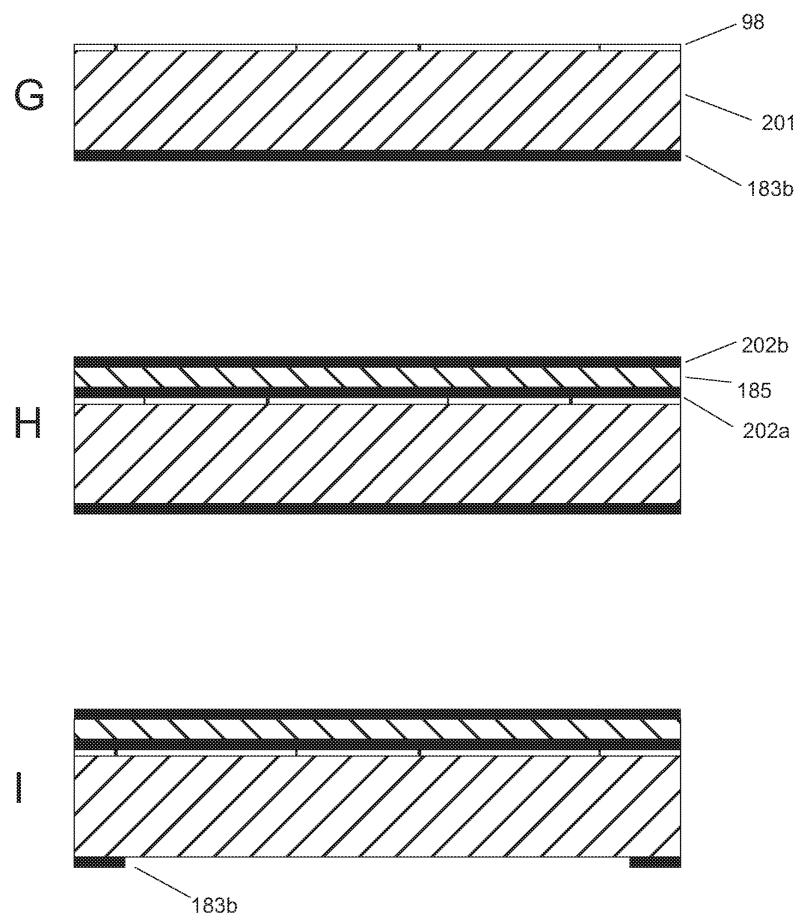


Figure 17c

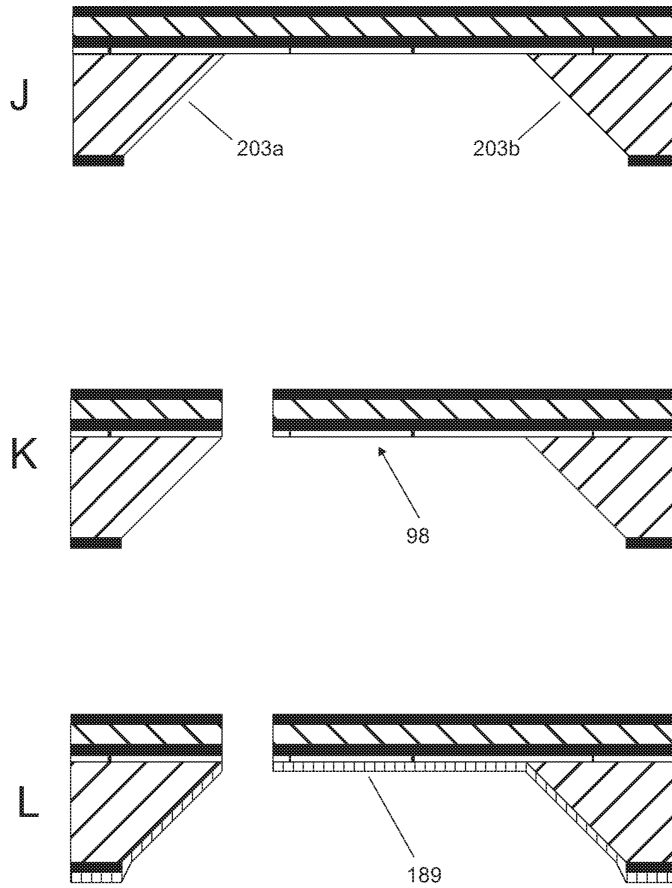


Figure 17d

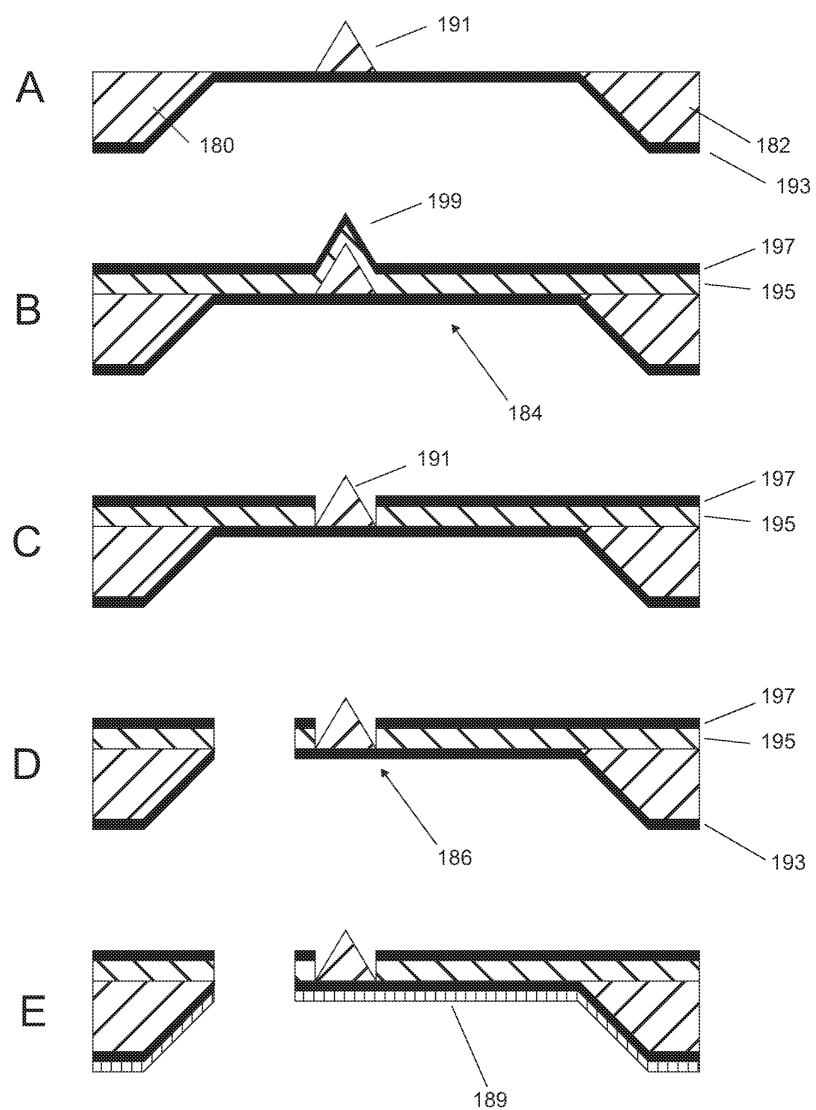


Figure 18

INTERNATIONAL SEARCH REPORT

 International application No
 PCT/IB2016/053013

A. CLASSIFICATION OF SUBJECT MATTER INV. G01Q60/38 B81B3/00 B81C1/00 G01Q70/14 ADD.		
According to International Patent Classification (IPC) or to both national classification and IPC		
B. FIELDS SEARCHED Minimum documentation searched (classification system followed by classification symbols) G01Q B81B B81C		
Documentation searched other than minimum documentation to the extent that such documents are included in the fields searched		
Electronic data base consulted during the international search (name of data base and, where practicable, search terms used) EPO-Internal, WPI Data		
C. DOCUMENTS CONSIDERED TO BE RELEVANT		
Category*	Citation of document, with indication, where appropriate, of the relevant passages	Relevant to claim No.
X	CN 104 155 478 A (INST ELECTRICAL ENG CAS) 19 November 2014 (2014-11-19) figures 2-4	1-3,5-26
Y		28-32
A		4,27
Y	----- US 2014/366230 A1 (WANG WEIJIE [US] ET AL) 11 December 2014 (2014-12-11) figures 5-12 paragraph [0076] - paragraph [0100] ----- -/--	28-32
<input checked="" type="checkbox"/> Further documents are listed in the continuation of Box C. <input checked="" type="checkbox"/> See patent family annex.		
* Special categories of cited documents : "A" document defining the general state of the art which is not considered to be of particular relevance "E" earlier application or patent but published on or after the international filing date "L" document which may throw doubts on priority claim(s) or which is cited to establish the publication date of another citation or other special reason (as specified) "O" document referring to an oral disclosure, use, exhibition or other means "P" document published prior to the international filing date but later than the priority date claimed "T" later document published after the international filing date or priority date and not in conflict with the application but cited to understand the principle or theory underlying the invention "X" document of particular relevance; the claimed invention cannot be considered novel or cannot be considered to involve an inventive step when the document is taken alone "Y" document of particular relevance; the claimed invention cannot be considered to involve an inventive step when the document is combined with one or more other such documents, such combination being obvious to a person skilled in the art "&" document member of the same patent family		
Date of the actual completion of the international search 30 August 2016		Date of mailing of the international search report 12/09/2016
Name and mailing address of the ISA/ European Patent Office, P.B. 5818 Patentlaan 2 NL - 2280 HV Rijswijk Tel. (+31-70) 340-2040, Fax: (+31-70) 340-3016		Authorized officer Polesello, Paolo

Form PCT/ISA/210 (second sheet) (April 2005)

INTERNATIONAL SEARCH REPORT

International application No
PCT/IB2016/053013

C(Continuation). DOCUMENTS CONSIDERED TO BE RELEVANT		
Category*	Citation of document, with indication, where appropriate, of the relevant passages	Relevant to claim No.
X	LIN ET AL: "Characterization and numerical evaluation of vibration on elastic-viscoelastic sandwich structures", COMPOSITE STRUCTURES, ELSEVIER SCIENCE LTD, GB, vol. 92, no. 3, 1 February 2010 (2010-02-01), pages 669-675, XP026747575, ISSN: 0263-8223, DOI: 10.1016/J.COMPSTRUCT.2009.09.025 [retrieved on 2009-09-19]	1-5,11, 15,24-27
A	figure 1 table 1 paragraph [0005] - paragraph [0006] paragraph [0008] -----	6-10, 12-14, 16-23, 28-32
X	SHUNJI WATANABE ET AL: "MICRO-FABRICATED PIEZOELECTRIC CANTILVER FOR ATOMIC FORCE MICROSCOPY", REVIEW OF SCIENTIFIC INSTRUMENTS, AIP, MELVILLE, NY, US, vol. 67, no. 11, 1 November 1996 (1996-11-01), pages 3898-3903, XP000635847, ISSN: 0034-6748, DOI: 10.1063/1.1147290 cited in the application	1-3, 5-21, 23-26
A	figures 3,4,6-8 paragraph [0111] -----	4,22, 27-32

1

Form PCT/ISA/210 (continuation of second sheet) (April 2005)

page 2 of 2

INTERNATIONAL SEARCH REPORT				International application No	
Information on patent family members				PCT/IB2016/053013	
Patent document cited in search report		Publication date	Patent family member(s)		Publication date
CN 104155478	A	19-11-2014	NONE		

US 2014366230	A1	11-12-2014	CN	104755942 A	01-07-2015
			EP	2898332 A1	29-07-2015
			JP	2015526743 A	10-09-2015
			US	2014068823 A1	06-03-2014
			US	2014366230 A1	11-12-2014
			WO	2014035974 A1	06-03-2014

12. CV

PERSONAL INFORMATION

Born: June 23th, 1985
 Civil status: Married, one child
 Address: Rue de Bassenges, 3B
 CH-1024 Ecublens, Switzerland

 Phone: +41 789 36 13 68
 e-mail: nahid.hosseini@epfl.ch



EDUCATION

2013-Present	PhD candidate in Microsystems and Microelectronics, Ecole Polytechnique Fédérale de Lausanne (EPFL), Lausanne, Switzerland.
2009-2012	Master in Microelectronic devices, Sharif University of Technology, Tehran, Iran.
2003-2008	Bachelor in Electrical Engineering, Sharif University of Technology, Tehran, Iran.

ACADEMIC EXPERIENCE

- | | |
|--------------|--|
| 2015-Present | <ul style="list-style-type: none"> A novel microfabrication platform for hermetically sealed, hybrid multilayer MEMS. Integration of sharp silicon nitride tips into high-speed SU8 cantilevers in a batch fabrication process. Batch fabrication of multilayer polymer cantilevers with integrated hard tips for high-speed atomic force microscopy. |
|--------------|--|

Obtained skills:

Clean room fabrication: Wet/dry etching, Photo/e-beam lithography, thin film deposition, wafer bonding, lift-off process, Electron beam induced deposition, and wire bonding.

Instrumentation: Low noise electronics, low noise AFM, high-speed AFM, Multiple scanning techniques like MFM and KPFM.

- Air and Water-Stable N-Type Doping and Encapsulation of Flexible MoS₂ Devices With SU8.
- Fabrication of self-sensing SU8 cantilevers based on MoS₂ piezoresistors.

Obtained skills:

Fabrication of MoS₂ based thin film transistors, electrical

measurements in vacuum.

- | | |
|-----------|---|
| 2015-2016 | <ul style="list-style-type: none"> Correlated AFM-SEM-FIB, a novel platform for nanomechanical mapping of polymer composites. <p><i>Obtained skills:</i>
Simultaneous AFM-SEM-FIB, Nanomechanical characterization, 3D imaging construction.</p> |
| 2014-2015 | <ul style="list-style-type: none"> Rise time reduction of thermal actuators operated in air and water through optimized pre-shaped open loop driving (In collaboration with Stanford university). <p><i>Obtained skills:</i>
System identification, linear and non-linear control engineering, digital and analogue filter design.</p> |
| 2013-2014 | <ul style="list-style-type: none"> A monolithic MEMS position sensor for closed-loop high-speed atomic force microscopy. <p><i>Obtained skills:</i>
Control engineering of closed loop systems, Assembly of AFM scanner, LABVIEW FPGA, characterization of piezoresistive position sensors, handling fragile MEMS devices.</p> |

RESEARCH INTERESTS

- Micro and Nanofabrication
 - Process Flow Design
 - Low noise Instrumentation
-

HIGHLIGHTED PUBLICATIONS

1. Hosseini N, Nievergelt AP, Adams JD, Stavrov VT, Fantner GE. A monolithic MEMS position sensor for closed-loop high-speed atomic force microscopy. *Nanotechnology*. 2016 Feb 22; 27(13):135705.
 2. Fantner GE, Adams JD, Hosseini N. Multilayer MEMS cantilevers (No. EPFL-PATENT-228130) 2016.
 3. Nievergelt AP, Erickson BW, Hosseini N, Adams JD, Fantner GE. Studying biological membranes with extended range high-speed atomic force microscopy. *Scientific reports*. 2015 Jul 14;5:11987.
 4. Larsen T, Doll JC, Loizeau F, Hosseini N, Peng AW, Fantner GE, Ricci AJ, Pruitt BL. Rise time reduction of thermal actuators operated in air and water through optimized pre-shaped open loop driving. *Journal of Micromechanics and Microengineering*. 2017 Feb 24; 27(4):045005.
 5. Kung YC*, Hosseini N*, Dumcenco D, Fantner GE, Kis A. Air and Water-Stable n-Type Doping and Encapsulation of Flexible MoS₂ Devices with SU8. *Advanced Electronic Materials*. 2019 Jan; 5(1):1800492.
 6. Hosseini N, Neuenschwander M, Peric O, Andany SH, Adams JD, Fantner GE. Integration of sharp silicon nitride tips into high-speed SU8 cantilevers in a batch fabrication process. In revision, *Beilstein journal of nanotechnology* (2019).
-

-
7. Hosseini N, Peric O, Neuenschwander M, Andany SH, Adams JD, Fantner GE. Batch fabrication of multilayer polymer cantilevers with integrated hard tips for high-speed atomic force microscopy. Submitted to Proceedings of the IEEE International Conference, *Transducers-2109*.
 8. Hosseini N, Neuenschwander M, Andany SH, Peric O, Adams JD, Fantner GE. A novel microfabrication platform for hermetically sealed hybrid multilayer self-sensing AFM cantilevers. Manuscript in preparation to be submitted to peer-reviewed journal, *Nature Nanotechnology*.
 9. Hosseini N, Andany SH, Hannebelle M, Winkler R, Plank H, Fantner GE. Correlated AFM-SEM-FIB, a novel platform for 3D nanomechanical mapping of polymer composites. Manuscript in preparation to be submitted to peer-reviewed journal, *Small*.
-

REFERENCES

Name	Function	Contact
Prof. Georg Fantner	Associate Professor	georg.fantner@epfl.ch +41 21 69 36431
Prof. Beth Pruitt	Full professor	blp@engineering.ucsb.edu +1 (805) 893-5115
Prof. Andras Kis	Associate Professor	andras.kis@epfl.ch +41 21 69 33925
